Polymer Electrolyte Discovery via Rational Design and High Throughput Methods

by

Michael A. Stolberg

Submitted to the Department of Materials Science and Engineering in partial fulfillment of the requirements for the degree(s) of

Doctor of Philosophy

at the

Massachusetts Institute of Technology

June, 2023

Authored by: Michael A. Stolberg
Department of Materials Science and Engineering
May 19th, 2023

Certified by: Jeremiah A. Johnson
Department of Chemistry
Thesis Advisor

Yang Shao-Horn
Department of Materials Science and Engineering
Thesis Advisor

Accepted by: Robert J. Macfarlane
Chair
Departmental Committee on Graduate Studies

Polymer Electrolyte Discovery via Rational Design and High Throughput Methods

by

Michael A. Stolberg

Submitted to the Department of Materials Science and Engineering on May 19th, 2023 in partial fulfillment of the requirements for the degree of Doctor of Philosophy

ABSTRACT

Storage of electrical energy is a cornerstone in the global endeavor to lower greenhouse gas emissions—in particular, electrochemical energy storage in the form of batteries can enable the electrification of transport through electric vehicles, as well as aid the transition to renewable energy generation such as wind and solar through stabilizing the grid and mitigating intermittency. Lithium-ion batteries, a pioneering technology to enable portable electronics, are seeing increased use in transportation and grid-scale applications due to their high energy density, and greatly decreasing production costs over the past decade. However, current lithium-ion batteries are reaching the theoretical energy density and must adhere to higher safety standards as they see use in larger scale formats. The next generation of cheaper, safer, and more energy-dense batteries will be enabled by advances in electrolytes which are the focus of this work.

In this thesis, we focus on solid polymer electrolytes, which have the potential to enable more energy-dense batteries, and display improved safety compared to the highly flammable and toxic liquid electrolytes in use today. We detail our work in two main areas: the rational design of highly dissociative ionenes, and the development of a high throughput platform to increase the scale and speed of polymer electrolyte research. In the former, we investigate the impact of anion dissociation energy on ion conduction in solid polymer electrolytes via a novel class of ionenes prepared using acyclic diene metathesis polymerization of highly dissociative, liquid crystalline, fluorinated aryl sulfonimide-tagged ("FAST") anion monomers. These polyanions form well-ordered lamellae that are thermally stable and provide anionic channels for ion hopping. Electrochemical impedance spectroscopy and differential scanning calorimetry experiments, along with nudged elastic band calculations, suggest that cation motion in these materials operates via an ion hopping mechanism, which is enabled by the highly dissociative nature of FAST anions. In parallel, we developed a high throughput platform to accelerate electrolyte research. We detail the engineering problems and solutions which resulted in an estimated 100X increase in sample throughput with vastly less researcher effort. The platform is then leveraged in two case studies, first by performing the largest one-to-one comparison of lithium and sodium ion conduction in poly(ethylene oxide) to date, and secondly, the platform is employed in a machine learning-guided Bayesian optimization system to explore and optimize the ionic conductivity of electrolytes based upon poly(caprolactone). This work sets the stage for continued automation and data-driven design of polymer electrolytes for safer and more energy-dense batteries.

Thesis supervisor: Jeremiah A. Johnson
Title: Professor of Chemistry

Thesis supervisor: Yang Shao-Horn
Title: JR East Professor of Engineering

ACKNOWLEDGEMENTS

A Ph.D. is not an endeavor to be undertaken lightly; it is mentally, physically, and even spiritually exhausting, and often does not ever seem like the end is in sight. Looking back on the past five years, it has been the people around me that have not only made this undertaking doable but at many times, dare I say, enjoyable. Through the good and the bad, our support networks allow us to be our best selves, and achieve the loftiest of goals. So, I would like to thank the people who have mentored, helped, and even just grabbed coffee (or a beer!) along the way.

I would first like to thank my parents and brother for the constant, unwavering, sometimes overwhelming but always good-intentioned support. Without their love and guidance, I would never have even gotten admitted to MIT, much less felt secure moving so far away from home, and eventually succeeding in obtaining my Ph.D. For always having my back, and always being available to talk through hard situations and vent when needed, I give my thanks. And to my grandfather, who attended MIT but never graduated and coincidentally passed away while I was on my visit weekend for graduate school admission it feels like fate, and I hope I have done him proud. I would also like to thank my partner for the majority of my time in grad school, Brianna, who gave constant support and love.

Next, I would like to thank the various mentors I have had throughout the years, both formal and informal. Yivan Jiang and Shuting Feng helped me to get situated in the Johnson and Shao-Horn labs respectively, and without them, I would have been quite lost. Megan Hill, Nate Oldenhuis, Chris Brown, and Jeffrey Lopez were all incredibly influential mentors for me, often not just for my projects but for help with my thought processes, writing, and just learning to become a better scientist overall. I am so grateful for all the guidance they gave and the friendship they provided (and continue to do so!)

And finally, I would like to thank my two advisors Jeremiah and Yang. Both have taught me so incredibly much throughout my time at MIT and I could not imagine being part of different labs! I thank you for the freedom to pursue my scientific interests, guidance on how to achieve milestones, and especially how to deal with “less than ideal collaborators”. The support and advocacy do not go unappreciated.

The Johnson and Shao-Horn groups have been home for the past five years, even through some of the strangest times any of us have seen in our lives to date, and it is due to the people within them that makes going to the lab every day enjoyable. While they often seem insignificant at the time, talking through science or just shooting the shit over some coffee has likely led to more advances than any sub-group meeting ever has. Furthermore, it has created friendships I am excited to continue outside of grad school and on for a lifetime. To all these people and those who I undoubtedly missed, I thank you!

-Michael A. Stolberg

CONTENTS

LIST OF FIGURES

LIST OF TABLES

CHAPTER 1 INTRODUCTION

THE GLOBAL NEED FOR ENERGY STORAGE

It is no secret that climate change brought on by increased greenhouse gas emissions has become the most pressing scientific challenge of the current day. Rising temperatures and sea levels, vanishing ice sheets and species, increased power of natural disasters, and even increased spread of disease have all been linked to climate change caused by human industrialization.[1] Global climate change, in addition to causing tremendous loss of life, is also predicted to have huge impacts on the global economy.[2] The World Economic Forum estimates that over half of the world's total GDP is at risk if climate change is not addressed.[2] On the other hand, it also represents an immense opportunity with investments into climate-change mitigating practices and technology worth more than an estimated $10 trillion annually.[2] While significant change is required from policy-makers globally to both mitigate and incentivize positive climate action, one way in which scientists can play a part is by developing the next generation of materials and technologies to combat this grand challenge.

While a multi-faceted approach to lowering greenhouse gas emissions across every sector is needed, low emission (renewable) energy generation paired with the electrification of industries has been identified as one key approach.[3] Importantly though, many renewable energy sources, such as wind and solar power, are inherently intermittent i.e., the wind stops blowing and the sun sets. Therefore, renewables must be used in conjunction with cheap, large-scale energy storage to enable full deployment. Large-scale energy storage also imparts myriad benefits to the energy grid, allowing for peak leveling, providing backup power during generation disruptions, and increased grid flexibility.[4,5] Electrochemical energy storage in the form of batteries is one potential solution to help increase energy storage capacity.

A key industry primed for electrification is transportation, but this too is dependent on the availability of large-scale, cheap energy storage. In 2021, 28% of the U.S. greenhouse gas emissions were due to transportation, the largest total contribution from a single sector.[6] In particular, replacing traditional internal combustion automobiles with fully electric vehicles (EVs) is likely the first attainable goal, with larger transportation such as freight and aviation coming later as more advanced technology develops. The transition towards electric vehicles (EVs) is already underway, with the number of EVs on the road rising from about 22,000 to over 2 million between 2011 and 2021.[7] This trend is expected to continue driven by increasing consumer demand for more sustainable automobiles, commitments to production of EVs by automakers, and government incentives for citizens and corporations alike.[7] Crucially, all EVs rely on battery packs, with the vast majority using lithium-ion batteries (LIBs), which will be the focus of this thesis.

An ionically conductive but electrically insulating electrolyte is at the heart of all electrochemical energy storage devices. Lithium-ion batteries (LIBs), redox-flow batteries, solid-oxide fuel cells, and proton exchange membrane (PEM) electrolyzers all rely on electrolytes to function. Advances in electrolytes will be instrumental in the future of many technologies to enable decarbonization. In this work, we will focus on electrolytes deeply, particularly polymer electrolytes geared toward lithium-ion batteries. While LIBs are the main focus, many of the principles, methods, and tools established could have impact on electrolytes as a whole and for many different applications.

COMPOSITION AND OPERATION OF LITHIUM-ION BATTERIES

Lithium-ion batteries (LIBs) have become a leading technology to facilitate energy storage on multiple scales. First becoming most prevalent in handheld electronics, as the cost of LIB production came down, they became the technology of choice to enable fully electric vehicles. LIBs have many properties making them well-suited to use in Evs. Compared to other battery chemistries such as lead-acid or nickel metal hydride, LIBs have much higher energy and power density meaning that a battery pack can give EVs ~ 300 miles of range and high performance. Furthermore, LIB production costs have dropped low enough that they are now feasible for grid-scale energy storage.[8]

A conventional modern-day LIB is composed of three main active components namely, the positive electrode (sometimes called the cathode), the negative electrode (sometimes called the anode), and the electrolyte. In addition, current collectors, binders, inert separators, and more components are required but will not be discussed here. While the primary focus of this work is new electrolyte materials, here we will briefly touch upon all the active components and the operating principles of a battery to give context to further electrolyte studies. Additionally, some next-generation battery chemistries and their constraints on electrolytes will be discussed.

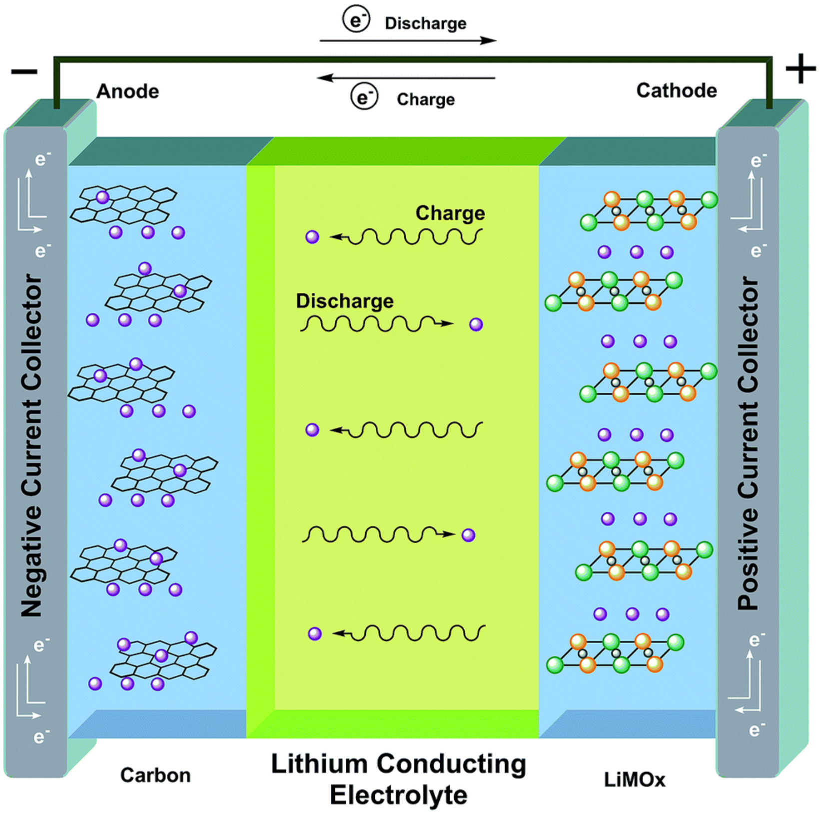

Figure 1-1: Schematic of a conventional LIB showing the different components. Used with permission from reference [9]

Conventional LIBs function by shuttling lithium ions back and forth between the active electrodes through the electrolyte. During discharge lithium ions undergo oxidation at the negative electrode (anode) and are released into the electrolyte solution. Lithium ions then flow through the electrolyte as driven by an electrochemical gradient. The ions then undergo reduction at the positive electrode (cathode). At the same time, since electrons cannot travel through the electrolyte, they are forced to travel through an external circuit. This flow of electrons creates an electric current. During charging of the battery, the exact same processes occur but in reverse. An electric current is applied which forces oxidation at the positive electrode, and reduction at the negative electrode.

The vast majority of commercial LIBs rely on intercalation electrodes, which can uptake and release lithium ions through redox reactions. Intercalation electrodes were first discovered by John B. Goodenough and M. Stanley Whittingham in the 1980s.[10–13] The classic example of this type of electrode is lithium cobalt oxide (Li_xCoO_2). Li_xCoO_2, is a layered transition metal oxide with a van Der Waals gap large enough for lithium cations to be easily inserted between the layers without significant changes in volume.[13] Additionally, for the intercalation reaction shown in Equation 1-1 the potential stays relatively constant around 4V relative to Li/Li$^+$ as x varies from 0 to 1.[13]

Equation 1-1

$$Positive\ electrode\colon\ Li_{1-x}\,CoO_2 + xLi^+ + xe^- \rightleftharpoons LiCoO_2$$

Equation 1-2

$$Negative\ electrode\colon Li\ (C_6) + e^- \rightleftharpoons C_6 + Li^+$$

In most commercial LIBs the anode is also made of an intercalation electrode, generally made of graphite as pioneered by Yoshino in 1985.[14] Here, the lithium ions can are intercalated between the layers of the graphite (Equation 1-2), maintaining a low redox potential relative to Li/Li$^+$ (~0.1 V) and when paired with the proper electrolyte allows for stable cycling.[11]

In addition to the anode and cathode, the third crucial component of a battery is the electrolyte. The electrolyte serves two critical purposes: conducting ions between the electrodes and electrically insulating the electrodes to prevent self-discharge of the battery. Most commercial lithium-ion batteries use high dielectric organic solvents with dissolved lithium salts as electrolytes. The organic solvents used are mixtures of carbonates such as ethylene carbonate (EC), dimethyl carbonate (DMC) or ether-type solvents such as dimethoxyethane (DME). The most commonly used salts are so called "non-coordinating" salts such as $LiPF_6$, $LiClO_4$, and LiTFSI (Lithium bis(trifluoromethanesulfonyl)imide), with $LiPF_6$ seeing the most commercial use due to its low cost.[11,15] Electrolytes composed of these components have been well studied and are formulated to have very advantageous properties such as high solubility of Li$^+$, low viscosity and thus high diffusivity of Li$^+$, as well as a wide electrochemical stability window allowing these electrolytes to withstand the high potential created by the electrodes. Additionally, electrolyte decomposition on the active electrode surfaces creates solid-electrolyte interfaces (SEIs), passivates the materials, prevents exfoliation, and enables stable cycling.[12] Often, the electrolyte is formulated to do this, and furthermore, small quantities of additives that assist in SEI stability.[15] Typically, inert porous polymer separators are used in the electrolyte layer to prevent short-circuiting of the electrodes and increase the safety of the cell.

NEXT-GENERATION BATTERIES AND SOLID ELECTROLYTES

As LIBs have grown in popularity and applications, it has become clear that next-generation batteries are needed. Targets for the next generation of batteries include making them more energy dense, cheaper, safer, and capable of faster charging.[16] The rising demand for electric vehicles, particularly increasing the range of such vehicles, requires more energy-dense batteries. Furthermore, the liquid electrolytes in use today are not mechanically robust and are highly flammable, requiring extensive safety measures and still posing a high risk if punctured. While electric vehicles are often just as safe or safer than internal combustion engine vehicles, damage to the battery pack can cause hazardous self-sustaining fires.[17] Much of the current research underway today is into new active materials, at both the positive and negative electrode. Higher voltage cathode materials and those with reduced amounts of precious metals such as cobalt are desired.[18] Replacement of the anode with higher capacity reactions (conversion electrodes) such as silicon-Li alloys can enable much higher energy capacities.[16] Transitioning fully to direct lithium plating and stripping at the negative electrode, so-called “lithium metal batteries” is one of the holy grails of the field due to their over-double theoretical capacity.[19] Even though Li-metal batteries have been studied for decades, they have yet to be commercialized due to the dendrite growth from the anode which can short-circuit the battery and initiate thermal runaway.[19] Furthermore, recent supply chain issues caused by the global pandemic have led to considerable increases in the cost of lithium precursors.[20] As such, there has been extensive interest in sodium-ion batteries due to sodium's much greater abundance and similar energy density.[21]

Crucially, advancements in the active materials must be accompanied by and are often enabled through the development of the electrolyte. For example, Xue and coworkers achieved stable cycling of a high-voltage lithium metal battery enabled by a novel sulfonamide based electrolyte which suppressed side reactions and transition metal dissolution from the cathode material.[22] Ultra stable cycling of a sodium metal-based battery was recently achieved utilizing a perfluoro-ether polymer electrolyte which was found to promote a stable solid electrolyte interface.[23] Transitioning to solid-state electrolytes such as polymers or inorganic ceramics has been identified as one of the most promising directions through removing the highly flammable liquid electrolyte,[24] suppressing dendrite growth mechanically,[25] and enabling single-ion conducting electrolytes which only transport the cation and limit dendrite growth.[26,27] The two main classes of all solid-state electrolytes under research today are inorganic ceramics, and organic polymers. Inorganic electrolytes are a broad class of materials that are typically crystalline ordered solids capable of ion conduction. Although materials exist which can conduct anions, we are primarily concerned with cationic conductors given their applicability toward LIBs. There are many promising classes under investigation including: LISICON and NASICON (lithium and sodium superionic conductor) compounds, perovskites, lithium halides, and lithium phosphates.[28] Inorganic ion conductors have many advantages including high ionic conductivity, lithium transference numbers equal to 1, low flammability and high mechanical integrity. Some ceramic ion conductors can have total ionic conductivities on par with liquids (~10^{-2} S/cm) at room temperature, often owing to the very high concentration of cations in the lattice (> 10M).[28] However, due to some key drawbacks, these materials have not yet seen widespread adoption. Many inorganic electrolyte materials are unstable at low reduction potentials and react with most of the anode materials in use today (and are even more reactive with lithium metal which is a desirable next-generation anode).[28] Furthermore, most inorganic electrolytes form very poor interfaces with the active materials, leading to high interfacial resistances deleterious to battery operation.[29] While solutions to these problems are also a highly active area of research, they will not be the focus of this work.

The field of polymer electrolytes began in the early 1970s when Fenton and coworkers reported that poly(ethylene oxide) (PEO) could dissolve alkali metal salts, and form crystalline complexes.[30] Armand and coworkers then discovered such PEO-salt complexes were ionically conductive, especially when above the melting point of the crystals.[31,32] While they have been a material of high interest since then, the field remains dominated by PEO. Polymer electrolytes are, in some ways, the antithesis of inorganic ceramics. They have favorable interfacial properties due to their visco-elastic nature, but they often maintain higher mechanical integrity and significantly reduced flammability as compared to liquid electrolytes. They also have very high processability, which would be necessary for commercialization. However, the main drawback of polymer electrolytes is the low overall ionic conductivity. The best-performing materials of today can reach ~ 10^{-3} S/cm (roughly the minimum level needed for functional batteries), but only at elevated temperatures of about 80 °C. At room temperature, the highest performing polymer electrolytes studies are in the range of $10^{-5} – 10^{-4}$ S/cm, an order of magnitude too low. One main thrust of the field, and this work, will be to study the ionic conductivity of polymer electrolytes, the descriptors of ion conduction, and how one can rationally design novel polymer electrolytes with exciting properties.

With so many new active materials considerations, finding the ideal electrolyte to enable the desired battery properties becomes an increasing challenge for the field, and advancements in instrumentation and techniques are required to overcome this challenge. In addition to developing new polymer electrolytes, in this work, we will develop new methods to help modernize the study of polymer electrolytes. In particular, we seek to leverage advances in computational methods and high throughput instruments toward accelerated polymer electrolyte discovery.

THESIS SCOPE

In this last chapter, we have motivated the pressing need for energy storage solutions to aid in decarbonizing transportation and enable increased deployment of renewable energy sources. The lithium-ion battery has been identified as one key player in aiding this transition, and furthermore, the lithium-ion conducting electrolyte is a critical component. Furthermore, as new battery technologies are continually under development, next generation electrolytes are needed to make batteries safer, cheaper, and more energy dense. The rest of this work will focus specifically on polymer electrolytes and the development of new strategies and methodologies to aid in the accelerated discovery of new materials.

In **Chapter 2,** we will discuss the fundamentals of ion transport in liquids, inorganic ceramics, and, most importantly polymer electrolytes. Mechanistic understanding of ion transport lays the foundation for designing and developing new materials.

In **Chapter 3**, we will discuss our work into promoting “decoupled” or “ion-hopping” conduction mechanism in polymer electrolytes. We will do this by rationally designing polyethylene-type polymers with highly dissociative Fluorinated Aryl Sulfonamide Tagged (FAST) anions directly in the backbone. The polymers were found to self-assemble into highly ordered lamellae creating “ionic channels”. It is found that such channels possess decoupled ion transport which is amongst the best studied to date.

In **Chapter 4**, we will focus on developing a high throughput tool to increase the speed of polymer electrolyte testing and subsequent discovery. Particular design challenges and solutions will be highlighted. Final performance metrics will be established. Then the use of the high throughput tool towards new polymer electrolyte discovery in two different case studies will be discussed.

In **Chapter 5** we perform the most extensive to-date direct comparison of lithium and sodium ionic conductivity in PEO. The data presented bring a new level of granularity, accuracy, and speed to the polymer electrolyte community and can be used as excellent reference measurements. Additionally, through the large-scale screen, we uncover a previously unknown trend in the glass transition temperature, crystallinity, and, subsequently the ionic conductivity of PEO-based polymer electrolytes.

In **Chapter 6**, we then turn our attention to development of a new active learning workflow for polymer electrolytes, tying together the high throughput instrument with a machine learning model to predict the ionic conductivity of new polymer electrolytes. We apply this workflow in an iterative Bayesian optimization scheme to find the optimal salt and concentration for ionic conductivity in poly(caprolactone) PCL. Our results show that we can find a plateaued maximum for ionic conductivity after only 3 batches and also that the uncertainty of the model is greatly reduced with each additional batch of data. The performance of the electrolytes is on par with the best reported PCL-based electrolytes in the literature. Overall, this work is just the first foray into active learning for polymer electrolytes, and opens up the space to much more complex studies in the future.

Finally, in **Chapter 7,** we conclude with some perspectives on the future of polymer electrolytes and their use in batteries and other applications, as well as the utility of computationally assisted materials design and discovery.

CHAPTER 2 FUNDAMENTALS OF ION TRANSPORT

Acknowledgment: Much of this chapter is inspired and motivated by the work of many members (including the author of this thesis) at MIT who contributed to the writing of a review article on a unified framework to unite liquid, solid, and inorganic ceramic ion conductors. Graham Leverick led the group and his thesis is cited in reference [33]. In addition, the group consisted of (in no particular order): Ryoichi Tatara, Jeffrey Lopez, Sokseiha Muy, Shuting Feng, Abraham Herzog-Arbeitman, Megan R. Hill, Arthur Frace-Lanord, Tian Xie, Yangming Wang, Kento Kimura, and Bo Qiao.

While at its core, ion transport is diffusion, the diffusing species (the ion) being charged results in stronger interactions with the surrounding media, which must be taken into account, resulting in a variety of different mechanisms of ion transport. Here we will briefly establish mechanisms and descriptors of ion transport in liquids, solid polymers, and inorganic lattices (such as ceramics). One useful analysis for ion conductors which can be done is the Walden analysis a version of which is shown in Figure 2-1A. Originally developed for liquid electrolytes and ionic liquids, the Walden analysis plots the molar ionic conductivity (Λ) versus the viscosity (η) of the solution on a log-log plot. It is found that many liquid ion conductors fall on the “ideal” line which has a one-to-one correspondence, the origins of which will be discussed in the next section. Ion conductors which fall below this line are often denoted as “subionic” and can occur for a variety of reasons which will be discussed. Perhaps more interesting are the conductors which fall above this line denoted as “superionic” which will also be touched upon.

Our group showed that the inverse viscosity can be replaced by the dielectric relaxation time in liquids,(τ_ε) which is the rate at which dipoles in the liquid can rearrange due to changes in electric fields, and the one-to-one relationship still holds. Recent work by Bockarova, Sokolov, and coworkers has extended the Walden analysis to include solid polymer electrolytes, where viscosity is replaced by the segmental relaxation time (τ_{seg}) the origins of which will also be further discussed.[34] Furthermore, our group has extended this analysis to include solid inorganic ceramics where viscosity is replaced with the hopping frequency of ionic motion (τ_{hop}), which is also related to inverse frequency of ionic vibrations in the lattice.[33] With these three important timescales identified, we can plot liquids, polymers, and ceramics on a unified axis (τ). Across the material classes, many ion conductors fall close to the "ideal" line highlighting a fundamental link between the total ionic conductivity and the time scale of the microscopic processes that underpin it. Furthermore, understanding the mechanisms of why certain materials fall where, allows us to motivate how we can design new materials that move towards the superionic regime. In Error! Reference source not found.**,** we will discuss one method in which we have worked towards achieving this in solid polymer ion conductors, connecting ion conduction mechanisms from inorganic ceramics to solid polymer electrolytes. In **Chapter 5**, we uncover a new phenomenon through high throughput screening, which may give insight into the fundamental upper bound for ion conduction in amorphous polymers.

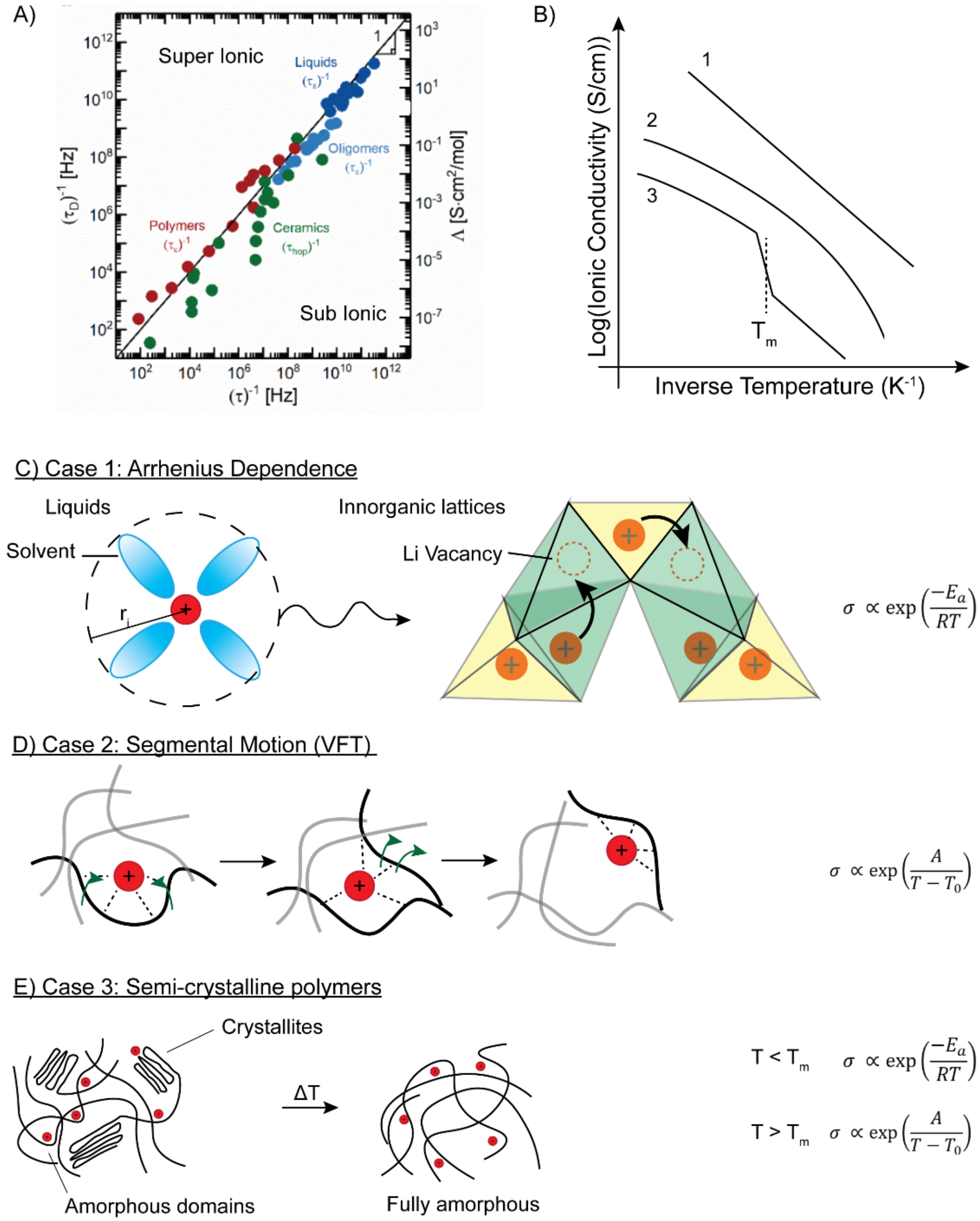

Figure 2-1 A) Walden style analysis showing the ideal line, and super and sub ionic regions. Figure used with permission from reference [33] B) Arrhenius analysis showing three different hypothetical profiles that can be observed experimentally. Note that the profiles are offset vertically for clarity. C) Illustration showing "ideal" Arrhenius behavior in both liquids and inorganic ceramics. D) Illustration showing segmental motion observed in polymer electrolytes. E) Illustration showing the cause of "step function" type ionic conductivity due to polymer crystallinity. Note: C-E the anions have been omitted for clarity but are indeed present in all cases.

LIQUIDS

Liquid electrolytes are the most prevalent currently in use today, and ion transport is relatively well understood (as compared to polymers or ceramics). A typical electrolyte system consists of a salt dissolved in either water or an organic solvent depending on the application. In the dilute regime, most electrolytes follow the "Walden rule" which states that the product of the molar ionic conductivity (Λ) and the viscosity (η) of a solution is a constant, or similarly plotting Λ versus η^{-1} on a log-log plot results in most points falling along the one-to-one line. In other words, the main controlling factor of ionic conductivity is the viscosity of the solution, which is typically controlled by the solvents used, salt concentration, and temperature. A Walden-type analysis is shown in Figure 2-1A) with liquid electrolytes labeled in dark blue. It has been found that the viscosity of most solutions is dependent upon the time scale of solvent rotations and relaxations (τ_ε).[33] Therefore instead, one can equivalently perform the Walden analysis with τ on the X-axis instead of η^{-1} which is the traditional Walden analysis. The purpose of this substitution is to allow cross-comparisons to polymers and even ceramics with essentially infinite viscosity (being solids), but still posses segmental and dielectric relaxations.[33]

It is often found that, in the dilute regime, each ion is surrounded by a relatively static solvation shell, and the entire complex will diffuse. Considered this way, one can treat the ion + solvation shell complex as a "hard sphere" and use the Stokes-Einstein relation to relate the diffusivity and viscosity of the solution:[35]

Equation 2-1

$$D_i = \frac{kT}{6\pi\eta r_i}$$

Where r_i is the radius of the sphere (in this case ion + solvation shell), k is the Boltzmann constant, and T is temperature. Building upon this, one can use the Nernst-Einstein relation, which states that the total ionic conductivity of a solution is related to the diffusion of all the ions in the solution (here shown for a binary electrolyte composed of only ±1 charges):[35]

Equation 2-2

$$\Lambda = \frac{F^2(D_+ + D_-)}{RT}$$

Substituting for the diffusivity of each ion and simplifying it is found that $\Lambda \propto \eta^{-1}$, which is directly the Walden Rule. Furthermore, it is found empirically that the viscosity of most liquid solutions will decrease exponentially with increasing temperature following the Andrade relation (where A and B are empirically measured parameters):[36]

Equation 2-3

$$\eta = A\, e^{B/T}$$

Substituting this relationship for viscosity one can arrive at:

Equation 2-4

$$\Lambda \propto \left(A\, e^{\frac{B}{T}}\right)^{-1} \propto Ae^{-B/T}$$

When measured experimentally, one often finds that the total ionic conductivity (σ) obeys the following relation:

Equation 2-5

$$\sigma = \sigma_0 e^{-\frac{E_a}{RT}}$$

Where σ is the total ionic conductivity, σ_0 is a fitting parameter, and E_a is denoted as the activation energy. Equation 2-5 is known as the Arrhenius relationship for ionic conductivity. Plotting the ionic conductivity versus inverse temperature (an Arrhenius plot), a straight line appears, the slope of which is the activation energy (normalized by the universal gas constant) (Figure 2-1B, Case 1).

While the Walden rule (and subsequently the Arrhenius relationship) is typically obeyed for many dilute electrolyte solutions, higher concentrations or low dielectric constant solvents can result in deviations. Much of the electrolytes in the sub-ionic regime have a significant presence of contact ion-pairs, in which the cation and anion remain closely associated in solution.[15] Contact ion-pairs do not contribute meaningfully to the ionic conductivity of the cation, which is of prime importance for LIBs.[15] The solubility of ion-pairs often depends on the dielectric constant of the solvent—in general higher dielectric solvents are able to screen charge better and keep the ions solvated.[15] However, most solvents with high dielectric constants are also more viscous, which will lower ionic conductivity as described above. This trade-off between ion solubility and viscosity has led to most electrolytes in use today being composed of mixtures of solvents to balance properties for optimal performance.[15]

Alternate diffusion mechanisms have been observed in specific cases and can result in non-Walden behavior. One of the few liquid electrolytes able to go into the super-ionic regime (above the line) are the protons in water.[37] For some aqueous proton conductors, the well-studied Grotthuss mechanism allows proton conductivity to exceed the diffusion of individual water molecules through a cooperative hydrogen bond exchange network.[37] Some recent works have observed a similar mechanism for Li^+ conduction in highly concentrated mixtures of $LiBF_4$ in sulfolane.[38] It is thought that the sulfolane and BF_4^- anions create an ordered “bridge-like” coordination that allows Li+ to hop between solvation sites faster than the vehicular diffusion described above.[38] While exciting case studies, such decoupled transport in liquids is not strictly necessary as most liquid electrolytes can already achieve sufficient ionic conductivity for most practical battery applications, and other properties such as stability and lifetime are more pressing.[15]

INORGANIC CERAMICS AND SOLIDS

Ion transport in inorganic solids can be well understood using principles of solid-state diffusion and transition-state theory. The cations and anions are arranged on a highly ordered crystallographic lattice in these solid materials. In principle, diffusion of either the cationic or anionic species can occur, and indeed high-temperature O_2^- conductors see extensive use in solid oxide fuel cells[39] Here we will primarily discuss materials where the cation (typically an alkali metal such as Li^+ or Na^+) is the mobile species.

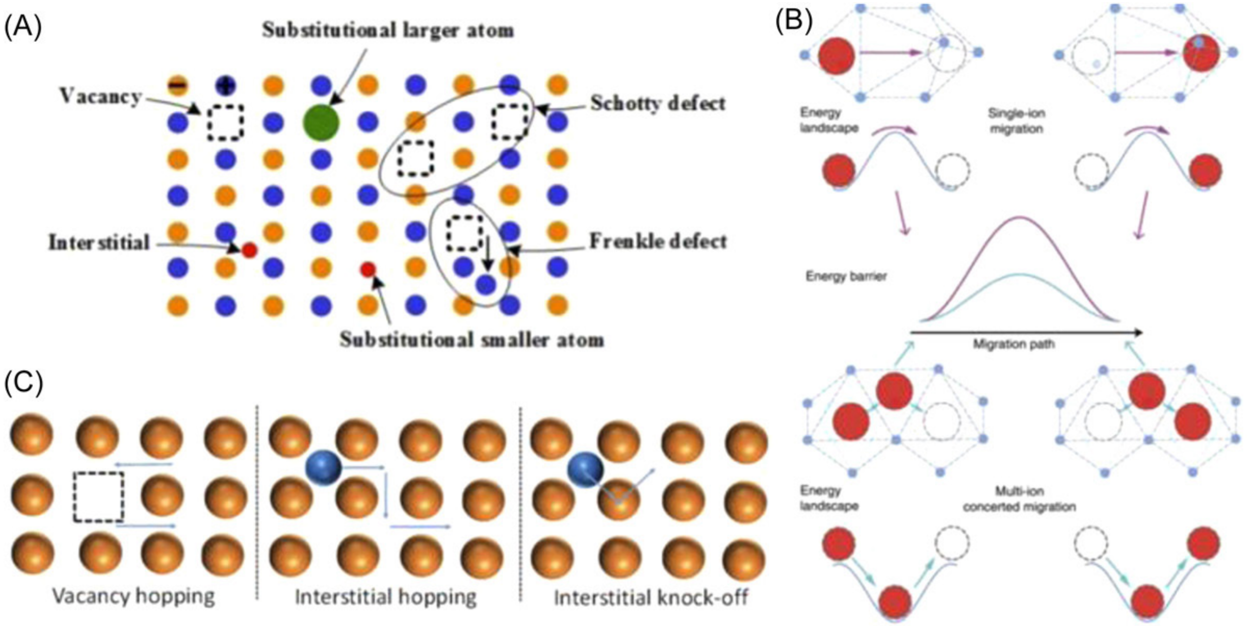

Figure 2-2: Overview of ion conduction in inorganic solids. Reproduced from reference [40] *A) Representation of defects arising in inorganic ceramics. Reproduced from reference* [41] B) schematic of the energy barriers for single-ion migration and the concerted multi-ion migration. Reproduced from reference [42] C) Ion migration mechanisms as they occur in inorganic ceramics. Reproduced from reference [29]

In systems where vacancies exist, it is found that a cation adjacent to a vacancy can execute a thermally excited jump into the vacant site. There is often an energy barrier associated with this jump due to the loss of coordination during the transition state and the reduced space through which the cation must squeeze (Figure 2-2B). Diffusion of ions via thermally activated jumps in lattices are well described by the transition state theory equation:[43]

Equation 2-6

$$D = \gamma(1-c)Za^2\nu_0 e^{\Delta S/k_b} * e^{-E_M/k_bT}$$

Where a is the jump distance, ν_0 is the attempt frequency ,and E_m is the migration energy.[43] The factor $(1-c)Z$ defines the number of neighboring unoccupied sites, while γ includes geometric and correlation factors.[43] Equation 2-6 can be similarly substituted into the Nernst-Einstein equation (Equation 2-2), but now D_- is defined to be zero as the anions are not mobile, yielding the equation for molar ionic conductivity of the cation as:

Equation 2-7

$$\Lambda = \frac{F^2}{T} * \gamma(1-c)Za^2\nu_0 e^{\Delta S/k_b} * e^{-E_M/k_bT}$$

Which, similar to liquid electrolytes, is often simplified to the experimentally used equation (it is often found that the prefactor does not change significantly over small temperature ranges):[43]

Equation 2-8

$$\sigma = \sigma_0 e^{-E_a/RT}$$

As with liquid electrolytes, the Arrhenius equation is produced with an activation energy E_a, and as such, most inorganic ion conductors appear as a straight line (Case 1) on an Arrhenius plot (Figure 2-1). Notably, from Equation 2-7, the term (1-c) is buried within σ_0. As such when c = 1 (i.e. all adjacent sites are fully occupied), the diffusivity goes to zero, indicating that vacant sites are necessary for ion conduction to occur.[43] Therefore, the creation and distribution of defects which produce vacant sites is crucial to the overall ionic conductivity of the material.[28,43] The defects that play the largest role in ion conduction are Frenkel defects, in which a cation moves to an interstitial site creating a vacancy, and Schottkey defects, in which a cation-anion pair move to an edge creating a pair of vacancies (Figure 2-2A).[41] Additional defects are often intentionally introduced by aliovalent doping of the lattice to increase the vacancy concentration.[28,40] There is found to be an optimal amount of doping where ionic conductivity is increased, but the host crystal structure is maintained. For example, doping the well-known garnet oxide Li7La3Zr2O12 (LLZO) with tantalum raises its room temperature ionic conductivity by about an order of magnitude compared to the undoped material.[44] Furthermore, it has been found that structural tuning to alter the connectivity of sites, the number of adjacent open sites, and the overall space a cation has to jump through can also affect the ionic conductivity of inorganic materials.[28] For example, it has been found that LLZO can exist in either a tetragonal or a cubic crystal structure, and the cubic structure formation is dependent on small amounts of aluminum impurities, which often arise from the crucibles used during synthesis.[44] The cubic form of LLZO has two orders of magnitude greater ionic conductivity, which is generally attributed to the Li sites only being partially occupied allowing for rapid ion exchange as compared to the tetragonal structure in which full occupancy of the Li sublattice considerably slows ion motion in good agreement with Equation 2-7.[45,46] Overall, the field has been able to achieve inorganic Li^+ ion conductors with ionic conductivity > $1*10^{-3}$ (S/cm) even at room temperature making them an attractive material class for the next generation of electrolytes. However, as described in Chapter 1 they have many other engineering hurdles to overcome before they are ready for deployment.

POLYMERS

Many parallels can be drawn between ion conduction in liquid electrolytes and polymer electrolytes. The transition from liquids to solid polymers is illustrated in Figure 2-3A). Ethylene oxide-based oligomers and polymers were produced, and ionic conductivity was measured as a function of the molecular weight of the host material. The lowest molecular weight data points are viscous liquids. As previously discussed, the ion conduction in liquid electrolytes is dominated by the viscosity of the solution.

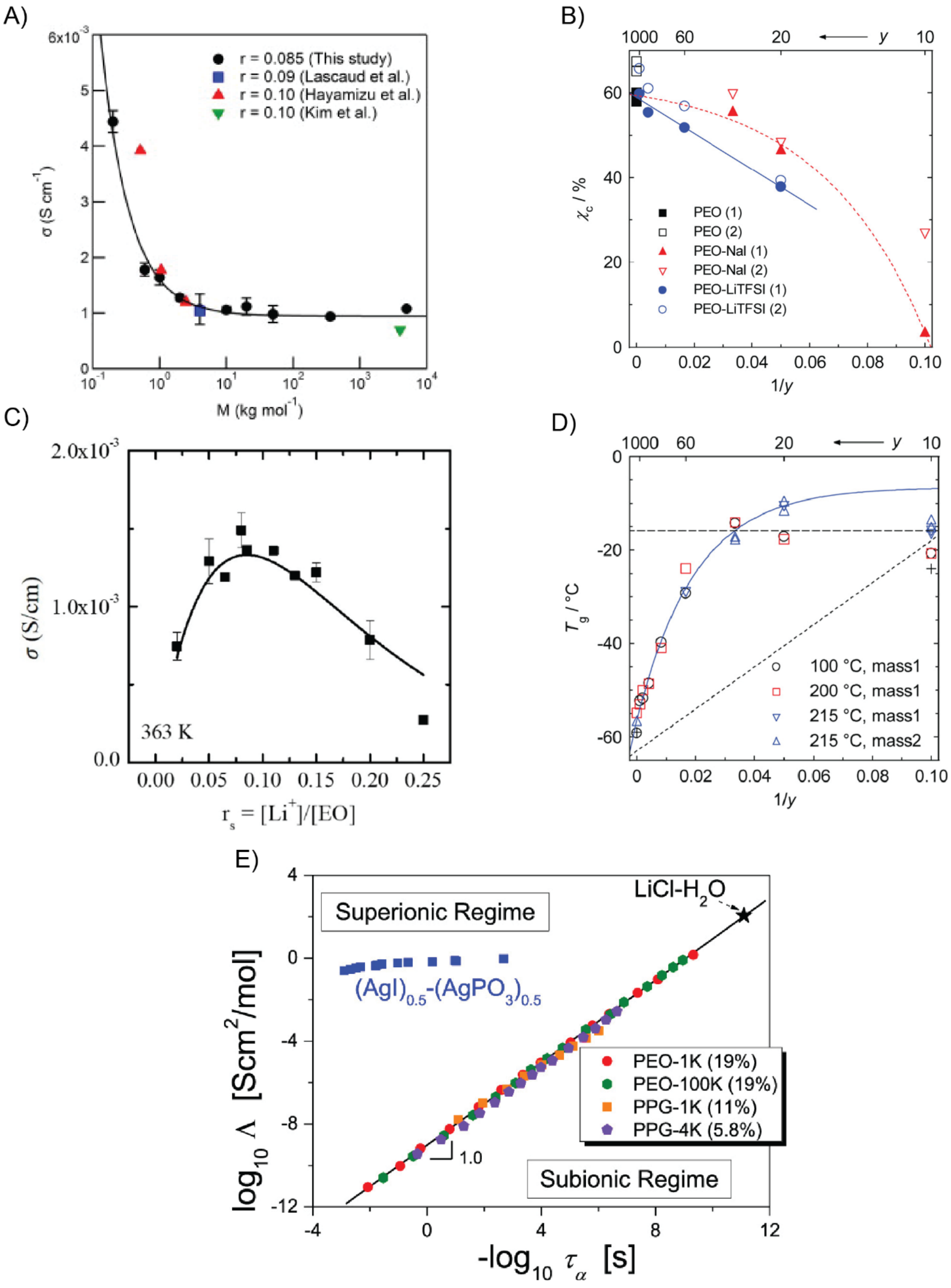

Figure 2-3 Descriptors of ionic conductivity in PEO-type polymers. A) Dependence of ionic conductivity on the molecular weight of the polymer. Reproduced from reference [47] B) Dependence of percent crystallinity (χ_c) on salt concentration. Reproduced from reference [48] C) Dependence of ionic conductivity on salt concentration (here as ratio r_s). Reproduced from reference [49]. D) Dependence of T_g on salt concentration. Reproduced from reference [48]. E) Walden analysis showing the relationship between molar ionic conductivity and the alpha relaxation time (τ_α). Reproduced from reference [34].

From classical polymer dynamics, the viscosity of a polymer (or oligomer) melt increases exponentially with the molecular weight $\eta \sim M^{3.4}$.[50] Therefore, one expects the ionic conductivity to decrease exponentially with molecular weight. While initially true, it is found that the ionic conductivity plateaus at M_w ~ 2,000 g/mol, after which it becomes independent of molecular weight. Known as the entanglement molecular weight (M_e) this cutoff indicates the transition from the vehicular diffusion (as described for liquids) to a segmental motion-type mechanism. It is also the point at which the polymer chains are long enough where entanglements between chains are sufficient for the material to behave as a free-standing solid.[50] In this regime, segmental motion speeds are independent of the molecular weight of the whole chain.[51] The rest of this section will be concerned with ion conduction in polymers well above their M_e.

As discussed in Chapter 1, the field of polymer electrolytes has been primarily dominated by PEO with a single dissolved lithium salt (most commonly LiTFSI). It is most important to discuss the mechanism of ion conduction within PEO, which is segmental motion through the amorphous domains. Most PEO-salt formulations are semi-crystalline, composed of both crystalline and amorphous domains. It is generally established that ion conduction occurs primarily in the amorphous domains. PEO's percent crystallinity decreases with increasing salt concentrations, creating a more amorphous material (Figure 2-3B).[48] A majority of non-PEO polymer electrolytes are also thought to follow the segmental motion mechanism; however, there is a growing field of polymers that do not follow this. Our work into promoting non-segmental motion “ion hopping” will be covered in the next chapter.

A simplified illustration of the segmental motion mechanism is shown Figure 2-1D, with the cation starting out coordinated by the polymer chain. The ability of PEO to dissolve lithium salts derives from the strong coordination of the ether oxygens in the backbone to the lithium cation. There is a strong similarity between the coordination structure of Li^+ in PEO, and that of Li^+ with crown ethers, which have long been established to chelate cations.[52] Indeed, crystal structures of $LiAsF_6$: PEO complexes showed the lithium cation sits at the center of a helical coil of EO segments, with coordination of either 5 or 6 oxygens.[53] A coordinated lithium will diffuse along with the segments of PEO until it reaches an adjacent chain (which can either be a separate segment of the same chain or a separate polymer chain), where it is thought to exchange coordination. This coordination exchange also acts as a transient crosslink between the polymer chains. Once the cation exchanges coordination fully, it can continue to diffuse with the new chain segment.

Similar to liquid electrolytes, it is observed that the ionic conductivity of SPEs has a distinct maximum at intermediate concentrations (typically around 2 molality, or a Li:EO ratio of about 1:10) (Figure 2-3C).[9,49] The origin of this maximum has been attributed to first, a linear increase in the carrier concentration, which is accompanied with a decrease in the segment mobility due to an increase in intermolecular crosslinks as described above. This microscopic picture of the motion of cations in relationship to the segmental motion of the polymer has been verified by neutron scattering experiments. Quasi-elastic neutron scattering (QENS) has been used extensively to observe the speed of segmental motion and relaxation processes in polymer melts.[54] Mao *et. Al.* observed a two to three orders of magnitude slowing in the alpha relaxation process of the polymer segments upon the addition of LiTFSI.[55] Further study by Mongcopa and coworkers were able to describe the maximum in ionic conductivity as a function of concentration by observing the “monomeric friction factor” (ζ) of the polymer with QENS. [49] The monomeric friction factor, describes the resistance to monomer motion in the Rouse model of polymer dynamics, which approximates the polymer as a long chain of beads connected by springs.[56,57] They find through QENS experiments that the friction factor of the polymer segments increases exponentially with the concentration of the salt. [49] They can describe the change in ionic conductivity with the concentration of salt (here called r_s) through the equation:[49]

Equation 2-9

$$\sigma = 0.043\, r_s * \frac{\zeta(\mathrm{r_s})}{\zeta(0)} = .043\, r_s * \exp\left(\frac{r_s}{.085}\right)$$

The replacement of $\frac{\zeta(\mathrm{r_s})}{\zeta(0)} = \exp\left(\frac{r_s}{.085}\right)$ comes directly from their experimental observations of the segmental relaxation times, showing the best link between the microscopic segmental motion and the overall ionic conductivity of the system to date.[49]

Additionally, the segmental motion mechanism can manifest in bulk observations. The total ionic conductivity of amorphous polymer electrolytes is often found to deviate from the Arrhenius relationship, following the empirically derived Vogell-Fulcher-Tammann equation (VFT) (Figure 2-1B, case 2). The VFT equation was originally derived to describe the viscosity of molten glasses as a function of temperature.[58]

Equation 2-10

$$\eta = \eta_0 \exp\left(\frac{B}{T - T_{VF}}\right)$$

Where η_0, B, T_{VF} are all empirically found material-specific parameters. T_{VF}, which is also often denoted T_0 is typically found to be about 50 K below the glass transition temperature(T_g). The origin of viscosity in polymer melts has been linked to the speed of relaxation of the polymer segments. In general, the temperature dependence of these relaxation times has also been linked to the quantity $(T - T_0)^{-1}$ by the Williams – Landel – Ferry (WLF) equation.[50] Given the established link between viscosity and ionic conductivity in liquid electrolytes already discussed, it is somewhat unsurprising that the ionic conductivity of amorphous polymer electrolytes will have a similar dependence on $(T - T_0)^{-1}$. While most polymer electrolytes are entangled enough that macroscopic viscosity is no longer meaningful, it is still found the ionic conductivity can be empirically fit by:[34,51]

Equation 2-11

$$\sigma = A \exp\left(\frac{-B}{T - T_0}\right) \approx A \exp\left(\frac{-B}{T - (T_g - 50)}\right)$$

Equation 2-11 is the VFT equation for ionic conductivity and is shown in Figure 2-1B, case 2. A, and B are typically empirically fit and vary by material. While B is sometimes referred to as the pseudo-activation energy (akin to E_a found in the Arrhenius equation), there is often no satisfying link between B and physical processes. The VFT equation also shows the strong dependence of ionic conductivity on the T_g of the electrolyte, or rather, how high above T_g operation is. Therefore significant development has been put into finding polymer electrolytes with low glass transition temperatures, such as by adding ultra-flexible siloxane groups known to lower T_g.[59] Unfortunately, it has been observed many times that the T_g (which is directly linked to the polymer mobility) will increase as salt is added due to the cations creating transient crosslinks between chains (Figure 2-3D).[48]

The alpha relaxation time, which can be measured through dielectric relaxation spectroscopy and is related to the glass transition, is a good descriptor of ionic conductivity in SPEs. Recent work by Bocharova and Sokolov has put forth a modified Walden plot (Figure 2-3E) in which the alpha relaxation time (τ_α) is used in lieu of macroscopic viscosity.[34] It is found that PEO and poly(propylene glycol) PPG electrolytes fall directly on the one-to-one line indicating that indeed microscopic segmental relaxation is a good descriptor of ionic conductivity. In general, such ion conductors can be thought of as "highly coupled" in which the speed of ion motion is directly dictated by the speed of the polymer segments.[34] Sokolov and coworkers also calculated that hitting target ionic conductivity of ~10^{-3} S/cm at room temperature requires alpha relaxation times on the order of 10^{-10} s.[34] For PEO based electrolytes above the entanglement threshold, it has been measured that segmental relaxation is typically 10^{-7}-10^{-6} s, orders of magnitude too slow.[34] From this perspective, to achieve high ionic conductivity there are two main strategies: 1) find polymers with far faster segmental relaxation times than PEO, or 2) find strategies to "decouple" the motion of ions from the polymer motion. Towards strategy 1, it has generally been established that very few known polymers exist in this range, and the few that approach these speeds do not contain the functional groups to solvate salts. Furthermore, as observed in PEO, if salt could be dissolved, it would likely cause considerable slowing of segmental dynamics. Therefore, much recent work in the field has been devoted to strategy 2: finding strategies to decouple the cation motion from the polymer segmental motion. *In the next chapter, we will discuss our work to rationally design polymer electrolytes to achieve decoupled ionic conductivity via an ion-hopping mechanism inspired by inorganic ceramics.*

CHAPTER 3 LAMELLAR IONENES WITH HIGHLY DISSOCIATIVE, ANIONIC CHANNELS PROVIDE LOWER BARRIERS FOR CATION TRANSPORT

This work was produced in collaboration with: Benjamin A. Paren, Pablo A. Leon, Christopher M. Brown, Gavin Winter, Kiarash Gordiz, Alberto Concellón, Rafael Gómez-Bombarelli, Yang Shao-Horn, and Jeremiah A. Johnson

It is cited in reference: [60]

DOI: https://doi.org/10.26434/chemrxiv-2023-fwgql

INTRODUCTION

Solid polymer electrolytes (SPEs) have been studied since the early 1980s as a promising alternative to conventional liquid electrolytes for next-generation batteries.[9,51] SPEs composed of high molecular weight polymers (typically >5,000 g/mol) have nearly zero vapor pressure and much higher autoignition points than common liquid electrolytes, rendering them potentially safer.[9] A sub-class of solid polymer electrolytes referred to as single ion conducting (SIC) polymers feature anionic groups within the polymer sidechains (i.e., ionomers) or backbones (i.e., ionenes).[61] SIC SPEs often display higher cation transference numbers (the fraction of charge carried by the cations), than conventional SPEs, which can increase battery power,[26,62] and suppress dendrite growth.[27] Nevertheless, dry SIC SPEs typically show low ionic conductivities due to their large energy barriers for polymer segmental motion and/or cation dissociation. As a result, liquid solvents[63,64] or poly(ethylene oxide) (PEO)[65,66] are often incorporated into SIC polymers to facilitate ion conduction via cation solvation, though such strategies remain limited by inherently slow polymer segmental relaxation (in the case of PEO blending),[34] or they may reduce electrolyte stability/safety (in the case of solvent addition).[61,67]

Inspired by the high ionic conductivities of solid ceramic ion conductors such as the Lithium Super Ionic Conductor (LISICON) family,[28] recent SPE designs have sought to exploit an "ion-hopping" or "decoupled" mechanism, wherein cations move between relatively stationary anionic sites at rates that are decoupled from polymer segmental relaxation,[34] the latter of which is inherently unable to provide cation mobility on par with ceramics and liquids.[68] Decoupled ion conduction is thought to be favored in materials that possess crystalline and/or highly-ordered, rigid anionic channels. For example, Winey and coworkers have suggested that decoupled ion transport occurs in SICs derived from carboxylate- or sulfonate-terminated alkanes that form lamellar and hexagonal phases (Figure 3-1A, **1** and **2**), respectively, driven by the crystallization of their long alkyl segments.[69,70] Sidechain-functionalized polymers with percolated ionic aggregates (**3**),[71] mesogenic sidechains that promoted nanoscale ordering (**4**),[72] or precisely placed dissociative ions (**5**)[73] have also been proposed to leverage decoupled ion conduction.[71,73,74] Nevertheless, the ion conductivities in the dry state for these materials are either low (much lower than traditional SPEs) or not reported; new design strategies are needed to facilitate cation mobility in crystalline, polyanion-based materials.

The previously reported decoupled SPEs tend to use anionic groups (e.g., carboxylates and sulfonates) that are more Lewis basic, i.e., less dissociative, than common anions used in battery electrolytes such as bis(trifluoromethanesulfonyl)imide (TFSI, **7**).[15] Even when softer, more dissociative anions such as sulfonimides are employed for polyanion designs, the linkers required to conjugate these anions to polymers tends to involve replacing at least one strongly electron withdrawing group, e.g., CF_3, with alkyl or aryl substituents, which leads to comparably more Lewis basic anions (e.g., **5** and **6**).[65,73] We hypothesized that the cation-anion association energy, i.e., the energy required to remove a cation from its corresponding anion, may be a useful descriptor to guide SPE design, as cation hopping requires dissociation from the polymer backbone and movement to an adjacent anionic site. To quantify the impacts of anion choice, we used density functional theory (DFT) calculations to compare the association energies of a Li^+ cation and various small-molecule analogs of commonly employed polyanions in implicit *N,N*-dimethylformamide (DMF) solvent (Figure 3-1B and Figure 8-1). As expected, the carboxylate and sulfonate anions (analogous to **1**–**4**) have the most negative (i.e., more favorable) association energies, and thus they are the least dissociative. Similarly, while sulfonimide derivatives analogous to **5** and **6** are indeed more dissociative than **1**–**4**, their electron rich substituents make them less dissociative than TFSI (**7**).

Guided by the hypothesis than lowering anion dissociation energy may lower the barrier to ion hopping in SPEs, we set out to design a new class of highly ordered, ionenes[75] with chemically tunable and dissociative anionic backbones derived from bis-pentafluorophenyl sulfonimide anions ("**FAST-C"**, Figure 1C).[76] Due to its strongly electron withdrawing pentafluorophenyl substituents, **FAST-C** features an association energy (−82 kJ/mol) more similar to that of TFSI (**7**) (−84 kJ/mol) than **1**–**6**. Moreover, nucleophilic aromatic substitution (S_NAr) of the *para*-positions of **FAST-C** with thiols is expected to have a minimal effect on its association energy (the Hammett parameters for *para*-thioether and *para*-fluorine are both ~0).[77]

Single-crystal X-ray structural analysis of the **FAST-C** Na^+ salt (Figure 3-1D) shows that it forms channels lined with anionic sulfonamides filled with Na^+ cations in the solid state, which could facilitate ion hopping if translated to SPEs. Guided by these considerations we targeted an ionene structure in which **FAST-C** anions are evenly spaced within a poly-alkenyl backbone to promote formation of ionic channels. We report here the synthesis of a new class of highly dissociative ionene SPEs—**pFAST-C20-M** (where is M = Li^+, Na^+, K^+, or Cs^+)—prepared from acyclic diene metathesis (ADMET) polymerization of liquid-crystalline, -alkenyl-terminated, thioether functionalized monomer **FAST-C20**. **pFAST-C20-M** polymers display semicrystalline, lamellar solid-state structures with cation-size-dependent channels lined with **FAST-C**-based anions. These materials display record low activation energies and amongst the highest overall ionic conductivities for ordered, solvent-free polyanion SPEs. Moreover, the addition of 25 wt. % (1 equiv to cation) of a cation-coordinating solvent (tetraglyme) boosted ionic conductivity in these materials by 3 orders-of-magnitude without disrupting their semicrystalline lamellar morphology. These results should drive the development of novel ionenes and related SPEs based on highly dissociative anions, which may contribute to the realization of optimal decoupled SIC SPEs in the future.

A.

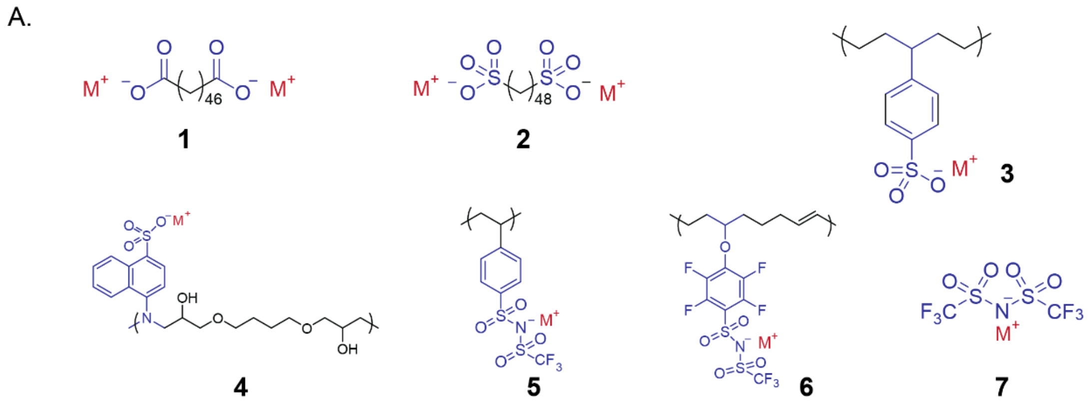

B.

Reference	+/- Solvent or Ethylene Oxide	DFT Association Energy in DMF* (kJ/mol)
1. Yan L. *et. Al.* ; 2019[14]	-	-159.3
2. Paren B. A. *et. Al.* ; 2022[15]	-	-120.6
3. Paren B. A. *et. Al.* ; 2020[18]	-	-110.5
4. Bresser D. *et. Al.* ; 2021[16]	+	-109.0
5. Stacy E. W. *et. Al.* ; 2018[17]	-	-107.45
6. Zhang W. *et. Al.* ; 2021[7]	+	-91.0
7. M-TFSI	-	-84.4
FAST-C	-	-82.4

Increasing Dissociativity

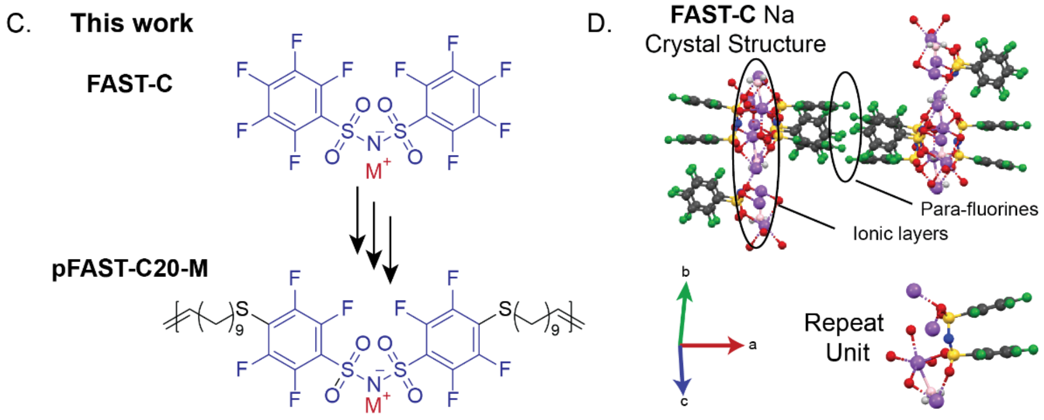

Figure 3-1 A) Structures of reported SPEs proposed to operate via decoupled ion transport. The portions highlighted in blue indicate the fragments that were used for DFT calculations. B) Association energies, as calculated by DFT, for model anions based on reported SPEs (**1**–**6**) for comparison to **TFSI** and **FAST-C** anions. Here, a less negative value

indicates a less stable salt complex, i.e., a greater extent of dissociation. (* = implicit solvent) C) Installation of terminal alkenes onto **FAST-C** via S_NAr enabled polymerization via ADMET to form a family of ionenes **pFAST-C20-M** with different cations M. The polymer structure is designed to promote the formation of highly ordered channels for ion hopping. D)I Single crystal X-ray diffraction structure for the **FAST-C** Na^+ salt, highlighting the layers of sodium cations and anionic channels. The *para*-fluorine atoms, which are linked together through alkenyl chains in **pFAST-C20-M** polymers, are aligned in parallel. Here a ball and stick model is used; see *Figure 8-2* for the structure shown as thermal ellipsoids.

MATERIALS AND METHODS

Materials:

All materials were purchased from Millipore Sigma and used without further purification unless otherwise noted. Pentafluorobenzenesulfonyl chloride was purchased from Acros Organics. Pentafluorbenzenesulfonamide was purchased from Synquest Labs.

Detailed synthetic methods for each reaction can be found in Section S3: Synthetic methods.

Density Functional Theory (DFT), Nudged Elastic Band (NEB), and interaction energy calculations.

Lithium-anion interaction energies were computed through a scheme of quantum chemical geometry optimizations using the ORCA ab initio quantum chemistry package.[78] Initial geometries of each anion were generated using RDKit[79] to convert SMILES strings into Cartesian coordinates. For each anion, a lithium cation was randomly placed between 1.5 and 4 Å of the anionic center. These clusters were refined first using semi-empirical tight-binding DFT (GFN2-xTB),[80] then B3LYP-D4[81–83]/def2-SVP[84,85] and finally using the ωB97X-D3[86]/def2-TZVP hybrid level of theory in ORCA. The energy of this final cluster was determined using the Universal Solvation Model (SMD)[87] implicit model for n,n-dimethylformamide (DMF) as the solvent. A Lebedev grid of 434 points is used for optimization with a 590-grid size for final energy computations. Separately, the minimum energy conformation of each anion (i.e., without a cation) was determined using the same sequence. The final interaction energy was computed as E(interaction) = E(cluster) − (E(Li^+) − E(anion)), where E(x) is the energy of the minimum energy configuration.

Density functional theory (DFT), using the pseudopotential projector-augmented wave method in the Vienna *Ab Initio* Simulation Package (VASP).[88–90] An energy cutoff of 520 eV was used for the plane-wave basis set. The Perdew-Burke-Ernzerhof (PBE) generalized gradient approximation (GGA) functional was used, [88] and the D3 dispersion correction, as originally implemented by Grimme et al.,[91,92] was also included in the calculation of forces and energy through VASP. A 3×2×1 Γ-centered k-point mesh was used to sample the Brillouin zone. The criterion for self-consistency was when the energy difference between subsequent electronic steps was less than 1 μeV. The optimized lattice parameters for the FAST-C parent salt variants are shown in Table 8-3. The minimum energy pathway for Li^+ ion hops in the lattice were calculated using the nudged elastic band (NEB) methodology following the formulations by Henkelman et al.,[91] to ensure the correct determination of the saddle point as implemented in VASP. Three middle images were considered for the NEB calculations. The convergence criterion for NEB calculations was set to an atomic force tolerance of 0.1 eV/Å and an electronic energy tolerance of 10 μeV, respectively. There are two algorithms for updating the geometry of each image in NEB: (1) a more robust, “coarser” conjugate gradient algorithm, which was used at the start; (2) a “finer” quasi-Newton algorithm that was used closer to convergence.

Single crystal growth and X-Ray Diffraction

Diffraction quality single crystals were grown via slow vapor diffusion of hexanes into a dilute solution of **FAST-C** in tetrahydrofuran. Single crystal X-ray diffraction was conducted at the MIT Department of Chemistry X-Ray diffraction facility on a Bruker Photon3 XRD system using a MoK_α source (wavelength =

0.71073 Å). The structure was solved using SHELX software. Views of the solved crystal structure as thermal ellipsoids and crystallographic information are shown in Figure 8-2.

Nuclear Magnetic Resonance (NMR) Spectroscopy

NMR experiments were conducted at the MIT Department of Chemistry Instrumentation Facility (DCIF). All samples were dissolved in acetone-d_6 at a concentration of ~ 1mg/mL unless otherwise noted. ^{1}H and ^{19}F NMR were conducted on a Bruker Avance Neo spectrometer with a proton frequency of 400.17 MHz. ^{13}C {^{1}H} NMR were conducted on a Bruker Avance Neo spectrometer with a proton frequency of 600.14 MHz.

Small and Wide Angle X-Ray Scattering (SAXS/WAXS)

SAXS and WAXS measurements for the liquid crystalline monomers (Figure 3-2C) were conducted at the Argonne National Laboratory Advanced Photon Source (APS) at beamline 12-ID-B. Samples of the material were loaded into wells between two Kapton films and annealed at 150 °C and cooled slowly before measurement. All data were acquired with an X-ray energy of 13.3 keV and an exposure time of 0.5 seconds. SAXS and WAXS patterns were acquired simultaneously on a Pilatus 2M and Pilatus 300K detector respectively. The sample to detector distance for SAXS was 2 meters. An in-situ heating plate was used for temperature control, and samples were allowed to equilibrate at each temperature for 5 minutes before data acquisition. 2D data were radially integrated to yield 1D traces, and the X-ray scattering peak positions were determined by fitting the scattering peaks to pseudo-Voigt functions

Additional SAXS measurements were performed as a function of temperature on the **pFAST-C20-M** polymers at MIT with a SAXSLAB system using a Rigaku 002 microfocus Cu source (λ=1.54 Å), and a

Pilatus 300K detector. Multiple sample-detector distances were used, covering a total *q* range of 0.015 – 2.4 $Å^{-1}$. The films used for EIS measurements were also used for X-ray scattering measurements. Samples were prepared in the Argon glove box in air-tight cells from Xenocs (part number SC-ST-1-HSFX) with mica windows, and heated using a Linkam HFSX350-GI stage. The films were measured at 25 °C, then from 40 – 180 °C on heating in 20 °C steps. For **pFAST-C20-Li, -Na,** and **-Cs**, the films were measured on cooling at the same temperatures after heating. The films were measured at each temperature for 20 minutes, dwelling for 2 minutes at each temperature before measurement to let the polymer equilibrate. The X-ray scattering peak positions were determined by fitting the scattering peaks to pseudo-Voigt functions.

Polarized-light Optical Microscopy (POM)

Liquid crystal properties of the materials were investigated POM using a Leica DMRXP polarized-light microscope fitted with a Linkam TMS 94 hot stage.

Differential Scanning Calorimetry (DSC) and Thermogravimetric Analysis (TGA)

For both DSC and TGA pieces (~1 – 10mg) of cast and dried polymer films were loaded into TA Tzero Aluminum DSC pans. For DSC the pans were hermetically sealed in an argon filled glovebox without exposure to air. DSC experiments were conducted on a TA Instruments Discovery 250 under a constant flow of nitrogen. An initial heating cycle from room temperature to 300 °C at 10 °C/min was run to remove thermal history followed by two subsequent cycles of cooling and heating at 10 °C/min between 300 °C and -50 °C were conducted. Peaks were fit and integrated using TA Instruments TRIOS software. TGA was conducted on a TA Instruments Q500 from room temperature to 450 °C at 10 °C/min under a nitrogen environment and analyzed using TA instruments TRIOS software.

Electrochemical Impedance Spectroscopy (EIS)

After cation exchange the polymers were lyophilized to dryness. The polymers were dissolved in dimethylformamide (3 – 4 wt % polymer in solution), and stirred for 15 – 30 minutes at room temperature. Polymer solution was cast onto 100 μm thick Teflon, on a hot plate at 130 °C. Solution was added 5 – 10 drops at a time, then evaporated (~typically about 5 minutes) before more solution was added. This process was repeated until achieving film thickness between 100 – 200 μm. Polymers were transferred to stainless steel electrodes (1.55 cm in diameter), and dried in a sealed vacuum oven at 180 °C for 24 hours. Samples were transferred to an argon filled glovebox without exposure to atmosphere. EIS samples were prepared by sandwiching the polymer between two stainless steel electrodes, and placing in an air-tight cell.

Ionic conductivity was determined using electrochemical impedance spectroscopy, which was measured using a VMP3 (Bio-Logic) potentiostat, with a frequency range of 1 Hz to 1 MHz with 100mV sinusoidal amplitude. The cell was measured upon heating in cooling, between 70 – 180 °C, with 10°C steps. A thermostat chamber (SU-241, Espec) was used for heating the cell, and the cell was equilibrated at each temperature for 1 h before conductivity was measured. After completion of conductivity measurements, cells were opened inside of an Ar glove box, where final thickness measurements were made of the polymer film. The film area was determined using ImageJ analysis software. The conductivity was calculated $\sigma = t^*/(R^*A)$, where R is the resistance determined from fitting the impedance results to a single-circuit model (Figure 8-3).

Swelling of polymer films with solvent

In an Ar filled glovebox, to an already dried film of **pFAST-C20-Li** polymer, anhydrous Tetraethylene glycol dimethyl ether (G4) was dropped on top. The film quickly swelled indicating a strong interaction of the G4 and polymer film. The preferred ratio of approximately five oxygen atoms (1 molecule) per cation where it is found that a solvate ionic liquid will form was targeted.[93] The resultant materials is 25 mass % of G4 and is significantly softer than the originally film. The sample was warmed slightly on a hot plate at 60 °C and flattened between two stainless steel electrodes and further sealed in a cell. EIS were conducted using the same procedure as for the dry polymer films. Pieces of the swollen material were sealed in an Ar filled glovebox into cells for SAXS and DSC measurements which were conducted using the same procedures as the dry materials.

RESULTS AND DISCUSSION

DESIGN AND SYNTHESIS OF FAST-C20 MONOMER.

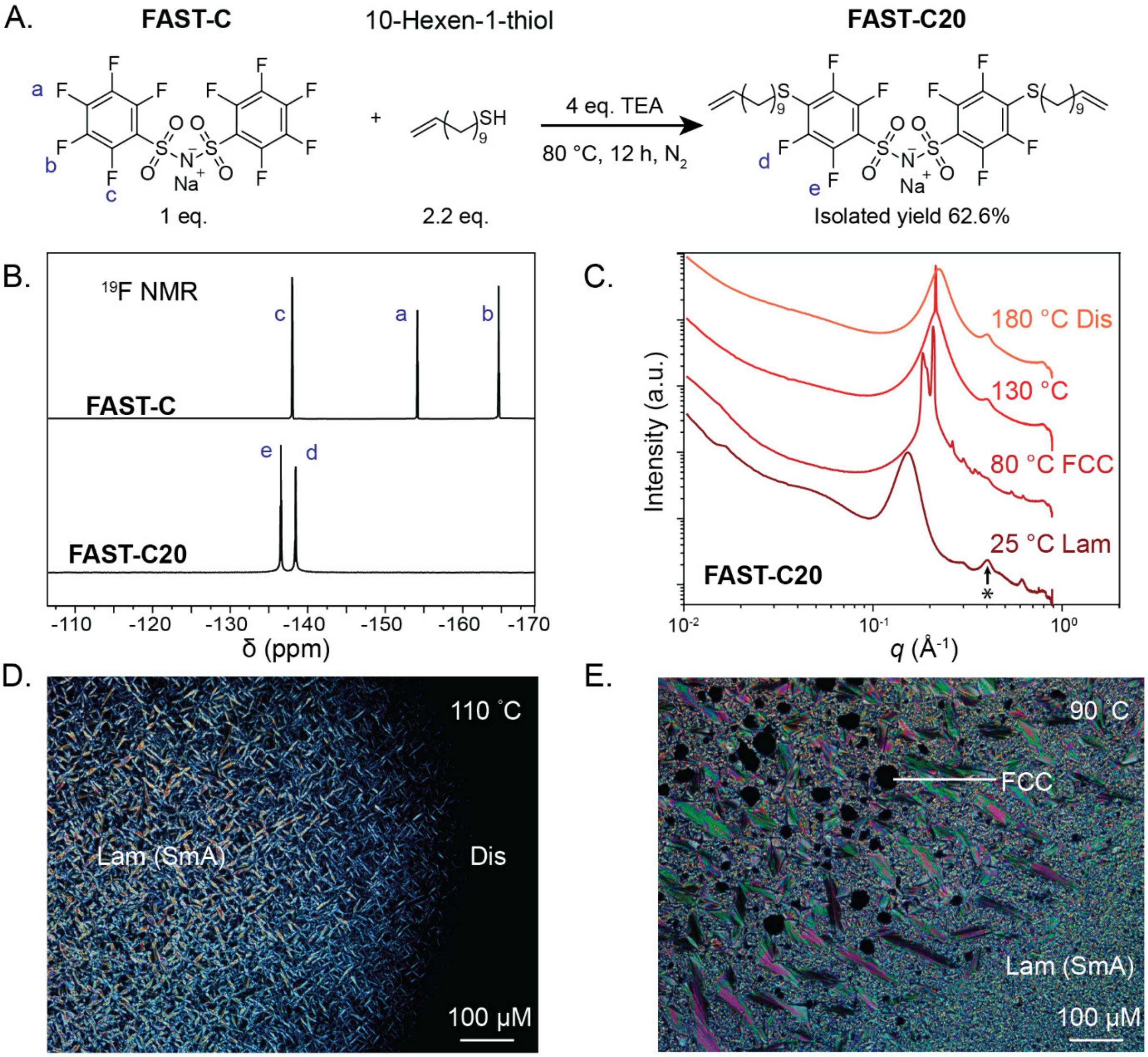

Figure 3-2 Synthesis and Characterization of FAST-C20 monomer. A) Scheme depicting the S_NAr reaction to synthesize the C20 monomer. B) ^{19}F Nuclear Magnetic Resonance (NMR) showing successful functionalization. The

original FAST-C salt has three distinct fluorine resonances, whereas the functionalized monomer only has two. C). Small Angle X-Ray scattering (SAXS) showing the multiple ordered phases present in the bulk monomer material. Peak patterns at 25, 80, and 180 °C were used to assign the phases as lamellar (Lam), face centered cubic (FCC), and disordered (Dis) respectively. Small peak at ~.4 $Å^{-1}$ present in all samples and labeled with * is due to the Kapton window used during data acquisition. D and E). Polarized optical microscopy (POM) showing the different liquid crystalline phases present in the monomer material. At 110 °C the appearance of bâtonnets indicates the nucleation of a smectic A (lamellar) phase from the disordered (isotropic) phase. As the temperature decreases to 90 °C the appearance of dark domains amongst the lamellar phase corresponds to the FCC phase identified in SAXS.

We targeted monomer **FAST-C20** (Figure 3-2A), which features (1) two alkene substituents for polymerization via ADMET; (2) long alkenyl chains to drive polymer crystallization;[94,95] and (3) highly dissociative thioether-linked **FAST-C** anions.[77] Heating **FAST-C** (1 equiv) and 10-undecene-1-thiol (2.2 equiv) at 80 °C in the presence of triethylamine (4 equiv) for 12 h provided **FAST-C20** as a waxy solid in 62% isolated yield on the 5 g scale following purification (Figure 3-2A, see Section S3: Synthetic methods for full synthetic details). ^{19}F NMR spectroscopy (Figure 3-2B) supported the symmetrical structure of **FAST-C20**, showing 2 peaks corresponding to the 2 sets of 4 equivalent F atoms on each side of the FAST anion, in contrast to the 3 distinct sets of F atoms on **FAST-C**. Variable-temperature small angle X-ray scattering (VT-SAXS) was used to investigate the bulk structure of **FAST-C20** (Figure 3-2C). At room temperature, a broad feature located at q = 0.15 $Å^{-1}$ was observed along with higher order reflections located at *2q*, *3q*, and *4q* (Figure 8-4), which are indicative of a lamellar structure with a *d*-spacing of $d = {}^{2\pi}/_{q} = 41.9$ Å. Upon heating to 80 °C, a series of peaks assigned to a face centered cubic (FCC) structure was observed with the lattice parameter a = 61.86 Å (Figure 8-5). We hypothesize that the molecules form conic sections or wedges, which self-assemble into micellar structures on an FCC lattice.[96–98] Further heating to 130 °C gave overlapping broad and sharp peaks with a domain spacing of 29.9 Å, suggesting a mixture of ordered and isotropic/disordered morphologies; further heating to 180 °C produced only a broad peak at d = 28.55 Å indicative of an isotropic/disordered phase.

These results are consistent with **FAST-C20** behaving as a liquid crystal, which was further supported by polarized optical microscopy (POM, Figure 3-2D, E). At 110 °C (Figure 3-2D), which lies between the ordered FCC (80 °C) and mixed phases (130 °C) observed by SAXS, the nucleation of bâtonnets directly from the isotropic phase, characteristic of a smectic A (SmA) liquid crystalline phase was observed.[99] The latter suggests that **FAST-C20** molecules are oriented in the same direction, with their long axis perpendicular to the layers. Upon cooling to 90 °C, dark domains appeared (Figure 3-2E) were assigned to FCC domains observed by SAXS, which are rotationally isotropic and, thus, inherently not birefringent. Upon cooling to 80 °C, most of the SmA phase receded and the POM textures appeared dark. Finally, the appearance of a second smectic phase was observed upon further cooling to 65 °C (Figure 8-6). As the two aryl rings form a hairpin in the **FAST-C** single crystal structure (Figure 3-1D), we propose that the internal angle between the two aryl rings can increase as a function of temperature resulting in the variety of liquid crystalline phases (Figure 8-7). Altogether, these POM results agree well with the VT-SAXS data, which suggest that **FAST-C20** has a high propensity to form ordered structures through nanoscale phase separation of its ionic and hydrocarbon segments, as observed for ionic liquid crystals.[100]

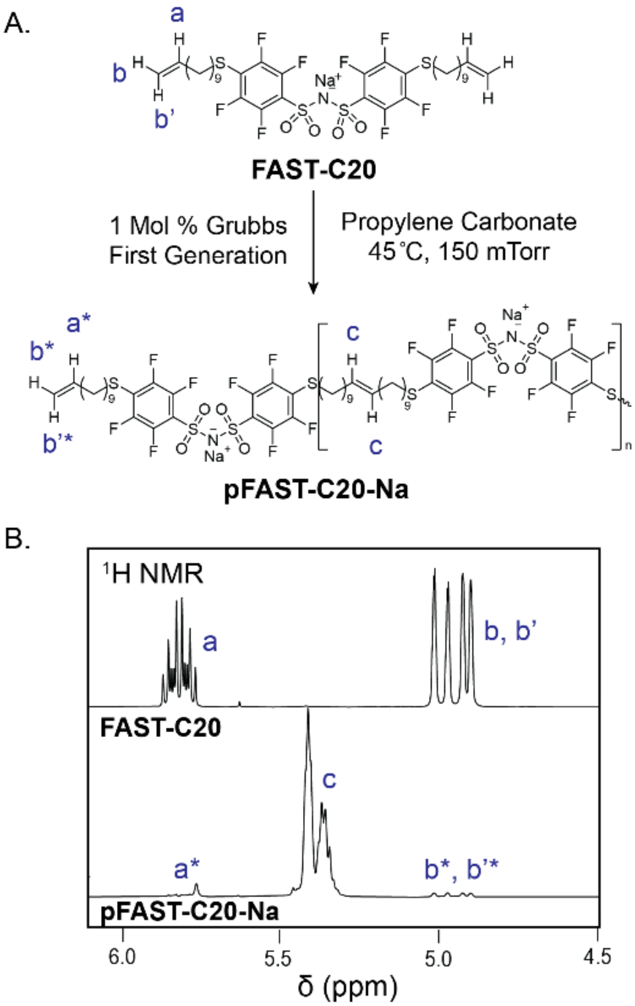

*Figure 3-3 ADMET Polymerization of FASTC-20 to yield pFAST-C20-Na. A) Synthesis of **pFAST-C20-Na** via ADMET polymerization of **FAST-C20**. The terminal protons of the **FAST-C20** (labeled as a, b, and b') become end groups (labeled as a*, b*, b'*) and internal alkenes (labeled c) in **pFAST-C20-Na**; integration of these peaks enables calculation of the number-average degree of polymerization and molar mass (neglecting cyclization). B) ^{1}H NMR spectra for **FAST-C20** (top) and **pFAST-C20-Na** (bottom) showing the relevant alkene resonances. The internal olefin (labeled as c) shows a mixture of trans and cis isomers as is expected for ADMET polymerization using Grubbs 1st-generation catalyst.[101] (600 MHz acetone-d$_6$, 25 °C).*

ADMET polymerization of FAST-C20 and cation exchange to provide a family of dissociative ionenes—pFAST-C20-M (where M = Na$^+$, Li$^+$, K$^+$, and Cs$^+$).

Next, we focused on the polymerization of **FAST-C20** via ADMET. Initially, we explored common conditions for ADMET of non-ionic monomers, which involved refluxing a mixture of **FAST-C20** and Grubbs 1st-generation catalyst (1 mol %) in dichloromethane under nitrogen flow to remove ethylene;[102] however, poor solubility of the growing polymers in dichloromethane led to poor/inconsistent conversions. By contrast, conducting the polymerization in propylene carbonate and under vacuum (150 mTorr) to remove ethylene (Figure 3-3A) ensured solubility of the oligomeric intermediates and polymer products gave consistently high monomer conversions as determined by ^{1}H NMR (Figure 3-3AB) (see Supporting Information for full details).[103] Upon quenching the reaction by addition of excess ethyl vinyl ether, the ionene product “**pFAST-C20-Na**” was isolated by precipitation into diethyl ether, filtration, and drying under vacuum at 180 °C for 12 h. The number-average degree of polymerization, N_n, number-average molar mass, M_n, and *cis*/*trans* ratio of backbone alkenes of **pFAST-C20-Na** were estimated by ^{1}H NMR integration to be ~130, ~106 kDa, and 1:1.4, respectively (Figure 3-3AB); the former values assume negligible cyclization. Additionally, no significant change was observed in the ^{19}F NMR spectra, indicating preservation of the tetrafluorinated aryl substituents (Figure 8-39). Size exclusion chromatography yielded a dispersity, $Đ$, of ~ 2, which is consistent with the step-growth nature of ADMET (Figure 8-41). Washing aliquots of **pFAST-C20-Na** with 1 M aqueous solutions of LiCl, KCl, or CsCl provided the Li^+, K^+, and Cs^+ analogs **pFAST-C20-Li**, **pFAST-C20-K**, and **pFAST-C20-Cs**, respectively, as confirmed by ^{7}Li,^{23}Na, and ^{133}Cs NMR, where appropriate (Figure 8-8). The cation exchanged ionenes were lyophilized to yield dry fluffy powders that were used for further study.

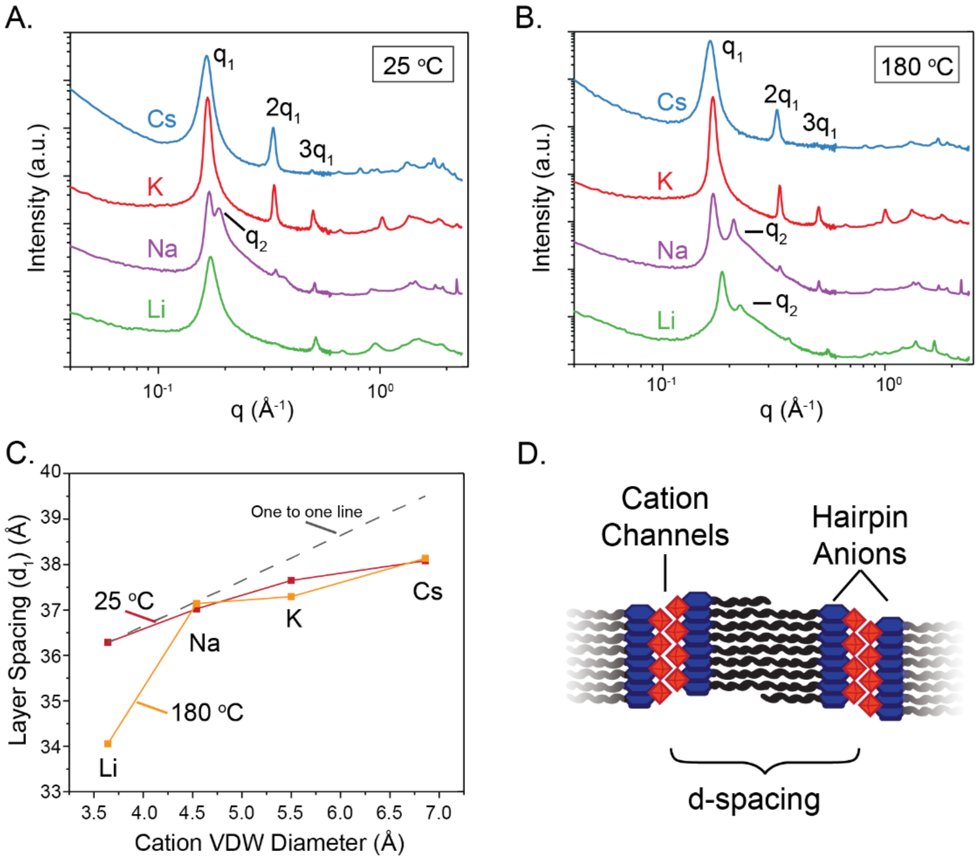

*Figure 3-4 Study of pFAST-C20-M polymer structures. A and B) Reduced Small Angle X-Ray Scattering (SAXS) patterns of the 4 different variants of the **pFAST-C20-M** ionenes (M = Li, Na, K, and Cs) at 25 °C and 180 °C, respectively. The traces are offset for clarity and plotted on a log-log scale with intensity (a.u.) versus the scattering vector q (Å^{-1}). C) Real space dimensions (d-spacings) of the lamellae for each ionene versus the corresponding Van der Waals (VDW) diameter of the cation. As the cation size increases so does the size of the lamellae. D) Illustration of hypothesized lamellar structure of **pFAST-C20-M** ionenes based on X-ray scattering information and the single-crystal X-ray structure of **FAST-C** shown in Figure 1D. Cations are represented as red tetrahedra. Anions are represented as blue hexagons. Alkyl spacers are represented as black chains.*

SOLID-STATE STRUCTURAL AND THERMAL CHARACTERIZATION OF PFAST-C20-M POLYMERS WITH VARIOUS CATIONS M.

Films of each ionene were prepared by drop-casting from dilute solutions in DMF and drying under vacuum at 180 °C. VT-SAXS and VT-wide-angle X-ray scattering (VT-WAXS) (Figure 3-4A) curves displayed primary scattering peaks for each **pFAST-C20-M** polymer (q_1) at ~.15–.19 Å^{-1} and higher-order reflections at $2q_1$ and/or $3q_1$, consistent with a lamellar structure. The room-temperature SAXS pattern for **pFAST-C20-Na** showed a second peak, q_2, with higher-order reflections, indicative of a second lamellar domain, which can be attributed to lamellae at a different tilt angle as has been observed in other systems.[69] Peaks in the high q WAXS region (0.8–1.5 Å^{-1}) were observed for each sample, which are indicative of backbone crystallinity. Notably, the WAXS peaks of orthorhombic[64,70,95] or monoclinic polyethylene,[104] often observed for polymers with long alkyl spacers, are not observed for any of the polymers studied here, which may be due to the presence of *cis* and *trans* olefins in the polymer backbones and/or the sterically bulky FAST anions. In the future, hydrogenation of the polymer backbone could potentially be used to test these hypotheses.

Unlike monomer **FAST-C20**, which displayed multiple structural transitions as a function of temperature (Figure 3-2C), the lamellar morphology of each polymer was maintained up to at least 180 °C (Figure 3-4B, Figure 8-9–8-12). **pFAST-C20-Li** was the only sample to show a significant change upon heating, displaying a shift to higher q and the emergence of a second set of peaks (q_2) with d_2 = 28.11 Å, indicative of a mixture of lamellar phases similar to those observed at room temperature for **pFAST-C20-Na.** These changes were reversible upon cooling to room temperature and waiting for ~5 days, suggesting that the single lamellar phase observed at room temperature is reasonably stable.

The *d*-spacings at room temperature and 180 °C for **pFAST-C20-M** increased with the Van der Waals diameters of the cations M (Figure 3-4C), which in consistent with a microstructure wherein the cations are sandwiched within anionic layers. The single-crystal X-ray structure of **FAST-C** (Figure 3-1D) similarly shows Na^+ ions sandwiched between layers of **FAST-C** anions with the perfluoroaryl rings of the latter folded away from the ion channels in hairpin structures, where the *para*-fluorine substituents are nearly parallel to each other. Thus, we propose that the solid-state structures of **pFAST-20C-M** polymers consist of layers of cations coordinated to hairpin-folded **FAST-C** anions (Figure 3-4D), each of which are linked to an adjacent layer by their *para*-C20 alkenyl segments. To further support for this proposed structure, we prepared analogs of **pFAST-C20-M** with shorter, 10 carbon spacers between each anion (**pFAST-C10-M**), following similar procedures to those used above for **pFAST-C20-Na**. SAXS/WAXS characterization of **pFAST-C10-M** revealed similar lamellar structures compared to **pFAST-C20-M**, with *d* spacings that increase monotonically with the cation diameter (Figure 8-13). Notably, however, the **pFAST-C10-M** lamella were all ~10.5 Å smaller than the **pFAST-C20-M** (Figure 8-14), regardless of cation size, supporting the notion that larger cations expand the ionic layers without impacting the alkenyl layers. Extrapolating these findings for **pFAST-C20-Na** and **pFAST-C10-Na** to a "zero carbon" spacer suggests that the ionic layers are ~13.1 Å thick, which agrees remarkably well with the observed distance—13.2 Å—between the *para*-carbon atoms of two **FAST-C** anions that span a single ionic layer in the crystal structure of **FAST-C** (Figure 3-1D; Figure 8-15).

Differential scanning calorimetry (DSC) was used to further investigate the thermal transitions in **pFAST-C20-M** (Figure 8-16–8-19). All of the ionenes, regardless of cation, showed endothermic transitions at >190 °C, which likely correlate to phase transitions in the lamellae or polymer backbone. In agreement with their VT-SAXS data, which displayed two sets of lamellae at 180 °C, **pFAST-C20-Li** and **pFAST-C20-Na** showed two endothermic transitions in the range of 180–260 °C. Additionally, glass transition temperatures were observed for **pFAST-C20-Li** and **pFAST-C20-Na** at ~ 100 °C, but were not detected for **pFAST-C20-K** and **pFAST-C20-Cs**, suggesting that the former may contain more amorphous domains in addition to the lamellae observed via SAXS. Finally, thermal gravimetric analysis (TGA) indicated that all of these ionenes were stable up to ~325 °C, with major degradation not occurring until >380 °C (Figure 8-20). Minimal (<4%) weight loss was observed before 325 °C, indicating the samples were dry.

IONIC CONDUCTIVITY OF PFAST-C20-M IONENES

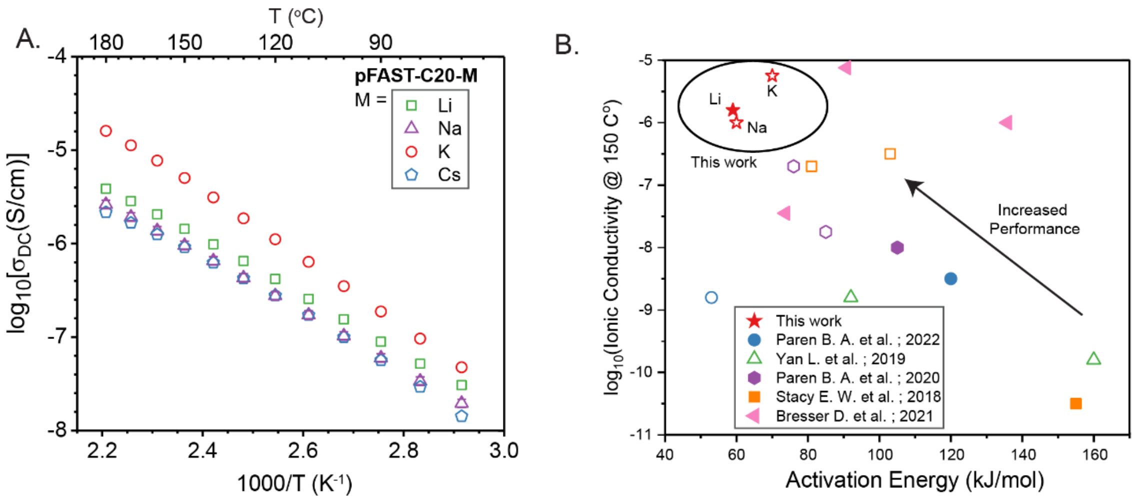

Figure 3-5 Ionic conductivity of pFAST-C20-M Polymers. a) Combined variable temperature EIS data of the four synthesized ion variants. B) Comparison of the activation energy and ionic conductivity at 150 °C for this work and related papers (references [69–71,73,74]). The literature data contains solvent-free single-ion conducting polymers possessing an Arrhenius profile and fitted activation energy. It is desirable to have the lowest activation energy and highest ionic conductivity. Solid markers denote lithium variants of the respective polymer system, while the hollow points are a mixture of Na, K, and Cs variants. Detailed structures from the references can be found in Figure 8-22

Given that **pFAST-C20-M** formed lamellar structures with cations sandwiched between anionic channels that are stable at high temperatures, we sought to characterize their ion conductivity. Figure 3-5A shows measured ionic conductivities versus inverse temperatures for the 4 different **pFAST-C20-M** ionenes. The conductivities span from ~10^{-8}–10^{-5} over the tested temperature range (80 to 180 °C, respectively) and are consistent and reversible over multiple cycles of heating and cooling between 80 and 180 °C (Figure 8-21; Table 8-1). While these conductivities are ~2–3 orders-of-magnitude lower than optimized SPEs that depend on segmental motion (e.g., PEO-based SPEs), the observations of linear conductivity versus 1000/T profiles for 3 of the 4 ionenes (**pFAST-C20-Na**, **pFAST-C20-Li**, and **pFAST-C20-K**) and reasonable conductivity well below T_m and T_g (including conductivity ~7–8 orders-of-magnitude greater that coupled SPEs at T_g) are consistent with a decoupled ion conduction mechanism for these samples.[34] These data can thus be fitted with an Arrhenius equation of the form:

Equation 2-5: $\boldsymbol{\sigma = \sigma_0 * exp(^{-E_a}/_{RT})}$

Where E_a is the activation energy of ionic transport in kJ/mol, σ_0 is a pre-exponential factor, R is the universal gas constant, and T is temperature. Interestingly, **pFAST-C20-Li** and **pFAST-C20-Na** were found to have similar activation energies of 59 and 60 kJ/mol, respectively. **PFAST-C20-K** displayed a higher activation energy of 70 kJ/mol, but overall greater ionic conductivity at all temperatures. While other works have suggested that larger, softer cations have lower activation energies for ionic transport,[70,71] for **pFAST-C20-M**, confinement of the cations to the ionic channels may impede hopping of larger cations. We note that the curvature in the conductivity versus 1/T plot for **pFAST-C20-Cs** suggests that these data are better fitted with the Vogell-Fulcher-Tammann (VTF) equation that is typically used for coupled SPEs (Figure 8-21; Table 8-1). Thus, we do not focus on this sample in the remaining discussion.

It is notable that the fitted Arrhenius activation energies for **pFAST-C20-Li**, **pFAST-C20-Na**, and **pFAST-C20-K** are amongst the lowest reported for dry ionene/ionomer conductors that are proposed to operate via a decoupled ion conduction mechanism (Figure 3-5B; see Figure 8-22 for structures of each referenced example). Similar, the ionic conductivities at 150 °C for our ionenes are amongst the highest of related systems. We proposed that this performance is directly related to the highly dissociative **FAST-C** molecular structure (Figure 3-1), demonstrating that molecular design at the level of anionic substituents in ionene conductors may provide a path toward optimal SPEs in the future.

INVESTIGATING THE MECHANISM OF ION CONDUCTION USING NUDGED ELASTIC BAND CALCULATIONS.

To gain further insight into the potential ion conduction mechanisms in these **pFAST-C20-M** ionenes, nudged elastic band (NEB) calculations were performed using the **FAST-C** crystal structure (Figure 3-1D) as a model and assuming that the ionic channels within bulk **pFAST-C20-M** ionenes have similar local structures (see Section S2: Calculation of the migration barrier of cations in the **FAST** structure**.**; Figure 8-25–8-29). Two ion-hopping mechanisms were explored: vacancy mediated and concerted. For the Li^+ ionene, both mechanisms had similar calculated energy barriers (~68 kJ/mol) and agreed well with the experimentally measured activation energy (~60 kJ/mol), suggesting that either may be operative in **pFAST-C20-Li**. For Na^+ and K^+ ionenes, the vacancy-mediated mechanism gave significantly lower calculated energy barriers (~70 kJ/mol versus 112 kJ/mol for vacancy-mediated and concerted mechanisms for Na^+, respectively), the former of which were consistent with the experimentally determined barriers of ~70 kJ/mol. These results suggest that stoichiometric imbalances, perhaps created at disordered interfaces or boundaries between crystalline domains as established for ceramic conductors,[105–107] may be advantageous to ion conduction in these ionenes. NEB calculations also indicated that the highest energy structure for each ion-hopping trajectory corresponded with loss of an oxygen ligand from adjacent **FAST-C** anions (See Figure 8-26–8-29), suggesting that further molecular engineering of the anion structure, perhaps via *ortho*-substitution to introduce additional weakly coordinating ligands, may provide a path toward even lower energy barriers.

SELECTIVE CATION SOLVATION LEADS TO SIGNIFICANT ION CONDUCTIVITY IMPROVEMENT IN IONENE SPEs

Given the well-defined anionic channels in **pFAST-C20-M**, we wondered if it would be possible to add a small amount of cation-coordinating solvent to further increase conductivity through those channels without disrupting their overall lamellar structure.[108] We were particularly inspired by Solvate Ionic liquids (SILs), which are a class of ionic liquids wherein strongly binding solvents form supramolecular solvent–cation complexes with virtually no “bulk” solvent.[93] This unique structure facilitates anion dissociation and can lead to improved ionic conductivity, low vapor pressure, and excellent electrochemical stability.[93,109] SIL formation requires highly dissociative anions such as TFSI; given the highly dissociative nature of **FAST-**

C, and our previous finding that *para*-thioether-functionalized fluorinated aryl sulfonamide salts similar to **FAST-C** form SILs in the presence of 1 equiv tetraglyme (G4),[77] we hypothesized that it may be possible facilitate the formation of SIL-like cation complexes within the channels of **pFAST-C20-Li** using G4 solvent.

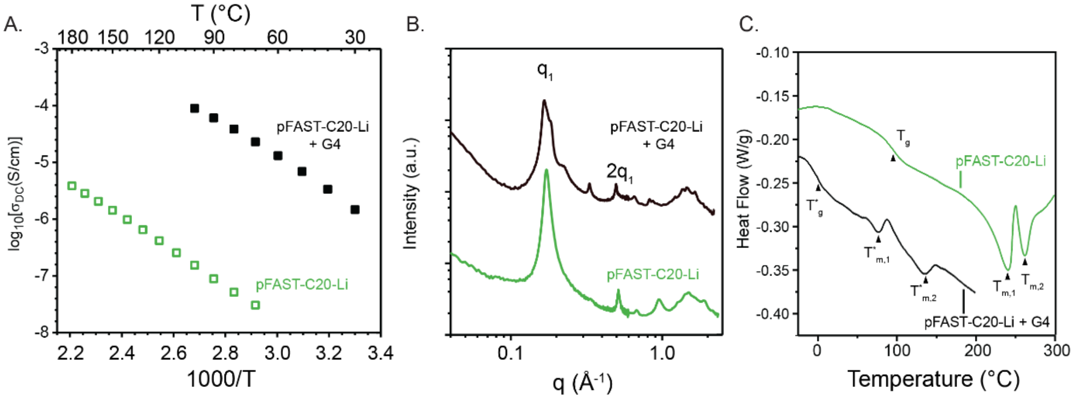

Figure 3-6 A) Ionic conductivities of **pFAST-C20-Li** (green trace) and **pFAST-C20-Li** + G4 (1 equiv per cation) (black trace). B) 1D SAXS and WAXS profiles **pFAST-C20-Li** and **pFAST-C20-Li** + G4**,** showing that the ordered lamellar structure is retained upon G4 addition with slight changes in the shape of the primary peak q_1 and in the high q region (>1.0 Å^{-1}). C) DSC traces (from the second heating cycle) for **pFAST-C20-Li** and **pFAST-C20-Li** + G4.

In support of our hypothesis, we observed significant increases in conductivity for **pFAST-20-Li** after exposure to 1 equiv of G4 (Figure 3-6A). For example, at 80 °C, the ionic conductivity of **pFAST-20-Li** + G4 was ~3 orders-of-magnitude greater than dry **pFAST-20-Li**. Fitting the conductivity data (Figure 8-23; Table 8-2) for **pFAST-20-Li** + G4 revealed a similar activation energy but a ~1000-fold larger pre-factor compared to dry **pFAST-20-Li**, suggesting that solvation leads to a larger number of mobile cations. Notably, VT-SAXS and VT-WAXS analysis (Figure 3-6B; Figure 8-24) suggested that the G4-containing material maintained a highly ordered lamellar structure with scattering peaks at q_1 = .166 Å^{-1}, $2q_1$, and $3q_1$ till at least 100 °C. Moreover, the lamellar *d*-spacing for **pFAST-20-Li + G4** (35.7 Å) was greater than that for dry **pFAST-C20-Li** (33.4 Å) by 2.3 Å, which is within the expected size difference of reported Li^+ coordinated by G4 or crown ethers compared to Li+ alone.[110,111] DSC analysis (Figure 3-6C) showed T_g and

T_m transitions for **pFAST-C20-Li** + G4 that were >100 °C lower than for the dry ionene, indicative of plasticization, which is expected to increase ion conductivity. Finally, crystallization of G4 ($T_c = -9.4$ °C)[112] was not observed, suggesting that the presence of minimal bulk G4.

CONCLUSIONS

Here, we introduce the concept of using highly dissociative, electron deficient anions as building blocks for ionene synthesis. Specifically, the symmetrical **FAST-C** anion that is highly dissociative, easily functionalizable via S_NAr, and capable of forming channel structures in the solid state was leveraged to generate a new diene monomer **FAST-C20** for ADMET polymerization. **FAST-C20** showed a high propensity to self-assemble on its own, forming multiple different thermally responsive liquid crystalline phases. After polymerization, the resulting ionenes—**pFAST-C20-M**— form highly ordered lamellar bulk materials driven by Van der Waals interactions of the C20 linkers and aggregation of the anionic **FAST-C** domains. Due to their highly ordered structures and dissociative anions, **pFAST-C20-M** polymers display amongst the highest overall ionic conductivities and lowest activation energies for ion conduction reported for dry polymer electrolytes proposed to operate via cation hopping. Furthermore, we show that cation solvation can be achieved without significant disruption to the overall lamellar structure, resulting in a ~three orders-of-magnitude increase to ionic conductivity. This work suggests that anion molecular design may offer a path to further improve the performance of decoupled solid polymer electrolytes. Looking forward, inspiration can be drawn from the ceramic ion conductor field, where vacancy assisted diffusion plays a key role in ion conduction, and large gains in ionic conductivity can be achieved by aliovalent doping.[113] Additionally, through future monomer designs, geometric connectivity and distances between anionic hopping sites can be tuned to further improve ionic conductivities and lower activation energies.[28] We expect that novel, highly dissociative anionic building blocks will be key to these endeavors.

CHAPTER 4 DEVELOPMENT OF A HIGH THROUGHPUT PLATFORM FOR ELECTROLYTE DISCOVERY

The following three chapters will concern the development, testing, and experimentation on a high throughput platform for polymer electrolyte testing. The work presented is the product of multiple years of effort from multiple people in a highly collaborative team that the author has been a part of for the entirety of the Ph.D. Much of the work was led by the author, and a majority of the data was collected by them, but additionally the author would like to acknowledge the following team members for their contributions: Jeffrey Lopez, Jurgis Ruza, Gabriel Bradford, Sawyer Cawthern, Abe Herzog-Arbeitman, and Christian Plaza-Rivera. From Unchained Labs, who led the engineering of the instrument: Bren Ehnebuske, Bjorn Monteen, Edis Miljevic, and Dan Kinder. Additionally, support from the Toyota Research Institute, not just for funding the project but also extensive help in seeing the platform completed through a challenging development process: Ha-Kyung Kwon, Brian Storey, and Daniel Schweigert.

Much of the scientific field has been going through a paradigm shift in recent years. The copious scope of available data combined with new computational tools to extract, process, and learn from this information has led to a shift toward "data-driven design." Data-driven design, while rooted in the same fundamental scientific methods of the past (i.e. observation, formulation of hypotheses, and experimentation), seeks to remove "human intuition" from the design and rather replace it with computational models which can intake a far greater amount of data, produce meaningful results, as well as uncover interesting outliners that human biases may miss.[114] One key data driven tool, machine learning (ML) has been influential in multiple research fields, realizing boons in computer vision, drug discovery,[115] natural language processing, and has also been applied to Li-ion battery research.[116,117] ML is particularly powerful for materials design as it can intake a high volume of data from many different sources and is computationally cheap compared to other predicative methods such as molecular dynamics simulations.[118] ML models can be trained to predict materials properties of interest with high accuracy and help guide experimentalists on which materials to synthesize and test first.

Hand-in-hand with data-driven design is an increased scale of experiments, enabling more efficient exploration techniques such as Bayesian optimization and providing new data sets from which more accurate ML predictive models can be trained.[119] ML becomes much more powerful when paired with high throughput experimentation in what is generally referred to as an "active learning" (or self-driving) lab.[119] In such a scheme, the ML model is iteratively retrained as new data is acquired, resulting in the ML model being able to progressively make better predictions to guide the next batch of experiments. In certain applications, inverse design has also been shown to be an incredibly powerful tool, in which optimization of a desired property is performed in an embedded latent space, and then back-output to the physical design for testing.[120] Data-driven methods have been successfully employed in chemistry and materials to discover photocatalysts for hydrogen evolution reaction,[121] metallic glasses,[118] and optical thin films[122,123] (to highlight just a few) yielding new top-performing materials much faster than traditional experimentation.

With these principles in mind, we set out to create a platform for the data-driven design of polymer electrolytes. While the overarching project encompasses many different data-driven aspects such as accelerating materials simulations using ML,[124] learned forcefields for more accurate and inexpensive materials predictions, and property predictions from database trained ML models, the ultimate goal of the platform was to perform active learning to optimize the ionic conductivity of polymer electrolytes. A critical component of this was the development of a high throughput platform to scale up polymer electrolyte synthesis, formulation, and testing while also collecting all experiments into a machine-readable database ready for ML. The project has been a collaborative effort between multiple research groups at MIT. In this Chapter, the design and development of the high throughput platform (collectively "the tool," "the robot," or "Wall-E"(to some)) will be detailed. In the subsequent chapters, two applications of the tool will be discussed, first an in-depth screen of ion conduction in PEO and second applying the HT tool in an active learning loop to optimize the formulation of electrolytes composed of a far less well-studied poly(caprolactone)(PCL).

OVERVIEW OF HIGH THROUGHPUT PLATFORM

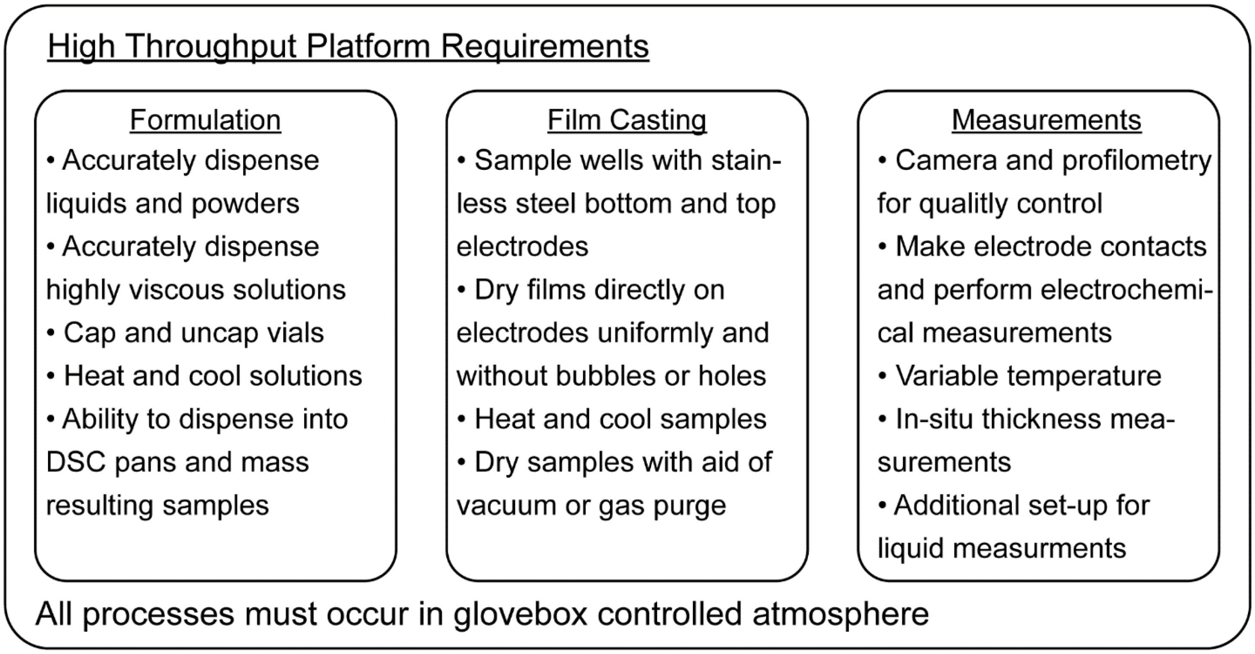

High Throughput Platform Requirements

Formulation
- Accurately dispense liquids and powders
- Accurately dispense highly viscous solutions
- Cap and uncap vials
- Heat and cool solutions
- Ability to dispense into DSC pans and mass resulting samples

Film Casting
- Sample wells with stainless steel bottom and top electrodes
- Dry films directly on electrodes uniformly and without bubbles or holes
- Heat and cool samples
- Dry samples with aid of vacuum or gas purge

Measurements
- Camera and profilometry for qualitly control
- Make electrode contacts and perform electrochemical measurements
- Variable temperature
- In-situ thickness measurements
- Additional set-up for liquid measurments

All processes must occur in glovebox controlled atmosphere

Figure 4-1 Design requirements for the high throughput platform

When setting out to develop a high throughput platform for polymer electrolyte research, it was important to consider the key design requirements and benchmarks for the instrument to hit. Where possible, it was also important to consider being able to accommodate as wide a range of materials and processes as possible without losing reliability. The main design requirements can be grouped into three large categories, indicative of the main steps for polymer electrolyte work: formulation, film casting, and measurements.

Formulation of polymer electrolytes, at their simplest, generally consist of a single salt dissolved in a polymer host e.g., LiTFSI in PEO. However, just a solid mixture of powders does not form a solid electrolyte, and rather a co-solvent is used to combine the materials. The combination of polymer, salt, and solvent forms the formulation precursor from which films can be cast and dried. The resultant films are solid solutions of salt dissolved in polymer. Therefore making such solutions requires accurate solid powder and liquid dispensing. Due to the high viscosity of high MW polymer solutions, the liquid dispensing must also be capable of dispensing highly viscous solutions accurately and without clogs, which can be difficult for air-based pipettes.

Polymer film casting is the next important step. Creating uniform height, bubble- and hole-free, polymer films from solution casting requires high tunability for both the solutions and drying procedures. Additionally, it is common in polymer electrolyte work to dry the films under reduced pressure and purge with inert gas to aid in the removal of residual water and solvent which can artificially boost ionic conductivity (and also create instability if used in a real battery). Accommodation for these procedures to occur in the glovebox had to be designed.

The final requirements after films are produced are measurements. Since the goal was to produce a much larger scale of reliable measurements, an optical camera and profilometer were identified as essential quality control elements to characterize the films. To make electrochemical measurements, the instrument must sandwich the polymer films between stainless steel electrodes, and make electrical contact with an external potentiostat. To measure ionic conductivity, the standard method used is electrochemical impedance spectroscopy (EIS), which after fitting to an equivalent circuit model will yield the bulk resistance (R) of the polymer film.[125] The ionic conductivity is then calculated from the equation:[125]

Equation 4-1

$$\sigma = \frac{l}{R * A}$$

Importantly for this method, a measurement of the contact area (A) and the film thickness (l) are also needed. The area is assumed to be the contact area of the electrodes and is the same for all samples. However, the thickness varies from sample to sample and also changes as a function of temperature and applied pressure. Subsequently, a method to measure thickness *in situ* is required. Variable-temperature

EIS can give insight into ion conduction mechanisms, and as such, integrated sample heating was also necessary.

Finally, there are throughput requirements to consider. When setting out to design a high throughput platform to generate data useful for machine learning, we needed to operate with scale and speed sufficient to generate enough data to train ML models accurately. We estimated that we would need to characterize around 15 samples daily at variable temperatures to generate about 2000 data points monthly. Additionally, the instrument should be able to work nearly autonomously, requiring human intervention for design creation and set-up and clean-up after experiments are complete. To meet these requirements we hired a third-party company, Unchained Labs, to develop the high throughput tool and accessories based on their existing platform called the "Big Kahuna". For various reasons, primarily the COVID-19 pandemic, much of the development became much more collaborative (as opposed to Unchained Labs independent development), with MIT researchers spearheading many of the features.Additionally, the requirements proved to be much more challenging to reach in practice, especially via remote working methods, which took about two years longer than anticipated. Much of the trials and tribulations along the way will not be documented here, rather, the final products and solutions will be highlighted. Suffice it to say that it was ROUGH!

OVERVIEW OF HT PLATFORM COMPONENTS

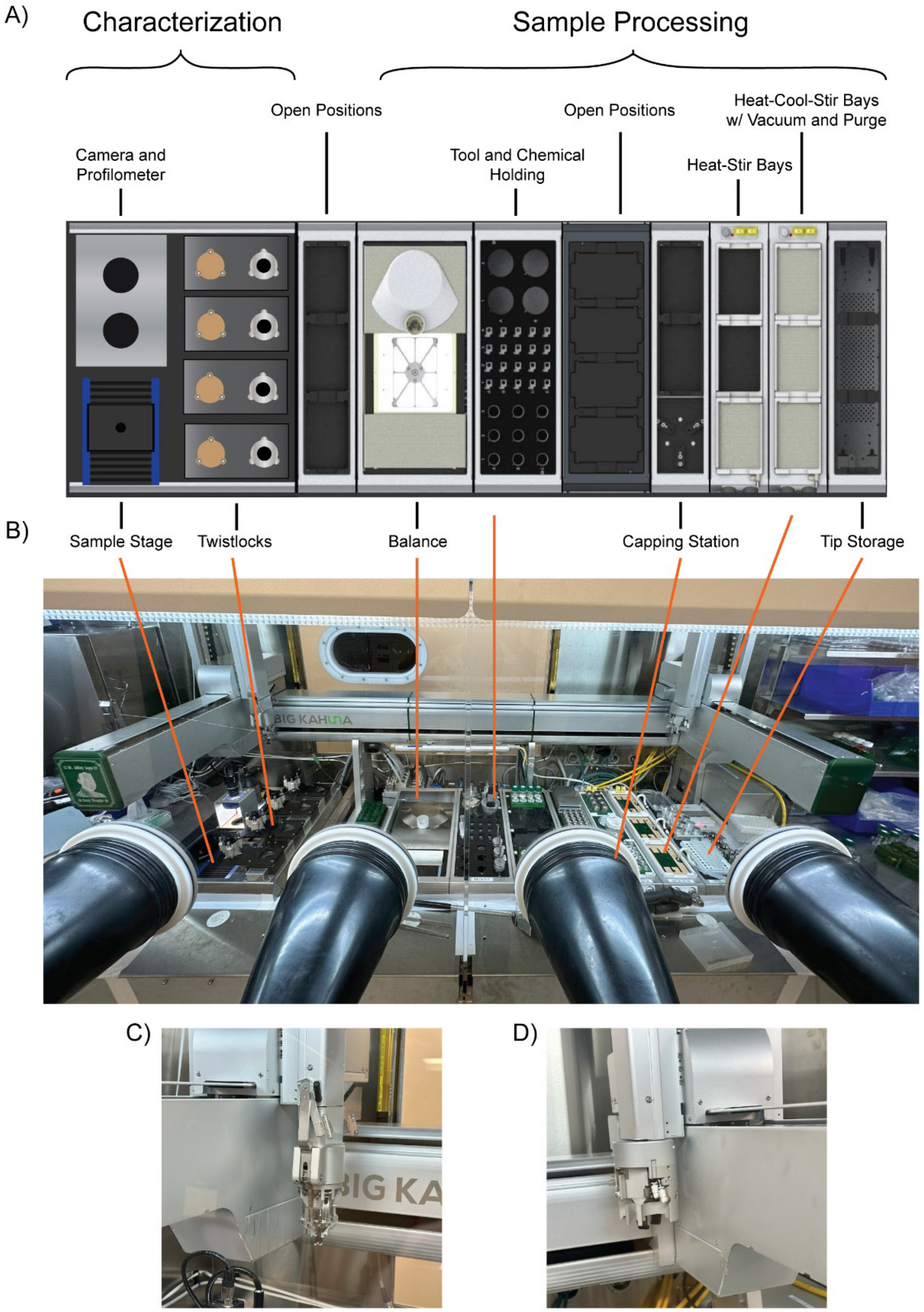

Figure 4-2 Overview of HT Platform A) Overhead view diagram of all deck components B) Side view of the platform within the glovebox C) Vial-Plate Gripper (VPG) arm, visible in back left of picture B D) Dispense head arm visible in back right of picture B. Part of illustration A) is reproduced from Unchained Labs ©Unchained Labs 2010-2021

Figure 4-2 shows the developed HT platform in the lab. The whole instrument is self-contained within an argon-filled glovebox to keep an inert and water-free atmosphere, as most battery chemicals require. The system comprises three primary components, the deck on which all samples and chemicals sit and two three-axis arms which carry out manipulations. The deck Figure 4-2A) consists of two main sections: the characterization section, which consists of an optical camera, profilometer, and “twistlock” assemblies that handle all aspects of the electrochemical measurements, and the sample processing section, which includes a balance, source chemical and tool storage, capping station, and heat-cool-stir bays. Sample plates are moved through the various deck positions by the vial-plate-gripper (VPG) arm (Figure 4-2C), and all other tools are handled by the dispense head arm (Figure 4-2D). The dispense head is equipped with various tools to accommodate liquid dispensing with various pipette sizes ranging from 10 µL to 10 mL, tools for powder dispensing, and even a vacuum head that can manipulate small objects such as the top electrodes. The platform can accommodate various user-defined protocols to execute different tasks and has very general use beyond just electrolyte formulation and testing.

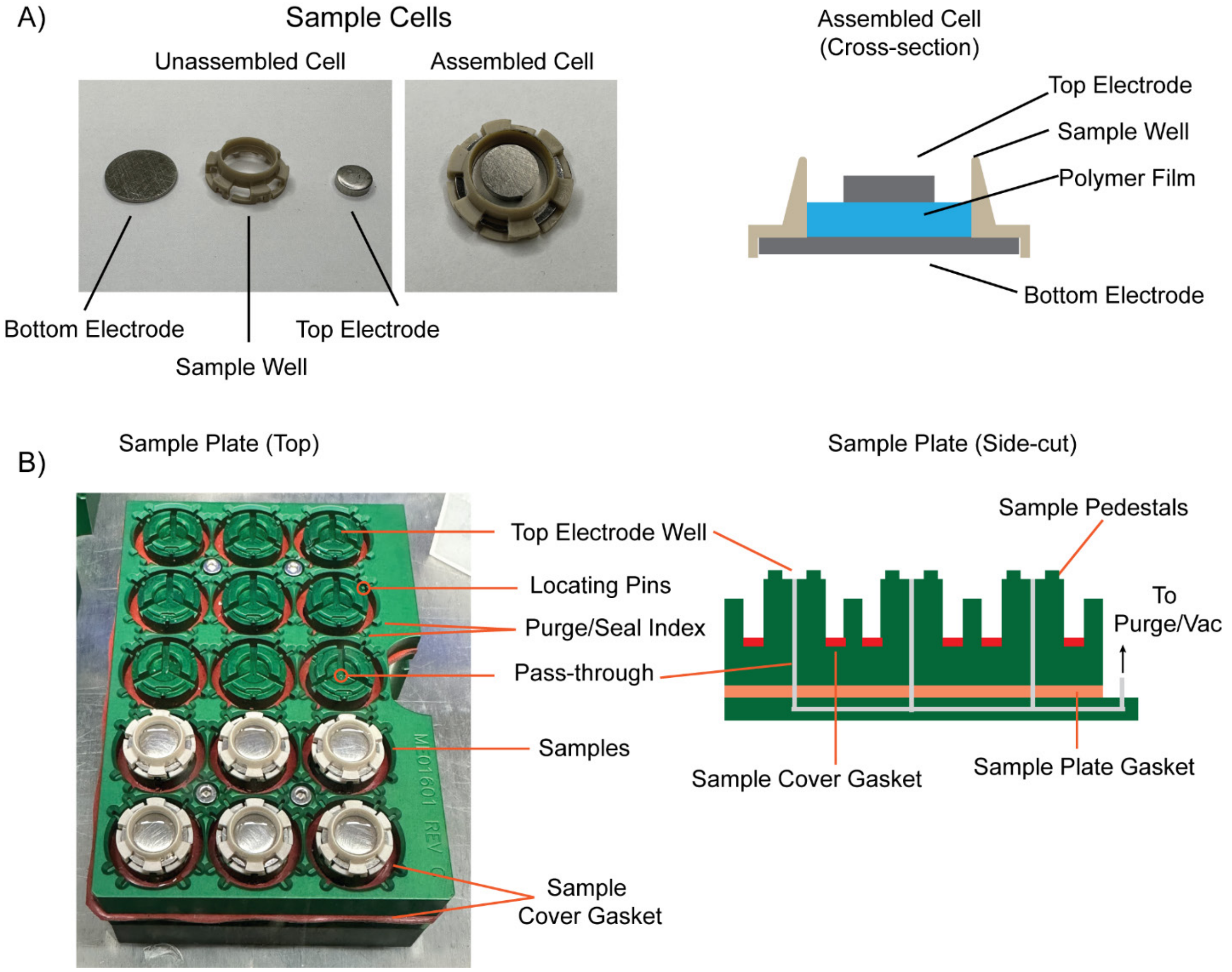

Figure 4-3 Sample cells and plates A) Pictures and cross-section illustration of key cell components, including the bottom and top electrodes, and the sample well, which aids film casting. B) Diagram of key features of sample plates which can hold 15 samples each. Not pictured are individual sample covers.

Custom sample cells and plate development were necessary to achieve all design requirements. The sample cells are composed of three main components, the bottom electrode onto which the polymer film is cast, a sample well (composed of poly(etheretherketone) (PEEK)) that holds the film precursor formulation as it dries, and the top electrode, which is added after the film has dried (Figure 4-3A). Importantly the top electrode must be added *after* the film has been dried down onto the electrode, which necessitates its storage elsewhere. This feature among others is achieved through the custom sample holder plates (Figure 4-3B). Each top electrode is stored beneath the sample and then added during sample loading for measurement. The sample pedestals also have locating pins that index to slots on the sample well to allow for accurate placement of samples as they are moved through the various stations by the VPG. The sample plates must also accommodate vacuum and purge to aid in sample drying. This is achieved through internal pass-throughs in each sample pedestal which connect to a gas line used for either purging in or vacuum out. Each sample well also has a cover which can be in one of two heights as determined by indexing pins along its outside. In the purge position, the covers sit a bit higher creating a small gap at the bottom of each well. In the seal (vacuum) position the bottom of each cover interfaces with the sample cover gasket allowing for a seal to form. Additionally, the entire bottom portion of the plate sits on a gasket in the bottom of the heat-cool-stir bays which creates a seal of the plate to the gas inlet. The materials used for each of these gaskets is essential for reliable operation, and multiple iterations were needed to achieve final results. Additionally, it was found that the sample covers do not seal well on their own, given they are lightweight, therefore, weights were designed which are added on top of each entire plate during vacuum to help create a good seal.

PROFILOMETRY AND FILM DRYING OPTIMIZATION

The electrode contact area is one key parameter that cannot be directly measured with our system. One must use the geometric area of the electrodes (0.50 cm^2). To ensure an accurate measurement of ionic conductivity, we aspire to have the contact area between the top electrode and the polymer be the same as the nominal geometric area. We also optimized the accuracy of the contact area through three main methods, first pressure is applied to the electrodes during measurement to compress the electrode onto the film, second the ionic conductivity measurements are performed from high temperature to low which softens the electrolyte first allowing for better contact, and finally measures were taken to optimize the formation of films with relatively uniform thickness across the measurement area. We knew that the edges of the mold would likely always cause issues, so the top electrodes are significantly smaller than the bottom electrodes. Therefore, we must optimize our films to be uniform across the center of the sample. Non-contact profilometry was used to map the thickness profile of the films across their area. Profilometry is an excellent tool for film optimization and one of the unique features available on our system. The output files are 2D heat maps of the film thickness across its entire area. We used a set of known-thickness polymer films to verify that the system produces accurate results. An example of the profilometer 2D heatmap and X-cross section of a 65 µm thick polyimide film are shown in Figure 4-4A). Here we can see the bare metal having close to zero measured thickness showing that the system can accurately find the base plane, and the film in green has an average measured thickness of about 62 µm, very close to the nominally defined thickness.

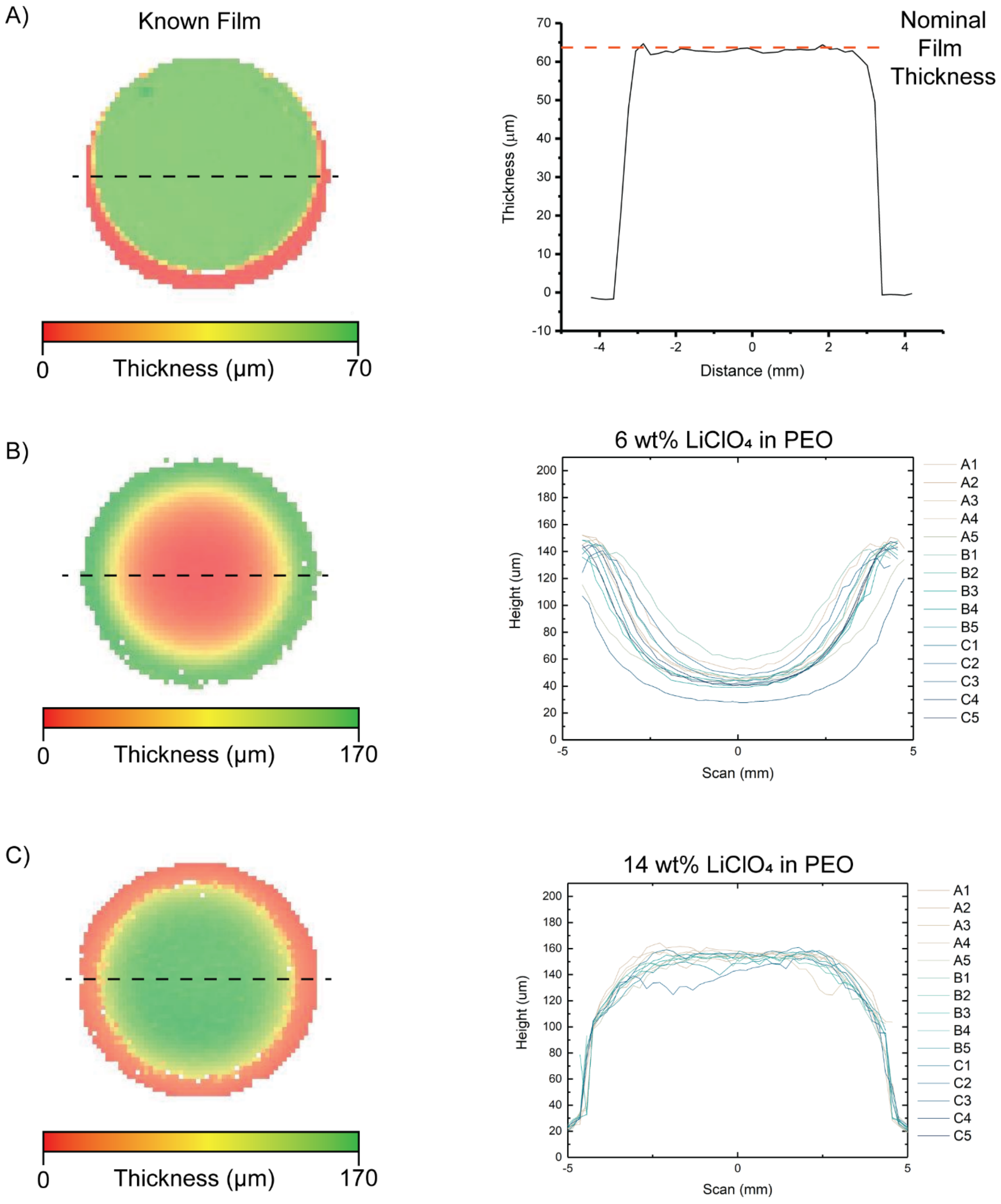

Figure 4-4 Profilometer data and X-cross sections of A) a known thickness poly-imide film B) 6 weight % $LiClO_4$ in PEO films cast from 50 mg/mL solutions in ACN. C) 14 weight % $LiClO_4$ in PEO films cast from 70 mg/mL solutions in ACN.

Initial films often showed a high degree of “cupping,” in which the edges of the films were far thicker than the center. Figure 4-4B) shows the cross sections of 15 PEO-$LiClO_4$ films cast from a precursor solution with a polymer in solvent (acetonitrile) concentration of 50 mg/mL. This cupping is likely due to a combination of the formulation crawling up the walls of the well due to capillary action, as well as the well-known “coffee-ring effect,” in which solvent evaporates faster from the edges of a droplet, causing the liquid to flow from the center towards the edges, and bringing solid particles along with.[126] Although many knobs were found to alter the film flatness (including deposition temperature, drying temperature, use of purge or vacuum, etc.), one of the most important found in this work was the polymer loading in solution. Increasing the polymer concentration increased the flatness of the resulting films. Figure 4-4C) shows PEO-$LiClO_4$ films cast from 70 mg/mL solutions. The films are much flatter, having only about ±10 µm across the center of the film. Interestingly, films formed in these conditions seem to pull away from the walls of the sample holder. Perhaps the increased polymer in solution wets the PEEK sample well less, resulting in this pull away. Once appropriate film forming conditions were found for the polymer system, they were followed for all samples in the set.

TWISTLOCKS AND IN-SITU THICKNESS MEASUREMENTS

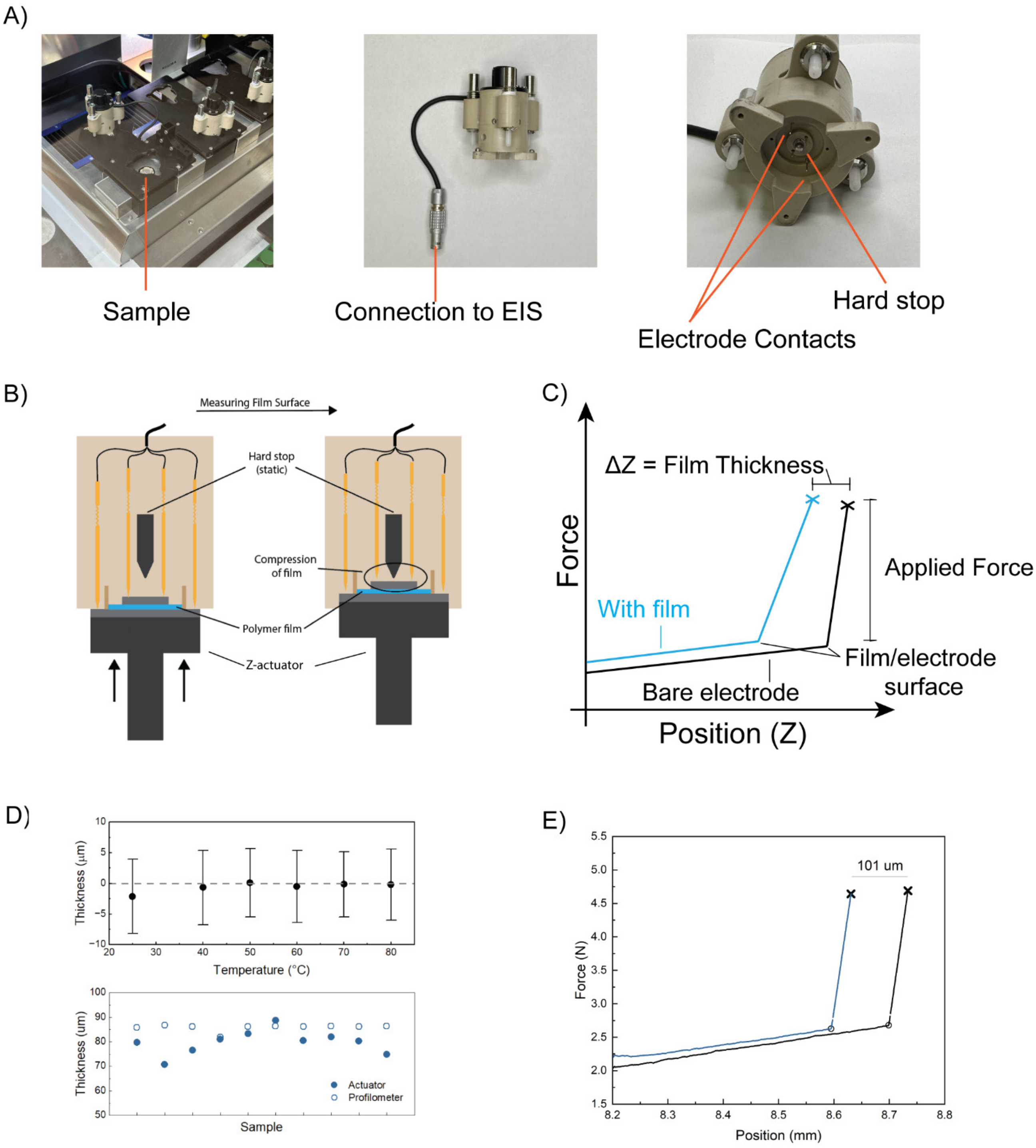

Figure 4-5 Twistlock assemblies and in situ thickness measurements. A) Photos of twistlock assemblies both in place on the robot and removed. B) Diagram depicting the thickness measurement process using the z-actuators. C) Illustration showing how the thickness measurement occurs. D) Averaged thickness measurements showing the spread on empty cells as a function of temperature (top) and on a standard 86 µm polyester film across multiple samples (bottom). E) Force versus position data collected by the instrument on a PEO-LiClO$_4$ film.

The twistlock assemblies combined with z-actuators handle all setup and measurements required to measure the prepared films' ionic conductivity. They are responsible for making electrical contacts to the external potentiostat, in-situ thickness measurements, and heating samples for variable-temperature EIS. Four twistlock assemblies on our tool allow the simultaneous characterization of four samples. Figure 4-5A) shows images of the twistlocks both in position on the tool and disconnected to highlight the internal features. In the underside of each twistlock are four electrical contacts, two connecting to the sample top electrode and two to the bottom electrode. In addition to the electrical contacts, the underside of each twistlock contains the “hard-stop” used for the thickness measurement procedure, as will be explained shortly. In the first photo, the nearest twistlock is in the disassembled state, revealing the sample sitting on top of the z-actuator below. Integrated into the top of the z-actuator (upon which the sample sits) is a resistive heating element and temperature probe, which allows for variable temperature EIS. Additionally, passive cooling is provided via an external chilling unit that blows cooled argon (the glovebox atmosphere) across all of the actuator bodies. The chiller accelerates the cooling time considerably and lowers the time delay between measurements.

Figure 4-5B & C) illustrates how the in-situ thickness measurement is performed. The samples sit on top of a linear actuator (z-actuator) which has micron level precision in movement, and also measures the force required to make each movement. During the thickness measurement procedure, the actuator raises and records the force. When the sample top-electrode begins to interact with the hard-stop positioned directly above the sample, the force required to move the actuator will rise dramatically as the actuator has to press against the entire assembly. At this position (labeled “film/electrode surface”), a very sudden slope change to the force vs. position graph is observed (Figure 4-5C). To apply pressure to the film, the system moves a specefied distance past this detected point. The movement is executed in either “force mode,” where the system moves until the desired force is applied, or “distance mode,” in which the system moves until the desired distance past this point regardless of the force required. We have found that for stiff films, “force mode” gives the most reproducible results, whereas distance mode excels for soft films to prevent the system from pushing the top electrode through the material. To account for variability in electrode materials each sample must be loaded as an empty cell to have an “uncoated” measurement, which measures the position the actuator must reach with just the top and bottom electrode loaded. This information is stored for every cell individually. During EIS measurement, each film thickness is measured by taking the difference between the new and uncoated positions, yielding just the thickness of the film.

It was found that the thickness measurement was insufficient to accurately measure the cells' thickness at elevated temperatures. When empty cells were loaded onto the actuators and their thicknesses were measured as a function of temperature, it was found that there was an over 60 µm increase in the thickness measured at 80 °C than at R.T. (See Figure 9-1). Considering the target film thicknesses for the polymers were ~ 100 µm, this large deviation was a very significant consideration. We concluded it was due to the thermal expansion of the entire assembly. To correct for it a “zero point” measurement could be made and stored for every temperature for which EIS was to be conducted. With this protocol in place, we could accurately account for the thermal expansion. Figure 4-5D) (top) shows the average and spread of the thickness of empty cells measured as a function of temperature. The values are close to zero thickness at every temperature (which is correct for empty cells) and have about 6 µm of spread, an acceptable degree of accuracy. We then applied known thickness (86 µm) polyester films to cells and measured how well the system performed. The thickness measured by the optical profilometer is nearly spot on to the known thickness. Across 10 samples the actuators gave a thickness measurement of 78.9 ±4.75 µm. This measurement slightly underestimates the thickness of the film, likely due to the compression. The measurement also has a similar spread to the empty cell measurements. With these methods established, we felt it was an appropriate way to handle in-situ thickness measurements. An example of the force vs. position curves on a polymer sample is shown in Figure 4-5E.

EIS MEASUREMENTS AND BENCHMARKING FORMULATIONS TO REFERENCE DATA

To measure ionic conductivity, electrochemical impedance spectroscopy (EIS) is used. EIS allows for the measurement of different electrochemical processes on a wide range of time-scales, as well as the association of those to equivalent circuit elements, which provide insight into the material's bulk properties.[127] EIS is performed by applying a small-amplitude stimulus (either current or voltage can be used) and measuring the response of the system as the frequency of the stimulus is varied.[127] It is found that different electrochemical processes occur on separate time scales, and are decoupled through the use of this frequency sweep. The high throughput tool typically operates in a four-point methodology, with one power and one sensing contact per electrode. Compared to the standard two-point EIS, four-point EIS provides more accurate measurement of the true polymer film resistance by eliminating ohmic drops associated with the resistance of the cables.[128] The system can operate in a two- or three-point method if desired.

EIS data is typically plotted in two ways: the Nyquist plot and the Bode Plot. In a Nyquist plot, the x-axis is typically the real portion of the impedance (Z’) and the y-axis is the negative of the complex portion of the impedance (Z’’). An example Nyquist plot is shown in Figure 4-6B). In the Bode plot the magnitude of the impedance (|Z|) is plotted versus the measurement frequency. Here we will only use Nyquist plots. One of EIS's main advantages is fitting the data to an equivalent circuit model representing different processes or elements. Importantly, any number of constitutive models can be fit to EIS data (especially one with many features), so it is essential to inform your model by the relevant physical processes.[127]

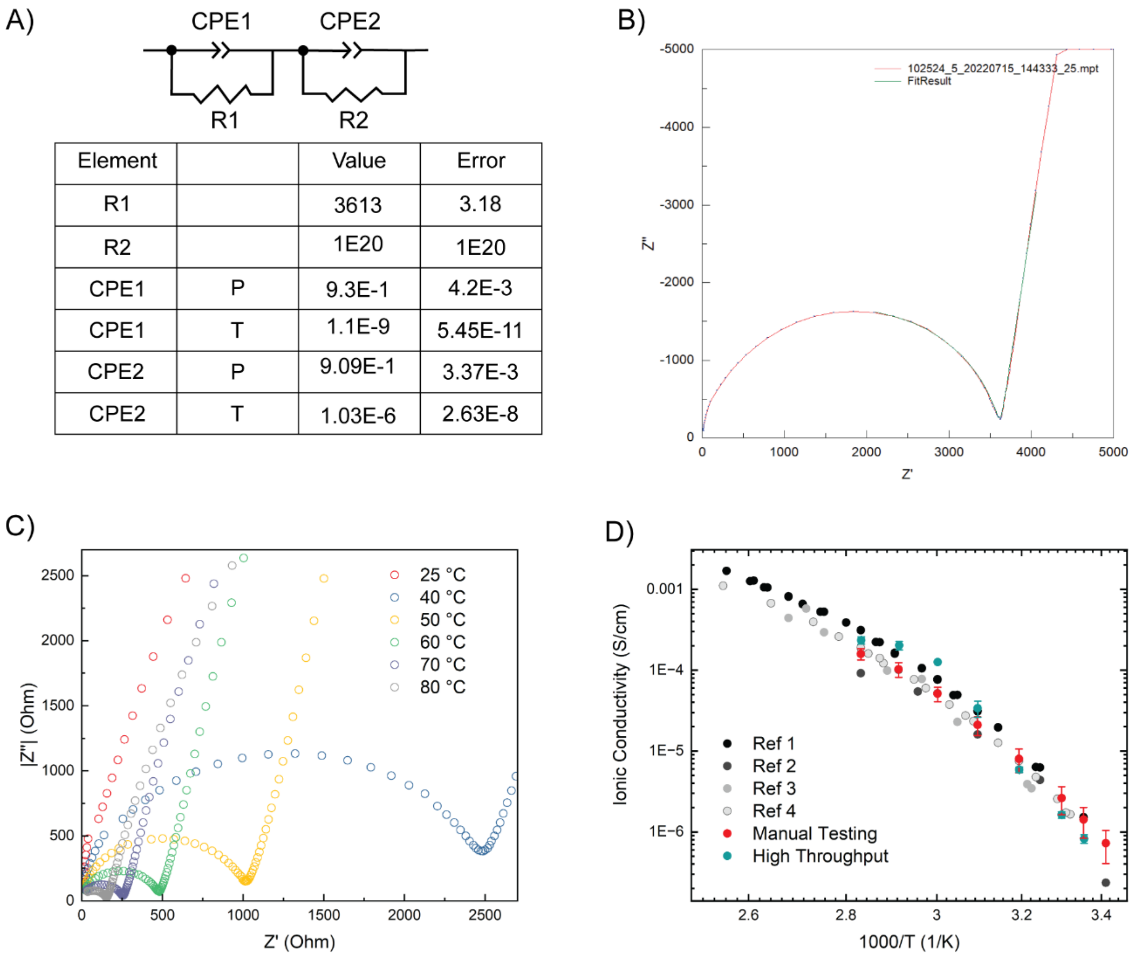

Element		Value	Error
R1		3613	3.18
R2		1E20	1E20
CPE1	P	9.3E-1	4.2E-3
CPE1	T	1.1E-9	5.45E-11
CPE2	P	9.09E-1	3.37E-3
CPE2	T	1.03E-6	2.63E-8

Figure 4-6 EIS spectroscopy A) equivalent circuit model used for modeling our polymer electrolytes along with the fitted parameters for the data shown in B). B) Nyquist plot of a PEO-NaFSI electrolyte film measured at 25 °C showing the portion of data that is fit to the model in green. C) Nyquist plots of PEO-$LiClO_4$ films measured at various temperatures showing the increase in the size of the semicircle. D) Comparison of measured ionic conductivity data performed on our system, by hand in our labs (through a "low throughput" method) and references from literature. Reference 1: [129] Reference 2: [130] Reference 3: [131] Reference 4: [132].

Figure 4-6A) shows the equivalent circuit model our high throughput tool uses for all the data in subsequent chapters. This model consists of resistors and constant phase elements (CPE). An example of a fitted Nyquist plot is shown in Figure 4-6B). The first set of elements consisting of R1 and CPE1 in parallel are responsible for the semi-circular form of the Nyquist plot and are attributed to the ionic conductivity of the bulk electrolyte. The second set of elements R2 and CPE2 would normally also make a semicircular shape, however, for ion conduction, a nearly vertical tail is observed due to the very high resistance encountered at the stainless-steel blocking electrodes in use. Thus, our fits typically result in R2 being extremely high (i.e., 1E20 Ω), giving the tail portion. The ionic conductivity of the sample is determined from the value of R1 in Equation 4-1. Our system uses an iterative algorithm to automatically identify and fit the "cusp" region of the Nyquist plot, which is most responsible for the value of R1. Figure 4-6C) shows example Nyquist plots as a function of temperature for a PEO-$LiClO_4$ sample. To benchmark our system, we compared our measured ionic conductivity data to multiple literature references of high quality. Figure 4-6D) shows the ionic conductivity as a function of temperature for a 23 wt% $LiClO_4$ in PEO samples compared to four literature references. The data produced by the high throughput tool falls well within the spread of data points of the literature references showing good agreement. Additionally, we made samples of the same electrolyte formulation from the high throughput tool to verify that our EIS and thickness measurement methods were accurate compared to the traditional manual methods. We also see good agreement between these data, the high throughput tool, and the literature references. Additional benchmark formulations compared to literature references are shown in Figure 9-2.

CHAPTER 5 APPLICATION OF HIGH THROUGHPUT WORKFLOW TO POLYMER ELECTROLYTE UNDERSTANDING AND DISCOVERY

Considering recently increased interest in sodium-ion batteries, we sought to leverage our high throughput tool to rapidly add to the knowledge base of sodium-ion conducting polymer electrolytes. While lithium-based electrolytes have been studied extensively, considerably less work has been done on sodium-ion conductors. The difference in the size and polarizability of the two cations is slight, however, it has been shown to result in differences in ion coordination. For example, crown ether coordination to cations is size dependent and 12-crown-4 more selectively binds lithium cations, while the larger 15-crown-5 prefers to bind sodium cations.[52] The difference in crown ether binding affinity suggests that changing cation may affect polymeric electrolytes, especially poly(ethylene oxide). Additionally, the data collected here robustly characterize the ionic conductivity landscape for both lithium and sodium salts in PEO, providing a useful foundation for future study of sodium ion polymer electrolytes.

METHODS

We chose to use four of the most commonly used anions in the polymer electrolyte community: perchlorate (ClO_4^-), hexafluorophosphate (PF_6^-), bis(trifluoromethane)sulfonimide ($TFSI^-$), and bis(fluorosulfonyl)imide (FSI^-). Lithium and sodium variants of each salt were dried at 80 °C under an active vacuum for >18 hours before use. Poly(ethylene oxide) with a molecular weight of ~600,000 g/mol was dried at 45 °C under an active vacuum for > 48 hours before use. Karl Fischer titration measured the water content of all materials, and they were found to have 70 ppm at a maximum, with most being around 20 ppm (Figure 9-3). All manipulations and measurements were carried out on the high throughput platform. Electrolyte formulations were prepared by dispensing the appropriate weight of salt and polymer powders before dissolving in anhydrous acetonitrile to achieve a solution with the appropriate viscosity for drop casting. Formulations were made at the following salt concentrations: 0.2, .75, 1.5, 2.25, 3.0, 3.75, 4.75, 5.75, and 7.0 molal (mol salt/kg polymer). As an aside, we find that molality is the most universal unit as it is independent of salt choice (i.e., a 1 molal solution will have the same moles of cation regardless of anion choice), as well as can be transferred between polymer backbones (i.e. a 1 molal solution created in poly(ethylene oxide) and poly(caprolactone) are still comparable) and strongly encourage the adoption of these units within the polymer electrolyte community. For reference, equivalent concentrations in the ratio of ethylene oxide repeat units to salt and weight % of salt in the total dried film are given in Table 9-1 for LiTFSI.

The majority of the solvent is removed by heating the substrates to 80 °C for > 8 hours in the glovebox atmosphere. To ensure the samples were fully dry, they were further heated to 100 °C with active vacuum for > 4 hours.). Three to five samples of each formulation were prepared, and all viable samples of the same formulation were averaged. EIS measurements were performed for each formulation going from high to low temperature at 80, 70, 60, 50, 40, and 25 °C with an applied pressure of 40 kPa and with an equilibration time of 5 minutes at each temperature step. Separately, a small portions of the same precursor formulations were dispensed into pans to perform DSC to measure the samples' glass transition temperature, melting point, and percent crystallinity.

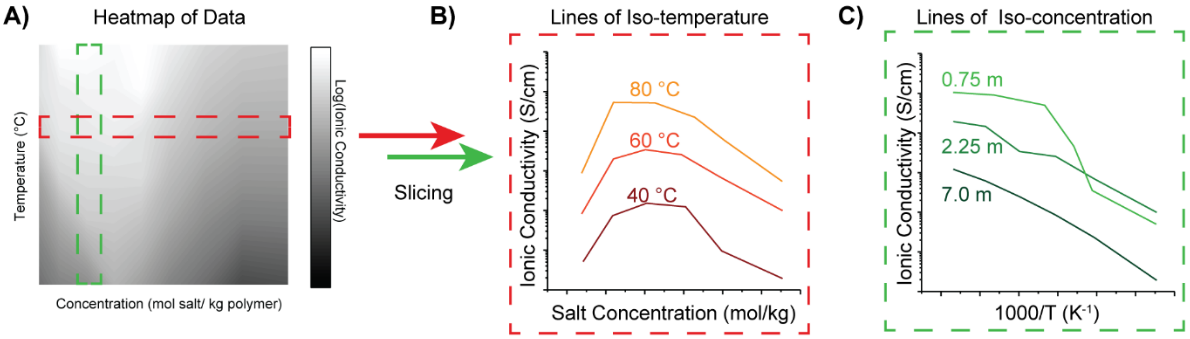

Figure 5-1 Diagram depicting decomposition of ionic conductivity heatmap. A) Heatmap of ionic conductivity of a given electrolyte system. B) Taking horizontal slices results in lines of iso-temperature plotted as a function of salt concentration. C) Taking vertical slices results in lines of iso-concentration plotted versus inverse temperature (an Arrhenius plot).

RESULTS

The primary output data of our high throughput workflow is the ionic conductivity of the electrolyte film, as a function of both temperature and concentration. Plotting all the data for a certain polymer-salt system allows the creation of a heatmap of ionic conductivity (shown here in grayscale) (Figure 5-1A). The 2D parameter space can be decomposed in orthogonal directions to produce the conventional views of ionic conductivity versus concentration (Figure 5-1B) and ionic conductivity versus temperature (plotted as the reduced temperature, 1000/T, Figure 5-1C).

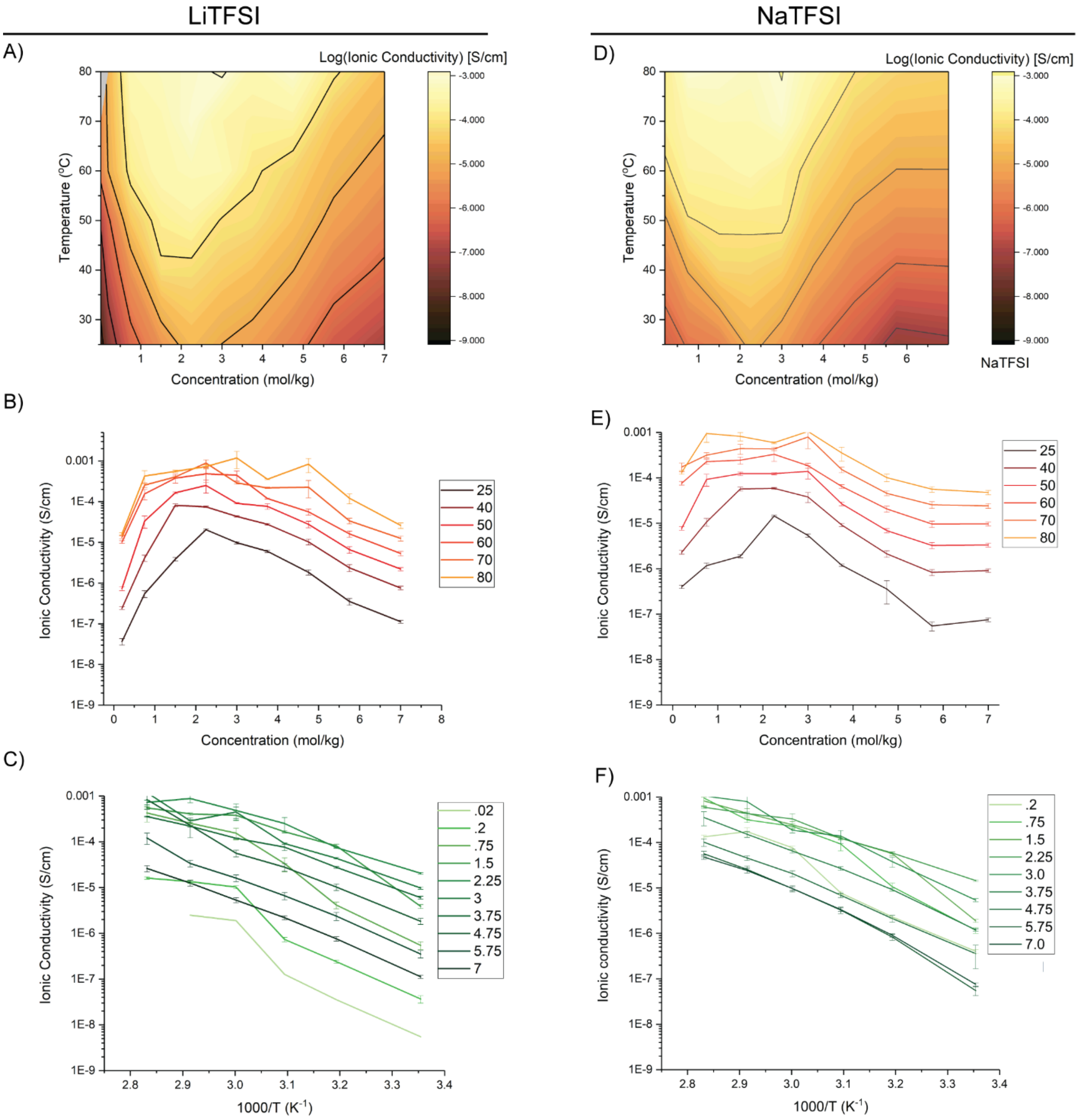

Figure 5-2 Ionic Conductivity of LiTFSI and NaTFSI in PEO. A) Heatmap of ionic conductivity for LiTFSI in PEO as a function of both temperature and concentration. B) Ionic conductivity of LiTFSI at lines of iso-temperature as a function of salt concentration. C) Ionic conductivity of LiTFSI at lines of iso-concentration as a function of inverse temperature, an Arrhenius-style plot. D-F) the same plots for NaTFSI. Plotted values are the average of all replications. Error bars are shown as the standard error of the replications.

Figure 5-2 A & B) show the ionic conductivity landscapes of LiTFSI and NaTFSI in PEO. From the general trend of these maps, there is similarity between the performance of these formulations.

Consistent with the trends established by the field, we observe the ionic conductivity of the samples rise as the salt concentration is increased and then begin to fall again at all temperatures (Figure 5-2 E & F). Note that for LiTFSI an additional concentration of 0.02 m was collected which shows that the ionic conductivity decreases precipitously when there are insufficient charge carriers in the sample. The peak ionic conductivity occurs at a salt concentration of 2.25 mol/kg (39.4 mass % or 10:1 mol EO: mol Li^+) for both lithium and sodium TFSI. The maxima occur due to competing interactions of increasing the active charge carrier concentration and decreasing the polymer mobility, indicated by an increase in the glass transition temperature (T_g) as explained in Chapter 2. The maxima also appear to become broader as the temperature increases (i.e., a wider range of concentrations have high ionic conductivity).

We also observe that the ionic conductivity increases with temperature (Figure 5-2 F & I). At low salt concentrations, it is observed that the ionic conductivity profile follows an Arrhenius relationship (Equation 2-5. $\sigma \propto \exp\left(\frac{E_a}{RT}\right)$) with a step change occurring around 60°C (1000/T ≈ 3.00 K^{-1}). This corresponds to the melting temperature of PEO, which has a semi-crystalline nature at low salt concentrations. As the polymer crystallites melt, there is a significant increase in ionic conductivity due to the presence of a much higher fraction of amorphous material. Consistent with the presence of the step change in ionic conductivity, we observe the melting of crystalline PEO in these same concentrations via DSC (Figure 9-4). As the salt concentration is increased, the PEO crystallization is suppressed. The resulting ionic conductivity curve for high salt concentration is more appropriately fit by the Vogell-Fulcher-Tammann (VTF) equation of the form: (Equation 2-11) $\sigma \propto \exp\left(\frac{A}{R(T-T_0)}\right)$ where T_0 is termed the "critical temperature" of the polymer system and is empirically found to be $T_0 \approx T_g$-50 (K).[133] Such a profile appears curved on the Arrhenius plot compared to the linear Arrhenius relationship. VTF-type profiles are observed for both Li and Na TFSI systems at concentrations > 1.5 mol salt/kg. Consistent with these data, the disappearance of the PEO melting peak in DSC was observed, along with the appearance of a much stronger glass transition temperature. Deeper discussion of this ion conduction mechanism is provided in Chapter 2.

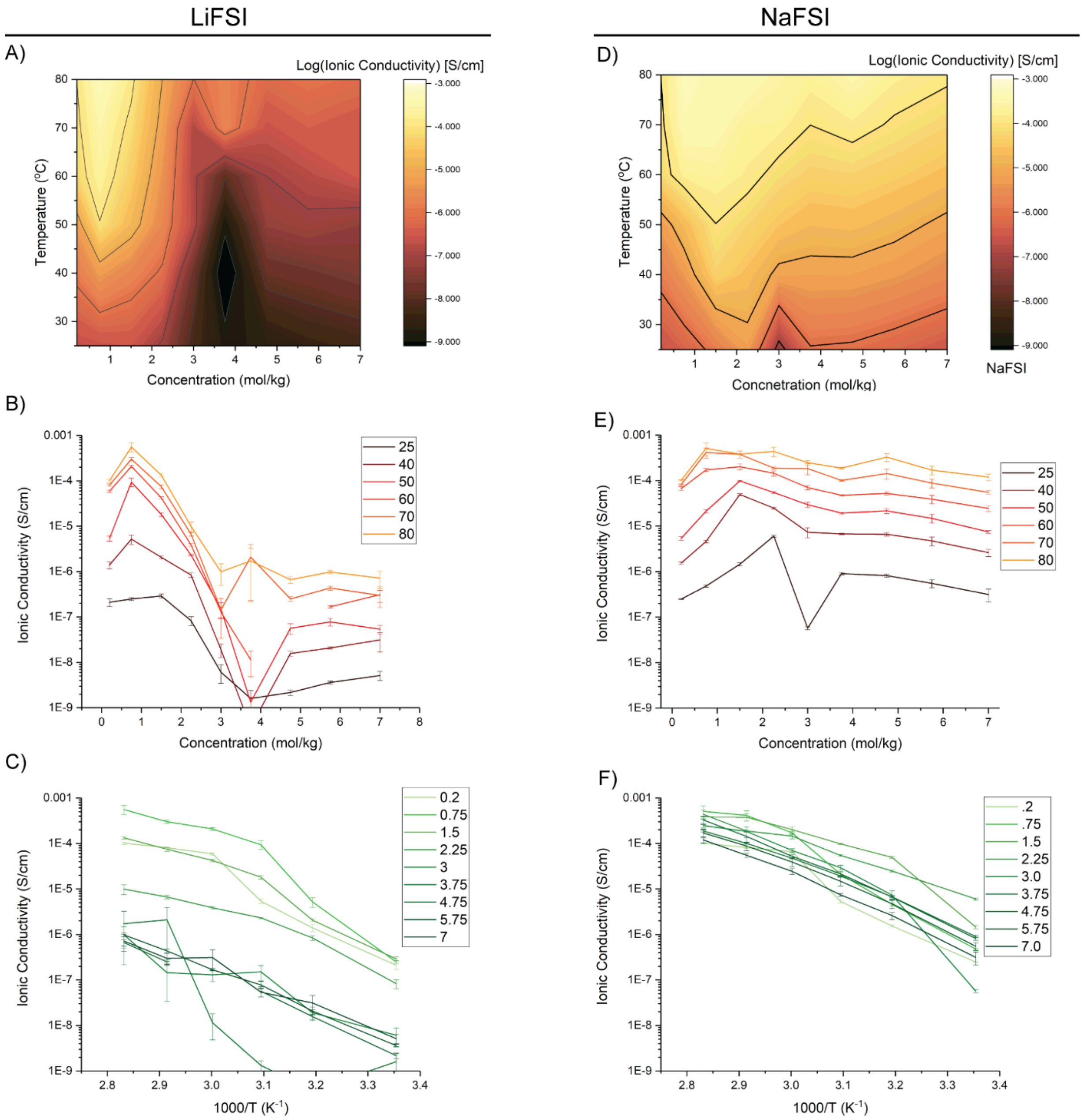

Figure 5-3 Ionic conductivity of LiFSI and NaFSI in PEO A) Heatmap of ionic conductivity for LiFSI in PEO as a function of both temperature and concentration. B) Ionic conductivity of LiFSI at lines of iso-temperature as function of salt concentration. C) Ionic conductivity of LiFSI at lines of iso-concentration as a function of inverse temperature, an

Arrhenius style plot. D-F) the same plots for NaFSI. Plotted values are the average of all replications. Error bars are shown as the standard error of the replications.

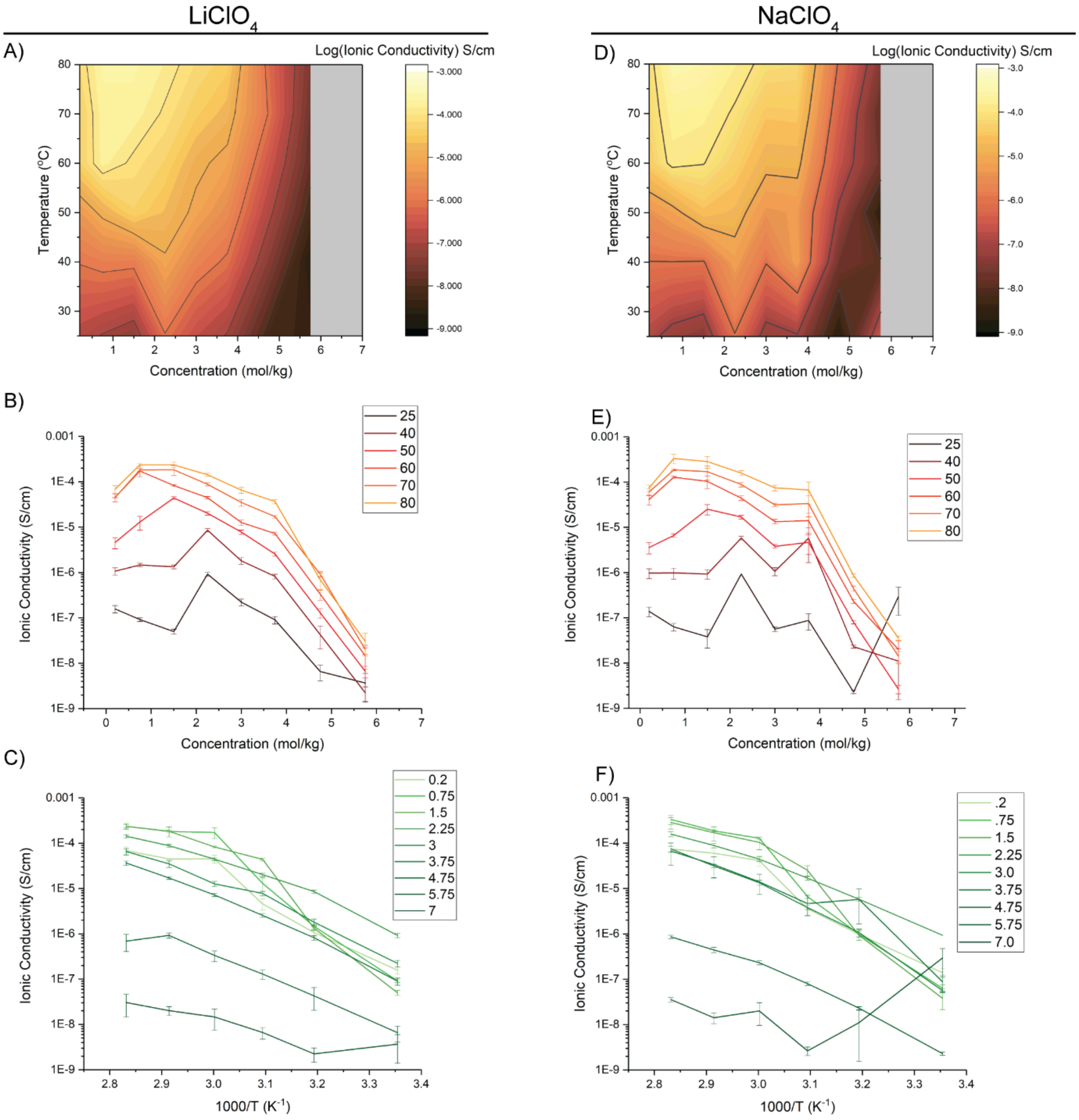

Figure 5-4 Ionic Conductivity of LiClO$_4$ and NaClO$_4$ in PEO. A) Heatmap of ionic conductivity for LiClO$_4$ in PEO as a function of both temperature and concentration. B) Ionic conductivity of LiClO$_4$ at lines of iso-temperature as a function of salt concentration. C) Ionic conductivity of LiClO$_4$ at lines of iso-concentration as a function of inverse temperature, an Arrhenius-style plot. D-F) the same plots for NaClO$_4$. Note that regions marked in grey did not have appreciable ionic conductivity and a reliable measurement could not be made likely due to the insolubility of the salt at this concentration. Plotted values are the average of all replications. Error bars are shown as the standard error of the replications.

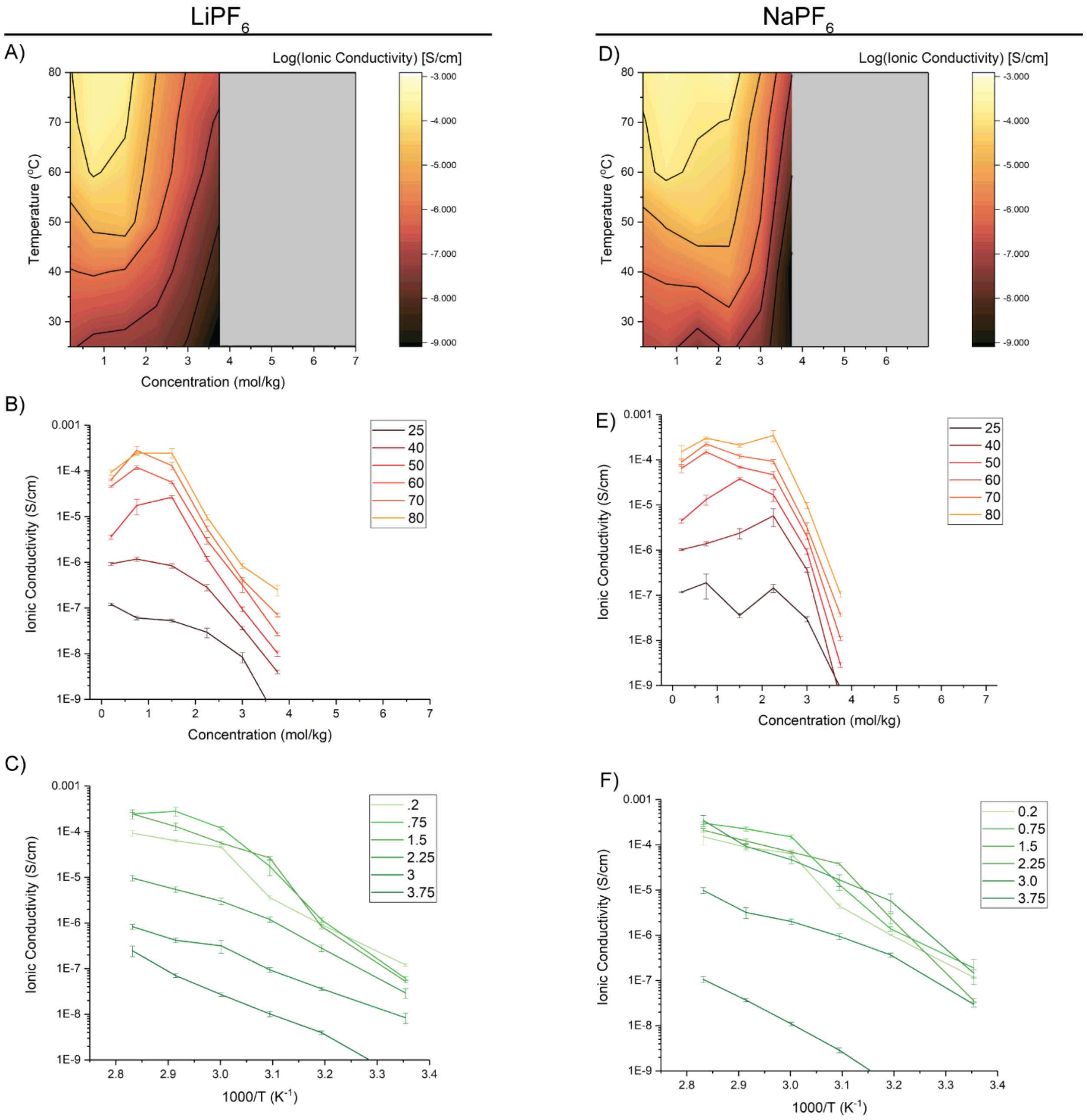

Figure 5-5 Ionic Conductivity of $LiPF_6$ and $NaPF_6$ in PEO. A) Heatmap of ionic conductivity for $LiPF_6$ in PEO as a function of both temperature and concentration. B) Ionic conductivity of $LiPF_6$ at lines of iso-temperature as function of salt concentration. C) Ionic conductivity of $LiPF_6$ at lines of iso-concentration as a function of inverse temperature, an Arrhenius style plot. D-F) the corresponding plots for $NaPF_6$. Note that regions marked in grey did not have appreciable ionic conductivity, and a reliable measurement could not be made, likely due to the insolubility of the salt at this concentration. Plotted values are the average of all replications. Error bars are shown as the standard error of the replications.

We then expanded the anions studied to include ClO_4^- , PF_6^-, and FSI^-. The equivalent graphs for each salt system can be found in (Figure 5-3 - Figure 5-5). Figure 9-4 shows the DSC data for each material system. *The total number of samples represented here is 330 individual electrolyte films at 70 unique formulations, nearly 2000 ionic conductivity measurements, and 70 DSC samples*. To aid in making meaningful comparisons across this vast body of data, we have condensed the performance of each system into a manageable number of descriptors plotted in Figure 5-6.

Our high throughput system was able to process 90 samples from raw starting materials to fully characterized electrolyte films in just under five days, which also includes 24 hours total of downtime due to the drying of the electrolyte films. This is an equivalent throughput of 18 samples per day (drying time include). With further optimization, for example via minimizing stirring and drying times, may allow for even higher throughput. Additionally, the workflow used here affords five repeats per polymer formulation. However, it was found that three samples were able to provide an accurate measurement due to the high degree of sample-to-sample repeatability. We estimate that this is up to 100 fold faster sample throughput as compared to a single researcher (assuming a majority of their time is being devoted to this). Furthermore, the operation of the tool requires significantly less researcher time, setup of each run only requires 1-2 hours of experimenter time, after which the system can run fully autonomously, barring no errors. While some errors are still in the system, most only require a brief human input to remedy and allow the run to continue.

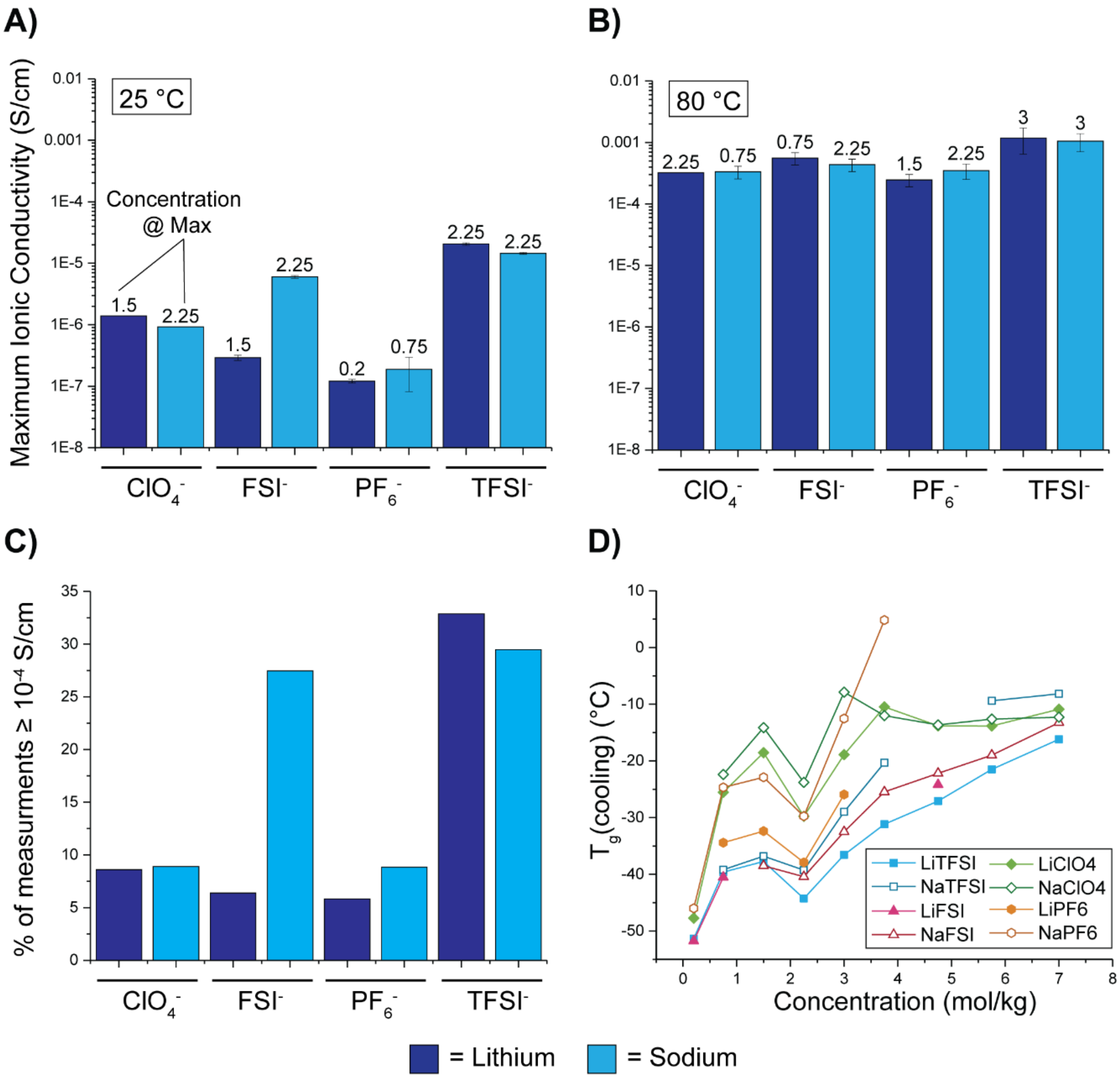

Figure 5-6 Direct comparisons of Lithium and Sodium conduction in PEO. A) Maximum ionic conductivity value measured for all salt concentrations at 25 °C for both lithium (dark blue) and sodium (light blue) salts in PEO. The value above each bar indicates the salt concentration at which the maxima occurs in mol/kg. Error bars are the standard error of n=3-5 samples. B) Maximum ionic conductivity value measured for all salts at 80 °C. C) Percent of the studied parameter space for which the ionic conductivity is ≥ 10^{-4} S/cm (linearly interpolated). D) Observed glass transition temperatures (T_g) of all salts plotted as a function of the formulation. Solid symbols are lithium salts, whereas hollow symbols are sodium.

Figure 5-6A) shows the maximum measured ionic conductivity for each anion with both lithium and sodium cations at 25 °C. At this temperature, the ionic conductivity ranges from ~10^{-7} – 10^{-5} S/cm depending on the anion chosen. The concentration at which maximum ionic conductivity was measured is labeled just above each bar. The PF_6 anion results in the lowest ionic conductivity attributed to high aggregation of PF_6 salts in PEO. Consistent with this, the maximum ionic conductivity for the PF_6 formulations was measured at 0.2 and 0.75 m for Li^+ and Na^+ salts respectively. In contrast, the highest-performing formulations were found to be the TFSI anion for Li^+ and Na^+. W attribute this to the high solubility of TFSI (due to the highly dissociative nature of the anion). Unlike PF_6, the maximum ionic conductivity for the TFSI-based system is found to occur at much higher concentrations, 2.25 m. There are significantly more charge carriers in the TFSI based system than the PF_6 likely causing the over 2 order of magnitude difference.

At 80 °C we observe that the choice of anion is far less important (Figure 5-6B). All systems prepared in this work, had measured ionic conductivities between ~ 10^{-4} to 10^{-3} S/cm, a much tighter range than at 25 °C. Additionally, we find that the maximum ionic conductivities generally occur in a higher concentration range, indicating the overall higher solubility of salts at elevated temperatures. At these temperatures, the PEO no longer has crystalline regions for any of the formulations (T_m of PEO is ~ 50-60 °C). Ions are likely more uniformly distributed among the amorphous polymer making the impact of anions less prevalent. Additionally, the increased temperature also decreases the presence of ion aggregation, making the distinction between more and less dissociative anions less severe.[15]

We sought to quantify the "breadth" of the formulation parameter space for which high ionic conductivity was measured for each system. To do this, we calculated the area of each heatmap with interpolated ionic conductivity ≥ 10^{-4} S/cm normalized to the total parameter space studied here (25- 80 °C and 0.2-7 m) (Figure 5-6C). In general, we find that the sodium variant of each salt has a slightly greater area of "high ionic conductivity" than the lithium variant, with LiTFSI being the exception. TFSI salts also perform much better than the other anions used here, having significantly broader areas of "high ionic conductivity." Interestingly, NaFSI has a much greater area (27%) of high ionic conductivity than LiFSI (7%). One initial thought was that perhaps the sodium salt was not as dry as the lithium salt, as trace water is known to cause significant increases in ionic conductivity artificially.[51] However, Karl-Fischer titration experiments to quantify the water content in all starting materials showed that they had similar levels (Figure 9-3). The presence of crystalline species observed at multiple concentrations in LiFSI not observed in NaFSI (Figure 9-6) may account for this discrepancy but requires further investigation. This may also be indicative of degradation.

The glass transition temperature is considered a descriptor of ionic conductivity. We have plotted the measured T_g as a function of salt concentration for each system in Figure 5-6D). It is generally found that the glass transition temperature increases as a function of salt concentration.[48] This effect is attributed to the ions acting as inter-chain crosslinks, which lower mobility and subsequently raise the T_g.[48] We observe that for many of the formulations produced the sodium version of the salt has a slightly higher T_g than the lithium version (by as much as 15 °C in some cases). Across many formulations, we observe that there appears to be a small "dip" (~ 5 °C) in the measured T_g at a concentration of 2.25 molal before a significant increase for all formulations measured in this work. It is also observed that most of the formulations measured in this dataset transition from a semi-crystalline to a fully amorphous material around the same concentration range in which the dip is observed (Figure 9-5). It is intriguing that the "dip" seems quite pervasive in all the salts tested here, and elucidating such trends is intractable without the large cross-comparable data set we have put together here.

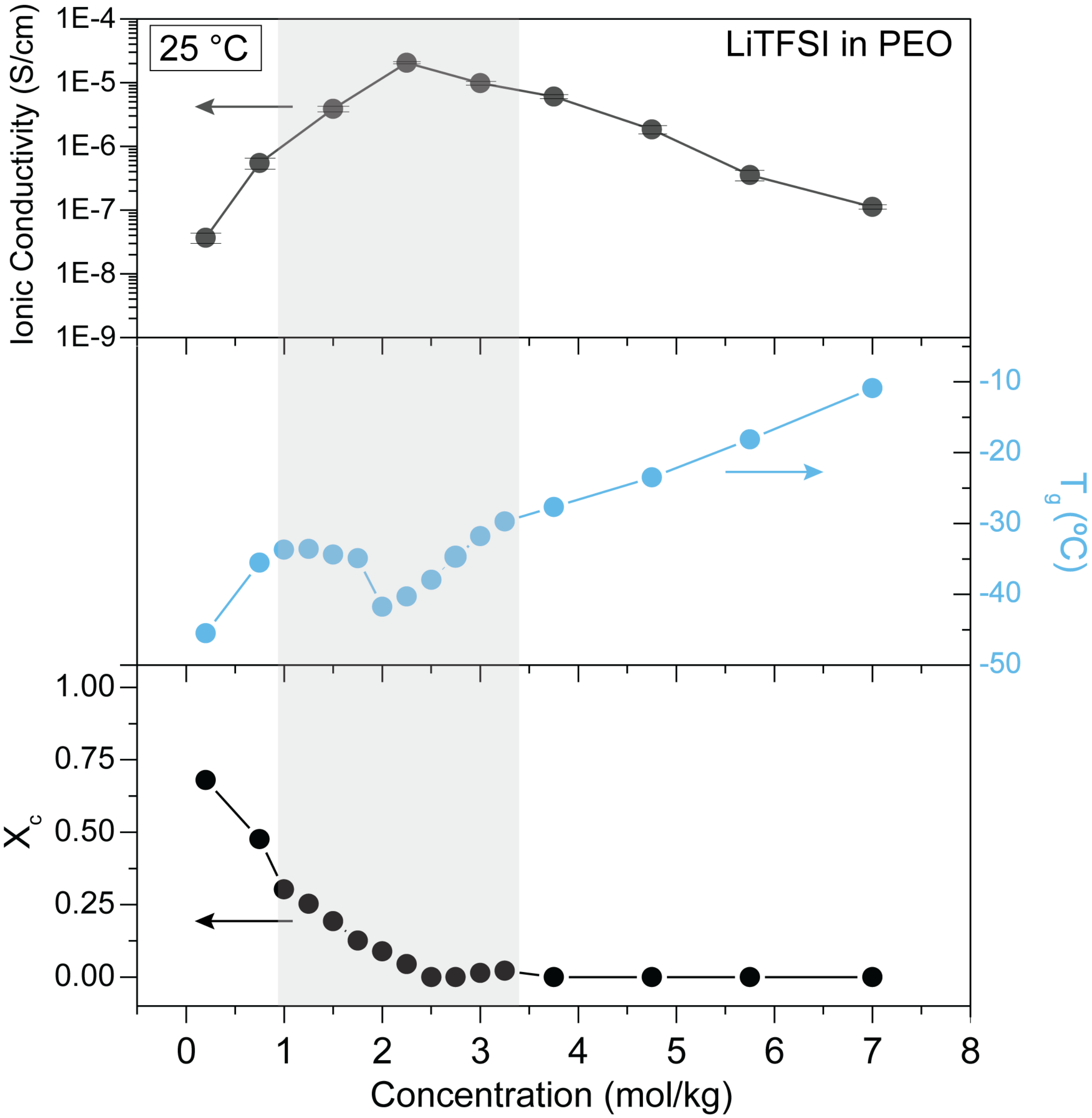

Figure 5-7 Stacked plot showing the Ionic Conductivity at 25 °C, Glass transition temperature (T_g), and fractional crystallinity (X_c) of LiTFSI in PEO electrolytes.

To our knowledge, the observation of this dip in glass transition temperature has not been previously reported. To investigate this deeper, we synthesized LiTFSI in PEO formulations at 0.25 m increments from 1.0 to 3.25. Differential scanning calorimetry was used to measure the glass transition temperature and percent crystallinity (X_c), which can be calculated as below:

Equation 5-1

$$X_C = \frac{\Delta H_m}{\Delta H_0}$$

Where ΔH_m is the enthalpy of the PEO melting transition, typically observed in the range 30-65 °C, and ΔH_0 is the melting enthalpy of a 100% crystalline PEO sample. This value has been measured to be 196 J/g.[134,135] Plotting these factors on a common X-scale as shown in Figure 5-7 we can see that there is a "goldilocks" zone around the maximum of ionic conductivity (observed at 2.25 m for LiTFSI at 25 °C). The minimum in glass transition occurs at 2 m (and only rises 2 °C at 2.25 m), and meanwhile the percent crystallinity reaches zero (by our DSC detection limit) at 2.5 m. At concentrations greater than this the T_g rises quickly, so the ionic conductivity decreases due to decreased chain mobility.[49] At concentrations less than this value the ionic conductivity must decrease due to a combination of factors: 1) the T_g rises slightly but then subsequently decreases at very low concentrations, 2) the X_c rises rapidly, 3) the total charge carrier concentration is lower. Overall, the discovery of this "dip" and subsequent goldilocks zone of ionic conductivity was only possible through the high degree of formulations our high throughput tool is able to screen, with high fidelity and cross-comparability.

The presences of it between 4 separate anions and 2 cations says it is somewhat fundamental to PEO-salt blends. Additionally its occurrence at the same concentration across 8 different salts suggests it may be a colligative property, i.e. one that depends only on the number of solutes and not their identity.[136] Furthermore, we suspect that the apparent rise in T_g when decreasing in concentration from the dip is linked to the rise in crystallinity. Our current top hypothesis is that the presence of crystallites act as rigid barriers to adjacent polymers in the amorphous domains. It has been shown that mobility of polymer chains grafted to surfaces have lower mobility and subsequently higher glass transition temperatures than those in the bulk.[137] Furthermore, it has been shown in semi-crystalline poly(l-lactic acid) that the presence of crystalline domains broadens and raises the T_g of the inter-crystal chains.[138] Some possible experiments we could use to probe this effect deeper would be measuring the size of the crystallites present in the PEO as a function of composition and examining the cation coordination environments (likely with FT-IR or Raman) in this goldilocks region.

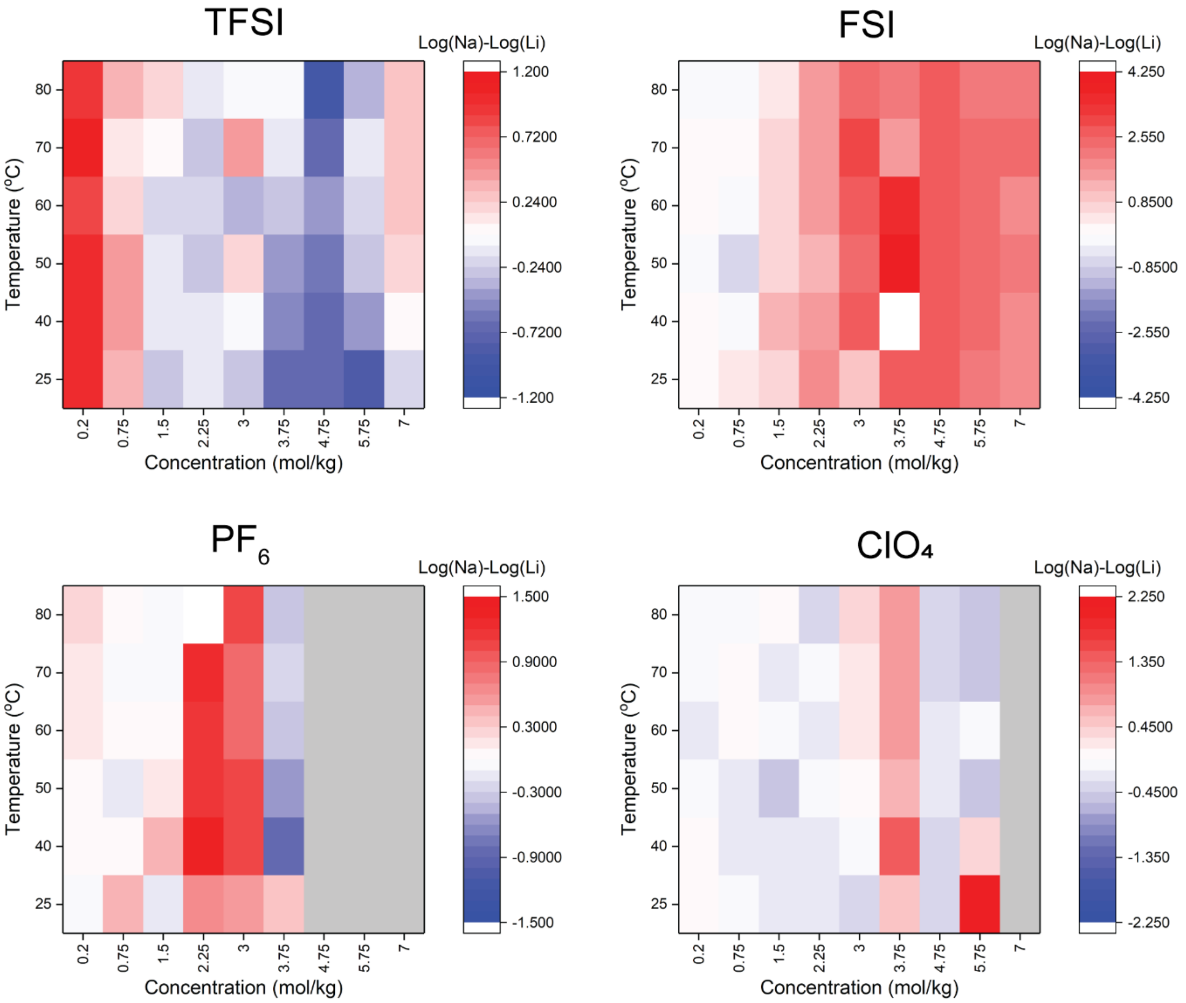

Figure 5-8 Direct comparisons of lithium and sodium ionic conductivity as color maps. Here the "value" of each cell is colored by the difference between the logarithm of sodium and lithium ionic conductivity. Higher (red) values indicate that the sodium ionic conductivity is great than the lithium, and vice versa for the blue cells. White cells have equivalent ionic conductivity. Grey regions indicated ionic conductivity was not measured.

Finally, to better visualize the differences between sodium and lithium ion conduction at every point, we created Figure 5-8. In these maps, we have plotted the value of $Log(\sigma_{Na}) - Log(\sigma_{Li})$ at every formulation and temperature. The color scale is such that red points indicate sodium ionic conductivity is higher than that of lithium, and vice versa for the blue points. Non-colored points do not have a significant difference. Note that each plot is on its own scale to emphasize the differences. Equivalent plots but all graphed on the same scale, are shown in Figure 9-7. The graphs show that overall there is no discernable trend as to whether sodium or lithium ionic conductivity will be higher. It appears sodium is favored for the FSI and PF6 salts, while for TFSI and $ClO_{4,}$ lithium is favored. From Figure 9-7when plotted on a relative scale, FSI shows by far the most dramatic difference between the two cations, which can also be easily seen in Figure 5-2, and was previously discussed. These data suggest that more nuanced experiments should be performed to understand the origin of the ionic conductivity difference. Raman spectroscopy may provide insight into the degree of salt dissociation in the solutions. Measurement of the transference number could determine if the changes in ionic conductivity are more due to the cation or anion motion.

CONCLUSIONS AND OUTLOOK

This chapter details our work utilizing the high throughput platform to rapidly and systematically characterize lithium and sodium ion conduction in PEO with 4 of the most commonly used battery anions, TFSI, FSI, PF_6 and ClO_4. The results contain 330 individual electrolyte films at 70 unique formulations, nearly 2000 ionic conductivity measurements, and 70 DSC samples. The sodium-based systems generally had similar or higher ionic conductivity than the lithium counterparts. As interest in sodium-based batteries grows, these results are invaluable for deciding which salt systems should be used. In addition, our results are broadly consistent with the previous body of literature and established principles of lithium-based ion conduction, which were discussed in Chapter 2. Furthermore, due to the scale of this experiment and the many concentrations studied, we were able to uncover a previously unknown trend which is the appearance of a dip in glass transition temperature at 2.25 m, which is coincident with the disappearance of crystallinity, and the also the peak of ionic conductivity for a majority of salts studied here. The data acquired here acts as a great demonstration of the utility and reliability of our high throughput system, and is also a vast body of data for training machine learning models towards active learning of new electrolytes, which will be discussed in the next chapter.

CHAPTER 6 ACTIVE LEARNING FOR POLYMER ELECTROLYTE DISCOVERY

The space of possible materials to synthesize is far vaster than would ever be possible to approach with traditional methods.[139] While the development of high throughput tools, such as the one described in the previous chapters, increases the scale of experiments, it is still dwarfed by the possible combinatorial spaces one could devise with only a few components. Therefore, new methods are needed to efficiently explore large parameter spaces, find optimal formulations, and learn heuristics.[140] Active learning (or "self-driving labs") can be a vital tool. Among the most popular methods to employ active learning is Bayesian optimization (BO) in which the parameter space is iteratively explored and optimized guided by the expected improvement and confidence bound of a predictive model.[141] Upon completion of each batch of experiments, the predictive model is retrained to include the new information and is subsequently used to suggest the next batch of experiments. It has been found that ML models work exceedingly well as the predictive models in BO schemes.[142] Such BO-ML paired workflows have been executed for reaction condition optimization,[141] and thin film optoelectronics synthesis, among many other examples.[122]

In this section, we sought to establish a BO-based active learning loop for the optimization of the ionic conductivity of new polymer electrolyte systems leveraging the high throughput instrument described in Chapter 5. To do so there are three main components: 1) a predictive model for the ionic conductivity of a polymer electrolyte, 2) a desired chemical space and BO-based sampling scheme, and 3) execution of the experiments on the HT system. This chapter has been the culmination of many years of research by multiple parties working on different aspects. In particular, the ML predictive model, which will be briefly described in the next section, was developed by Gabriel Bradford with help from Jeffrey Lopez and the author and is cited in reference[117]. Jurgis Ruza and the author primarily developed the BO-based sampling scheme, and the experiments were executed mainly by the author with assistance from Sawyer Cawthern. While the scope of the material used here is somewhat limited, this study demonstrates the utility of high throughput active learning and opens up wide potential for future work on the HT system.

A PREDICTIVE ML MODEL FOR IONIC CONDUCTIVITY OF POLYMER ELECTROLYTES

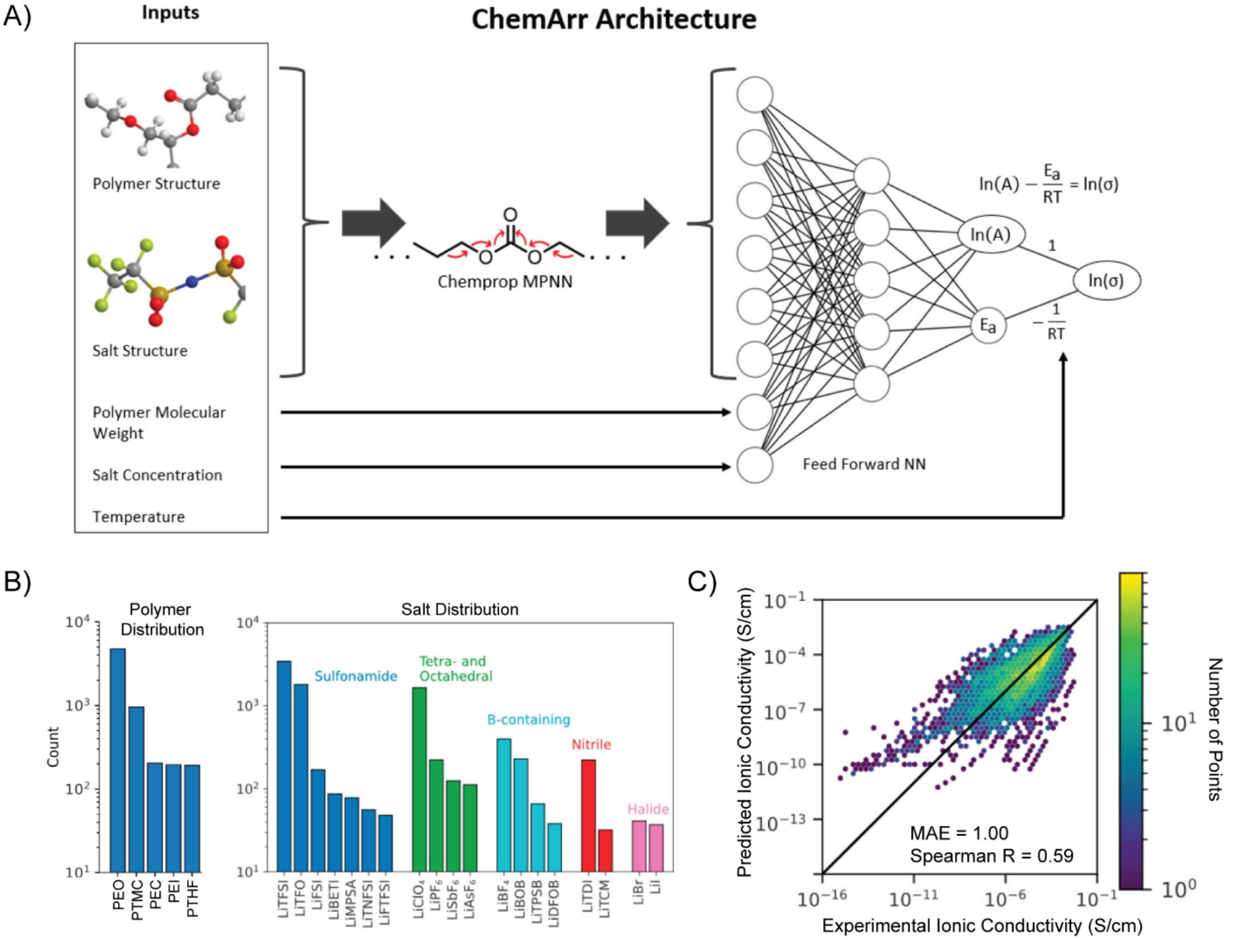

Figure 6-1 Predictive Machine Learning Model for Ionic Conductivity A) Depiction of the model input parameters, chemical fingerprinting, and feed-forward neural network to predict the Arrhenius parameters for ionic conductivity of a solid polymer electrolyte. B) Makeup of the literature data training set showing the top 5 polymers and the majority of anions represented. C) Parity plot showing the good agreement between the experimentally measured ionic conductivity and the model-predicted ionic conductivity after training was completed. The trained model can

predict accurately within one order of magnitude given by the MAE =1.00 log(S/cm). Figures adapted from reference[117]

The first element of the proposed active learning loop is a surrogate model which can predict the desired property based on some input variables. Namely, for this work, we required a model that can predict the ionic conductivity of a polymer electrolyte formulation based on the chemical composition (i.e. which polymer, salt, concentration etc.). Figure 6-1A shows the overall structure of the ML model (called ChemArr). The input parameters of ChemArr are 1) the polymer repeat unit as a molecular graph, 2) the salt chemical structure as a molecular graph, 3) the logarithm of the polymer molecular weight, 4) the salt concentration, and 5) the temperature. From these input parameters, ChemArr then utilizes ChemProp, a message passing network that generates a numeric feature vector based on the input polymer and salt structure (inputs 1 and 2).[143] Such learned representations of molecules have been shown to outperform many other molecular fingerprinting techniques.[143] The learned representation of the polymer and salt is then concatenated with inputs 3-5 to yield the input string for the feed-forward neural network. The penultimate network layer outputs the natural logarithm of the pre-factor, ln(A), and activation energy, E_a, of the Arrhenius equation for ionic conductivity (Equation 2-5). ChemArr assumes an Arrhenius dependence for the ionic conductivity variation with temperature. As detailed in Chapter 2, the ionic conductivity of most polymer electrolytes does not follow an Arrhenius dependence, often either exhibiting a two-slope behavior due to the semicrystalline nature of the polymer, or following a VFT dependence. However, in this work it was found that machine learning models failed to capture the nuance of either of these dependencies. Therefore, Arrhenius dependence was used as a simpler model which ML was able to learn with accuracy.

To train the ChemArr model, a vast literature data set had to be collected. To do so, manual extraction from 135 publications of existing polymer electrolyte literature yielded 7,133 individual ionic conductivity data points. This dataset was then combined with two previously published data sets,[144,145] yielding another 6,250 data points. All data points were screened for indicators of good experimental practice, such as ample drying of starting materials and handling in a dry environment to eliminate water. The final experimental data set is the largest known to date, containing over 12,000 ionic conductivity data points from 247 unique polymers, and 81 unique salts. Figure 6-1B) shows the composition of this data set into the most represented polymers and salts. One key issue with the polymer electrolyte community as a whole is a heavy skew towards just a few materials. PEO alone makes up over 1/3 of the total data points in our training set. Similarly, for salts, LiTFSI, Lithium trifluoro-methanesulfonate (LiTFO), and $LiClO_4$ combined makeup about 1/3 of the data. While generally found that these materials are top performers, it also makes predictions for other materials less accurate due to the heavy influence on the ML model by just a few species. This distinct lack of data coverage for other materials has been one key driving force for the creation of the high throughput tool covered in this thesis, as well as the necessity for accelerated materials design towards alternate materials.

The objective function of training the ML model was minimizing the difference between the predicted and experimentally measured ionic conductivity. Training was done in 10-fold cross validation, where in each fold 70% of the data was allocated for training, 20% for validation and 10% for testing. The data splits were chosen such that polymer structures in the testing and validation sets were not in the training set to establish how the model handles unseen structures. Figure 6-1C) shows the predictions of the trained model. Here data points that lie close to the diagonal have good agreement between the model prediction and the measured value. It was found that the trained models had a mean absolute error (MAE) of 1.00. Since the model predicts in logarithmic value, it can predict ionic conductivity to within one or of magnitude on average. Given that the experimental error in ionic conductivity measurements can be around half an order of magnitude in some cases, this is an acceptable error level. The trained model can now be used to predict the performance of new polymer electrolytes. Overall, this work provides a much-needed first attempt at predicting polymer electrolyte ionic conductivity purely from the chemical structures and formulations and also provides a framework for further optimization as more data is acquired. The following sections will detail how this trained ML model was further used in an active learning loop. For more details on the work, please refer to reference [117]

BATCH-BASED BAYESIAN OPTIMIZATION SAMPLING

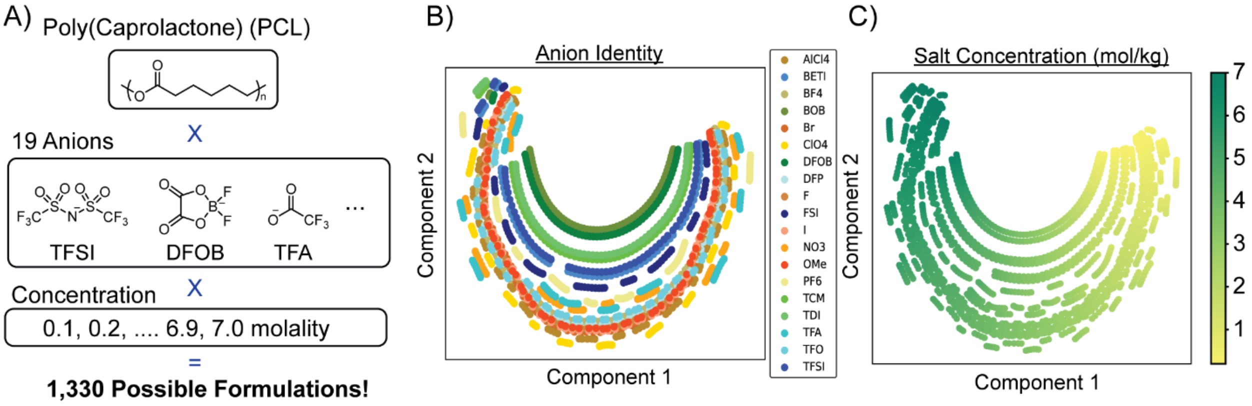

Figure 6-2 Overview of chemical space for Bayesian Optimization study A) Combinatorial space composed of a single polymer host PCL, 19 lithium salts, and 70 possible concentrations resulting in over 1300 possible unique formulations. B) Dimensionally reduced embedding showing a 2D depiction of the entire chemical space plotted by composite parameters component 1 and component 2. Here the anion is highlighted in different colors showing different salts coalesce into "bands". C) The same embedding space now labeled with concentration showing how it increases from right to left across the bands.

The chemical design space was composed of the single polymer host material (PCL), 19 lithium salts, and any salt concentration between 0.2 and 7 m taken at 0.1 intervals, resulting in over 1,300 possible formulations to be explored (Figure 6-2A). All anions included in the study are shown in Figure 9-8. Poly(ε-caprolactone) (PCL) was chosen as the electrolyte host material as it is a promising alternative to PEO but has been studied significantly less. PCL is widely commercially available, has a low T_g of ~ -60 °C,[146] and has been shown to dissolve lithium sal, suppressing its crystallinity similar to PEO.[147] PCL as an electrolyte material has been shown to have ionic conductivity similar to that of PEO—a 40 weight % LiTFSI produced by Eriksson and coworkers was recently measured to have ionic conductivity of 5 $*10^{-4}$ S/cm and 1 *10^{-5} S/cm at 90 and 30 °C respectively.[148] Additionally, PCL is biodegradable via hydrolysis and can be broken down by many bacteria, making it a potentially more sustainable material than PEO.[146,147] Compared to PEO, PCL has been dramatically less well studied as an electrolyte material, with only a handful of papers, and only being studied with TFSI, FSI, SCN, and ClO_4 anions.[147–150] This existing data allows for the machine learning model to have some training on previous results as a starting point but also leaves the parameter space wide open for the exploration of novel materials. The above qualities made the optimization of PCL-based electrolytes an attractive first test of the active learning platform.

To make the chemical space interpretable by the ML surrogate model, the composition of each electrolyte is embedded into a high dimensional (~800 length) vector which encodes the chemical structure of the polymer, salt, concentration, and temperature as described in the above section. This vector can then be dimensionally reduced to obtain a more interpretable representation of the chemical space in 2 or 3 dimensions. Figure 6-2B) shows this dimensionally reduced space for all 1330 unique formulations labeled by the anion. The embedding preserves some chemical information with each anion forming a unique "band". Additionally, chemically similar anions tend to appear together, such as FSI and TFSI, which are both fluorinated sulfonimides, appear adjacent on the plot. Figure 6-2C shows the dimensionally reduced space colored via salt concentration, we observe the concentration increases from right to left continuously. Additionally, each point in this space has an associated ML-based ionic conductivity prediction and uncertainty as predicted by ChemArr. It is from this dimensionally reduced embedding space that the BO optimization sampling is made.

BO optimization seeks a tradeoff between exploring the parameter space and exploiting the high objective. While traditionally, BO optimization is updated at every sequential point (i.e. feedback after every test point), due to the necessity for long drying times for polymer films we chose to operate in batches of 9 unique formulations with 5 replications per formulation. While batch-based methods have been successful, it remains an open question what is the optimal strategy to obtain each batch. To obtain a chemically diverse batch we employted the following rules: 1) Suggestions were sequentially sampled from the embedding space reduced to 3 dimensions (shown here in 2 for visualization); 2) After sampling, a volume around that point was excluded from the following suggestions in the same batch which prevents the BO algorithm from exclusively sampling the same area; 3) No more than 2 suggestions with the same salt were taken per batch. These rules were enforced to sample the chemical space and ensure exploration. Figure 6-3 shows an example of this sampling scheme in practice is shown in.

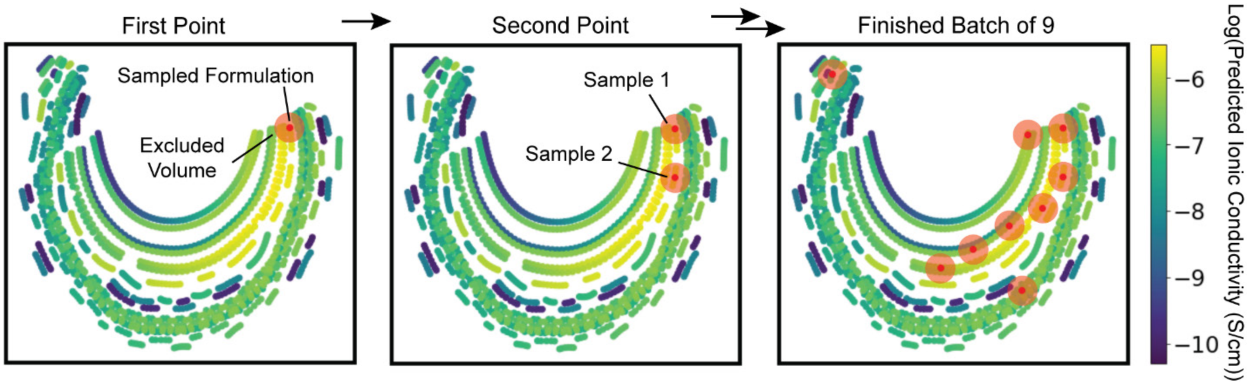

Figure 6-3 Iterative batch sampling strategy to ensure a balance of expected ionic conductivity improvement and exploration of high uncertainty across the chemical space

HIGH THROUGHPUT EXPERIMENTATION AND RESULTS

With the required computational pieces in place, the final aspect was optimization of the HT workflow to provide the best results. Preliminary experiments with PCL 80,000 g/mol showed that flat films could be obtained if high viscosity solutions were used. 150 mg polymer per mL of solvent (acetonitrile) afforded a viscous polymer solution with good solubility when heated at 50 °C. Interestingly, it was found that after a long time at room temperature, this solution froze or crystallized to a waxy solid but would melt upon heating. The polymer solution showed good solubility of lithium salts, and subsequently yielded smooth polymer films when dried of solvent. Preliminary films composed of PCL with dissolved LiTFSI showed adequate ionic conductivity for measurements in good agreement with previous literature studies on these formulations.[148] A drying program of 8 hours at 60 °C followed by 4 hours at 80 °C under dynamic vacuum was used for all samples. Variable temperature EIS was conducted for all samples with an applied force of 1.5 N at 30, 50, 70, and 90 °C. It was found that many formulations had relatively low ionic conductivity, which made measurements difficult as they were at the resistance limit of our instrumentation. This was especially apparent for very high salt concentrations past the solubility limit of the salt in the polymer. It was found that this effect could be reduced by lowering the quantity of formulation dispensed, resulting in a thinner film and, subsequently, lower resistance. Starting in the second batch, all formulations were deposited such that the resultant salt + polymer mass after drying of solvent would be between 40 and 60 mg, which was found to yield films around 80-120 µm thick. These optimizations resulted in more successful measurements per formulation and generally lower experimental error. Five active learning batches were produced for a total of 45 unique formulations, 225 individual samples, and 900 ionic conductivity measurements (including V.T). All data and predictions in the subsequent figures are shown for 30 °C, which was the optimization goal.

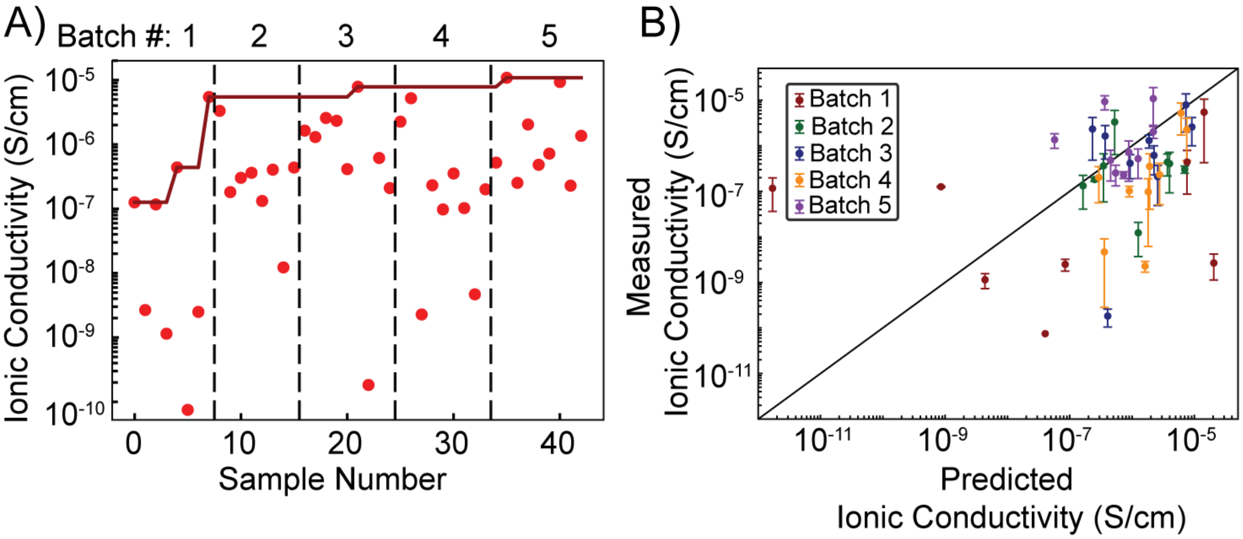

Figure 6-4 Active learning optimization of PCL-based electrolytes. A) Plot showing the ionic conductivity of all measured formulations as a function of sample number. The dark line tracks the overall top-performing formulation. B) Parity plot showing the agreement of the pre-measurment predicted ionic conductivity and the actual value as measured in the experiment. Error bars shown are the standard deviation of all replications with successful measurements. Both data sets are for measurements at 30 °C.

Figure 6-4A) shows how the experimentally measured ionic conductivity as a function of sample number (as suggested by the BO algorithm). Interestingly, a formulation with quite high ionic conductivity was suggested within this first batch. This results suggests that the initial training (as described in the previous sections) for the ML model was able to find formulations of high ionic conductivity in PCL, even though there were only about 100 data points (including V. T.) for PCL in that training set, suggesting a high degree of similarity between PCL ion conduction behavior and the other polymers in the training set (a majority of which is PEO). The maximum ionic conductivity rose another half an order of magnitude throughout the rest of the experiment, with the final top performing formulation being LiFSI (1 molal) with an ionic conductivity of $1.09\times10^{-5} \pm 2\times10^{-6}$ S/cm at 30 °C which is on par with the best previously reported formulations.[151,152] PEO with 1 m LiFSI would have an ionic conductivity of ~ 5×10^{-7} based upon our measurements in the previous chapter (Figure 5-3), significantly less than PCL. Indeed the top-performing PEO formulation (LiTFSI 2.25 m) at 30 °C would likely be only slightly higher than our PCL formulation at ~ 4×10^{-5} (S/cm) (Figure 5-2). The parity plot also shows the same data, which compares the predicted ionic conductivity to the experimentally measured ionic conductivity (Figure 6-4B). This parity plot qualitatively shows the model becoming more accurate through the course of the study. Batch 1 had a very high spread, with points very far from the parity line, while Batch 5 is much more tightly grouped near the parity line. All experimentally measured data and predicted ionic conductivity values for this study are tabulated in Table 9-2 – 9-5.

The top 10 measured formulations are given in Table 6-1. We find that the highly dissociative sulfonimides (FSI, TFSI, and BETI) make up 8 out of these top 10, with the other two top formulations being boron-centered anions (BF_4 and DFOB). We also find that there is generally an even split between formulations for which the model overpredicts the ionic conductivity (a negative percent difference) and those where it underpredicts (a positive percent difference). Given the high spread in percent differences, the model still has a way to go if prediction accuracy is the only concern. Given that our increase in ionic conductivity plateaued quite fast, it perhaps suggests that any further gains in ionic conductivity with just a PCL system would be marginal.

Table 6-1 Top 10 performing formulations found by BO optimization of lithium salts in PCL

Sample #	Anion	Concentration (mol/kg)	Batch #	Measured σ (S/cm)	Measured SD (S/cm)	Predicted σ (S/cm)	Percent Difference (%)
35	FSI	1	5	1.09E-05	2.81E-06	2.19E-06	79.85
40	BF4	2.4	5	9.33E-06	1.25E-05	3.64E-07	96.09
21	TFSI	1.2	3	7.88E-06	1.99E-06	7.33E-06	7.00
7	TFSI	1.4	1	5.46E-06	4.24E-07	1.43E-05	-162.37
26	BETI	1.2	4	5.21E-06	1.72E-06	6.10E-06	-17.07
8	DFOB	2.2	2	3.32E-06	6.37E-07	5.27E-07	84.15
18	TFSI	2	3	2.58E-06	9.96E-07	9.12E-06	-253.65
19	FSI	3.7	3	2.33E-06	4.82E-07	2.32E-07	90.05
25	TFSI	2.2	4	2.26E-06	4.75E-07	7.54E-06	-234.36
37	BETI	1.5	5	2.04E-06	1.46E-06	2.20E-06	-7.79

MODEL EVOLUTION AND LEARNING

One key objective of this study was to observe how the machine learning model changed and evolved as new experimental data was added. One issue, since the training set had so little PCL-based training data, is that the model generally predicts based on inferences made on PEO-based materials. We sought to understand how quickly the model can adapt and learn in mostly “unknown” materials space and perhaps also see how transferable its previous training is to this new chemical space.

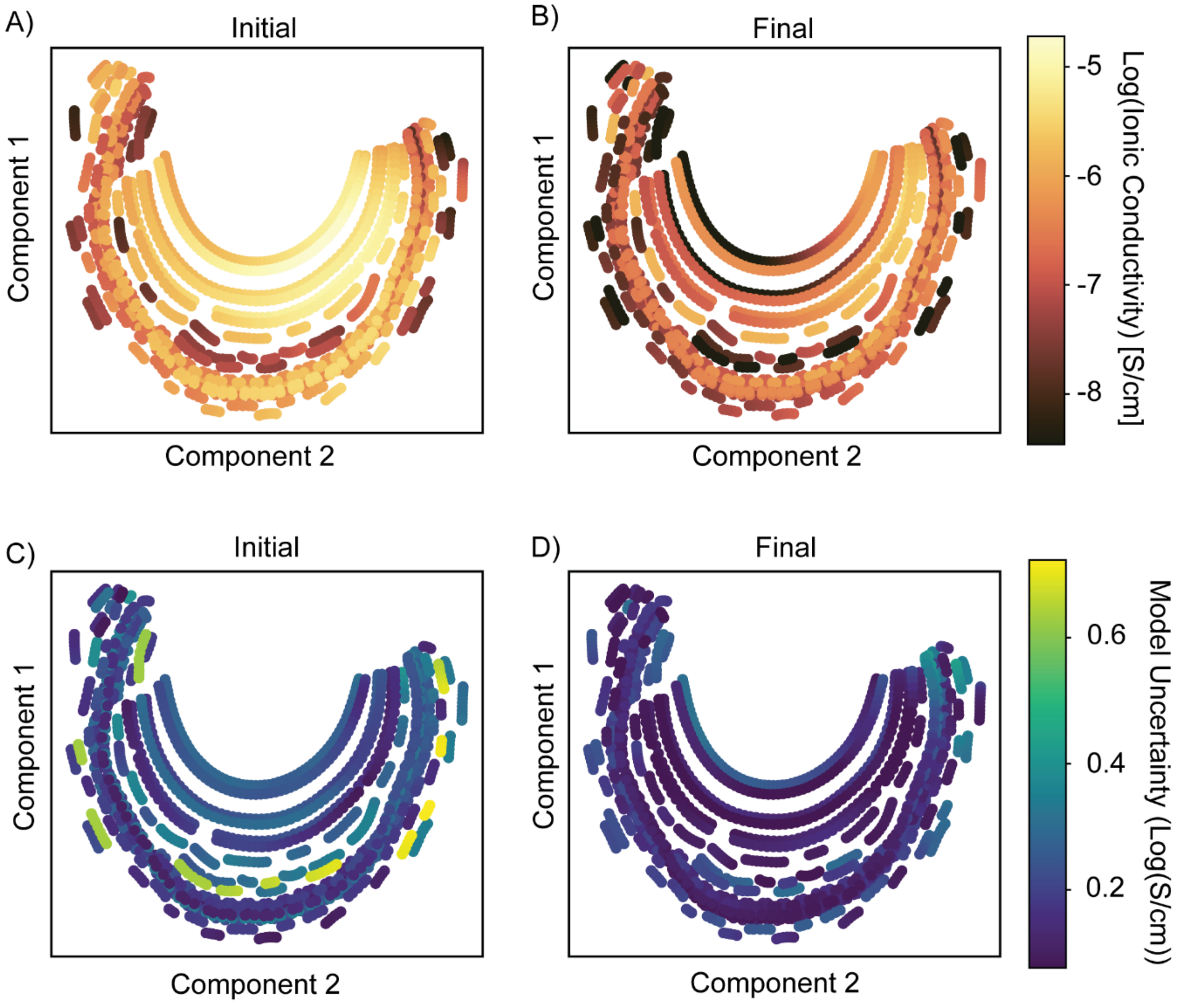

Figure 6-5 Evolution of ML model shown in ionic conductivity (A & B) and model uncertainty (C & D). Initial plots were made before any experimental PCL data was added to the training set. Final plots are after batch 5 data was incorporated and the model was re-trained one final time.

Figure 6-5 shows the evolution of the ML model predictions for the entire chemical space in the study from before any data was collected and after the final retraining was performed. From plots A) and B) we can see that the predictions of ionic conductivity change dramatically across the entire chemical space. Overall, there is a shift towards lower ionic conductivity across the space (getting darker). While this may be disappointing in terms of performance, it reflects reality more correctly. In general, the model tended to "overpredict" ionic conductivity for many formulations, seen in Figure 6-4B) by the abundance of points below the parity line. Observation of this trend in the final model training is unsurprising. We speculate this may be due to a variety of factors. As stated previously much of the model is trained upon PEO, which in general has slightly higher ionic conductivity than PCL-based electrolytes skewing the predictions. Additionally, the model (especially as initially trained) does not “understand” the solubility of salts in the polymer. This makes sense since the majority of the training data will be reported for soluble formulations. Therefore, quite a few earlier predicted formulations were for very high salt concentrations, which proved insoluble in the dried electrolyte (typically observed by the resultant film looking “chalky” with salt crashed out and subsequently very poor ionic conductivity. As the model evolved, it begins to learn this, and the high concentration regime for most salts lowers in predicted ionic conductivity (Figure 9-9).

Figure 6-5 C & D) show the evolution of the model uncertainty between the initial and final models. Supportive of the intuition that more data will make the model more certain of predictions, we find that the overall chemical space shifts towards darker values and becomes much more uniform in uncertainty over time. The average uncertainty of the entire model predictions over the chemical space is shown in Figure 6-6B). Encouragingly when we split the model predictions into points within the excluded volumes around every formulation suggestion (sampled) and points outside of these regions (non-sampled) we see that the uncertainty for both is falling. This suggests that adding data is changing the entire model as a whole and not just points of similar formulation to those sampled.

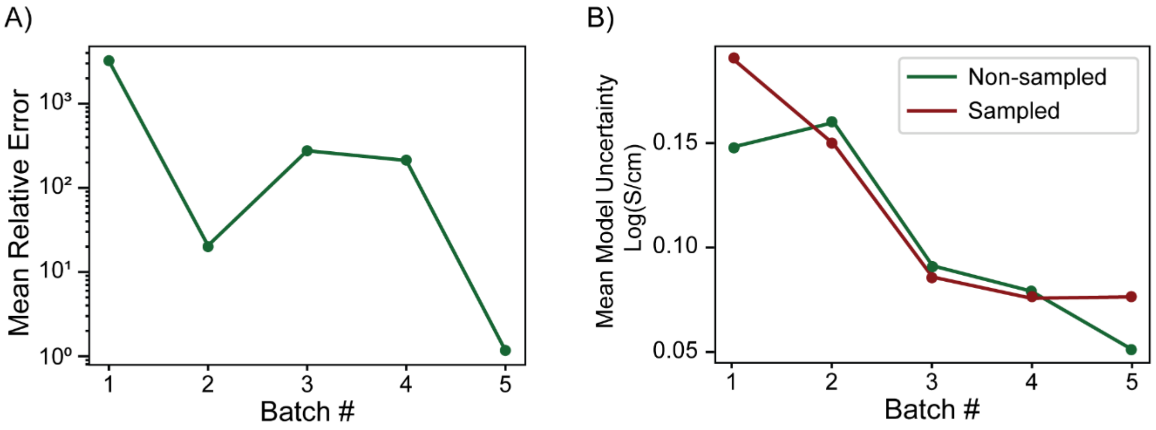

Figure 6-6 A) Mean relative error of each batch of experimental data. B) Mean model uncertainty of each batch of experimental data (before running the samples).

Figure 6-7 shows a comparison of the entire chemical space predictions before the study and with the final trained ML model split up by anion type. These data are the same as those depicted in Figure 6-5, but reveal more about which salts perform best. Consistent with the top-performing experimentally tested formulations, the model predicts that sulfonamides (FSI, TFSI, and BETI) have the highest density of points of high ionic conductivity. Similarly, boron-containing points display a large lobe at higher ionic conductivities. Still, there is a long tail due to some formulations which were measured to have very low ionic conductivity (due to salt insolubility). Additionally, each anion group well depicts the overall shift towards lower ionic conductivities than were initially predicted, displaying the evolution of the model.

Additionally, we found that during the experiment, some anions (Br, DFP, F, and TFO) were never suggested by the sampling scheme (owing to their predicted low ionic conductivity). Therefore, to force exploration of these anions, we hand-chose two concentrations from each to study in a batch. The data for these experiments are shown in Table 9-6 – 9-9. Consistent with the predictions, many formulations had very low ionic conductivity, sometimes preventing accurate measurements. As such, these data were not included in the training set of the final ML model.

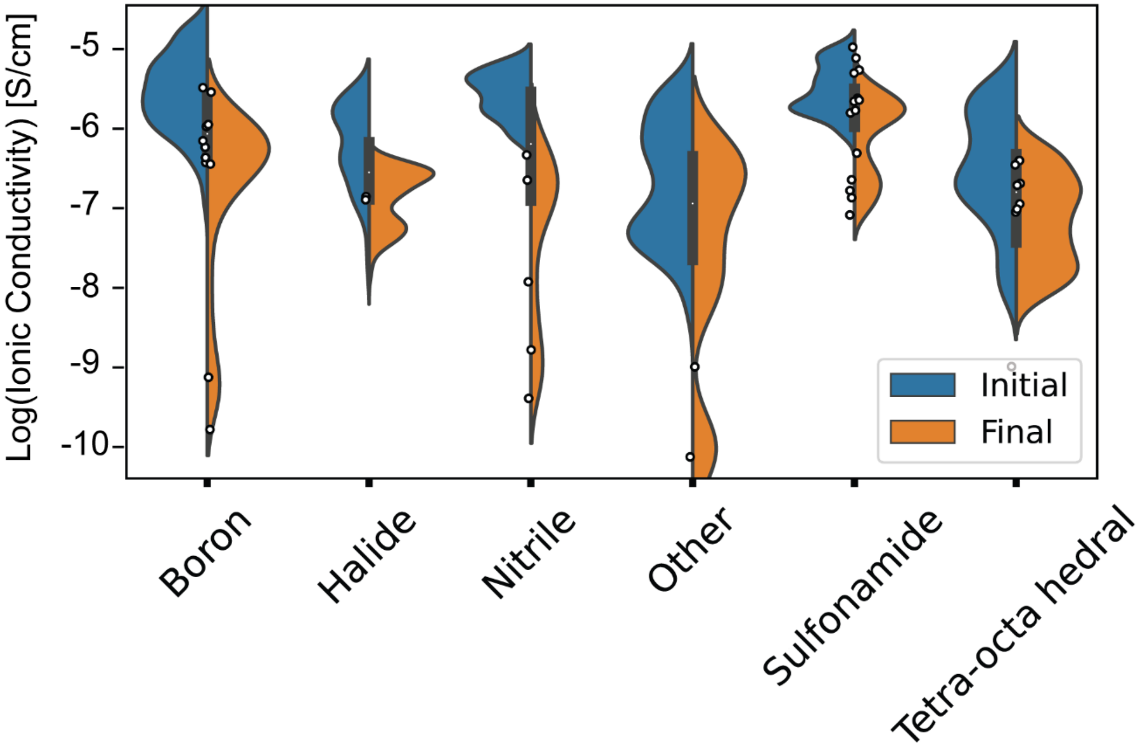

Figure 6-7 Plots depicting the evolution of the model predictions over the course of the experiment as grouped by anion type. Distance from the center depicts the relative number of formulations with that ionic conductivity value. Experimentally tested data points are shown as small dots.

CONCLUSIONS

In this chapter, we have detailed our first foray into instituting an active learning platform for ML-guided optimization of polymer electrolytes. Three main components had to be created and integrated. First, a literature-trained machine learning model that could predict the ionic conductivity of a given polymer electrolyte based on its chemical constituents was designed and trained to predict to within one order of magnitude on average. Second, the ML model was used to guide a Bayesian optimization sampling system that sought to explore a vast chemical space efficiently while balancing exploring new formulations to lower model uncertainty and exploiting regions of high predicted ionic conductivity. These two parts were then used to guide high throughput experimentation on the automated tool. In just one month, 45 polymer + salt formulations were tested (in 5 times replication) in 5 batch-based runs. By the end of the experiment, new formulations directly on par with the previous best reported were found, and the polymer (PCL) data pool was expanded over sevenfold. As the experiment progressed, the ML model learned to more accurately predict the ionic conductivity across the whole chemical space, reflected in declines in the model uncertainty of predictions, as well as the error between prediction and measured results declining. This experiment shows the utility of ML and high throughput experimentation and sets the stage for more extensive studies on even more novel polymer systems. Some exciting opportunities will be proposed in the next and final Chapter!

CHAPTER 7 CONCLUSIONS, OUTLOOK, AND PERSPECTIVES

This thesis has explored polymer electrolytes from various perspectives, strategies, and methodologies. Throughout the work, we have seen the progression from so-called “human-centered” to “data-driven” design of new polymer electrolytes. This progression has required the development of new chemistry, hardware, tools and methods.

To set the stage, the fundamentals of ionic conductivity in liquids and solids were detailed in **Chapter 2**. We then leveraged that fundamental understanding in **Chapter 3** to translate the ion-hopping mechanism observed in inorganic ceramic electrolytes to polymeric materials. This was enabled by two main strategies: promoting the formation of highly ordered structures with ionic channels, and the use of highly dissociative anions—both of which were only enabled by the rational design of the chemical structure of the polymer. Dissociative “FAST” anions were chemically modified with alkenyl-terminated carbon chains to enable ADMET polymerization and promote the formation of ordered lamellae. The formed structures were found to depend on both spacer length and cation choice. EIS measurements of the ionic conductivity showed that it followed an Arrhenius relationship with varying temperatures suggesting that cation conduction occurred through an ion-hopping mechanism. This was supported by NEB calculations using the parent salt FAST-C crystal structure as a surrogate model for the ion channels in the polymer, resulting in a very similar activation energy to those measured on the polymeric materials. The synthesized materials also had some of the lowest activation energies and highest ionic conductivities for polymers with ion-hopping mechanisms. Finally, we showed that a dramatic increase in ionic conductivity could be achieved by adding 1 molar equivalent of a cation-coordinating solvent. This work showed the utility of rational polymer design based on fundamental principles towards improving ionic conductivity in ion-hopping in polymer electrolytes.

Chapters 4, 5, and **6** all concerned developing and using a high throughput platform to increase the scale and speed of polymer electrolyte research. In **Chapter 4,** we detailed the different requirements and functions of the high throughput tool and some of the engineering challenges and developments required to make the system work. The performance of the custom components was benchmarked and ionic conductivity measurements were found to be accurate compared to literature references. The high throughput tool was then used in two case studies. In **Chapter 5** we leveraged the throughput capabilities to perform what is likely the most comprehensive screening of polymer electrolytes produced by a lab. All experiments were conducted with the same conditions and in replications giving a high degree of cross-comparability. We directly compared lithium and sodium conduction in PEO, fully characterizing the ionic conductivity of four of the most highly used salts in both cations. Additionally, the production of an associated DSC sample with every formulation revealed a previously unknown dip in glass transition at intermediate concentrations, often coinciding with the maximum ionic conductivity. We believe this trend across concentrations and anions was only found due to the high degree of fidelity and extensive scope of samples our system affords. Finally, in **Chapter 6** we employed the high throughput tool in an active learning loop, combining it with a machine learning model to predict ionic conductivity and guide the efficient exploration of a novel polymer electrolyte space. With this system, we could rapidly find formulations with relatively high ionic conductivity at room temperature and on par with the highest literature-reported values. Additionally, we demonstrated that the machine learning model is able to become more accurate over time in both prediction and uncertainty. We have presented the utility of using machine learning in conjunction with high throughput experimentation to increase the speed of new polymer electrolyte discovery. This work sets the stage for future exciting high throughput electrolyte research to enable the next generation of batteries!

OUTLOOK ON THIS WORK AND FUTURE PERSPECTIVES

ON ION-HOPPING IN POLYMERS

It is evident that the polymers presented in **Chapter 3** have overall low ionic conductivity as compared with the best-performing inorganic ceramics they were inspired by. While absolute ionic conductivity was not the primary goal of that study, it is worthwhile to think about ways to improve upon these materials. One key difference between the polymers presented in **Chapter 3** and inorganic ion-conductors is the concentration of cations. Inorganic ceramic electrolytes can have cation concentrations as high as 40 molar![153] In contrast, for the **pFAST-C20-Li** polymer, there is a cation concentration of approximately 1.3×10^{-6} molar (if we assume the polymer has a density of 1 g/cm^3 typical of many polymers, including polyethylene which the backbone is similar to). This near six order of magnitude difference could make up a large portion of the gap between our materials and inorganic ion conductors—especially considering the activation energy for ion conduction we observe is well within the range observed for inorganic materials.[28,33]

Therefore, if we seek to improve upon the absolute ionic conductivity of ion-hopping in polymer electrolytes, it may be prudent to consider ways to increase the concentration in these materials. Indeed we did consider this point throughout this study. One of the original motivators to make the 10-carbon spacer material shown in Figure 8-13 was precisely this. We hypothesized that the ionic conductivity of this material would be higher than that of the ones with the 20-carbon spacer purely due to the higher concentration of cations, however, it is quite a marginal improvement in concentration compared to the inorganic materials. This material proved synthetically difficult to polymerize in large scales; we observed the polymer crashing out of solution as it polymerized and did not reach high molecular weights. We also considered making a 4-carbon spacer polymer, but this material did not polymerize at all! The monomer was largely insoluble in dichloromethane and dichloroethane. We did not attempt to polymerize it in polycarbonate as that route was discovered much later. It may have worked, but we also speculate that in the 4-carbon spacer material, the sulfur atom is close enough to the catalyst that it chelates the ruthenium center and prevents polymerization. Such chelate structures have been synthesized in our labs. Furthermore, even in this minimally carbon-spaced polymer there is still only 1 cation per ~500 g/mol anion of the FAST-C salt. Therefore, one needs to consider how to maintain order, lower activation energy, and raise cation concentration to realize better ionic conductivity in this class of materials.

On Data-Driven Design Versus Human-Centered Design

Much of the work presented in this thesis has been geared towards establishing a platform for executing data-driven design for the accelerated discovery of polymer electrolytes. This is perhaps partly motivated by the "hotness" of machine learning in the current society and within science. Many view it as a next generation or additional pillar of science. While I feel that this is likely true (at least partially), it is also essential to consider the bounds on the technology, where it fails, and where it may not be applicable. Here are some interesting vignettes and perspectives from my personal experience in the field. *I think an over-arching principle is that your ML model is only ever as good as your training set of data, therefore, many of the conclusions being drawn by a model are just consequences of the training set.*

Two key challenges we faced in developing and using our ML model as described in **Chapter 6** were chemical compatibility and salt solubility. One of the salts we included in the study was lithium methoxide, which was actually predicted to have relatively high ionic conductivity. However, when we formulated it with polycaprolactone, it was found that the precursor solution quickly became much less viscous than the other samples. We attempted to cast films of this formulation but they leaked out the sides of the wells due to the reduced viscosity. Subsequently, we were unable to get ionic conductivity measurements. The most likely cause of this is that lithium methoxide is very nucleophilic, and poly(caprolactone) is susceptible to nucleophilic attack at the ester bond. The salt likely degraded the polymer quickly, leading to oligomers and lower viscosity. This highlights the importance of using good chemical intuition alongside machine learning model predictions to guide research. Another similar issue occurred with the use of $LiPF_6$. $LiPF_6$ is known to be quite unstable, having an equilibrium with LiF and the gaseous product PF_5 at room temperature and rapidly reacting with trace water to form HF and PF_5OH.[15] Early on in the Bayesian optimization experiment, the model suggested making a formulation with a very high $LiPF_6$ concentration (>5 molal). However, during the Li/Na study presented in **Chapter 5**, we found that at concentrations above 3.75 molal, the samples showed signs of heavy degradation, turning dark brown and discoloring the inside portions of our sample plates and covers. We suspect that the trace water residual in our polymer/solvents combined with the high salt concentration caused significant degradation to the samples. Therefore, we put a concentration limit the ML model for PF_6 to lower the chances of this happening.

Inspired by these challenges, we have considered how one may be able to teach the machine-learning model about solubility limits and chemical incompatibility. I think these ideas also approach a broader question of skewness in machine learning models for property predictions. Due to the somewhat competitive nature of scientific research, there is a tendency to favor publishing positive or improved results. While this perhaps makes the most exciting research, it does not lend itself well to machine learning. This can be seen easily in Figure 6-1 where the largest concentration of points occurs around the ionic conductivity range of $\sim 10^{-5} - 10^{-3}$ S/cm which is on the upper end of the observed range. If one considers all possible combinations of polymers and salts, the vast majority of them would likely have zero ionic conductivity, given that most polymers will not dissolve salts. *So, for the most accurate machine learning model, it needs to learn what makes a good electrolyte and what makes a bad electrolyte.* While I admit that spending resources to verify that polymers any chemist would know to be terrible ion conductors just for the sake of training the ML model is not productive, perhaps just aiming to capture more data in the $10^{-10} – 10^{-5}$ range could help make the model more accurate. I think this is perhaps huge benefit of the high throughput tool as well as open databases in general. Given the statistical nature of high throughput approaches, you tend to sample a much more comprehensive range of ionic conductivity values. This is shown well in both of our studies, especially the PCL one, where we covered six orders of magnitude relatively evenly (albeit still with a skew towards higher values). It was also found that acquiring these low ionic conductivity data points drastically adjusted the predictions in subsequent rounds. *I think this also is emblematic of no ML model is better than its training data, and it is pretty evident we need more data across all spectrums to improve our model.* Another idea is to use multiple models for formulations, one for ionic conductivity as we have implemented here, but then another could be trained to predict salt solubility or even a third for chemical compatibility. Then the final put-forth formulations could take inputs from all of the models for a higher probability of designing a good sample. Considering the huge degree of interest in machine learning, self-driving labs, and high throughput experimentation across a variety of fields, strategies to remedy the above issues are forthcoming!

CHAPTER 8 APPENDIX-A: SUPPLEMENTAL FIGURES FOR “ SEMI-CRYSTALLINE, SINGLE-ION CONDUCTING POLYMERS WITH HIGHLY DISSOCIATIVE ANIONS: FAST PATHWAYS FOR DECOUPLED CATION TRANSPORT”

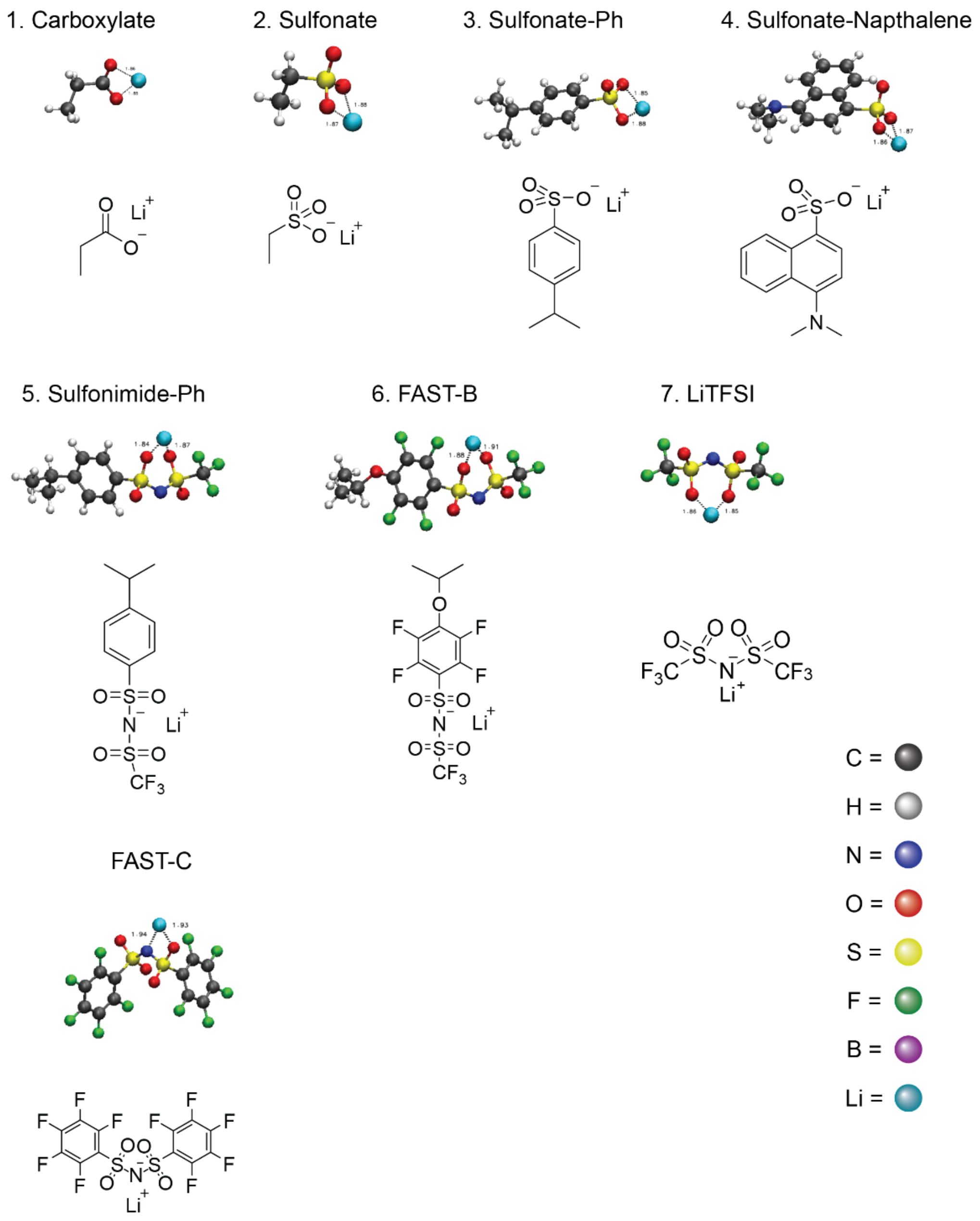

Figure 8-1 Final Poses and Chemical Structures of Li-anion clusters. Structures were chosen by taking the “anionic” segment from every polymeric structure. Those attached to alkyl backbones were cut at two carbons past the anionic segment. The final geometries were found via DFT optimization scheme to progressively find the lowest energy

cluster. It was found that in the clusters, the Li cation most often coordinated to nearby oxygen atoms with a distance of 1.8-2.0 Å.

SECTION S1: EXPERIMENTAL SUPPLEMENTARY FIGURES

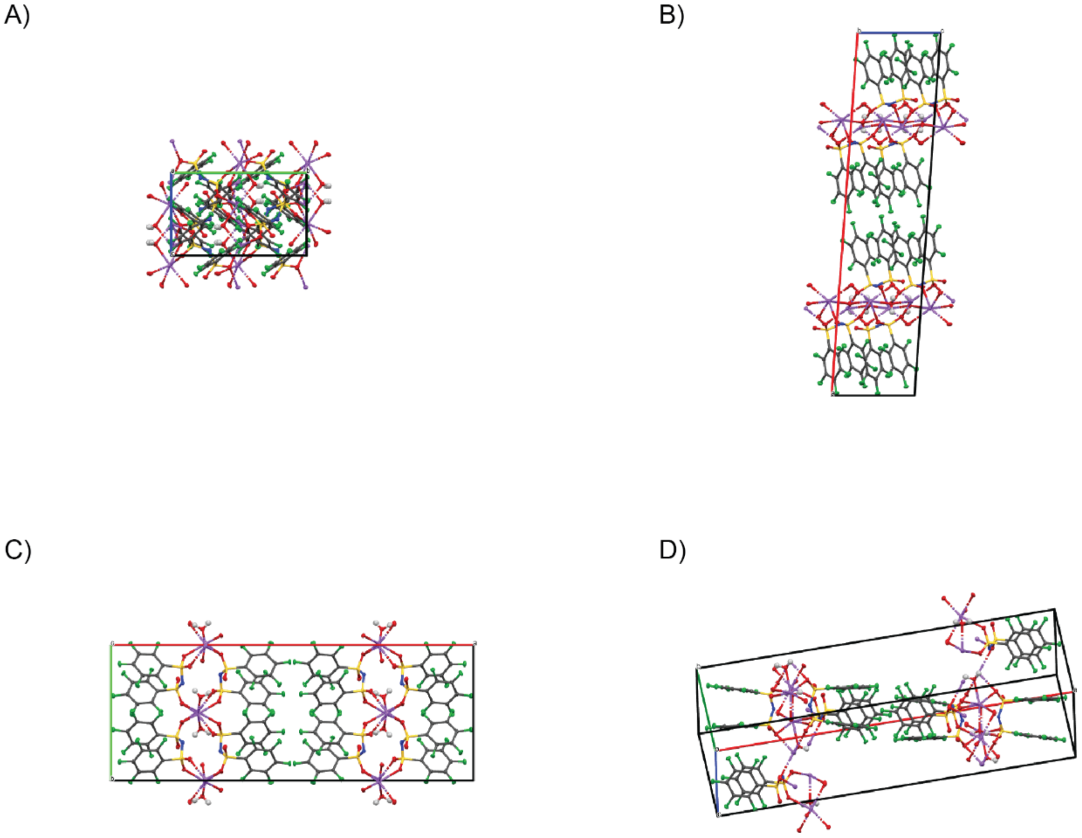

Figure 8-2 Different views of the solved crystal structure of FAST-C: A) along the a axis, B) along the b axis, C) and along the c axis, (D an isometric view to highlight the ionic channel structure of the sodium cations. Each repeat unit of the crystal has one water molecule co-crystallized so the formula is $C_{12}F_{10}NNaO_4S_2 \bullet H_2O$ with a formula weight of 517.26. The space group is monoclinic 'C 2/c'. The unit cell has the following dimensions: a= 33.5050 Å, b= 12.5079 Å, and c= 7.6439 Å and angles α= 90.0 ° β= 94.1094 °, and γ= 90.0 ° degrees.

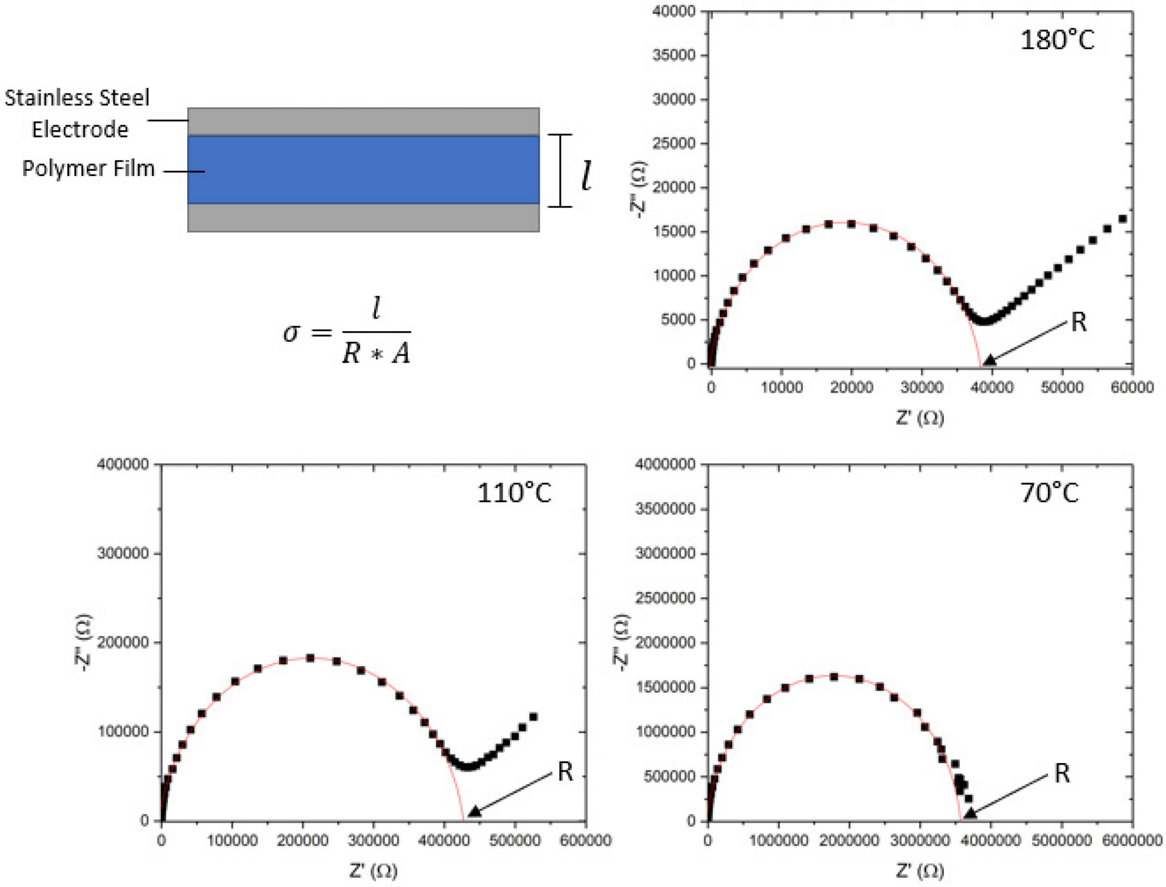

$$\sigma = \frac{l}{R * A}$$

Figure 8-3 Example EIS plots and fits to equivalent circuit model: Cartoon depicting the cell used to measure electrochemical impedance spectroscopy. Typical polymer film thicknesses were between 100 and 200 microns. The three panels show Nyquist plots of the EIS data for the C20Li polymer at 180, 110, and 70 °C in the black squares. The data were fitted to an equivalent RC circuit which is shown with the red line. The bulk resistance, R, is taken as the X-intercept of the fitted semicircle (labeled).

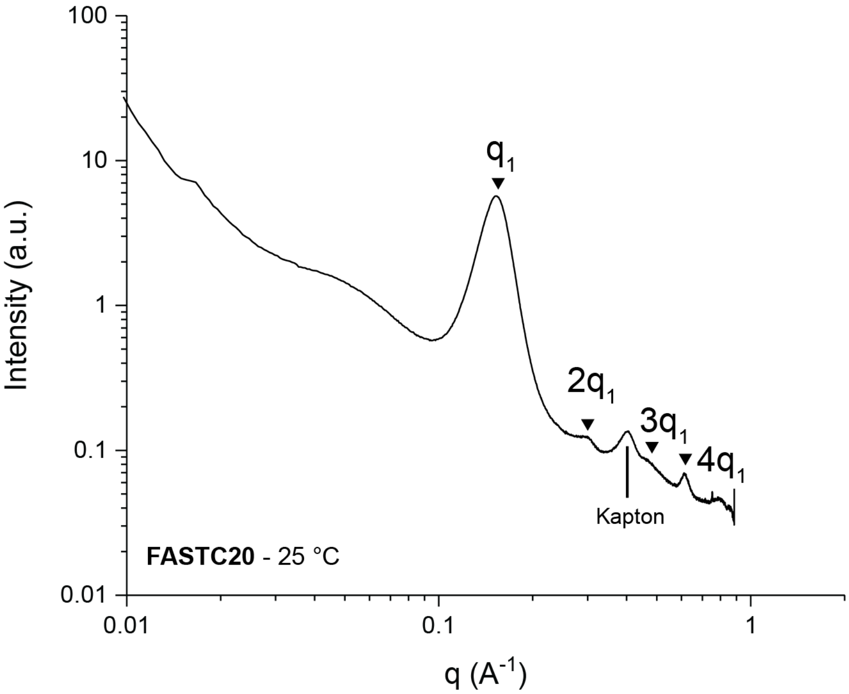

Figure 8-4 SAXS of FAST-C20 liquid crystal at 25 °C: showing a lamellar structure with primary scattering peak observed at q_1*=.15 Å*$^{-1}$ *and higher order reflections observed at 2*q_1*, 3*q_1*, and 4*q^1 *indicating a lamellar structure with d-spacing = 41.9 Å.*

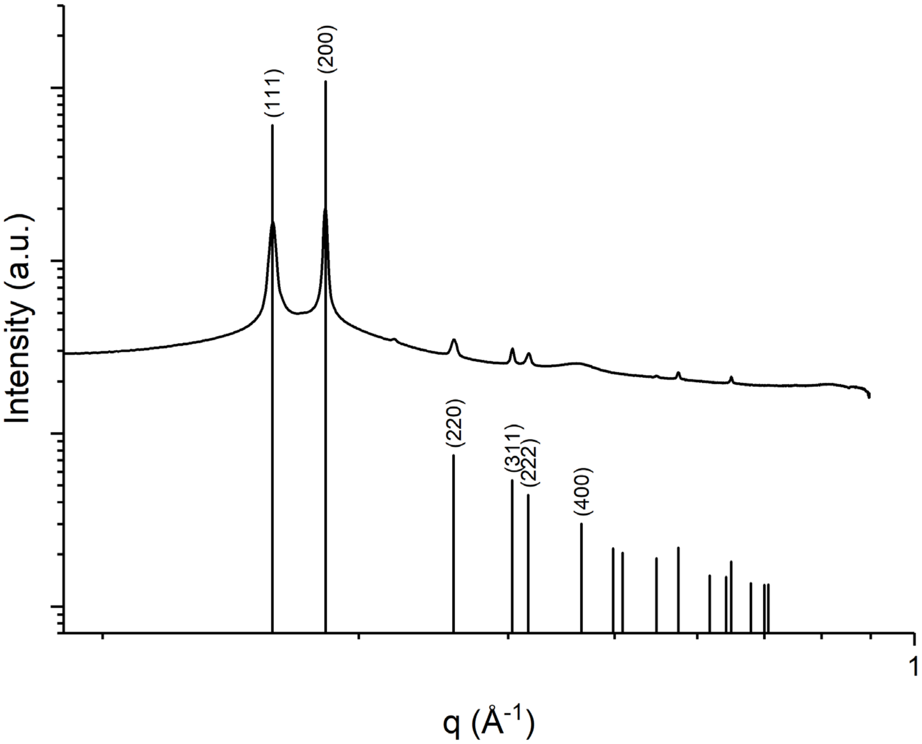

Figure 8-5 SAXS scattering pattern for FAST-C20 at 80 °Cand predicted peak locations for an FCC lattice. Here the (111) reflection was fit to the center of the lowest q peak, and the rest are calculated from this position. The lattice parameter is a= 61.86 Å, and thus the radius of the spheres are given by $r = \frac{a}{2*\sqrt{2}}$ *= 21.5 Å.*

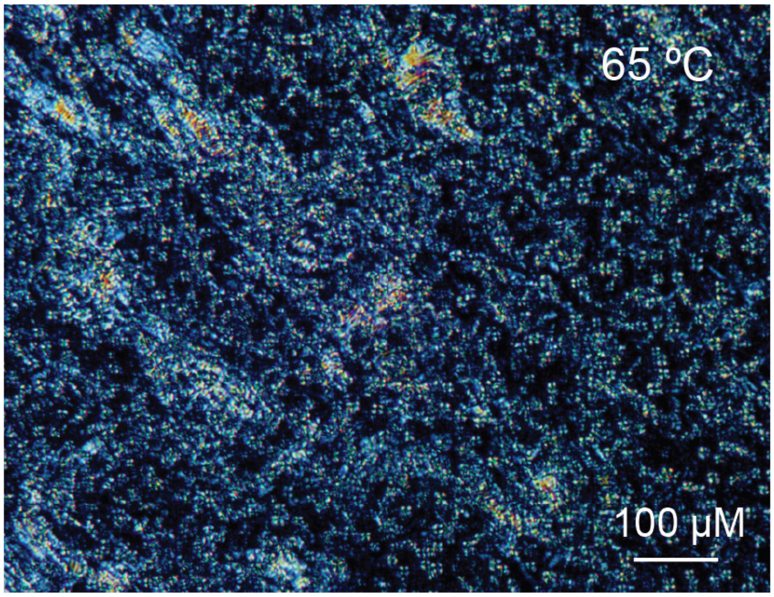

Figure 8-6 Polarized Optical Microscopy (POM) image of FAST-C20 collected at 65 °C. The small Maltese cross shapes observed are focal conic domains which appeared directly from the non-birefringent FCC phase. Due to the presence of focal conic domains combined with the lamellar pattern found by SAXS at 25 °C, we assign this phase a second smectic phase. Given the presence of the FCC phase at 80 °C it is likely that the molecular orientations in the high temperature and low temperature smectic phases are different.

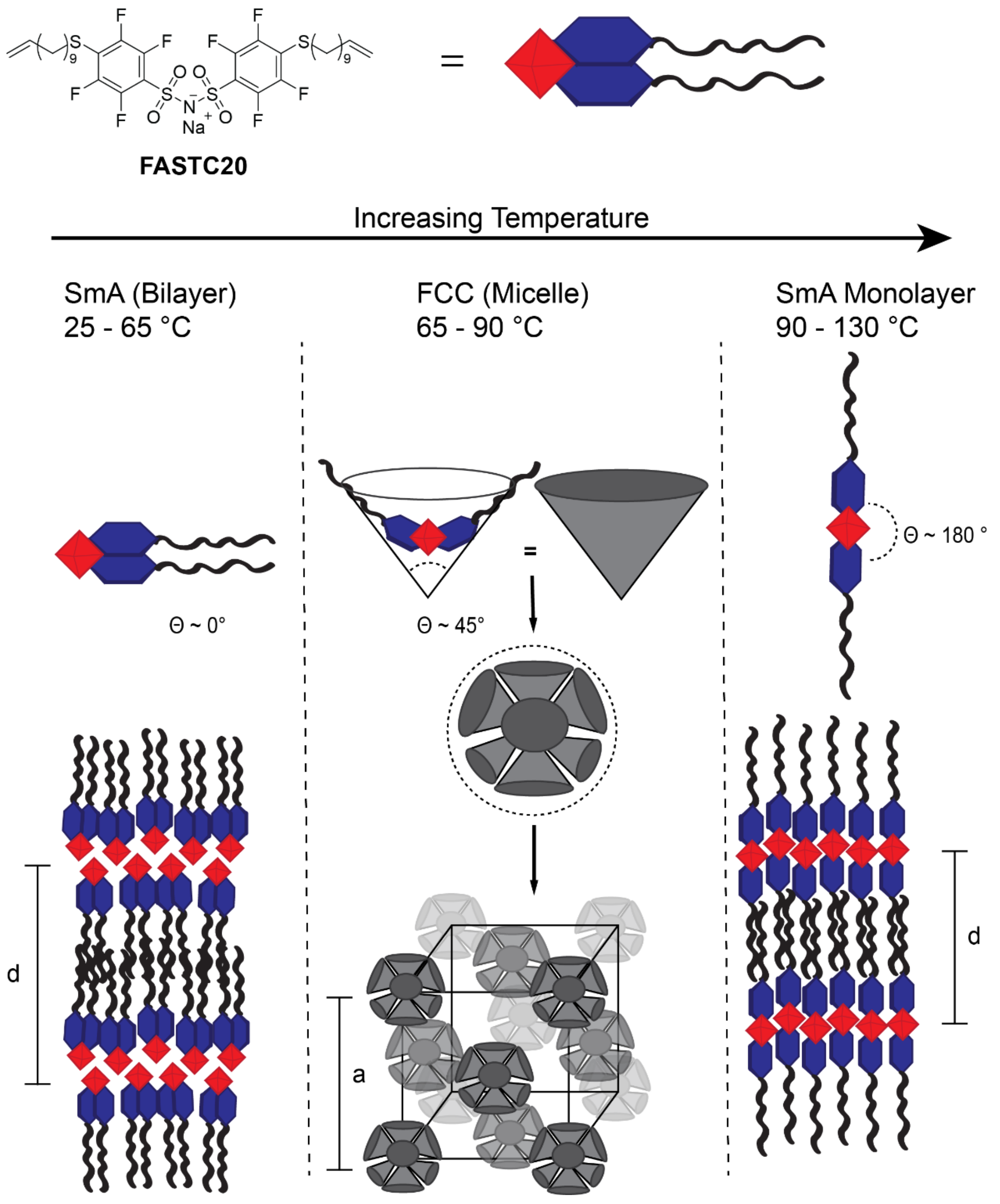

Figure 8-7 One possible orientation of the FAST-C20 molecules in the multiple liquid crystalline phases We hypothesize that the folded or "hairpin" configuration would be the lowest energy conformation. This conformation is observed in the single crystal structure of ***FAST-C*** *(Figure 1D). Additionally, the final lowest energy pose of both* ***FAST-C*** *as calculated by our DFT optimization scheme were also somewhat hair-pinned (Figure S1). Such a conformation is likely to form a bilayer type SmA phase where the ionic portions separate from the alkyl tails. As the temperature is increased, the molecules are able to access higher energy conformations. Consistent with the finding that the d-spacing in the high temperature phase is actually smaller than low T SmA phase, we hypothesize that this may adopt a "monolayer" type orientation where rings are stretched, but there is only one ionic portion per layer as a opposed to two. We further hypothesize that at intermediate temperature the internal angle is more intermediate. We propose that the intermediate conformers form wedges or cones which are able to self-assemble into micellar structures which then pack onto an FCC lattice as observed in SAXS. Such structures have been purposefully designed*

and observed in the field of dendrimer liquid crystals.[96,98] *While the model proposed here is consistent with the observations made in SAXS, and POM, there are likely other configurations which would be as well, and definitive assignment is infeasible.*

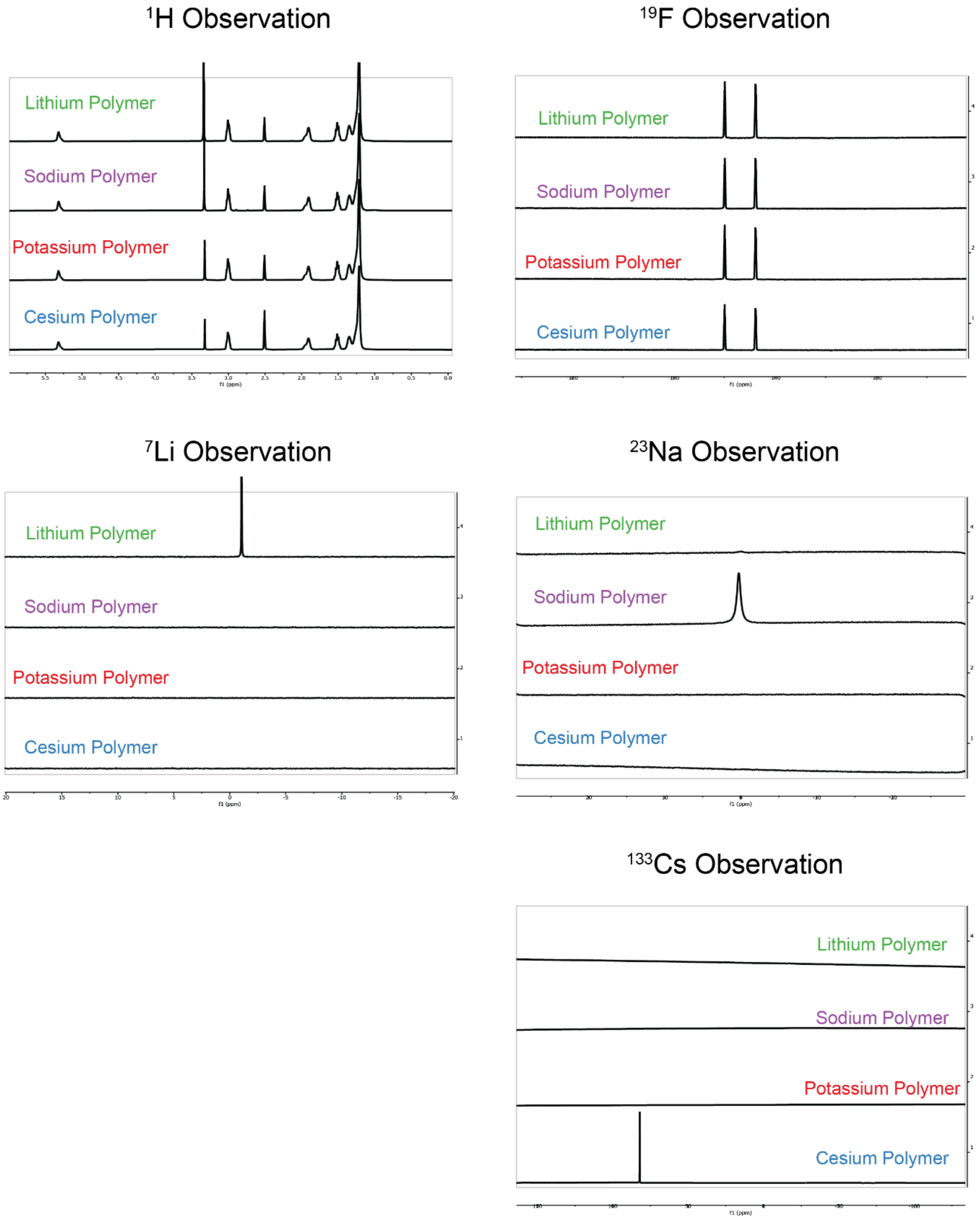

Figure 8-8 NMR observations to confirm successful cation exchange.All samples are dissolved in DMSO-d_6 at an approximate concentration of 10mg/mL, and all NMRs shown here are conducted on a single sample for each

polymer variant. The proton and fluorine traces were used to confirm that each solution does indeed have polymer dissolved, and all the peaks are identical between samples. All polymers are synthesized as the sodium ion variant and then washed with the corresponding MCl solution to reach the final desired cation. As expected, each variant only shows a peak in the corresponding nuclei observation (i.e. only the lithium variant is the only one to show a peak under ^{7}*Li observation). Unfortunately, the NMR probes available to us are not capable of observing* ^{39}*K. However, for the potassium variant polymer we do observe the disappearance of the* ^{23}*Na signal indicating all of the original sodium cations have been exchanged.*

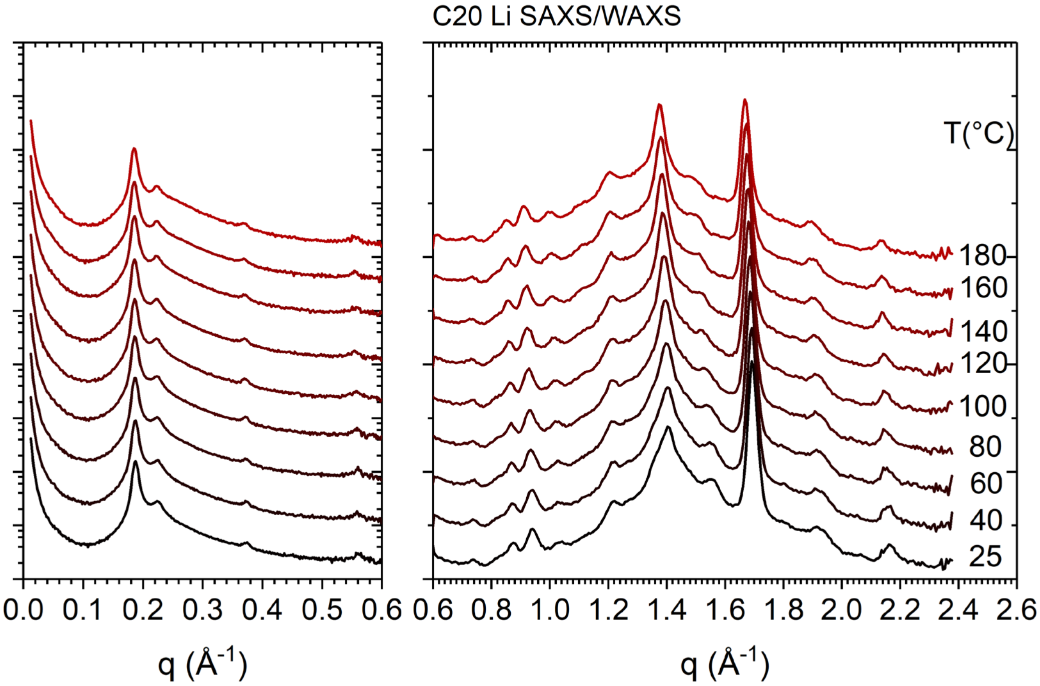

Figure 8-9 Small and Wide Angle X-Ray Scattering (SAXS/WAXS) curves collected at variable temperatures upon cooling of pFAST-C20-Li material.

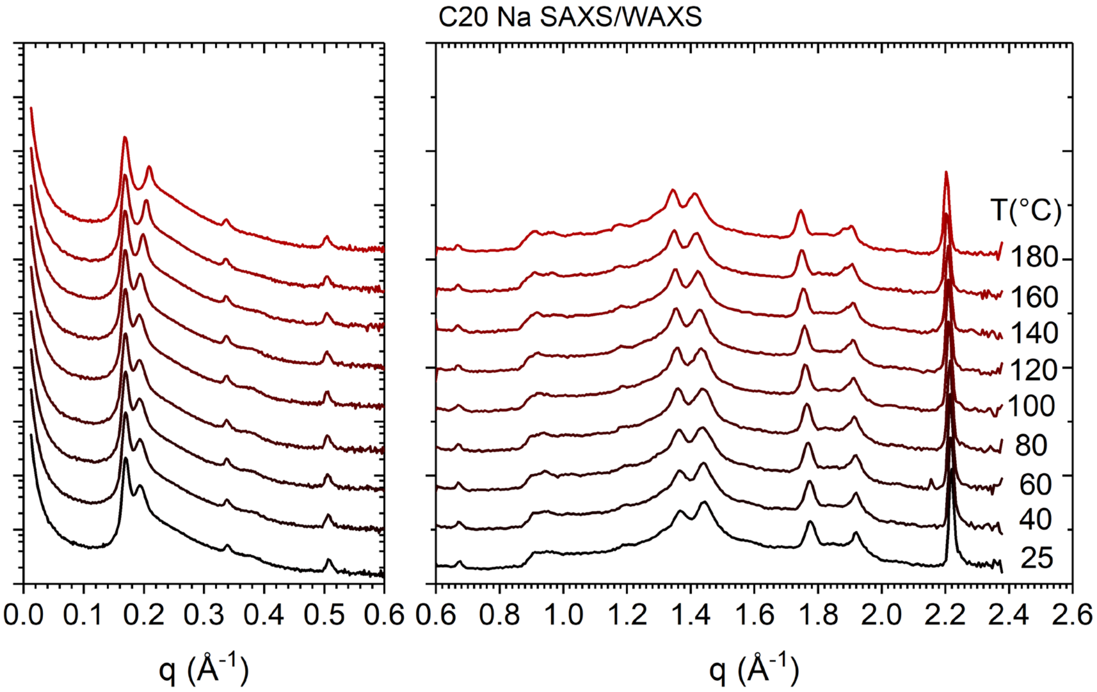

Figure 8-10 SAXS/WAXS curves collected at variable temperatures upon cooling of C20 Sodium material.

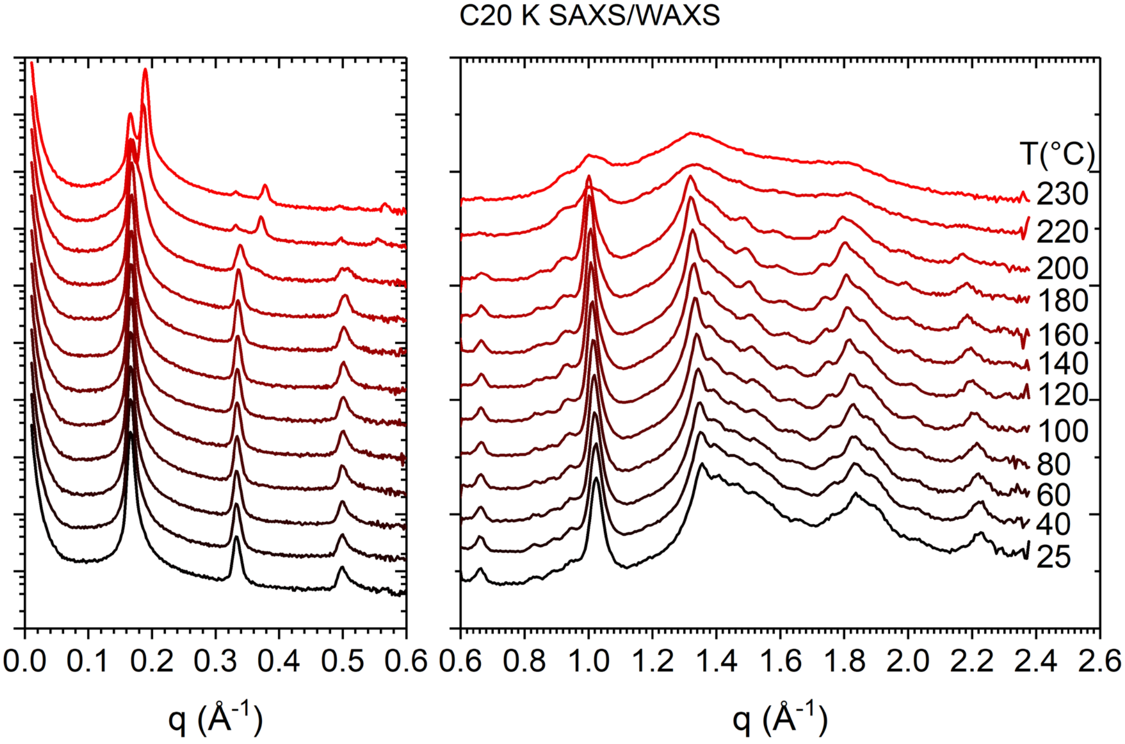

Figure 8-11 SAXS/WAXS curves collected at variable temperatures upon heating of C20 Potassium material.

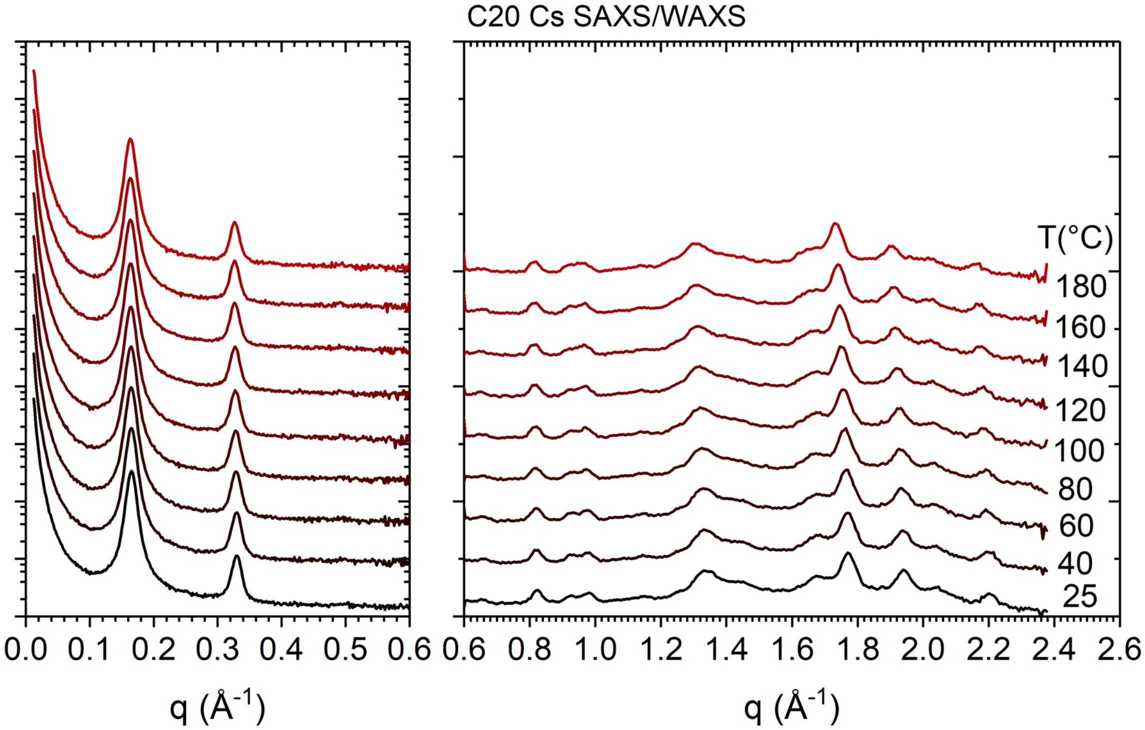

Figure 8-12 SAXS/WAXS curves collected at variable temperatures upon cooling of C20 Cesium material.

C10 Polymer Structure

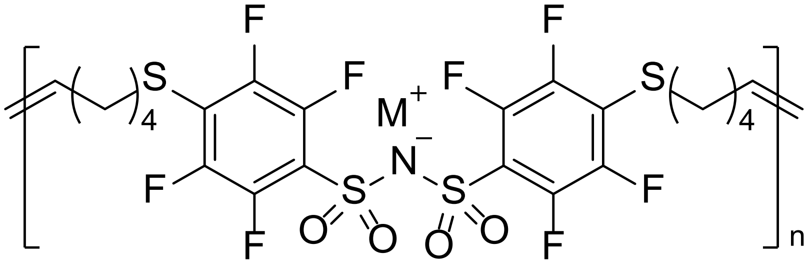

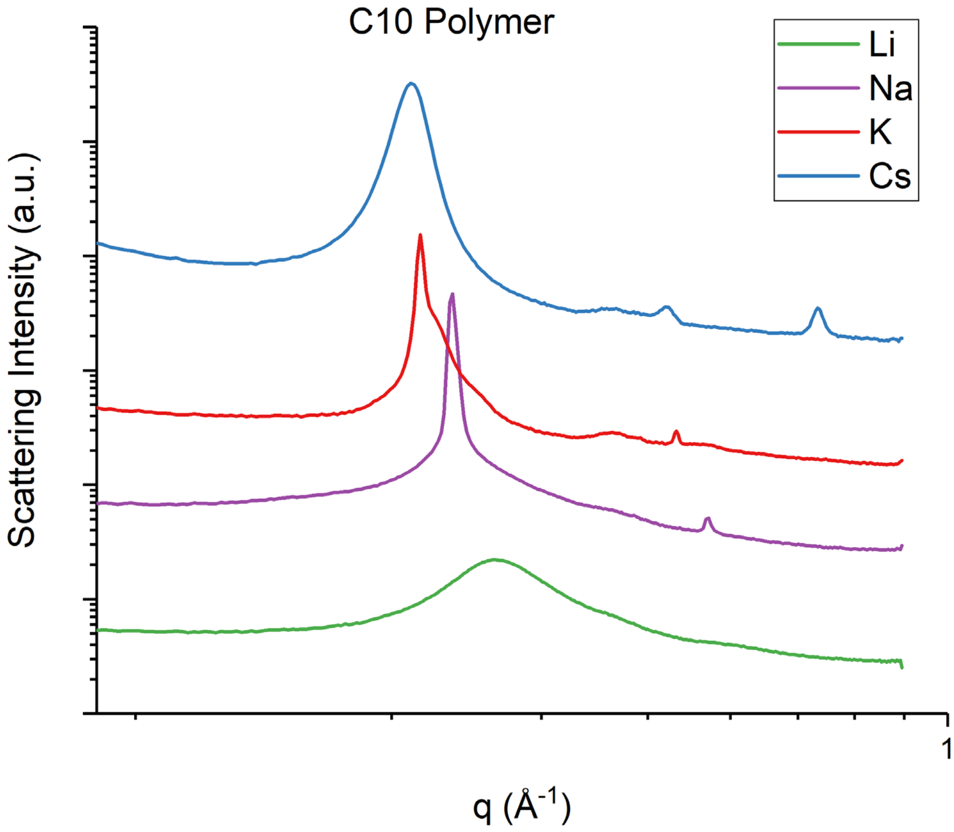

Figure 8-13 Structure and SAXS scattering for the C10 polymer cation variants. Polymers were prepared following the same method as the C20 polymer with minimal modifications. Films were cast following the same procedure as the C20 polymers. The SAXS data shown here were collected at Argonne National Lab at the Advanced Photon Source (APS) Facility on beamline 12-ID-B with an X-ray energy of 13.3 keV at 30 °C.

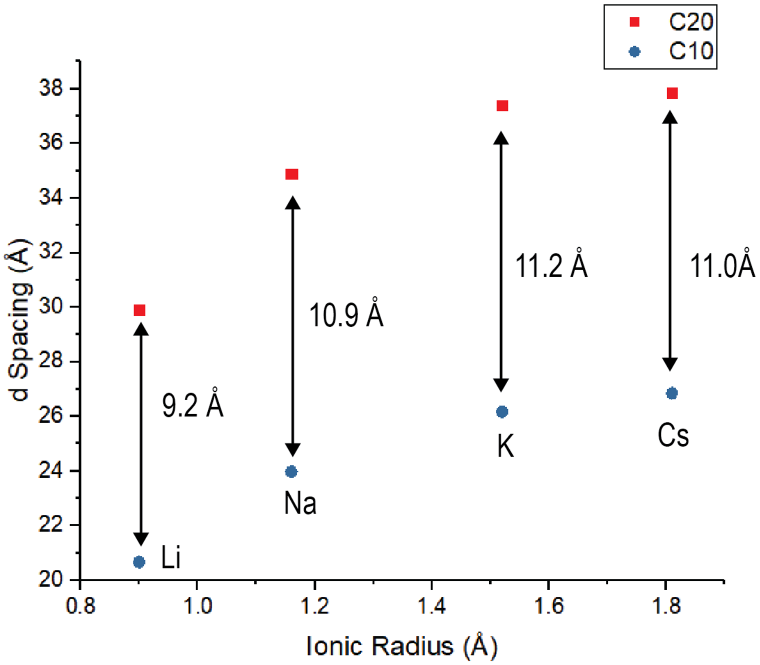

Figure 8-14 d-spacings of the C10 and C20 polymer lamellae for all four cation variants at 30 °C. Both polymer backbones increase monotonically with increasing cation size. The average difference in size due to the extra 10 carbon spacer is 10.5 Å.

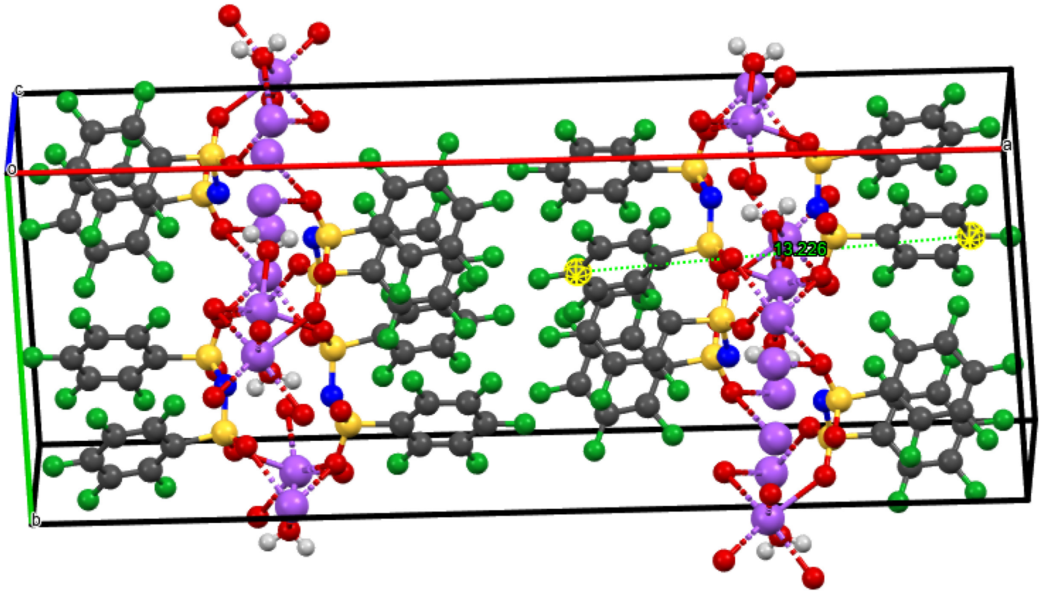

Figure 8-15 FAST-C Na crystal structure showing packing of the crystal. A distance of 13.2 Å for a single "ionic region" is measured between the two furthest carbon atoms on the aryl rings (highlighted here in yellow) on the right hand side of the image.

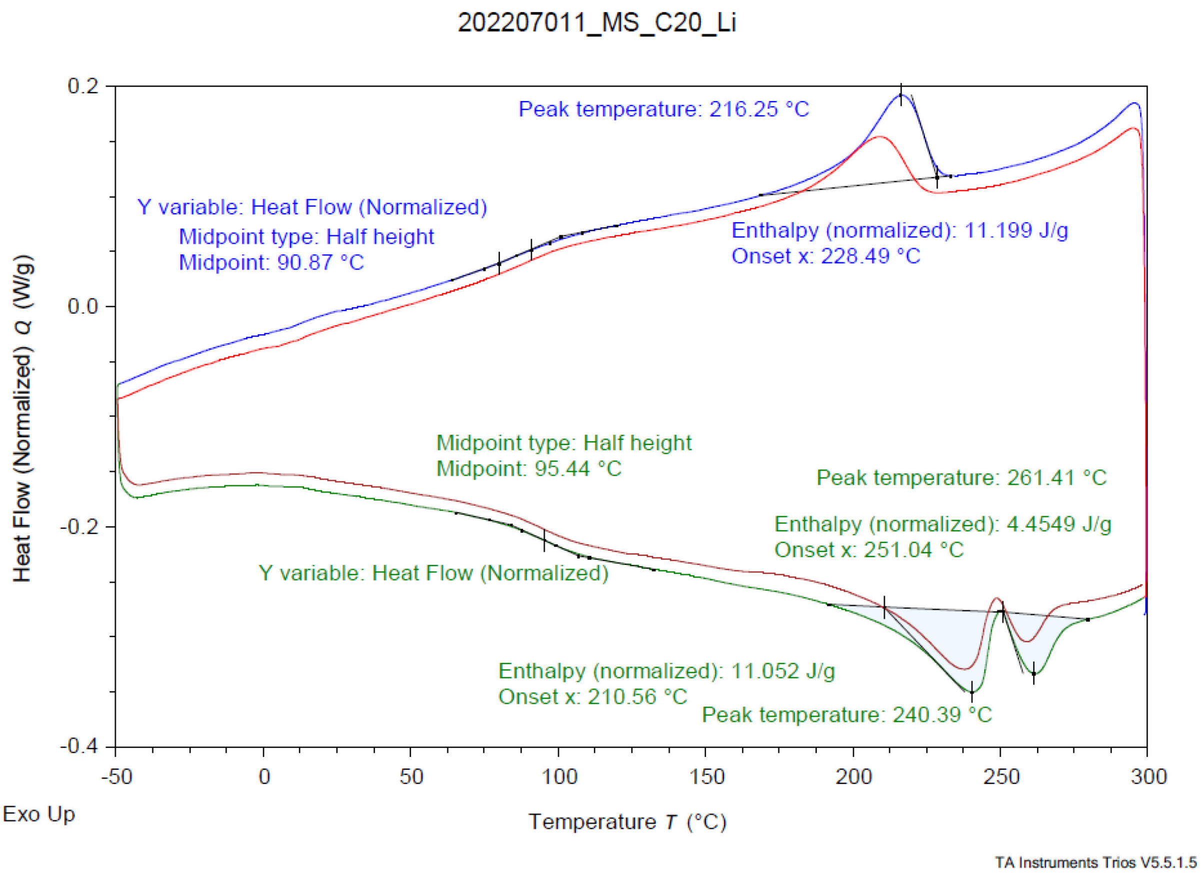

Figure 8-16 Differential Scanning Calorimetry (DSC) curves for the C20 Lithium material. Data shown are from the second (blue & green traces) and third (brown & red traces) cycle of heating/cooling.

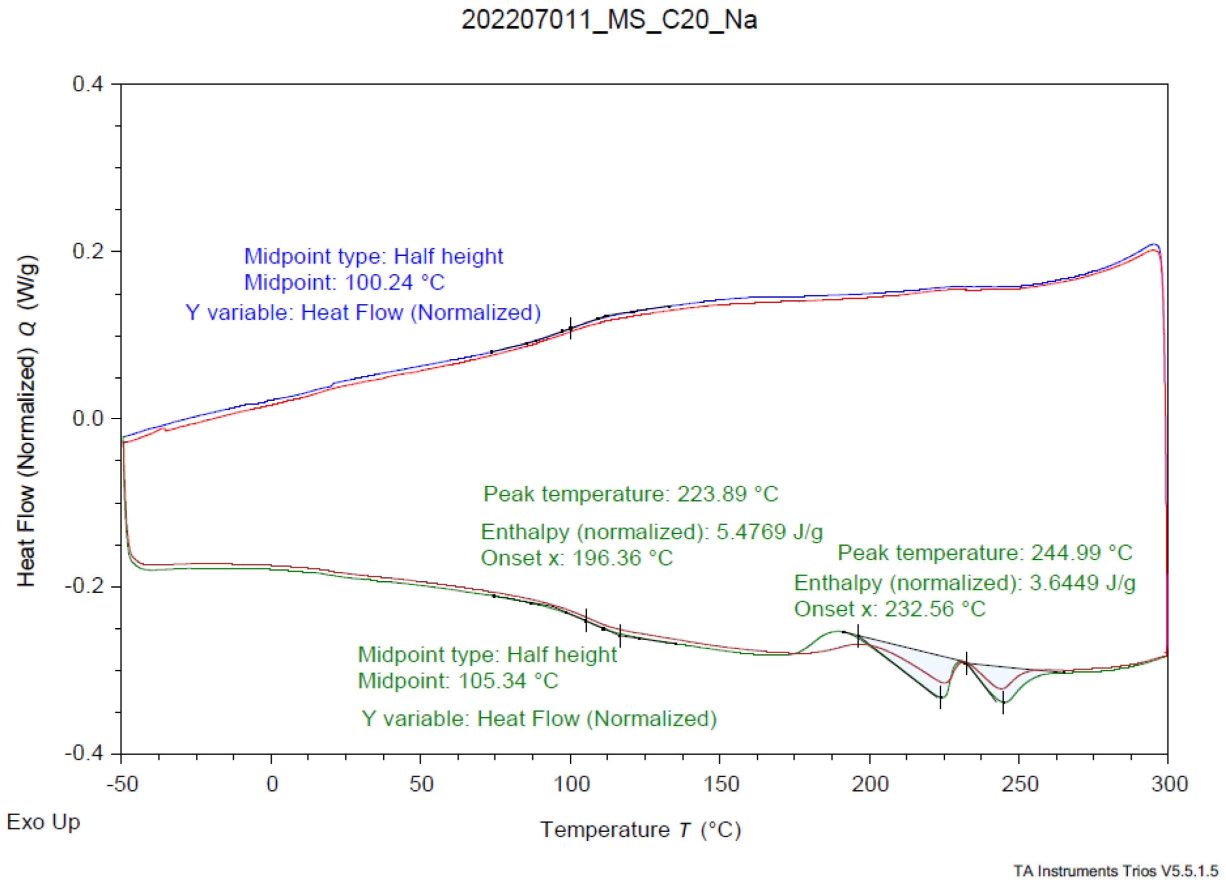

Figure 8-17 Differential Scanning Calorimetry (DSC) curves for the C20 Sodium material. Data shown are from the second (blue & green traces) and third (brown & red traces) cycle of heating/cooling.

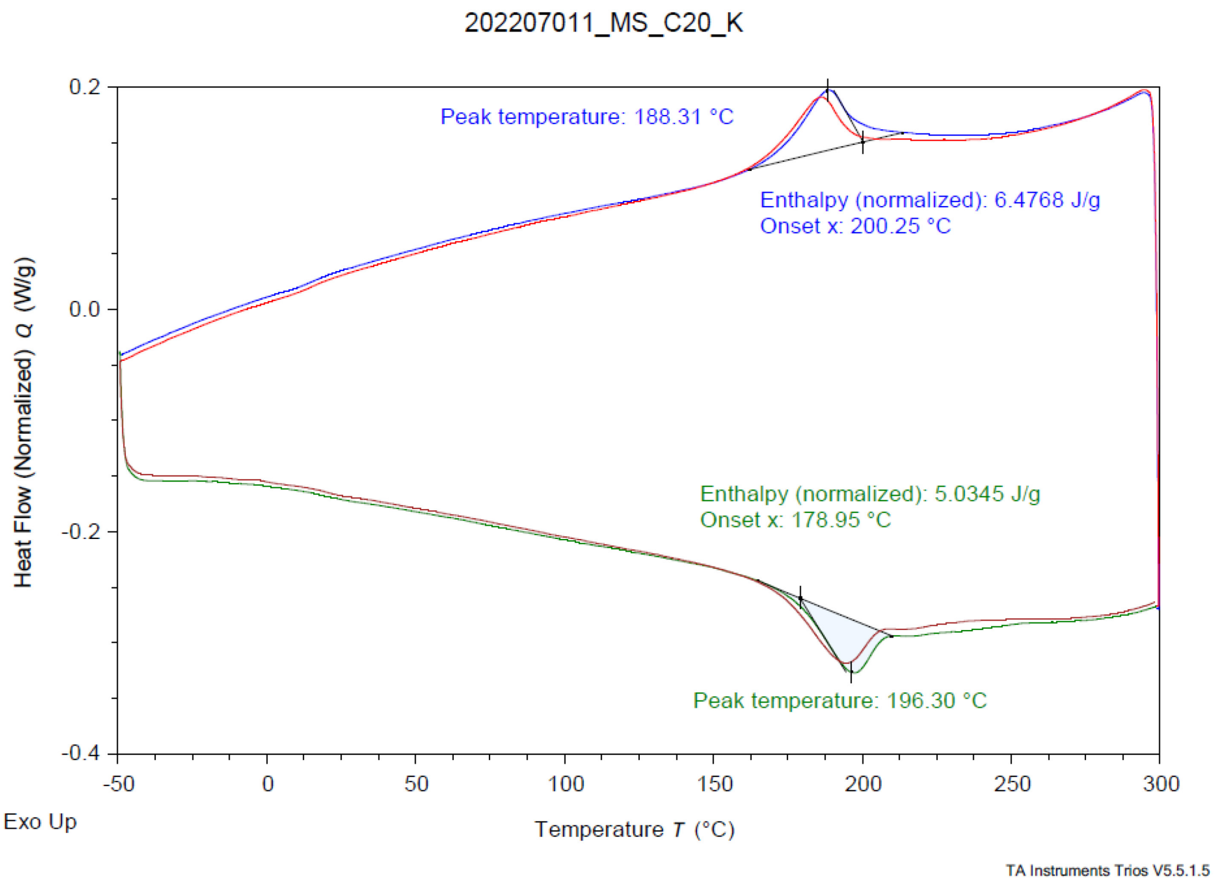

Figure 8-18 Differential Scanning Calorimetry (DSC) curves for the C20 Potassium material. Data shown are from the second (blue & green traces) and third (brown & red traces) cycle of heating/cooling.

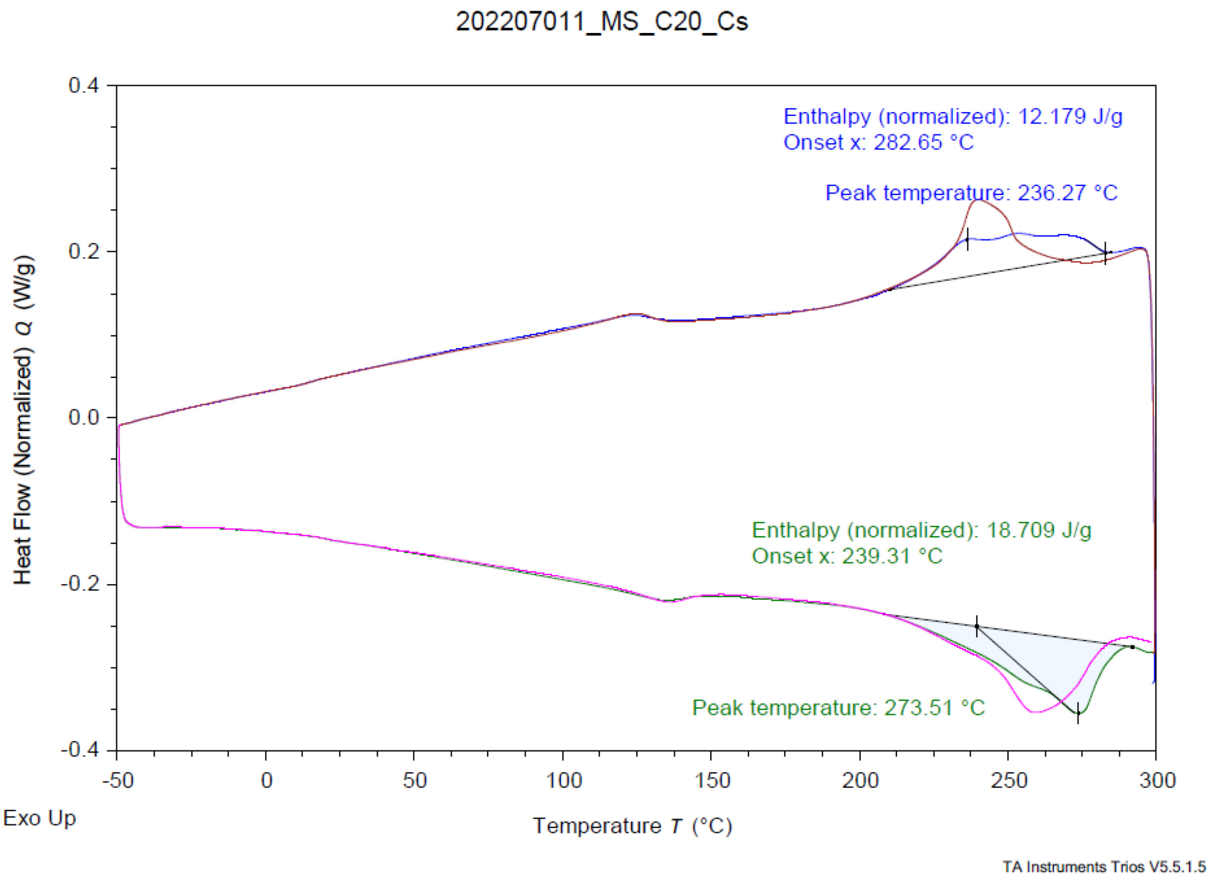

Figure 8-19 Differential Scanning Calorimetry (DSC) curves for the C20 Cesium material. Data shown are from the second (blue & green traces) and third (brown & red traces) cycle of heating/cooling.

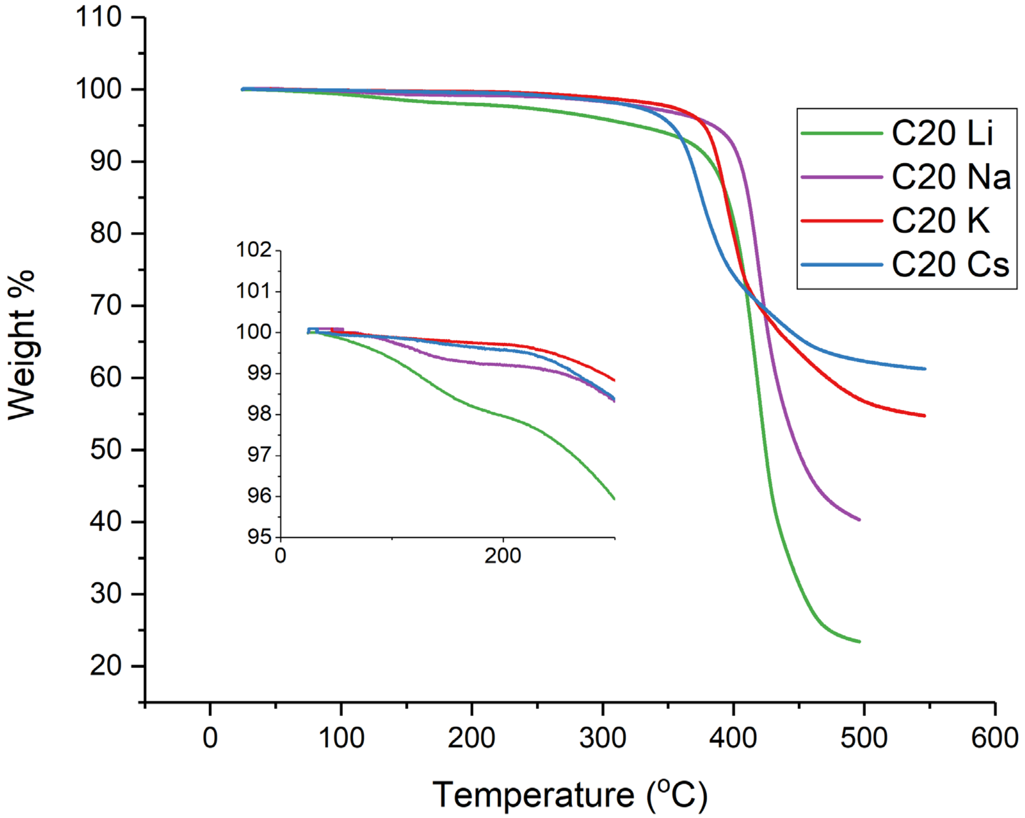

Figure 8-20 Thermal gravimetric analysis (TGA) of all polymer variants showing their high thermal stability. The inset shows the first few % of weight loss up until 300 °C. The temperature at which the samples lost 5 weight% are 325.6, 384.3, 377.5 and 352.77 °C for Li, Na, K, Cs variants respectively. The decomposition temperature (taken as the peak of the derivative of the weight loss) are 418.5, 419.5, 403.0, and 384.4 °C.

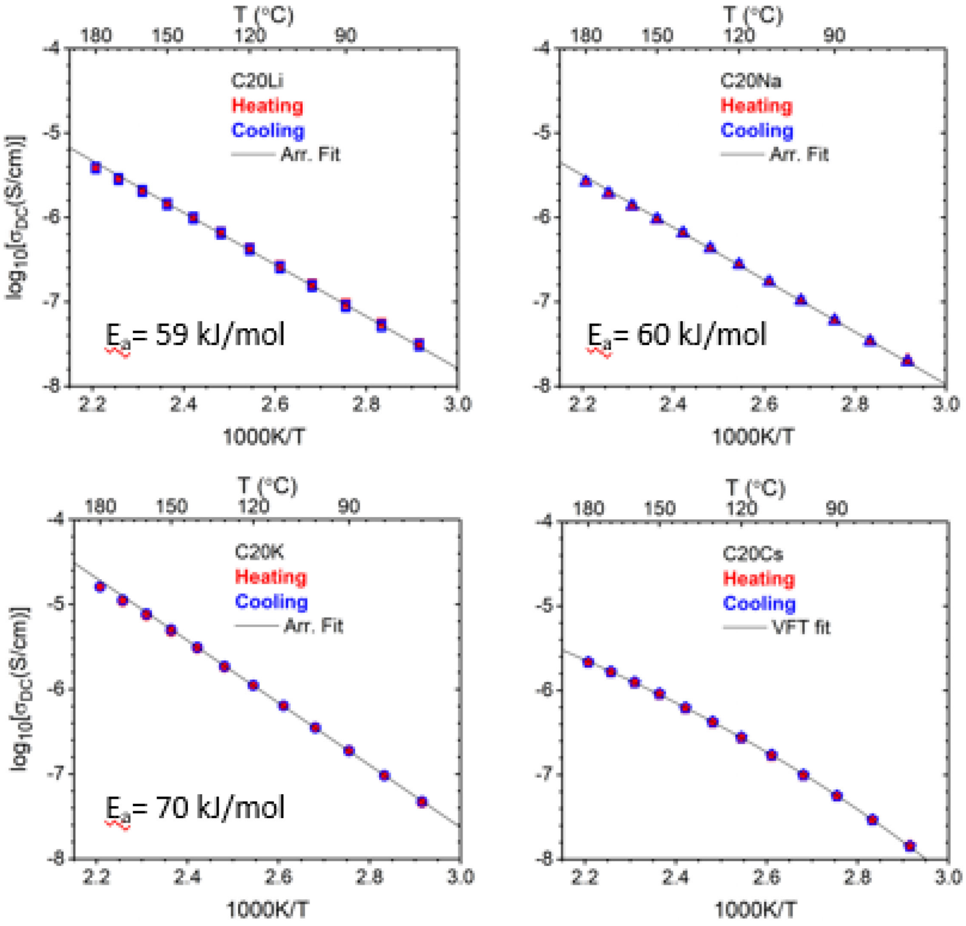

Figure 8-21 Electrochemical Impedance Spectroscopy (EIS) data collected for the four polymer variants collected on heating and cooling between 70 and 180 °C. The very close overlap of the heating and cooling curves shows that the structures responsible for ion conduction are stable over this temperature range. The black line in each plot shows the fit of the data to either the Arrhenius equation $\sigma = \sigma_0 exp\,(\frac{E_a}{RT})$ *or the VFT equation* $\sigma = Aexp(\frac{B}{T-T_0})$.

Table 8-1: Arrhenius and VFT fitted parameters for the ***pFAST-C20-M*** *materials ionic conductivity.*

Cation	σ_0 (S/cm)	E_a (kJ/mol)	$R^2_{Arrhenius}$	A (S/cm)	B(1/K)	T_0 (K)	R^2_{VFT}
Li	28.2	58.9	0.999	-	-	-	-
Na	24.5	59.8	0.999	-	-	-	-
K	2.4E3	70.2	0.9999	-	-	-	-
Cs	-	-	-	2.5E-3	1853	190	0.9999

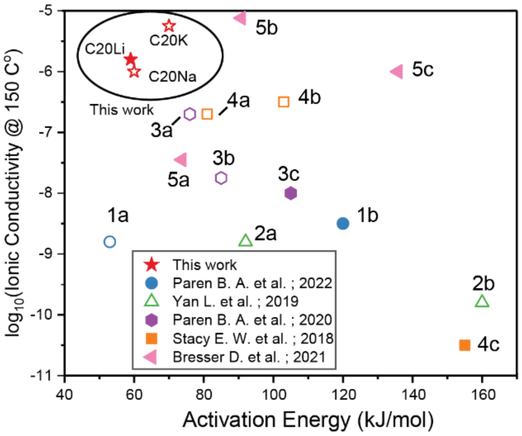

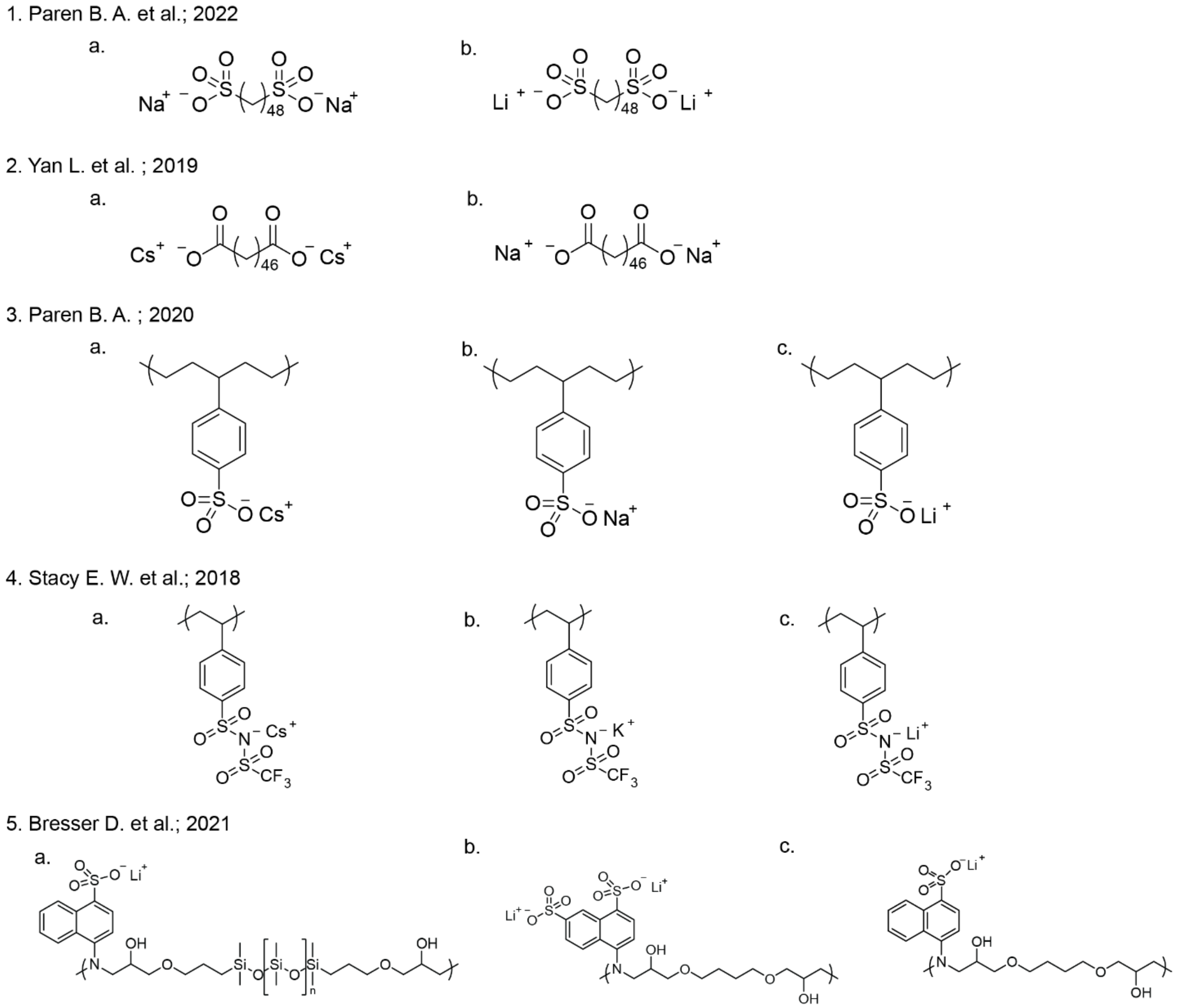

Figure 8-22 Chemical structures for each data point referenced in Figure 3-5, points are labeled on the graph above. Structures and values from references [69–71,73,74].

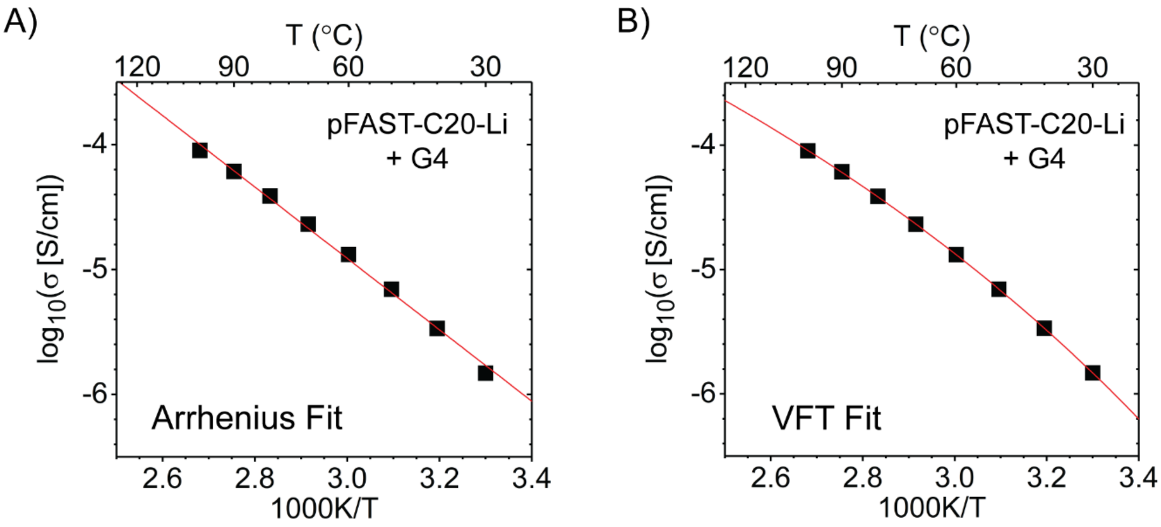

Figure 8-23: Variable temperature ionic conductivity of C20Li + G4 fit to both the Arrhenius equation (A) and the VFT equation (B). While both fits appear quite applicable, we do note that the VFT fit captures the slightly curved profile better. Fitted parameters are in the table below

Table 8-2: Fitted Arrhenius and VFT parameters for the C20Li + G4 system.

σ_0 (S/cm)	E_a (kJ/mol)	$R^2_{\text{Arrhenius}}$	A (S/cm)	B(1/K)	T_0 (K)	R^2_{VFT}
4.55E3	54.7	.99572	.26	1636	168	.99996

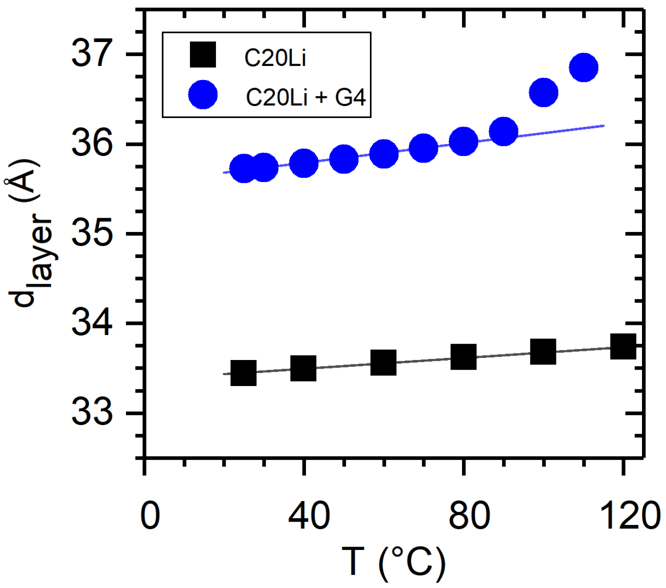

Figure 8-24 Layer spacings for C20Li and C20Li with tetraglyme(G4) added taken from the primary layer peak in variable temperature SAXS upon heating. Both samples increase in spacing slightly upon heating until ~100C where the sample with G4 starts to show a larger increase, the source of which is still unknown.

SECTION S2: CALCULATION OF THE MIGRATION BARRIER OF CATIONS IN THE **FAST** STRUCTURE.

Computational limitations associated with running the exact polymer structure led to the use of the **FAST-C** parent salt as a surrogate material system to better understand the ion conduction mechanism **pFAST-C20-M**. The choice of using the FAST-C structure for computations places the focus on the crystalline parent salt, thereby abstracting away the disorder at interfaces between domains of crystalline polymer. To study the migration barrier against the cation hop, we used nudged elastic band (NEB) calculations. Two possible hopping mechanisms were considered: 1) vacancy-mediated, and (2) concerted. For vacancy-mediated hop, some non-stoichiometry was needed to facilitate the ion hop, however, concerted hop could be examined using the exact stoichiometric structure for the calculations. A single vacancy was then introduced in the 132-atom unit cell, which had a nominal stoichiometry of $M_4C_{48}H_8F_{40}N_4O_{20}S_8$ ($M=Li^+$, Na^+, K^+, Cs^+), and NEB calculations driven by density functional theory (DFT) were performed to assess the energy barriers for ion hopping in the parent salt crystal. Figure 8-25 and Table 8-3 demonstrate that the energy barriers calculated by NEB for Li^+ and Na^+ are approximately 0.7 eV (68 kJ/mol), in good agreement with the experimentally determined migration barriers of 60-70 kJ/mol. However, for K^+, the difference between the computational and experimental migration barriers is more significant. This could be attributed to the fact that the computational investigation of K^+ hopping in the FAST-C lattice is based on experimentally relaxed relative equilibrium atomic positions obtained for Na^+ structure, which may not reflect the actual relative atomic positions in the K^+ structure. Thus, the migration barrier experimentally measured for K^+ hopping in the FAST structure might have been evaluated for a different structure than that of Na^+. In the case of Cs^+, the comparison of computationally obtained migration barriers is challenging because the Arrhenius behavior was absent in the temperature-dependent diffusivity measurement of the Cs^+ structure. This complicates the extraction of the familiar Arrhenius-based migration barrier from the experiment. It should be mentioned that for creation of vacancies, the effect of charge compensation should also be considered in the calculations. We tested charge-compensated and non-charge-compensated simulation boxes in our calculations and the difference in the obtained migration barriers based on these methods were only on the order of meV, which shows that the effect of charge compensation in these calculations is negligible.

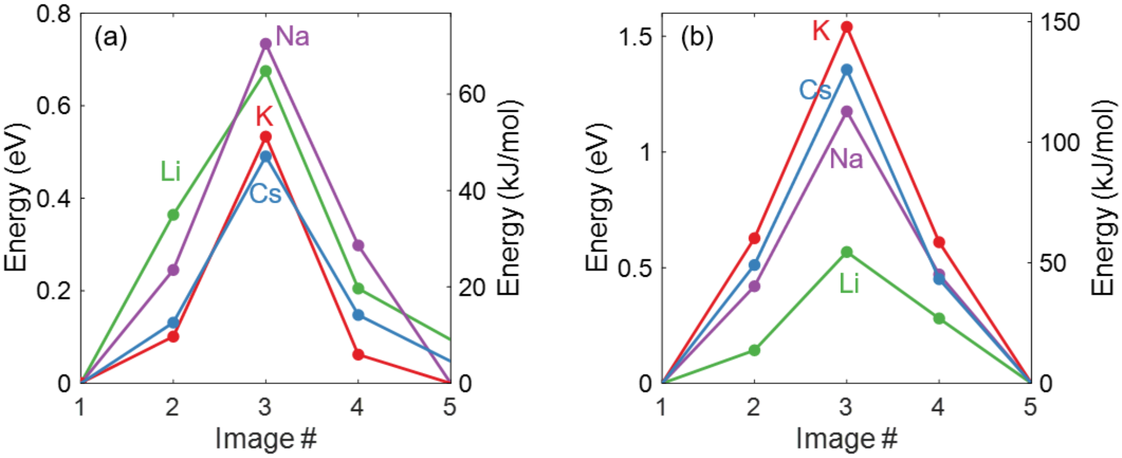

Figure 8-25 Energy landscape along the reaction coordinate expressed as image number (#) for a) vacancy-mediated and b) concerted hopping mechanisms for the four cations investigated in this study simulated with the presence of water in the simulation box.

One possible hypothesis to explain the migration barrier for hopping cations in the FAST-C lattice is that the coordination number of the cation at the hopping origin and its change at the transition state could be correlated with the barrier. However, our analysis did not reveal a clear correlation between changes in the coordination number of cations and the migration barrier against their hop in the FAST-C lattice. Instead, we propose that the general trend of decreasing computational migration barriers for vacancy-mediated hop of cations in the FAST-C lattice (as shown in Table S1) could be explained by considering two factors. Firstly, the polarizability of the elements generally decreases down the Alkaline-metal-earth column,[154] which softens the interaction of the hopping core with surrounding atoms in the lattice, particularly for atoms such as K^+ with higher polarizability. Secondly, as observed from Table S2, the computationally obtained relaxed structures for different FAST-C structures expand by transitioning from Li^+ to Cs^+. This leads to a higher volume (available space) for the cation in the larger lattice to hop, resulting in a smaller migration barrier,[155] compared to the cation that has access to less available volume because of the smaller lattice.

One possible factor that could affect the trend in the calculated migration barriers for different cation hops in the FAST-C lattice is the presence of water molecules in the simulation cell. Water molecules could potentially interact strongly with the hopping cation and play a significant role in determining the migration barrier. To investigate this hypothesis, we conducted NEB calculations for a simulation cell without any water molecules present. However, due to convergence difficulties, we were only able to obtain migration barriers for the Li^+ and Na^+ hops in the FAST-C lattice without water content. Interestingly, the migration barriers for Li^+ and Na^+ in the FAST-C lattice without water were only slightly different from the ones obtained for the FAST-C lattice with water content ($MB_{Li+\ with\ water}$ = 0.68 eV, $MB_{Li+\ without\ water}$ = 0.65 eV, $MB_{Na+\ with\ water}$ = 0.73 eV, and $MB_{Na+\ without\ water}$ = 0.71 eV). These results suggest that the influence of water molecules on determining the migration barriers for cation hops in the FAST-C lattice is minimal.

In addition to the vacancy-mediated calculated migration barriers, shown in Figure S24(a), we also calculated the migration barriers for the cation hop in the FAST-C structures using the concerted hop mechanism, which does not need the presence of any vacancies. As shown in Figure S24(b) and Table S1, the migration barrier for the hop of Na^+, K^+, and Cs^+ is significantly higher than those for vacancy-mediated hops. For Na^+, the smallest difference is observed where the migration barrier for the concerted hop is 0.44 eV larger than that for the vacancy-mediated hop. Interestingly, for Li^+ hop in the FAST-C structure, both the vacancy-mediated and concerted hops exhibit similar migration barriers of 0.68 eV and 0.57 eV, respectively. This suggests that both hopping mechanisms may be present for the Li^+ hop in the FAST-C structure.

Table 8-3 Migration barrier values against the hop of different cations in the FAST-C lattice following vacancy-mediated and concerted hopping mechanisms.

	Vacancy-mediated		**concerted**	
	MB (eV)	**MB (kJ/mol)**	**MB (eV)**	**MB (kJ/mol)**
Li^+	0.68	64.80	0.57	54.52
Na^+	0.73	70.45	1.18	112.85
K^+	0.53	51.18	1.54	147.91
Cs^+	0.49	47.09	1.36	130.17

Table 8-4 Optimized lattice parameters for the parent salt in FAST-C structure using the prescribed relaxation strategy described in the methods section. The FAST-C parent salt crystal structure containing Na⁺ ions was resolved using small-angle X-ray scattering and served as the starting point for the geometry/structure optimization for all cations investigated in this study.

Stoichiometry	**Cation**	**a (Å)**	**b (Å)**	**c (Å)**	**α**	**β**	**γ**	**Unit cell volume (Å^3)**
$C_{48}H_8F_{40}Li_{4-x}N_4O_{20}S_8$	Li$^+$ (one vacancy in unit cell)	7.47381	12.71974	18.18681	110.47°	98.71°	90.00°	1598.48
$C_{48}H_8F_{40}N_4Na_{4-x}O_{20}S_8$	Na$^+$ (one vacancy in unit cell)	7.69119	12.51638	17.96867	110.34°	94.08°	90.00°	1616.80
$C_{48}H_8F_{40}K_{4-x}N_4O_{20}S_8$	K$^+$ (one vacancy in unit cell)	8.16325	12.40611	18.38356	109.72°	93.30°	90.00°	1749.31
$C_{48}Cs_{4-x}H_8F_{40}N_4O_{20}S_8$	Cs$^+$ (one vacancy in unit cell)	8.83172	11.95595	18.75061	109.07°	92.94°	89.82°	1868.57

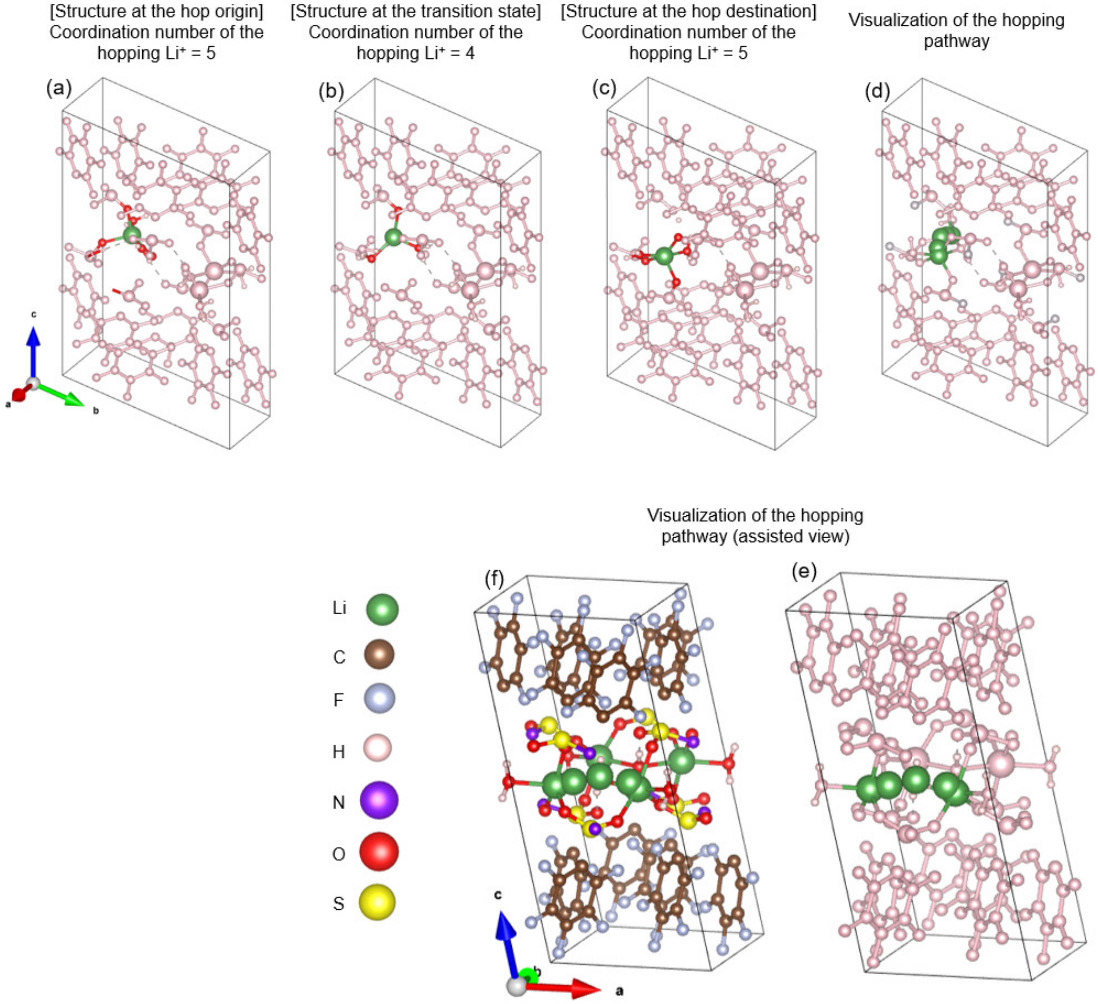

Figure 8-26 Representation of the Li+ hop in the lattice. Coordination number of the hopping Li$^+$ is shown at a) the hop origin, b) the transition state, and c) the hop destination. In panels a), (b), and c) all atoms are greyed out except the hopping Li$^+$ and its first nearest neighbors for better visualization. Visualization of the hopping Li$^+$ along its hopping pathway is also shown in panel d), with assisted views in panels e) and f), which is the colored version of panel e).

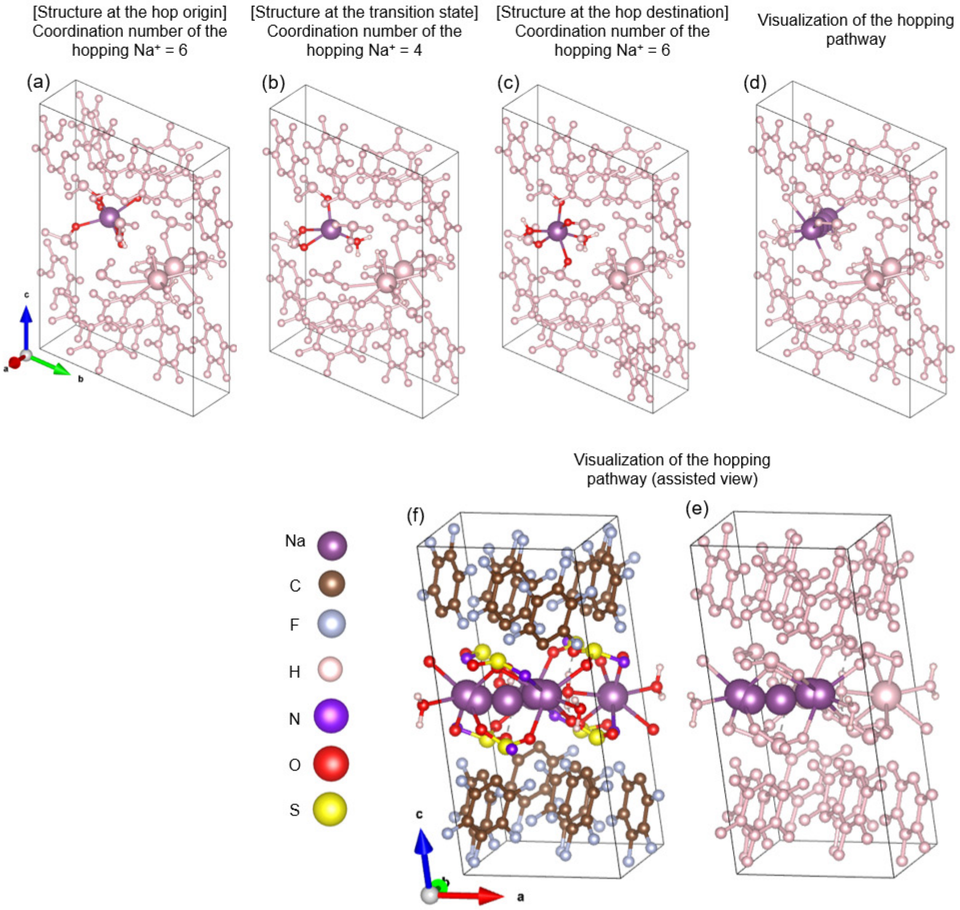

Figure 8-27 Representation of the Na+ hop in the lattice. Coordination number of the hopping Na^+ is shown at a) the hop origin, b) the transition state, and c) the hop destination. In panels a), b), and c) all atoms are greyed out except the hopping Na^+ and its first nearest neighbors for better visualization. Visualization of the hopping Na^+ along its hopping pathway is also shown in panel d), with assisted views in panels e) and f), which is the colored version of panel e).

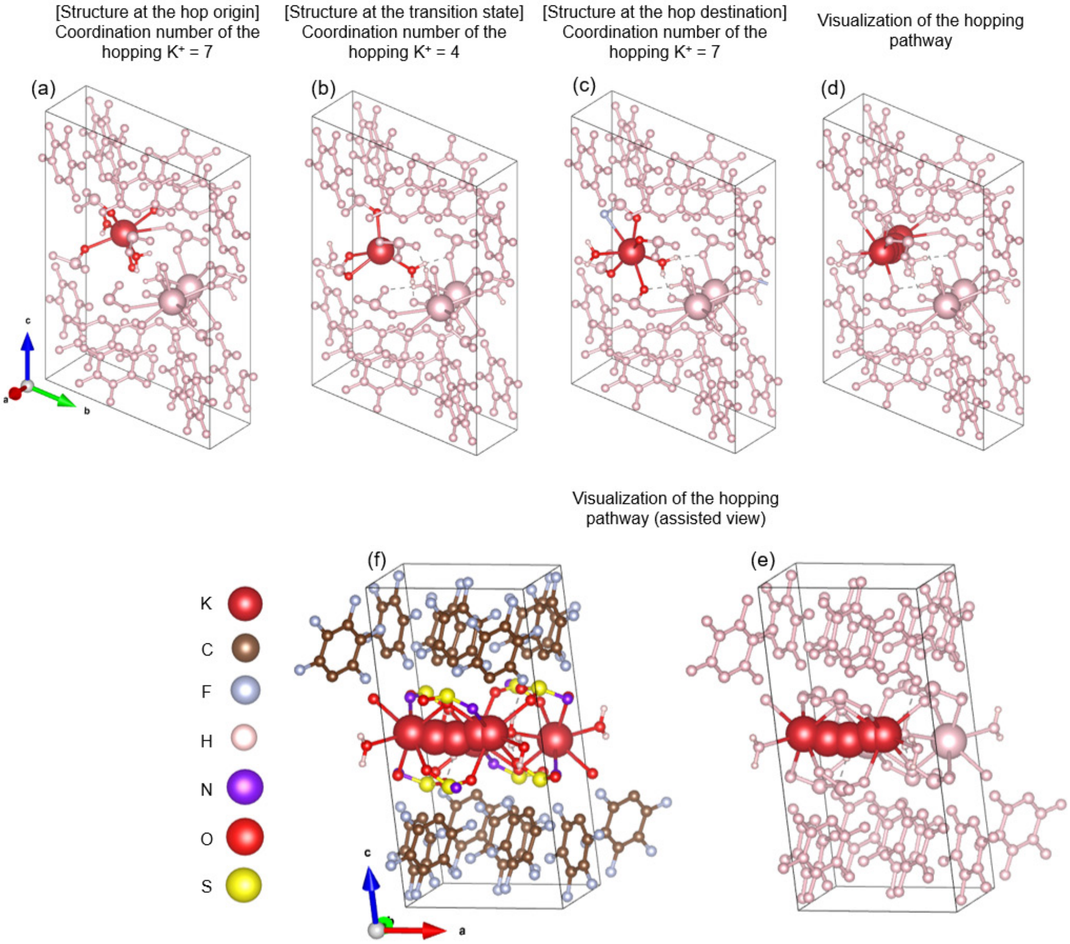

[Structure at the hop origin] Coordination number of the hopping K⁺ = 7

[Structure at the transition state] Coordination number of the hopping K⁺ = 4

[Structure at the hop destination] Coordination number of the hopping K⁺ = 7

Visualization of the hopping pathway

Visualization of the hopping pathway (assisted view)

Figure 8-28 Representation of the K+ hop in the lattice. Coordination number of the hopping K⁺ is shown at a) the hop origin, b) the transition state, and c) the hop destination. In panels a), b), and c) all atoms are greyed out except the hopping K⁺ and its first nearest neighbors for better visualization. Visualization of the hopping K⁺ along its hopping pathway is also shown in panel d), with assisted views in panels e) and f), which is the colored version of panel e).

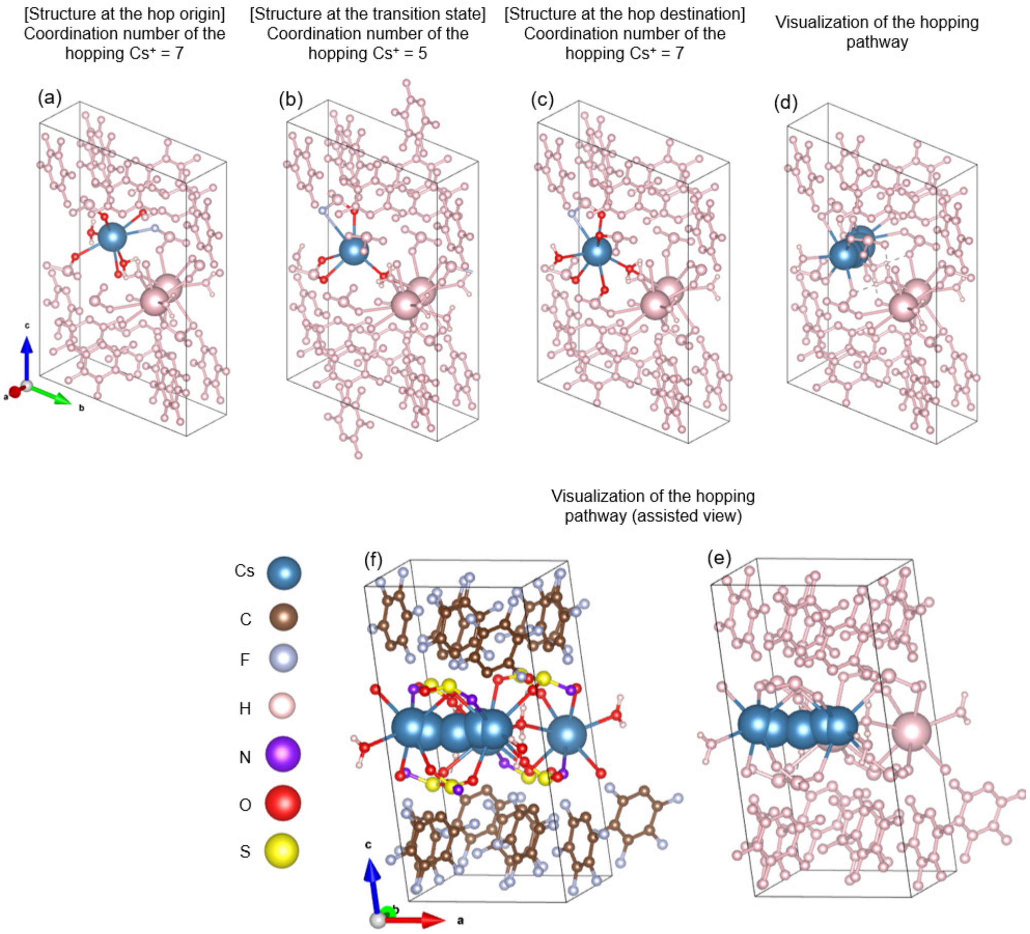

Figure 8-29 Representation of the Cs+ hop in the lattice. Coordination number of the hopping Cs$^+$ is shown at a) the hop origin, b) the transition state, and c) the hop destination. In panels a), b), and c) all atoms are greyed out except the hopping Cs$^+$ and its first nearest neighbors for better visualization. Visualization of the hopping Cs$^+$ along its hopping pathway is also shown in panel d), with assisted views in panels e) and f), which is the colored version of panel e).

SECTION S3: SYNTHETIC METHODS

SYNTHESIS OF **FAST-C**

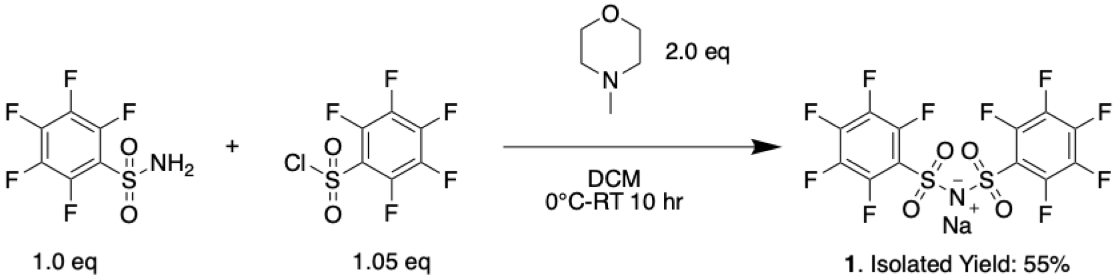

To a 250 mL round bottom flask, 1.47 g (5.6 mmol, 1 eq) pentafluorobenzene sulfonamide and 1.3 mL (11.2 mmol, 2 eq) *N*-methylmorpholine were dissolved in ~35 mL of DCM which was taken from a solvent distillation system. The mixture was cooled to 0 °C and stirred with a magnetic stir bar. A solution of 1.6 g (5.8 mmol, 1.05 eq) 2,3,4,5,6-pentafluorobenzene sulfonyl chloride was in 7.5 mL DCM was added dropwise into the flask. The reaction was warmed to room temperature overnight for a total reaction time of 18 h. DCM was then removed under vacuum and the residue was dissolved in ~100 mL of ethyl acetate. The organics were washed with 100 mL of 1M HCl followed by two washes with ~ 100 mL of a saturated NaCl solution. The organic layer was dried over sodium sulfate and ethyl acetate was removed under vacuum to yield a chunky off-white solid salt. The salt was then redissolved in minimal acetone ~ 1g/mL and 10 equivalents (v/v) of cold DCM were added to the flask to precipitate out a powder. The resultant mixture was then filtered on a frit and the solids were collected and dried under high vacuum overnight to give **FAST-C** in good yield (1.47 g, 50 %) and high purity.

^{19}F NMR (471 MHz, Acetone-d_6) δ -137.14 – -138.86 (m), -154.54 (ddd, *J* = 26.3, 21.0, 5.8 Hz), -164.86 (td, *J* = 27.7, 26.3, 10.9 Hz).

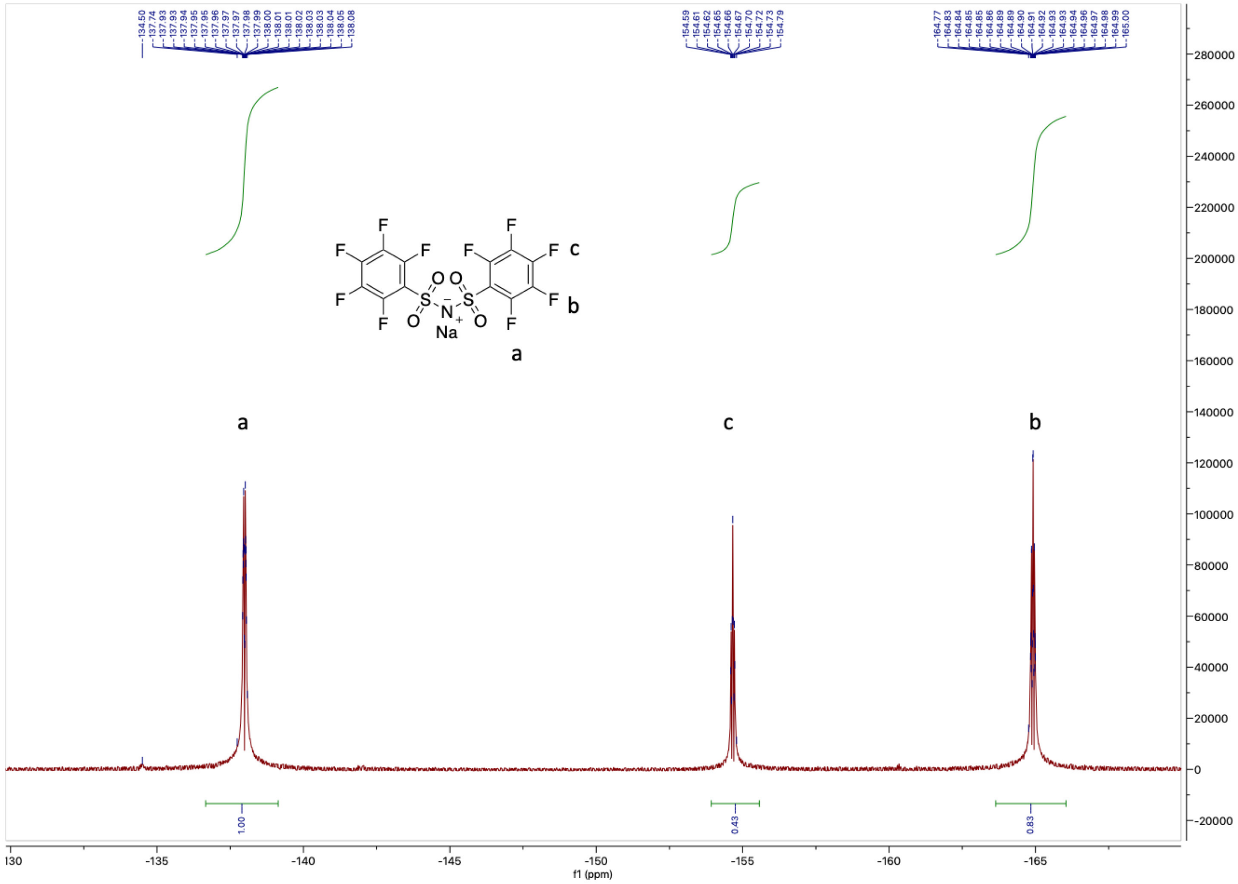

Figure 8-30 ^{19}F NMR of compound FAST-C

SYNTHESIS OF UNDEC-10-EN-1-YL 4-METHYLBENZENESULFONATE

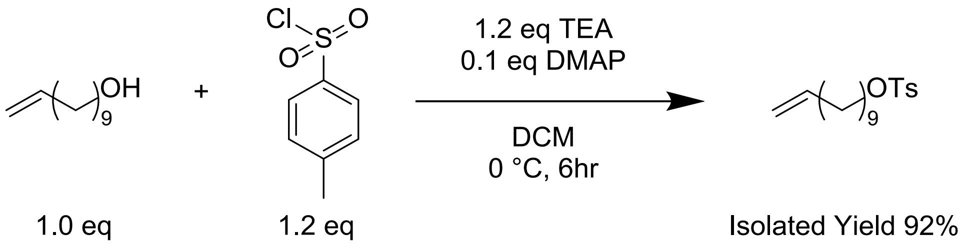

3.2 g (1.9 mmol, 1 eq) of undec-10-en-1-ol was measured into a 100 mL RBF and 37.6 mL or DCM were added to make a 0.5 M solution. The flask was cooled to 0 °C and then 3.2 mL (2.3 mmol, 1.2 eq) of triethylamine and 0.23 g (0.19 mmol, 0.1 eq) of 4-dimethylaminopyridine were added. In a separate vessel 4.30 g (0.023 mol, 1.2 eq) of 4-toluenesulfonyl chloride was dissolved in minimal DCM (~5 mL) using stirring and sonication to ensure solubility. This solution was then slowly added to the 100 mL RBF while maintaining stirring. The reaction was kept at 0 °C and monitored via thin layer chromatography. After six hours the reaction was quenched with the addition of 10 mL of 1M HCl solution before removal of DCM under vacuum. The residual was then redissolved in ethyl acetate (~100 mL) and washed once with 200 mL of 1M HCl solution and twice with 100 mL of a saturated sodium bicarbonate solution. The organic layer was collected and dried over sodium sulfate before the solvent was removed under vacuum to yield the product as a yellow tinted oil 5.9 g, 92% yield.

^{1}H NMR (400 MHz, Chloroform-*d*) δ 7.85 – 7.72 (m, 2H), 7.34 (d, *J* = 8.0 Hz, 2H), 5.80 (ddt, *J* = 16.9, 10.2, 6.7 Hz, 1H), 5.07 – 4.85 (m, 2H), 4.02 (t, *J* = 6.5 Hz, 2H), 2.44 (s, 3H), 2.03 (td, *J* = 7.6, 5.9 Hz, 2H), 1.72 – 1.53 (m, 2H), 1.46 – 1.01 (m, 14H). ^{13}C NMR (101 MHz, Chloroform-*d*) δ 144.64, 139.09, 133.24, 129.81, 127.85, 114.16, 70.70, 33.76, 29.30, 29.03, 28.87, 28.79, 25.30, 21.60.

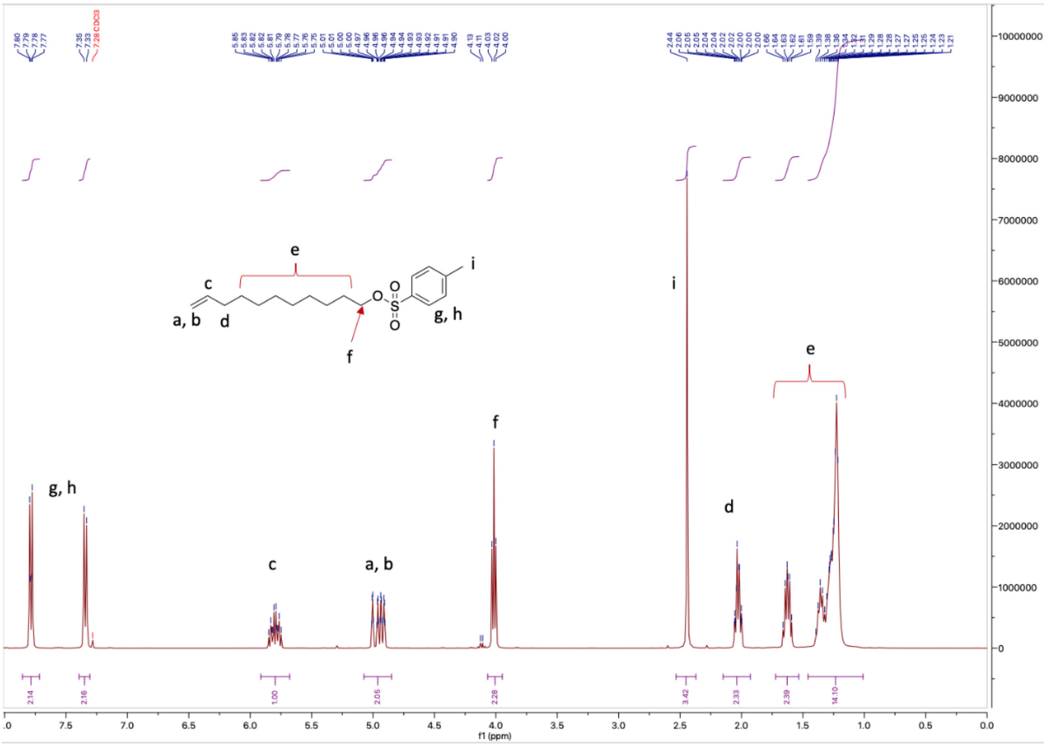

Figure 8-31 ^{1}H NMR of product undec-10-en-1-yl 4-methylbenzenesulfonate collected in CDCl$_3$

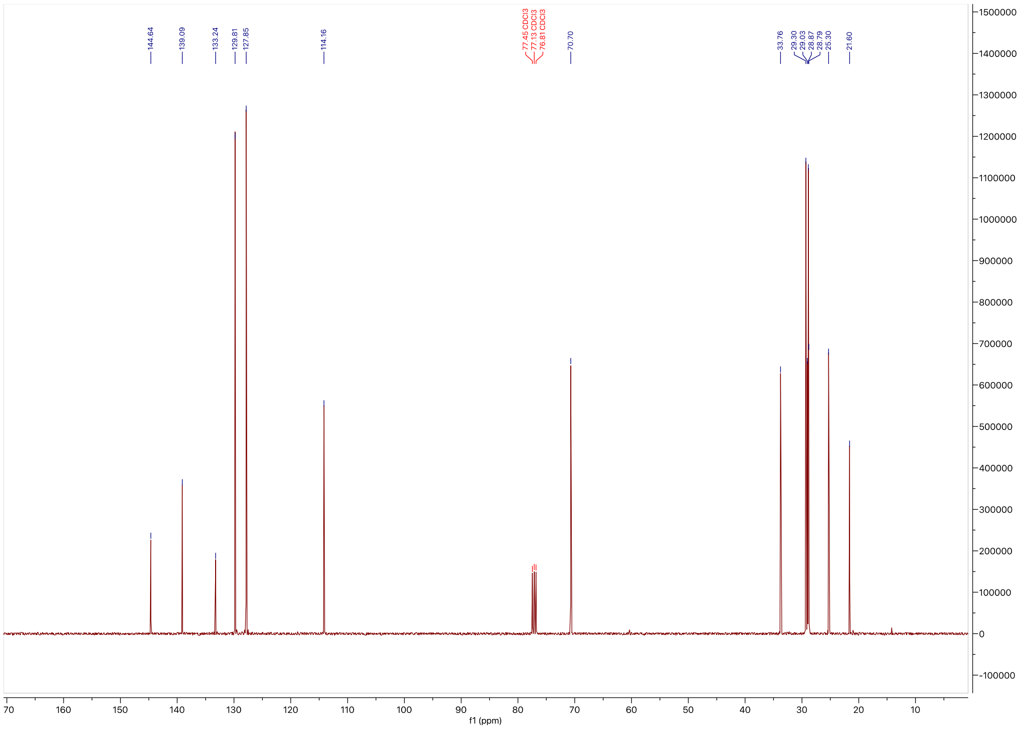

Figure 8-32 ^{13}C NMR of product undec-10-en-1-yl 4-methylbenzenesulfonate collected in CDCl$_3$

SYNTHESIS OF UNDEC-10-ENE-1-THIOL

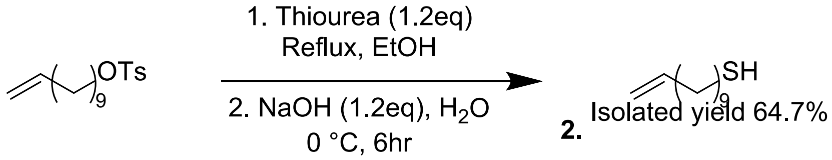

To a 250mL RBF 5.8g (1.8mmol, 1eq) of undec-10-en-1-yl 4-methylbenzenesulfonate was added. The oil was dissolved in ~100mL of 200 proof ethanol and equipped with a magnetic stirring bar. To this, 2.0 g (2.6 mmol, 1.5 eq) thiourea was added. The RBF was then equipped with a reflux condenser and then heated until reflux at 80 °C. The reaction was monitored via TLC, taking about 8 hours to reach completion.

The reaction was allowed to cool to room temperature and was then cooled to 0 °C. 0.86 g (2.1 mmol, 1.2 eq) of sodium hydroxide dissolved in 8 mL of water were added slowly causing a yellowish-white precipitate to form in the solution. The authors note that this step must be done cooled to avoid auto-oligomerization likely via thiol-ene reactions. The reaction was then allowed to stir for another 3 hours at 0 °C. 1M HCl was added dropwise to bring the pH to ~8 after which a majority of the ethanol was removed via evaporation under reduced pressure. To extract, 100 mL of ethyl acetate were added and the remaining water was drained. The organic layer was washed with one wash of saturated bicarbonate solution and one wash of water. The organic layer was collected, dried over sodium sulfate and solvent was evaporated to yield a yellowish oil. The product oil was run through a silica plug using hexanes as the eluent to purify. **Undec-10-ene-1-thiol** was obtained as a clear oil in good yield ~64.7%. It was found that this product tends to oxidize if left in air, often resulting in the oil turning cloudy, lowering the yield of subsequent reactions. To avoid this, any **undec-10-ene-1-thiol** synthesized was used directly in the next reactions, or if stored was done so as a dilute solution in DCM at -20°C under N_2. If being stored for a long time, 1.1 equivalents of dithiothreitol (DTT) were added as a reducing agent. This can be removed before further reactions using a silica plug with hexanes as the eluent.

^{1}H NMR (400 MHz, Chloroform-*d*) δ 5.83 (ddt, J = 16.9, 10.2, 6.7 Hz, 1H), 5.09 – 4.86 (m, 2H), 2.54 (q, J = 7.4 Hz, 2H), 2.06 (q, J = 7.1 Hz, 2H), 1.62 (p, J = 7.3 Hz, 2H), 1.50 – 1.19 (m, 15H). ^{13}C NMR (101 MHz, Chloroform-d) δ 139.17, 114.13, 34.06, 33.81, 29.46, 29.42, 29.11, 29.07, 28.93, 28.38, 24.65.

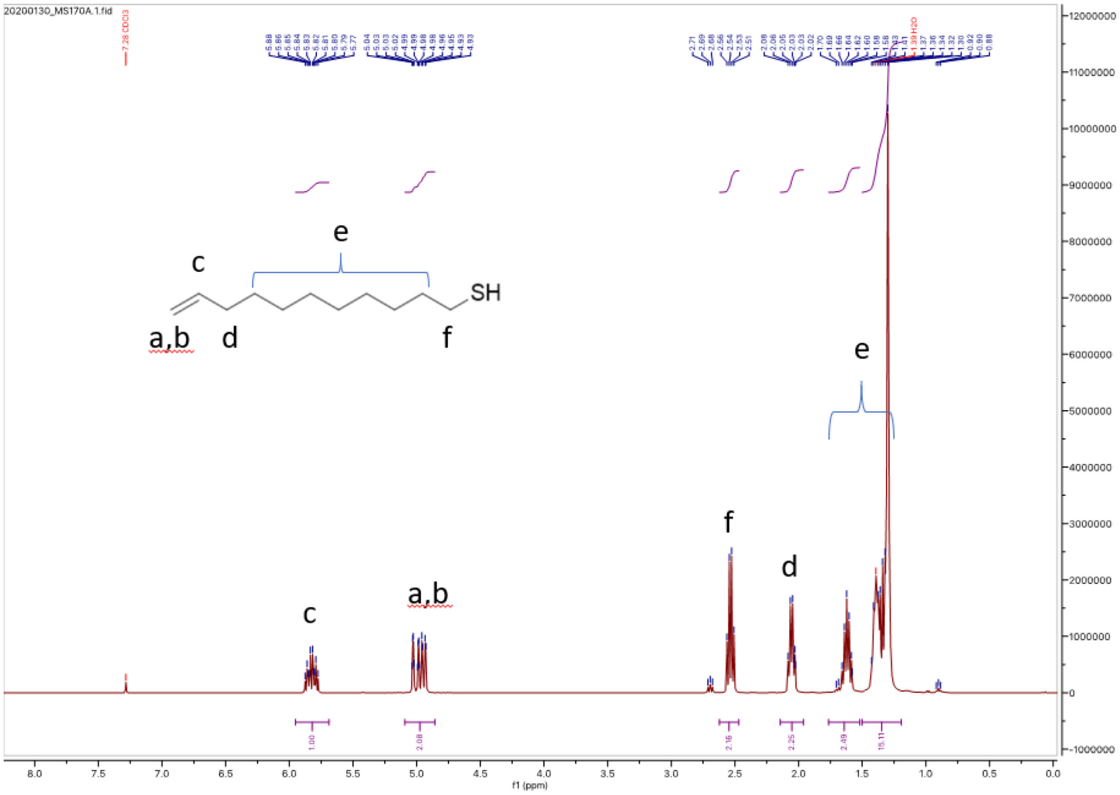

Figure 8-33 ^{1}*H NMR of 10-undecen-1-thiol*

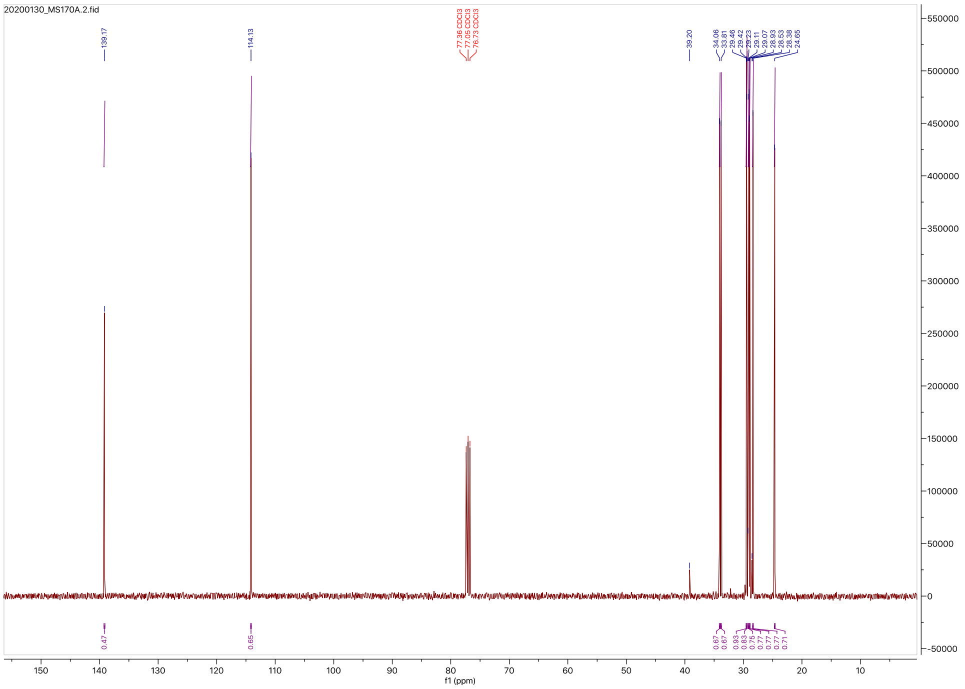

Figure 8-34 ^{13}*C NMR of 10-undecen-1-thiol*

SYNTHESIS OF **FAST-C20**

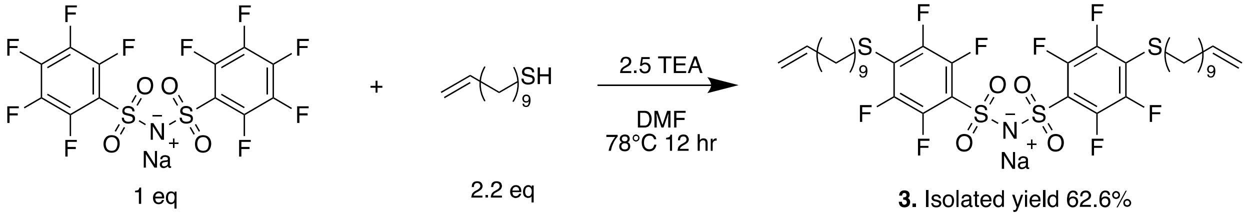

To a 100 mL Schlenk flask 1.26 g (2.5mmol, 1eq) of **FAST-C** were added and dissolved in 74 mL of DMF. The solution was stirred and sparged with N_2 for greater than 30 minutes. After this initial sparging, 1.04 g (5.5mmol, 2.2 eq) of **10-undecen-1-thiol** were added and the solution was sparged for an additional 5 minutes. Then 1.40 mL (10mmol, 4 eq) of triethylamine was added and the reaction vessel was sealed. The vessel was lowered into a 75°C oil bath and reaction was monitored via fluorine NMR. Once the reaction was no longer progressing (~24 hours) the DMF was removed via evaporation under reduced pressure. The residue was dissolved in ethyl acetate and washed with a 1M HCl solution followed by a wash with saturated sodium bicarbonate solution. The organics were collected, dried over sodium sulfate, and the solvent was evaporated to yield 2.03g of crude material. The crude material was run through a silica column with a gradient of hexanes and acetone (v/v). The excess thiol is removed by a steep gradient to 15% acetone over 2 column volumes, and then the gradient is slowed to selectively elute the desired product, going from 15 to 25% acetone over 10 column volumes. A slow separation was found to remove any trace amounts of mono-substituted products that may be present in the crude reaction mixture (Figure S35). Removal of these was found to be crucial to obtaining high degrees of polymerization in the subsequent step. The fractions were combined, solvent was evaporated, and the product was dried under high vacuum to give 1.29g of **FAST-C20**, a 62.6% yield. The product is a white waxy solid. ^{1}H NMR (400 MHz, Acetone-d6) δ 5.82 (ddt, J = 17.0, 10.3, 6.7 Hz, 1H), 5.13 – 4.79 (m, 2H), 3.08 (t, J = 7.3 Hz, 2H), 1.77 – 1.25 (m, 15H). 19F NMR (376 MHz, Acetone-d6) δ -136.17 – -136.84 (m), -138.01 – -138.77 (m).

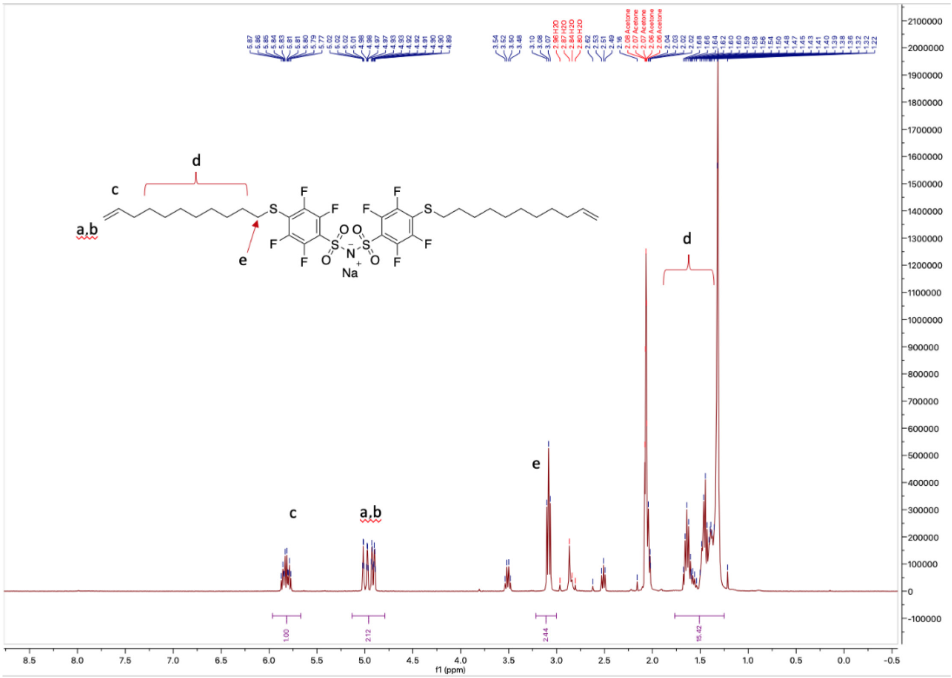

Figure 8-35 ^{1}H NMR of FAST-C20

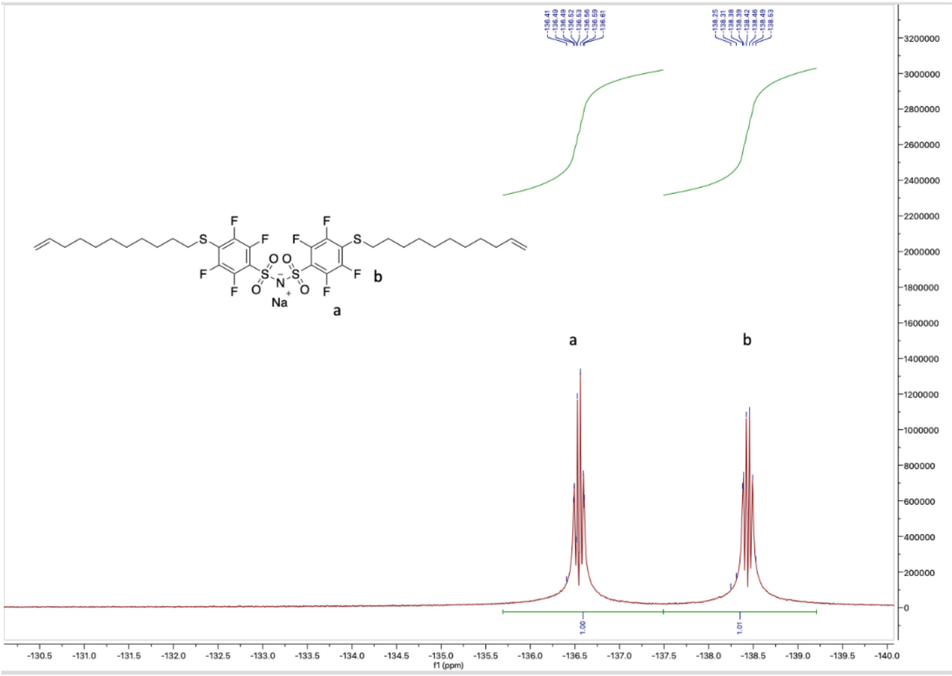

Figure 8-36 ^{19}F NMR of FAST-C20

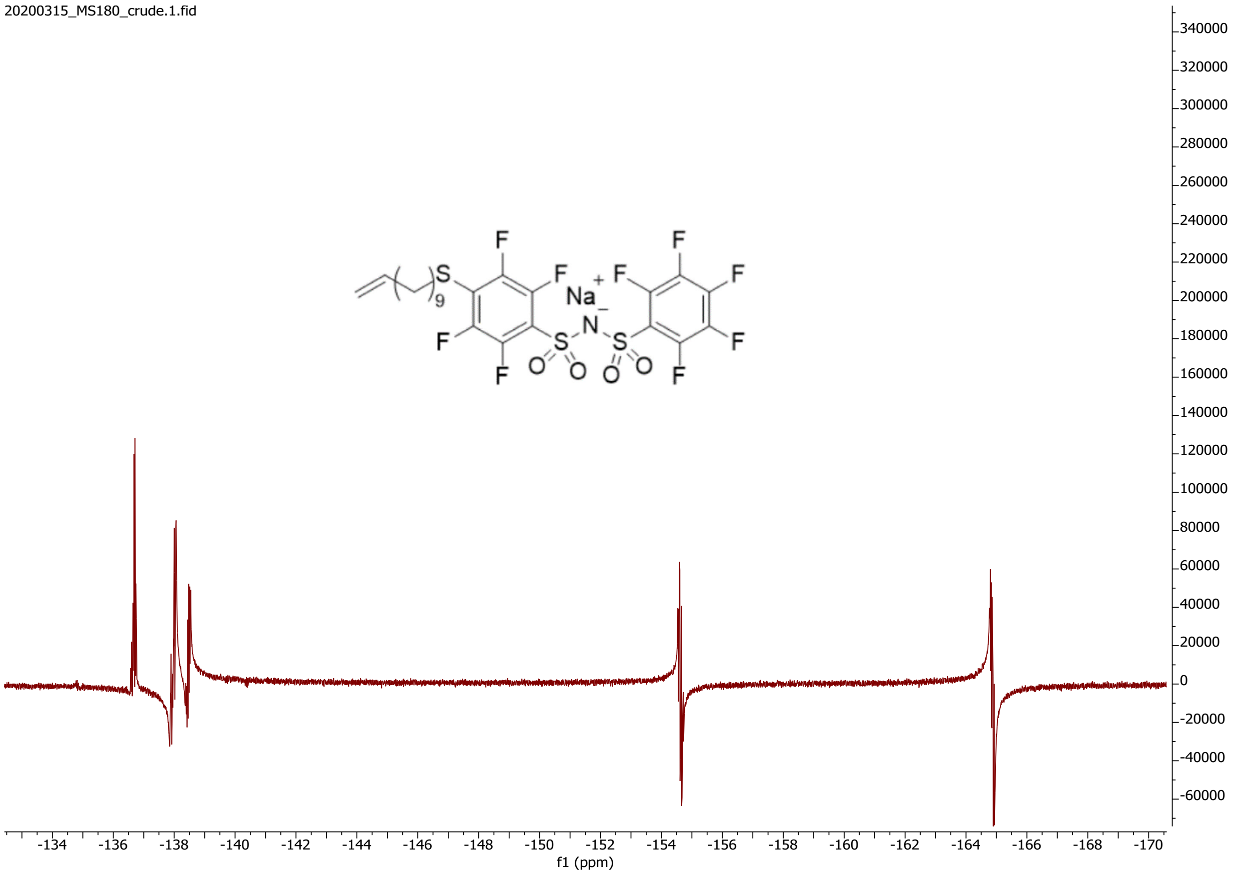

Figure 8-37 ^{19}F NMR spectra of the monofunctional product. The presence of 5 unique resonances are due to the 5 unique fluorine atoms present when FAST-C is monofunctionalized.

ADMET POLYMERIZATION OF **FAST-C20**

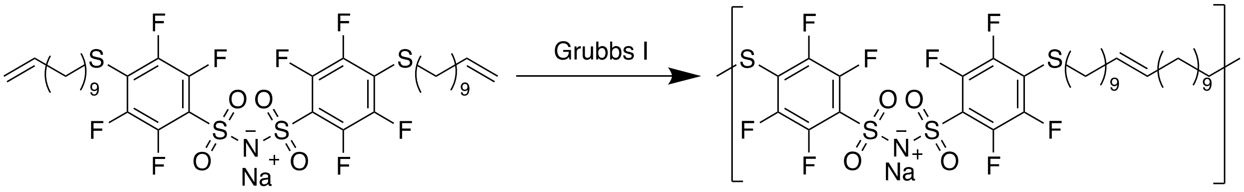

1.75 g (2.12 mmol) of **3** were dissolved in 35mL propylene carbonate and added into a 100mL Schlenk flask equipped with a magnetic stir bar. The solution was then subjected to three freeze pump thaw cycles. The solution was then frozen once more, and 17.3 mg (1 mol%) of Grubbs first generation catalyst was added. The flask was lowered into an oil bath at 45°C and vacuum of ~ 800 mtorr was applied. The reaction was allowed to run up to 3 days and the conversion was monitored by NMR. Once the polymerization was no longer progressing the solution was exposed to air. The polymer was precipitated into cold diethyl ether and the solids were collected to yield an off white powder. To further remove all residual propylene carbonate solvent, the polymer solids were heating in a vacuum oven at 180 °C overnight at which point the solids were slightly discolored. No decomposition was observed by NMR.

During optimization of this polymerization method it was found that the final degree of polymerization reached was strongly dependent on the procedure used. Interestingly, it was found that the presence of water in the propylene carbonate solvent actually aided polymerization. When solvent that had previously been dried over 3Å molecular sieves to remove water was used, only low degrees of polymerization (N_n<20) were obtained. However, using propylene carbonate which had been exposed to atmosphere and likely contained water yielded more consistently high degrees of polymerization (N_n >100). We hypothesize that the presence of water helps to solvate the growing chains and allow for higher degrees of polymerization to be reached. Careful studies in which precise amounts of water are intentionally added could be done to support this hypothesis.

1H NMR (400 MHz, Acetone-d6) δ 5.39 (dt, J = 24.2, 4.5 Hz, 0H), 3.09 (t, J = 7.3 Hz, 1H), 2.10 (s, 6H), 1.99 (s, 1H), 1.64 (p, J = 7.4 Hz, 1H), 1.32 (s, 4H). 19F NMR (376 MHz, Acetone-d6) δ -136.54 (dq, J = 19.7, 9.7, 7.5 Hz), -138.45 (dd, J = 25.9, 13.1 Hz)

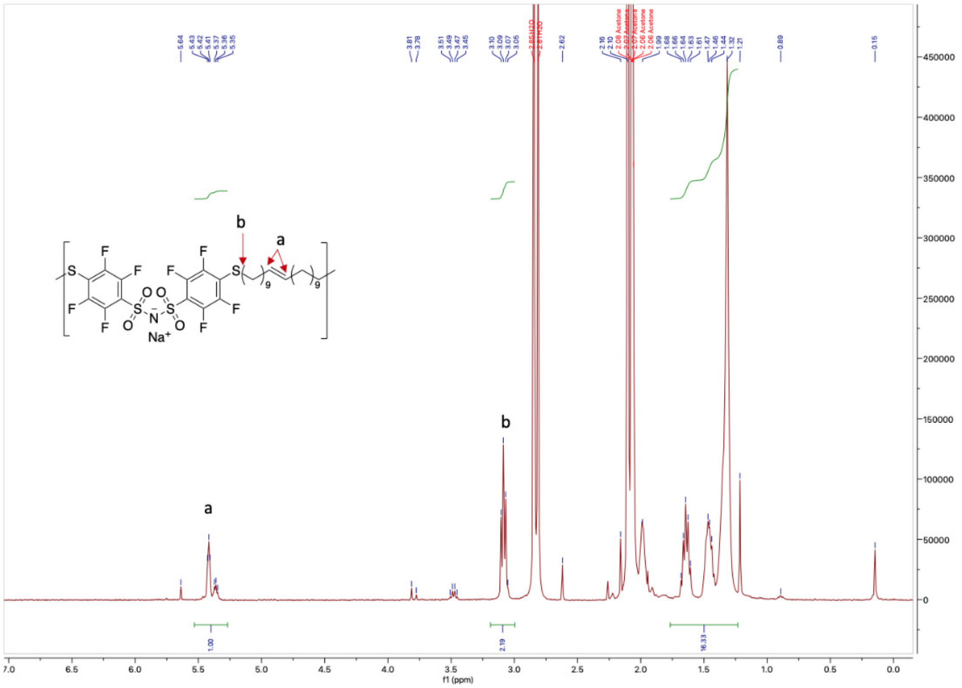

Figure 8-38 ^{1}H NMR of pFASTC20-Na

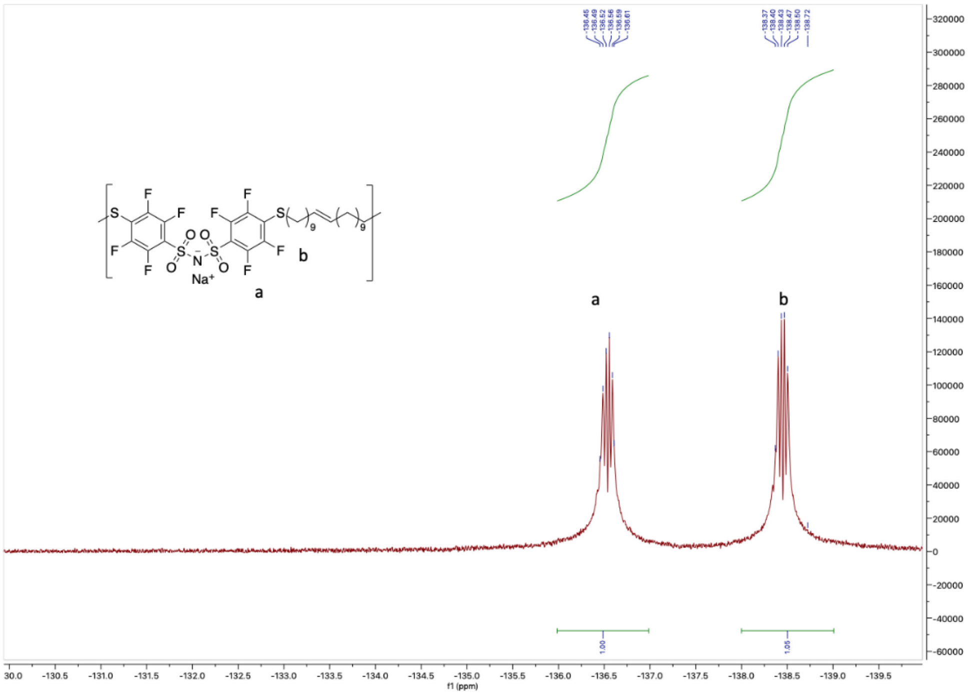

Figure 8-39 ^{19}F NMR of pFASTC20-Na

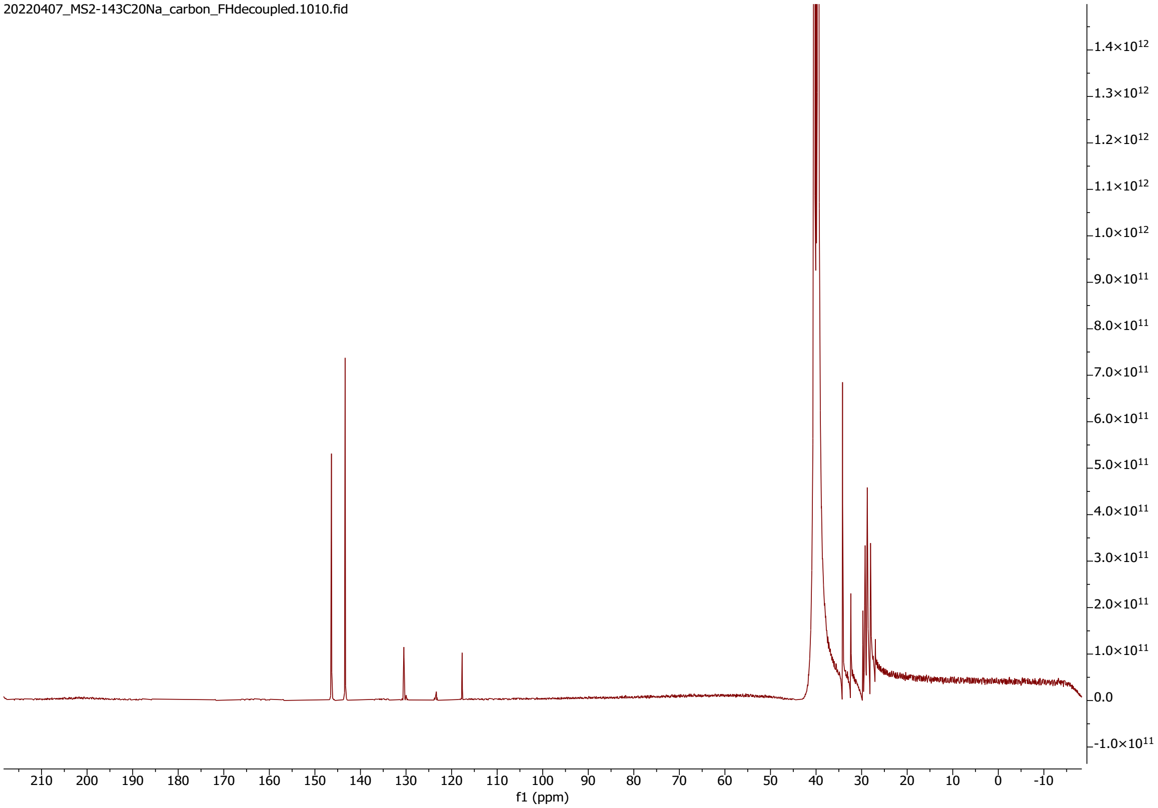

Figure 8-40 ^{13}C NMR of pFASTC20-Na Conducted in DMSO-d$_6$. Large peak at ~ 39ppm is due to the NMR solvent.

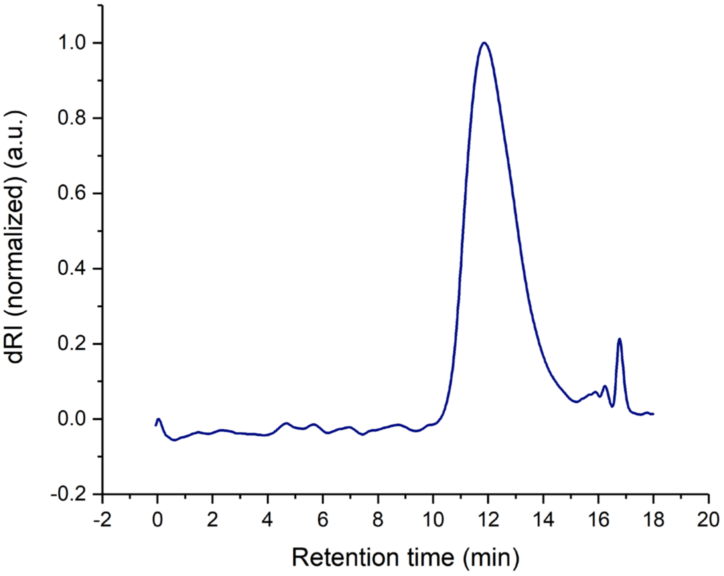

Figure 8-41 Size exclusion chromatography (SEC) trace of pFASTC20-Na which was found to have a dispersity of 1.97.

CHAPTER 9 APPENDIX B: SUPPLEMENTAL ROBOT FIGURES AND DATA

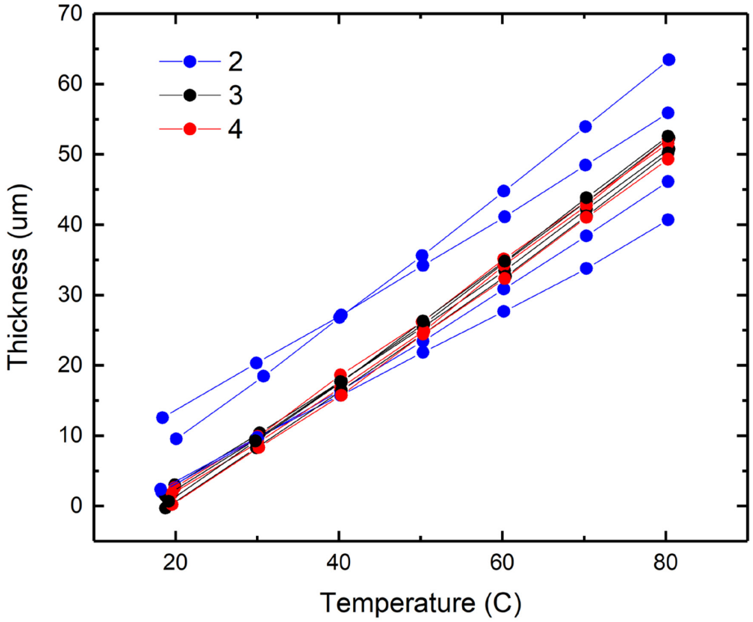

Figure 9-1 Thickness measurements applied to empty cells before variable temperature compensation system was devised showing the increase in measured thickness due to thermal expansion. 2,3,4 refer to the twistlocks upon which each measurement was made.

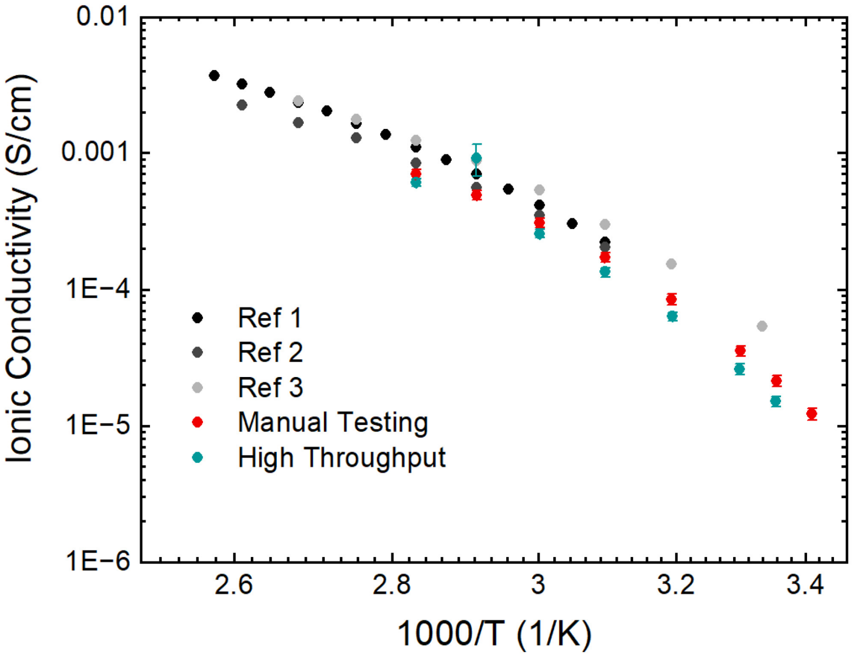

Figure 9-2 Benchmarking comparison of data produced by the HT tool to manual testing and literature references. The data shown here are all for 45 wt % LiTFSI in PEO. Ref1[156] , Ref 2[157], Ref 3[158]

Table 9-1 Conversion of concentrations between molality, mol(EO) repeat units: mol cations (which will be the same for all salts), and weight percent of salt (in the total dried film) for LiTFSI.

Molality (mol/kg Polymer)	Mol EO: Mol Cation	Wt % of salt (for LiTFSI)
0.2	113 : 1	5.4
0.75	30 :1	17.7
1.5	15 : 1	30.09
2.25	10 : 1	39.4
3.0	7.5 : 1	46.27
3.75	6.0 : 1	51.84
4.75	4.8 : 1	57.7
5.75	4.0 : 1	62.3
7.0	3.2 :1	66.78

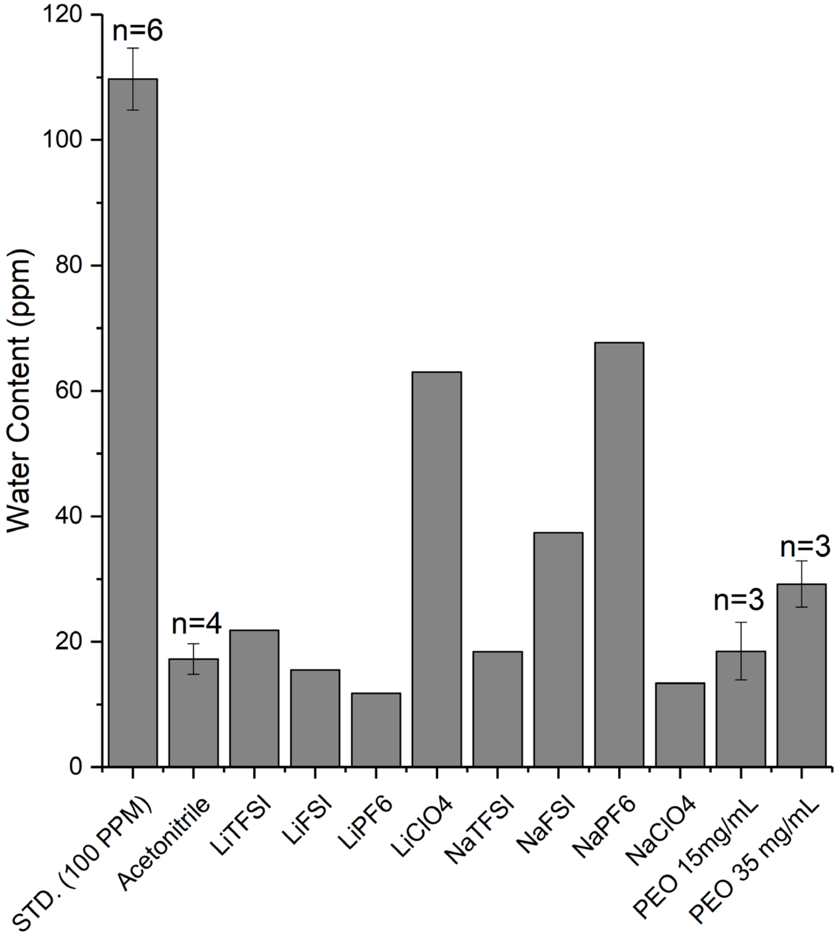

Figure 9-3 Water content measurements of materials used on the high throughput tool. All measurements were made using Karl-Fischer titration. Measurement of a 100 ppm water standard showed that our instrument slightly overmeasures the water content by about 10 ppm. All salts were dissolved in acetonitrile at a 50mg/mL concentration in the glovebox. Around 1.5mL of solution was used for each test. Note that $LiPF_6$ and $NaPF_6$ were used as received and not dried given their known thermal instability.

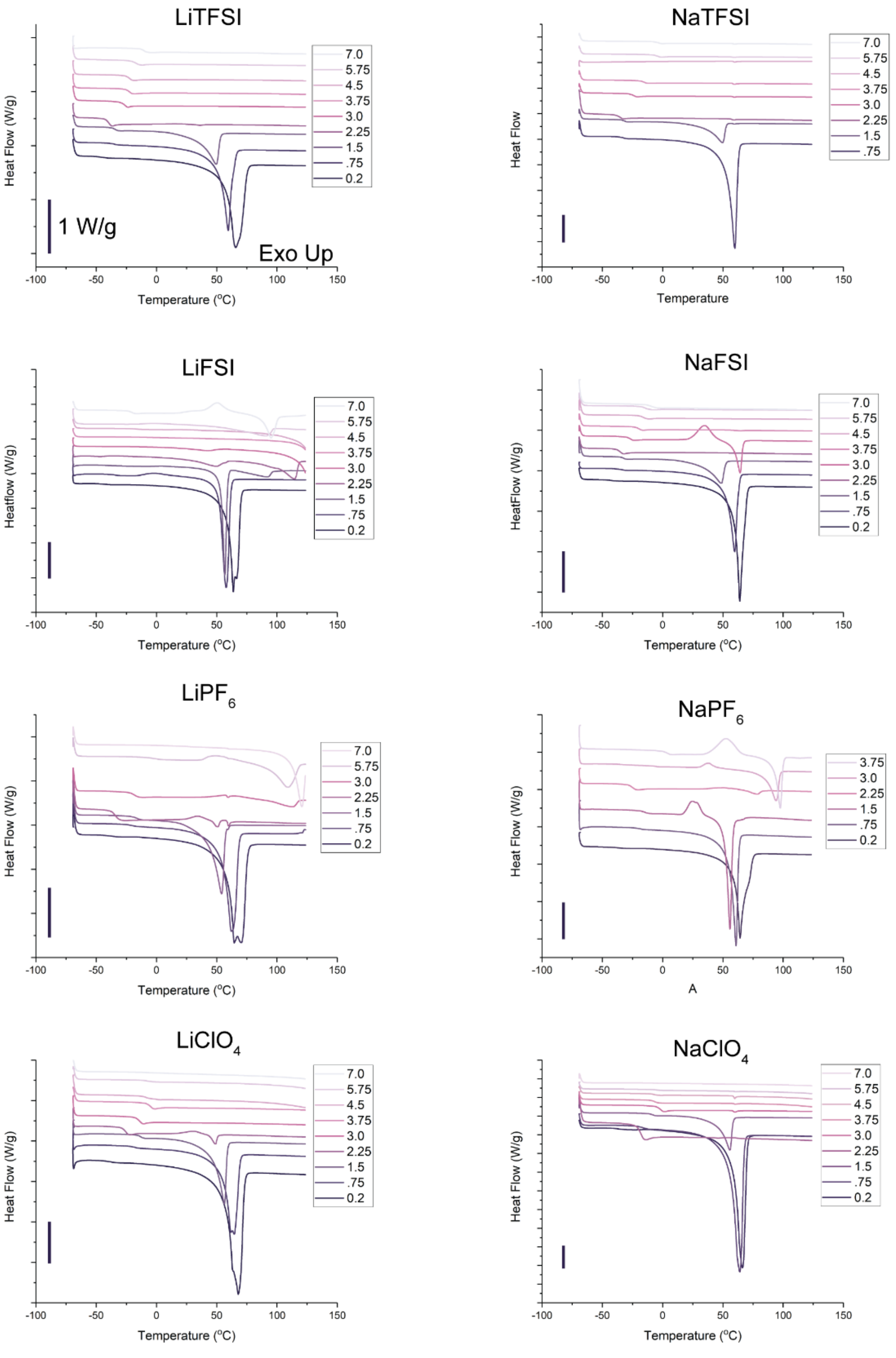

Figure 9-4 DSC heating traces for all salts in PEO. All traces are taken from the second heating cycle and plotted Exothermic Up. The bar on each graph denotes a heatflow of 1 W/g as the traces are offset for clarity. Concentration of each salt is given in the legend in molality.

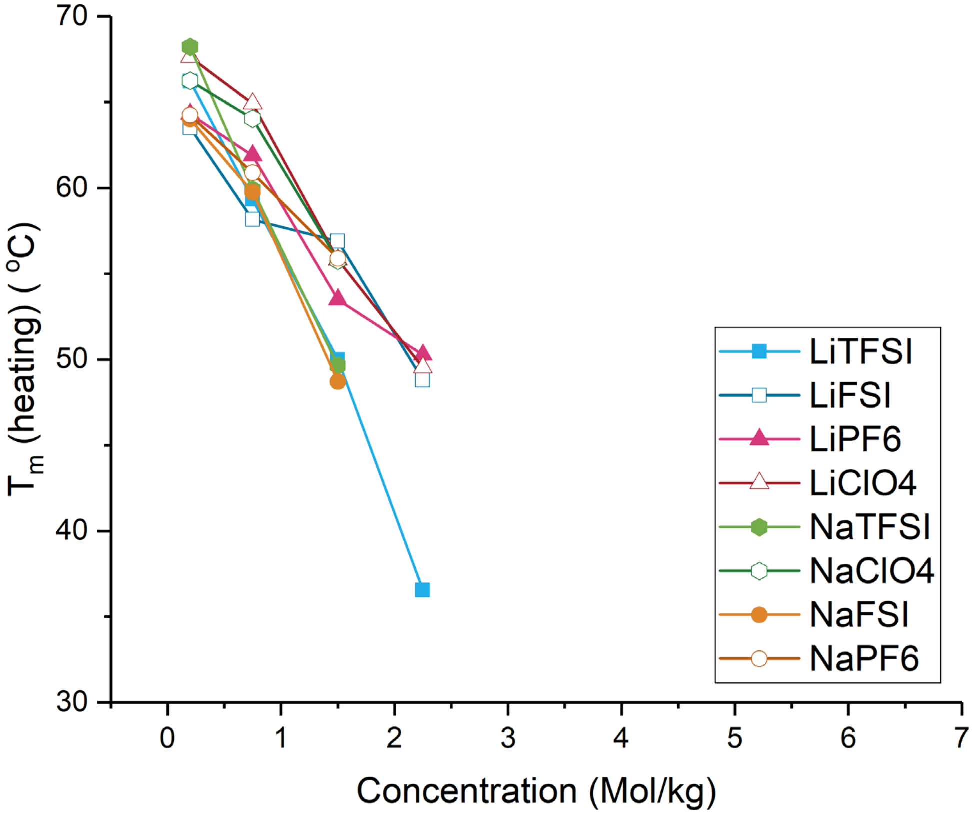

Figure 9-5 Melting temperatures (Tm) taken from the second heating scans of DSC of all the PEO formulations. Melting peaks which can be assigned to PEO directly were not observed in concentrations above 2.25 molal.

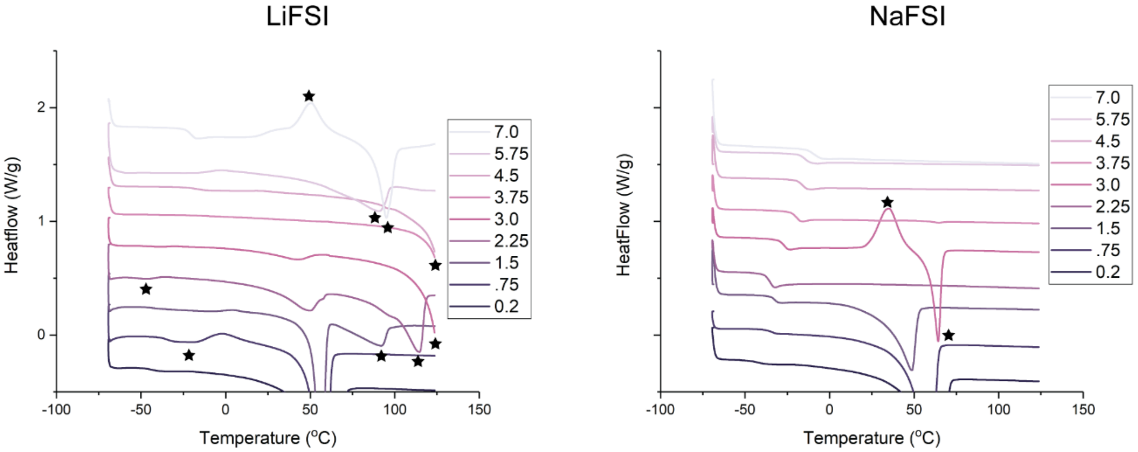

Figure 9-6 Close up DSC traces of Li and Na FSI -PEO formulations. Irregular features are denoted with the star icons. LiFSI seems to display an abundance of odd peaks that are absent in NaFSI formulations.

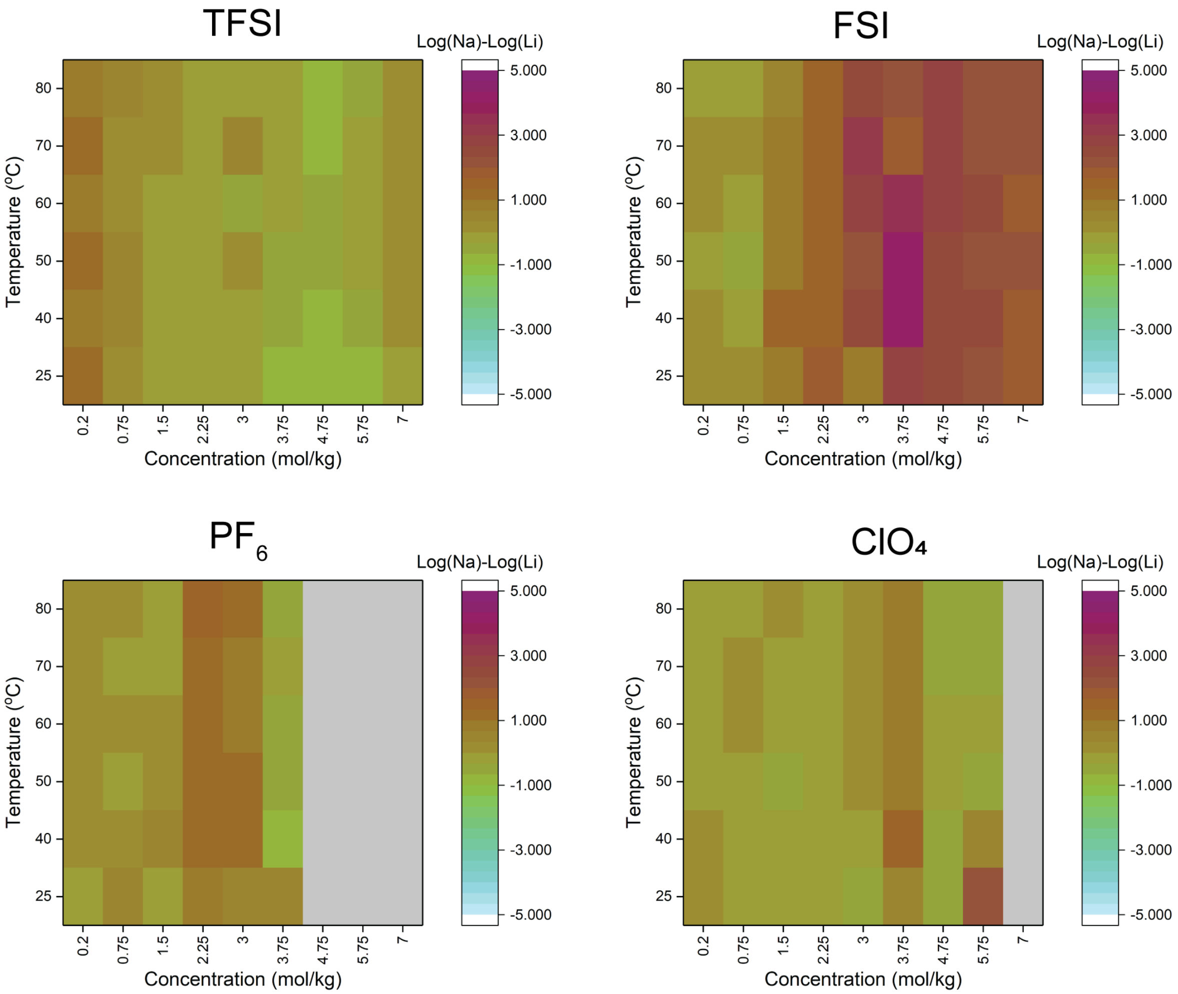

Figure 9-7 Difference in ionic conductivity at each formulation and temperature plotted on the same scale. Purple points favor sodium whereas blue/green favor lithium. Yellow points have very similar ionic conductivity.

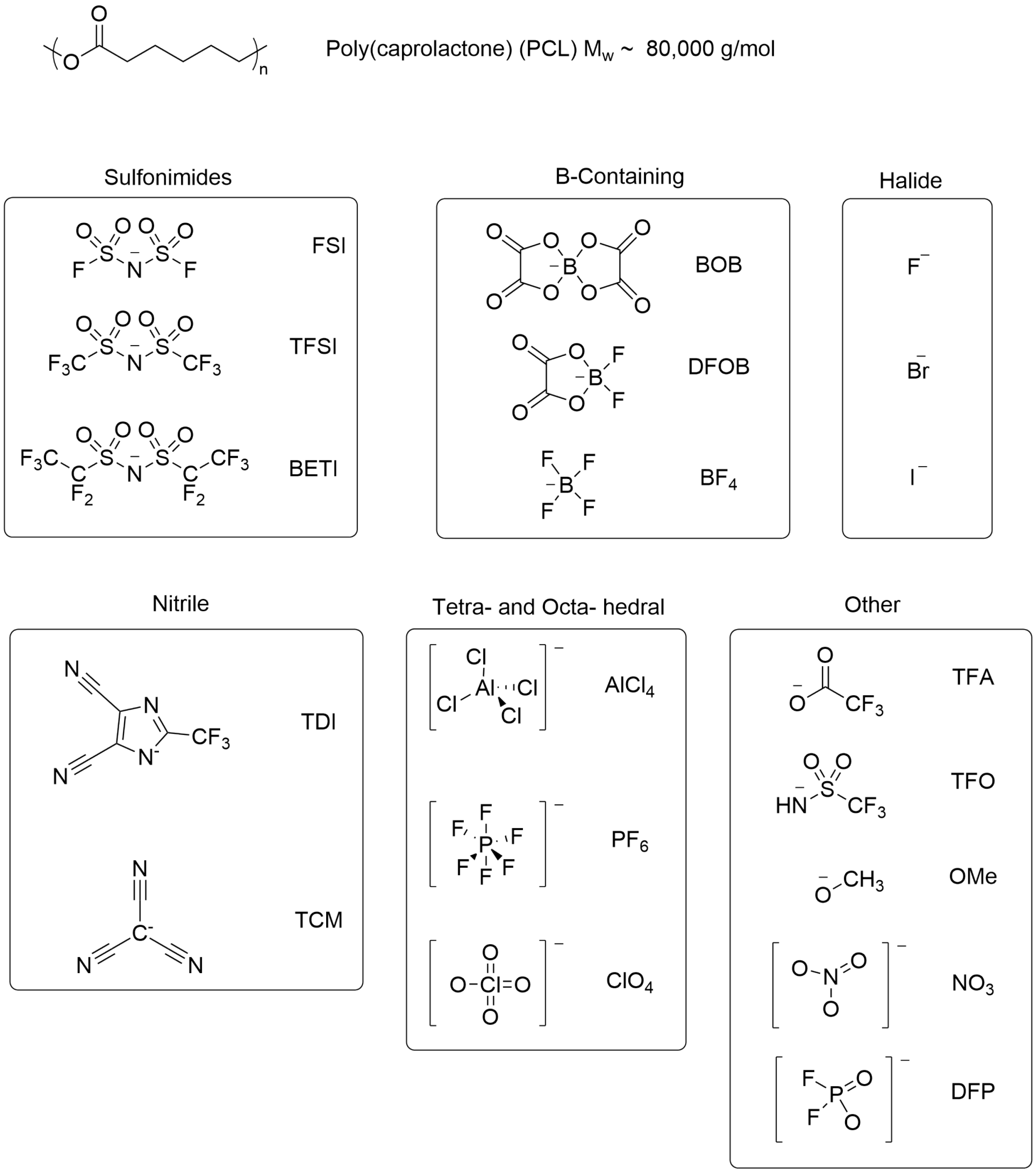

Figure 9-8 Chemical structures of all 19 anions used in PCL optimization study along with their given abbreviations and groupings by category.

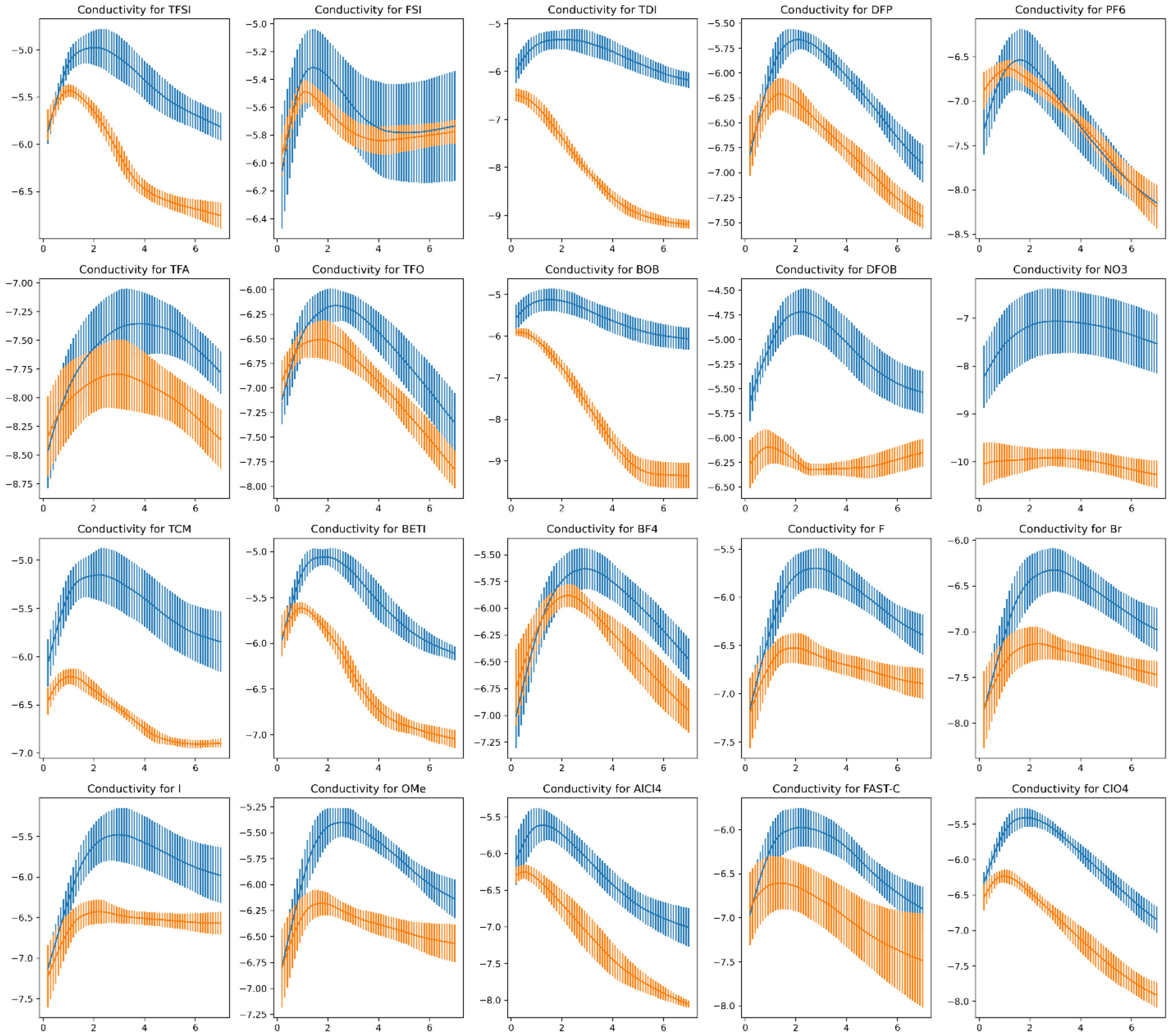

Figure 9-9 Initial (blue) and Final (orange) model predicted ionic conductivity for the entire chemical space in PCL at 30 °C. The dark line in each is the predicted value, and error bars are the prediction uncertainty of the model.

Table 9-2 Ionic conductivity data of polymer electrolytes formulated with poly(caprolactone) (PCL) measured at 30 °C

Anion	Concentration (mol/kg)	Batch	Measured Log(σ) [S/cm]	Measured Std. Dev. [S/cm]	Predicted Log(σ) [S/cm]	Model Uncertainty [S/cm]
$AlCl_4$	0.5	4	-6.710	0.116	-6.535	0.239
$AlCl_4$	6.1	1	-8.990	0.297	-6.895	0.226
BETI	1.2	4	-5.301	0.160	-5.214	0.095
BETI	1.5	5	-5.770	0.278	-5.658	0.122
BETI	5.5	4	-7.084	0.340	-6.045	0.234
BF_4	2.4	5	-5.540	1.131	-6.439	0.213
BOB	0.2	3	-6.233	0.157	-5.648	0.224
BOB	0.3	5	-6.152	0.096	-6.052	0.131
BOB	0.6	1	-6.363	0.085	-5.306	0.284
BOB	5.1	3	-9.781	0.231	-6.390	0.392
ClO_4	1.9	4	-6.454	0.050	-5.719	0.169
ClO_4	2.0	2	-6.400	0.092	-5.398	0.138
ClO_4	2.2	3	-6.688	0.111	-5.590	0.157
ClO_4	2.3	2	-6.400	0.211	-5.432	0.163
ClO_4	2.5	4	-7.011	0.027	-5.740	0.201
DFOB	2.2	2	-5.484	0.079	-6.278	0.748
DFOB	2.5	1	-9.125	0.871	-4.731	0.246
DFOB	2.9	3	-5.948	0.278	-5.727	0.429
DFOB	3.8	2	-6.445	0.067	-6.457	0.667
DFOB	4.0	3	-6.425	0.217	-6.032	0.468
DFOB	7.0	5	-5.972	0.391	-7.243	0.366
FSI	0.2	5	-6.307	0.171	-5.903	0.336
FSI	1.0	5	-4.974	0.118	-5.660	0.246
FSI	3.0	3	-5.801	0.127	-6.432	0.582
FSI	3.7	3	-5.640	0.096	-6.635	0.593
I	3.5	2	-6.854	0.343	-6.601	0.705
I	4.9	2	-6.893	0.133	-6.787	0.731
NO_3	3.0	1	-8.993	0.951	-7.063	0.677
NO_3	5.2	1	-10.125		-7.222	0.633
PF_6	1.9	1	-7.047	0.416	-6.561	0.354
PF_6	3.9	1	-6.945	0.127	-7.251	0.297
TCM	2.1	5	-6.647	0.267	-6.264	0.300
TCM	2.9	5	-6.330	0.154	-6.344	0.289
TCM	7.0	2	-7.924	0.133	-5.901	0.480
TDI	3.3	4	-8.780	0.456	-5.791	0.255
TDI	6.6	4	-9.390	1.139	-6.444	0.204
TFSI	0.9	2	-6.778	0.738	-5.154	0.165
TFSI	1.2	3	-5.112	0.107	-5.135	0.127
TFSI	1.4	1	-5.263	0.034	-5.022	0.138

TFSI	2.0	3	-5.617	0.186	-5.040	0.123
TFSI	2.2	4	-5.656	0.106	-5.122	0.143
TFSI	3.6	5	-6.867	0.572	-6.136	0.103
TFSI	4.4	4	-6.642	0.095	-5.558	0.113

Table 9-3 Ionic conductivity data of polymer electrolytes formulated with poly(caprolactone) (PCL) measured at 50 °C

Anion	Concentration (mol/kg)	Batch	Measured Log(σ) [S/cm]	Measured Std. Dev. [S/cm]	Predicted Log(σ) [S/cm]	Model Uncertainty [S/cm]
$AlCl_4$	0.5	4	-4.897	0.080	-5.546	0.194
$AlCl_4$	6.1	1	-6.955	0.017	-6.237	0.207
BETI	1.2	4	-4.728	0.141	-4.414	0.074
BETI	1.5	5	-5.013	0.224	-4.887	0.125
BETI	5.5	4	-6.119	0.225	-5.281	0.193
BF_4	2.4	5	-4.971	0.890	-5.653	0.198
BOB	0.2	3	-4.750	0.073	-4.828	0.206
BOB	0.3	5	-4.753	0.400	-5.202	0.137
BOB	0.6	1	-4.687	0.246	-4.567	0.224
BOB	5.1	3	-8.587	0.361	-5.615	0.411
ClO_4	1.9	4	-5.529	0.097	-4.719	0.169
ClO_4	2.0	2	-5.507	0.101	-4.488	0.134
ClO_4	2.2	3	-5.737	0.129	-4.630	0.155
ClO_4	2.3	2	-5.509	0.151	-4.525	0.158
ClO_4	2.5	4	-5.900	0.089	-4.748	0.204
DFOB	2.2	2	-4.676	0.168	-5.667	0.765
DFOB	2.5	1	-8.557	1.137	-4.144	0.240
DFOB	2.9	3	-5.088	0.209	-5.012	0.435
DFOB	3.8	2	-5.473	0.156	-5.858	0.692
DFOB	4.0	3	-5.424	0.196	-5.324	0.479
DFOB	7.0	5	-5.194	0.310	-6.554	0.348
FSI	0.2	5	-4.903	0.154	-5.062	0.320
FSI	1.0	5	-4.364	0.145	-4.829	0.232
FSI	3.0	3	-4.994	0.134	-5.569	0.620
FSI	3.7	3	-4.889	0.219	-5.777	0.625
I	3.5	2	-5.611	0.330	-5.848	0.681
I	4.9	2	-5.686	0.172	-6.044	0.707
NO_3	3.0	1	-8.945	0.102	-6.047	0.610
NO_3	5.2	1	-8.943		-6.222	0.564
PF_6	1.9	1	-5.962	0.336	-5.607	0.332
PF_6	3.9	1	-6.023	0.488	-6.309	0.285
TCM	2.1	5	-5.633	0.246	-5.462	0.276
TCM	2.9	5	-5.458	0.185	-5.548	0.265

TCM	7.0	2	-5.670	0.286	-5.247	0.441
TDI	3.3	4	-7.340	0.367	-4.933	0.254
TDI	6.6	4	-8.666	0.373	-5.605	0.195
TFSI	0.9	2	-4.492	0.030	-4.490	0.144
TFSI	1.2	3	-4.506	0.063	-4.425	0.101
TFSI	1.4	1	-4.496	0.155	-4.370	0.128
TFSI	2.0	3	-4.925	0.233	-4.341	0.103
TFSI	2.2	4	-4.930	0.093	-4.404	0.121
TFSI	3.6	5	-5.853	0.398	-5.427	0.101
TFSI	4.4	4	-5.727	0.104	-4.858	0.110

Table 9-4 Ionic conductivity data of polymer electrolytes formulated with poly(caprolactone) (PCL) measured at 70 °C

Anion	Concentration (mol/kg)	Batch	Measured Log(σ) [S/cm]	Measured Std. Dev. [S/cm]	Predicted Log(σ) [S/cm]	Model Uncertainty [S/cm]
$AlCl_4$	0.5	4	-4.381	0.141	-4.673	0.174
$AlCl_4$	6.1	1	-6.611	1.460	-5.655	0.197
BETI	1.2	4	-4.215	0.190	-3.706	0.094
BETI	1.5	5	-4.405	0.382	-4.206	0.131
BETI	5.5	4	-5.428	0.198	-4.606	0.168
BF_4	2.4	5	-4.375	0.970	-4.958	0.189
BOB	0.2	3	-4.351	0.105	-4.104	0.236
BOB	0.3	5	-4.197	0.114	-4.451	0.160
BOB	0.6	1	-3.805	0.253	-3.914	0.177
BOB	5.1	3	-8.075	0.351	-4.929	0.447
ClO_4	1.9	4	-4.876	0.169	-3.835	0.176
ClO_4	2.0	2	-4.845	0.107	-3.684	0.139
ClO_4	2.2	3	-5.048	0.144	-3.781	0.161
ClO_4	2.3	2	-4.846	0.138	-3.723	0.161
ClO_4	2.5	4	-5.144	0.106	-3.871	0.212
DFOB	2.2	2	-4.148	0.088	-5.127	0.781
DFOB	2.5	1	-7.643	0.092	-3.625	0.238
DFOB	2.9	3	-4.450	0.218	-4.381	0.446
DFOB	3.8	2	-4.545	0.208	-5.329	0.714
DFOB	4.0	3	-4.686	0.227	-4.699	0.492
DFOB	7.0	5	-4.632	0.190	-5.945	0.333
FSI	0.2	5	-4.562	0.145	-4.319	0.308
FSI	1.0	5	-3.809	0.349	-4.095	0.224
FSI	3.0	3	-4.418	0.128	-4.808	0.660
FSI	3.7	3	-4.265	0.253	-5.019	0.661
I	3.5	2	-4.818	0.216	-5.183	0.663
I	4.9	2	-4.663	0.031	-5.388	0.690

NO_3	3.0	1	-7.932	0.010	-5.148	0.552
NO_3	5.2	1	-7.850	0.105	-5.339	0.504
PF_6	1.9	1	-5.047	0.100	-4.764	0.315
PF_6	3.9	1	-5.259	0.663	-5.478	0.277
TCM	2.1	5	-4.932	0.240	-4.754	0.260
TCM	2.9	5	-4.823	0.203	-4.844	0.249
TCM	7.0	2	-4.960	0.215	-4.670	0.409
TDI	3.3	4	-6.319	0.305	-4.176	0.255
TDI	6.6	4	-7.621	0.268	-4.864	0.189
TFSI	0.9	2	-4.038	0.041	-3.903	0.127
TFSI	1.2	3	-4.059	0.058	-3.797	0.083
TFSI	1.4	1	-4.083	0.108	-3.794	0.119
TFSI	2.0	3	-4.390	0.258	-3.723	0.091
TFSI	2.2	4	-4.406	0.111	-3.769	0.104
TFSI	3.6	5	-5.119	0.321	-4.801	0.099
TFSI	4.4	4	-5.051	0.113	-4.238	0.114

Table 9-5 Ionic conductivity data of polymer electrolytes formulated with poly(caprolactone) (PCL) measured at 90 °C

Anion	**Concentration (mol/kg)**	**Batch**	**Measured Log(σ) [S/cm]**	**Measured Std. Dev. [S/cm]**	**Predicted Log(σ) [S/cm]**	**Model Uncertainty [S/cm]**
$AlCl_4$	0.5	4	-4.078	0.075	-3.896	0.179
$AlCl_4$	6.1	1	-5.252	0.896	-5.138	0.196
BETI	1.2	4	-3.869	0.169	-3.077	0.130
BETI	1.5	5	-3.960	0.425	-3.600	0.140
BETI	5.5	4	-4.895	0.170	-4.006	0.159
BF_4	2.4	5	-4.358		-4.341	0.185
BOB	0.2	3	-4.076	0.058	-3.459	0.289
BOB	0.3	5	-3.809	0.246	-3.783	0.189
BOB	0.6	1	-3.490	0.192	-3.333	0.146
BOB	5.1	3	-7.368	0.547	-4.320	0.491
ClO_4	1.9	4	-4.846	0.475	-3.049	0.188
ClO_4	2.0	2	-4.360	0.109	-2.968	0.150
ClO_4	2.2	3	-4.567	0.131	-3.027	0.171
ClO_4	2.3	2	-4.361	0.114	-3.010	0.170
ClO_4	2.5	4	-4.616	0.070	-3.090	0.224
DFOB	2.2	2	-3.539	0.245	-4.646	0.797
DFOB	2.5	1	-7.271	0.045	-3.164	0.239
DFOB	2.9	3	-3.850	0.435	-3.819	0.459
DFOB	3.8	2	-4.090	0.151	-4.858	0.736
DFOB	4.0	3	-4.059	0.387	-4.142	0.507
DFOB	7.0	5	-4.122	0.286	-5.403	0.320

FSI	0.2	5	-4.193	0.041	-3.658	0.299
FSI	1.0	5	-3.515	0.222	-3.442	0.219
FSI	3.0	3	-3.982	0.111	-4.130	0.701
FSI	3.7	3	-3.926	0.145	-4.344	0.697
I	3.5	2	-4.102	0.370	-4.592	0.649
I	4.9	2	-3.810	0.172	-4.804	0.677
NO_3	3.0	1	-7.842	0.187	-4.349	0.503
NO_3	5.2	1	-7.788		-4.553	0.453
PF_6	1.9	1	-4.408	0.192	-4.014	0.301
PF_6	3.9	1	-4.352	0.230	-4.738	0.272
TCM	2.1	5	-4.401	0.224	-4.125	0.250
TCM	2.9	5	-4.161	0.032	-4.218	0.239
TCM	7.0	2	-4.393	0.149	-4.156	0.384
TDI	3.3	4	-5.553	0.252	-3.502	0.256
TDI	6.6	4	-6.864	0.216	-4.205	0.185
TFSI	0.9	2	-3.739	0.089	-3.381	0.115
TFSI	1.2	3	-3.560	0.263	-3.239	0.073
TFSI	1.4	1	-3.664	0.172	-3.281	0.112
TFSI	2.0	3	-4.012	0.185	-3.174	0.087
TFSI	2.2	4	-3.885	0.179	-3.204	0.092
TFSI	3.6	5	-4.644	0.251	-4.244	0.098
TFSI	4.4	4	-4.488	0.160	-3.687	0.123

Table 9-6 Ionic conductivity data of hand-selected polymer electrolytes formulated with poly(caprolactone) (PCL) measured at 30 °C

Anion	**Concentration (mol/kg)**	**Batch**	**Measured Log(σ) [S/cm]**	**Measured Std. Dev. [S/cm]**	**Predicted Log(σ) [S/cm]**	**Model Uncertainty [S/cm]**
BF4	2.3	6	-6.227659204	0.06709913	-5.88143839	0.10590369
Br	2.2	6	-7.774716113	0.49217834	-7.13259275	0.18652719
Br	3.2	6	-8.153186375	0.12508861	-7.19023159	0.12409016
DFP	0.6	6	-9.032920266		-6.45328224	0.2082573
DFP	1.6	6	-9.436768503	0.21026037	-6.22595278	0.16717358
F	3.2	6	-9.952919971	0.42599625	-6.63845402	0.11260136
TFO	0.8	6	-7.474628018	0.14981316	-6.60803647	0.1301092
TFO	1.8	6	-6.274905479		-6.50699029	0.19619624

Table 9-7 Ionic conductivity data of hand-selected polymer electrolytes formulated with poly(caprolactone) (PCL) measured at 50 °C

Anion	**Concentration (mol/kg)**	**Batch**	**Measured Log(σ) [S/cm]**	**Measured Std. Dev. [S/cm]**	**Predicted Log(σ) [S/cm]**	**Model Uncertainty [S/cm]**
BF4	2.3	6	-5.39436048	0.0440114	-5.14982365	0.0959059
Br	2.2	6	-6.95845999	0.3616173	-6.18336334	0.15924925

Br	3.2	6	-7.14826189	0.15299834	-6.24819961	0.09756593
DFP	0.6	6	-7.50863831		-5.57888093	0.19730288
DFP	1.6	6	-7.49576447	0.06038527	-5.36593508	0.1489481
F	3.2	6	-8.13050302	0.36315147	-5.78320076	0.09167352
TFO	0.8	6	-5.99749362	0.18562856	-5.69546935	0.10980048
TFO	1.8	6	-5.68925889	0.09385861	-5.60617084	0.17494428

Table 9-8 Ionic conductivity data of hand-selected polymer electrolytes formulated with poly(caprolactone) (PCL) measured at 70 °C

Anion	**Concentration (mol/kg)**	**Batch**	**Measured Log(σ) [S/cm]**	**Measured Std. Dev. [S/cm]**	**Predicted Log(σ) [S/cm]**	**Model Uncertainty [S/cm]**
BF4	2.3	6	-4.81998902	0.07921626	-4.50352842	0.09022605
Br	2.2	6	-6.21926101	0.3193284	-5.34483124	0.13756996
Br	3.2	6	-6.35793732	0.18881961	-5.41602558	0.07938058
DFP	0.6	6				
DFP	1.6	6	-7.1215248	0.04834974	-4.60621099	0.1332798
F	3.2	6	-7.89109657	0.28592058	-5.02768549	0.0780103
TFO	0.8	6	-5.78275547	0.07060772	-4.88932405	0.09331913
TFO	1.8	6	-5.19997064		-4.81040323	0.15721485

Table 9-9 Ionic conductivity data of hand-selected polymer electrolytes formulated with poly(caprolactone) (PCL) measured at 90 °C

Anion	**Concentration (mol/kg)**	**Batch**	**Measured Log(σ) [S/cm]**	**Measured Std. Dev. [S/cm]**	**Predicted Log(σ) [S/cm]**	**Model Uncertainty [S/cm]**
BF4	2.3	6	-4.50473398	0.04666	-3.92845028	0.08815882
Br	2.2	6	-5.77232033	0.27398	-4.59869937	0.12122777
Br	3.2	6	-5.77580413	0.28503	-4.67555116	0.07068507
DFP	0.6	6	-6.79588002		-4.1191366	0.18187114
DFP	1.6	6	-6.7117485	0.11696	-3.93020305	0.11981346
F	3.2	6	-7.4803737	0.25429	-4.35542259	0.07192119
TFO	0.8	6	-5.31734979	0.21303	-4.17201019	0.08052316
TFO	1.8	6	-4.80248376	0.11862	-4.1023235	0.14257349

CHAPTER 10 APPENDIX C: REFERENCES

1. Effects | Facts – Climate Change: Vital Signs of the Planet. https://climate.nasa.gov/effects/.
2. 5 critical incentives that could protect nature and climate | World Economic Forum. https://www.weforum.org/agenda/2021/11/5-critical-incentives-that-could-protect-nature-and-the-climate/.
3. Rockström, J. *et al.* A roadmap for rapid decarbonization. *Science (1979)* **355**, 1269–1271 (2017).
4. Blair, N. *et al.* Storage Futures Study: Key Learnings for the Coming Decades.
5. Ibrahim, H., Ilinca, A. & Perron, J. Energy storage systems-Characteristics and comparisons. *Renewable and Sustainable Energy Reviews* vol. 12 1221–1250 Preprint at https://doi.org/10.1016/j.rser.2007.01.023 (2008).
6. Sources of Greenhouse Gas Emissions | US EPA. https://www.epa.gov/ghgemissions/sources-greenhouse-gas-emissions.
7. Charging into the future: the transition to electric vehicles : Beyond the Numbers: U.S. Bureau of Labor Statistics. https://www.bls.gov/opub/btn/volume-12/charging-into-the-future-the-transition-to-electric-vehicles.htm.
8. Hesse, H., Schimpe, M., Kucevic, D. & Jossen, A. Lithium-Ion Battery Storage for the Grid—A Review of Stationary Battery Storage System Design Tailored for Applications in Modern Power Grids. *Energies (Basel)* **10**, 2107 (2017).
9. Xue, Z., He, D. & Xie, X. Poly(ethylene oxide)-based electrolytes for lithium-ion batteries. *Journal of Materials Chemistry A* vol. 3 19218–19253 Preprint at https://doi.org/10.1039/c5ta03471j (2015).
10. Whittingham, M. S. & Gamble, F. R. The lithium intercalates of the transition metal dichalcogenides. *Mater Res Bull* **10**, 363–371 (1975).
11. Li, M., Lu, J., Chen, Z. & Amine, K. 30 Years of Lithium-Ion Batteries. *Advanced Materials* **30**, 1800561 (2018).
12. Xie, J. & Lu, Y. C. A retrospective on lithium-ion batteries. *Nature Communications 2020 11:1* **11**, 1–4 (2020).
13. Goodenough, J. B. Oxide Cathodes. *Advances in Lithium-Ion Batteries* 135–154 (2002) doi:10.1007/0-306-47508-1_5.
14. Yoshino, A., Sanechika, K. & Nakajima, T. Secondary battery. (1986).
15. Xu, K. Nonaqueous liquid electrolytes for lithium-based rechargeable batteries. *Chem Rev* **104**, 4303–4417 (2004).

16. Wu, F., Maier, J. & Yu, Y. Guidelines and trends for next-generation rechargeable lithium and lithium-ion batteries. *Chemical Society Reviews* vol. 49 1569–1614 Preprint at https://doi.org/10.1039/c7cs00863e (2020).

17. Why Electric Cars Burn, Why It's Probably Overhyped and How to Fix It - CNET. https://www.cnet.com/roadshow/news/why-electric-cars-burn-why-its-probably-overhyped-and-how-to-fix-it/.

18. Grey, C. P. & Hall, D. S. Prospects for lithium-ion batteries and beyond—a 2030 vision. *Nature Communications 2020 11:1* **11**, 1–4 (2020).

19. Ye, H., Zhang, Y., Yin, Y. X., Cao, F. F. & Guo, Y. G. An Outlook on Low-Volume-Change Lithium Metal Anodes for Long-Life Batteries. *ACS Cent Sci* **6**, 661–671 (2020).

20. Lithium-ion Battery Pack Prices Rise for First Time to an Average of $151/kWh | BloombergNEF. https://about.bnef.com/blog/lithium-ion-battery-pack-prices-rise-for-first-time-to-an-average-of-151-kwh/.

21. Usiskin, R. *et al.* Fundamentals, status and promise of sodium-based batteries. *Nature Reviews Materials 2021 6:11* **6**, 1020–1035 (2021).

22. Xue, W. *et al.* Ultra-high-voltage Ni-rich layered cathodes in practical Li metal batteries enabled by a sulfonamide-based electrolyte. *Nature Energy 2021 6:5* **6**, 495–505 (2021).

23. Wang, X. *et al.* Ultra-stable all-solid-state sodium metal batteries enabled by perfluoropolyether-based electrolytes. *Nature Materials 2022 21:9* **21**, 1057–1065 (2022).

24. Huang, Z. *et al.* A solvent-anchored non-flammable electrolyte. *Matter* (2022) doi:10.1016/j.matt.2022.11.003.

25. Monroe, C. & Newman, J. The Impact of Elastic Deformation on Deposition Kinetics at Lithium/Polymer Interfaces. *J Electrochem Soc* **152**, A396 (2005).

26. Doyle, M., Fuller, T. F. & Newman, J. The importance of the lithium ion transference number in lithium/polymer cells. *Electrochim Acta* **39**, 2073–2081 (1994).

27. Li, S. *et al.* Single-Ion Homopolymer Electrolytes with High Transference Number Prepared by Click Chemistry and Photoinduced Metal-Free Atom-Transfer Radical Polymerization. *ACS Energy Lett* **3**, 20–27 (2018).

28. Bachman, J. C. *et al.* Inorganic Solid-State Electrolytes for Lithium Batteries: Mechanisms and Properties Governing Ion Conduction. *Chem Rev* **116**, 140–162 (2016).

29. Gao, Z. *et al.* Promises, Challenges, and Recent Progress of Inorganic Solid-State Electrolytes for All-Solid-State Lithium Batteries. *Advanced Materials* **30**, 1705702 (2018).

30. Fenton, D. E., Parker, J. M. & Wright, P. V. Complexes of alkali metal ions with poly(ethylene oxide). *Polymer (Guildf)* **14**, 589 (1973).

31. Armand, M. Polymer solid electrolytes - an overview. *Solid State Ion* **9–10**, 745–754 (1983).

32. Mindemark, J., Lacey, M. J., Bowden, T. & Brandell, D. Beyond PEO—Alternative host materials for Li+-conducting solid polymer electrolytes. *Progress in Polymer Science* vol. 81 114–143 Preprint at https://doi.org/10.1016/j.progpolymsci.2017.12.004 (2018).

33. Leverick, G. Towards comprehensive design of electrolytes for electrochemical energy storage. (2022).

34. Bocharova, V. & Sokolov, A. P. Perspectives for Polymer Electrolytes: A View from Fundamentals of Ionic Conductivity. *Macromolecules* **53**, 4141–4157 (2020).

35. Smedley, S. I. *The Interpretation of Ionic Conductivity in Liquids*. *The Interpretation of Ionic Conductivity in Liquids* (Springer US, 1980). doi:10.1007/978-1-4684-3818-5.

36. Bird, B. R., Stewart, W. E. & Lightfoot, E. N. *Transport Phenomena*. (John Wiley & Sons, Inc., 2002).

37. Agmon, N. The Grotthuss mechanism. *Chem Phys Lett* **244**, 456–462 (1995).

38. Dokko, K. *et al.* Direct Evidence for Li Ion Hopping Conduction in Highly Concentrated Sulfolane-Based Liquid Electrolytes. *J Phys Chem B* **122**, 10736–10745 (2018).

39. Roth, D. B. & Gellert, M. Oxide-ion conductors by design. *Nature 2000 404:6780* **404**, 821–823 (2000).

40. Yang, H. & Wu, N. Ionic conductivity and ion transport mechanisms of solid-state lithium-ion battery electrolytes: A review. *Energy Sci Eng* **10**, 1643–1671 (2022).

41. Zhang, B. *et al.* Mechanisms and properties of ion-transport in inorganic solid electrolytes. *Energy Storage Mater* **10**, 139–159 (2018).

42. He, X., Zhu, Y. & Mo, Y. Origin of fast ion diffusion in super-ionic conductors. *Nature Communications 2017 8:1* **8**, 1–7 (2017).

43. Tuller, H. Ionic conduction and applications. in *Springer Handbooks* 1 (Springer, 2017). doi:10.1007/978-3-319-48933-9_11.

44. Li, Y., Han, J. T., Wang, C. A., Xie, H. & Goodenough, J. B. Optimizing Li + conductivity in a garnet framework. *J Mater Chem* **22**, 15357–15361 (2012).

45. Shin, D. O. *et al.* Synergistic multi-doping effects on the Li7La3Zr2O12 solid electrolyte for fast lithium ion conduction. *Scientific Reports 2015 5:1* **5**, 1–9 (2015).

46. Buschmann, H. *et al.* Structure and dynamics of the fast lithium ion conductor “Li7La3Zr2O12”. *Physical Chemistry Chemical Physics* **13**, 19378–19392 (2011).

47. Teran, A. A., Tang, M. H., Mullin, S. A. & Balsara, N. P. Effect of molecular weight on conductivity of polymer electrolytes. *Solid State Ion* **203**, 18–21 (2011).

48. Stolwijk, N. A. *et al.* Salt-concentration dependence of the glass transition temperature in PEO-NaI and PEO-LiTFSI polymer electrolytes. *Macromolecules* **46**, 8580–8588 (2013).

49. Mongcopa, K. I. S. *et al.* Relationship between Segmental Dynamics Measured by Quasi-Elastic Neutron Scattering and Conductivity in Polymer Electrolytes. *ACS Macro Lett* **7**, 504–508 (2018).

50. Hiemenz, P. C. & Lodge, T. P. *Polymer Chemistry*. (CRC Press, 2007).

51. Hallinan, D. T. & Balsara, N. P. Polymer Electrolytes. *Annu Rev Mater Res* **43**, 503–525 (2013).

52. Liou, C.-C. & Brodbelt, J. S. Determination of Orders of Relative Alkali Metal Ion Affinities of Crown Ethers and Acyclic Analogs by the Kinetic Method. (1992).

53. Stoeva, Z., Martin-Litas, I., Staunton, E., Andreev, Y. G. & Bruce, P. G. Ionic conductivity in the crystalline polymer electrolytes PEO6:LiXF6, X = P, As, Sb. *J Am Chem Soc* **125**, 4619–4626 (2003).

54. Guomin Mao, † *et al.* α-Relaxation in PEO−LiTFSI Polymer Electrolytes. (2001) doi:10.1021/MA010108E.

55. Mao, G., Perea, R. F., Howells, W. S., Price, D. L. & Saboungi, M.-L. Relaxation in polymer electrolytes on the nanosecond timescale. *Nature* **405**, 163–165 (2000).

56. Doi, M. (Masao). *Introduction to polymer physics*. (Clarendon Press, 1996).

57. Rouse, P. E. A Theory of the Linear Viscoelastic Properties of Dilute Solutions of Coiling Polymers. *J Chem Phys* **21**, 1272 (2004).

58. Fulcher, G. S. ANALYSIS OF RECENT MEASUREMENTS OF THE VISCOSITY OF GLASSES. *Journal of the American Ceramic Society* **8**, 339–355 (1925).

59. Wang, Q. *et al.* Siloxane-based polymer electrolytes for solid-state lithium batteries. *Energy Storage Mater* **23**, 466–490 (2019).

60. Stolberg, M. A. *et al.* Lamellar ionenes with highly dissociative, anionic channels provide low barriers for cation transport. (2023) doi:10.26434/CHEMRXIV-2023-FWGQL.

61. Zhang, H. *et al.* Single lithium-ion conducting solid polymer electrolytes: advances and perspectives. *Chem Soc Rev* **46**, 797–815 (2017).

62. Thomas, K. E., Sloop, S. E., Kerr, J. B. & Newman, J. Comparison of lithium-polymer cell performance with unity and nonunity transference numbers. *J Power Sources* **89**, 132–138 (2000).

63. Dewing, B. L., Bible, N. G., Ellison, C. J. & Mahanthappa, M. K. Electrochemically Stable, High Transference Number Lithium Bis(malonato)borate Polymer Solution Electrolytes. *Chemistry of Materials* acs.chemmater.9b05219 (2020) doi:10.1021/acs.chemmater.9b05219.

64. Park, J., Staiger, A., Mecking, S. & Winey, K. I. Enhanced Li-Ion Transport through Selectively Solvated Ionic Layers of Single-Ion Conducting Multiblock Copolymers. *ACS Macro Lett* 1008–1013 (2022) doi:10.1021/ACSMACROLETT.2C00288.

65. Zhang, W. *et al.* Molecularly Tunable Polyanions for Single-Ion Conductors and Poly(solvate ionic liquids). *Chemistry of Materials* **33**, 524–534 (2021).

66. Elmore, C. *et al.* Ion Transport in Solvent-Free, Crosslinked, Single-Ion Conducting Polymer Electrolytes for Post-Lithium Ion Batteries. *Batteries* **4**, 28 (2018).

67. Gao, J., Wang, C., Han, D. W. & Shin, D. M. Single-ion conducting polymer electrolytes as a key jigsaw piece for next-generation battery applications. *Chem Sci* **12**, 13248–13272 (2021).

68. Krauskopf, T. *et al.* Comparing the Descriptors for Investigating the Influence of Lattice Dynamics on Ionic Transport Using the Superionic Conductor $Na_3PS_{4-x}Se_x$. *J Am Chem Soc* **140**, 14464–14473 (2018).

69. Yan, L., Häußler, M., Bauer, J., Mecking, S. & Winey, K. I. Monodisperse and Telechelic Polyethylenes Form Extended Chain Crystals with Ionic Layers. *Macromolecules* **52**, 4949–4956 (2019).

70. Paren, B. A., Häußler, M., Rathenow, P., Mecking, S. & Winey, K. I. Decoupled Cation Transport within Layered Assemblies in Sulfonated and Crystalline Telechelic Polyethylenes. *Macromolecules* **55**, 2813–2820 (2022).

71. Paren, B. A. *et al.* Percolated ionic aggregate morphologies and decoupled ion transport in precise sulfonated polymers synthesized by ring-opening metathesis polymerization. *Macromolecules* **53**, 8960–8973 (2020).

72. Bresser, D. *et al.* Organic Liquid Crystals as Single-Ion Li+ Conductors. *ChemSusChem* **14**, 655–661 (2021).

73. Stacy, E. W. *et al.* Fundamental Limitations of Ionic Conductivity in Polymerized Ionic Liquids. *Macromolecules* **51**, 8637–8645 (2018).

74. Bresser, D., Lyonnard, S., Iojoiu, C., Picard, L. & Passerini, S. Decoupling segmental relaxation and ionic conductivity for lithium-ion polymer electrolytes. *Molecular Systems Design and Engineering* vol. 4 779–792 Preprint at https://doi.org/10.1039/c9me00038k (2019).

75. Mc Naught, a. D. & Wilkinson, a. Compendium of Chemical Terminology-Gold Book. *Iupac* 1670 (2012) doi:10.1351/goldbook.

76. Huang, M. *et al.* Fluorinated Aryl Sulfonimide Tagged (FAST) salts: modular synthesis and structure–property relationships for battery applications. *Energy Environ Sci* **11**, 1326–1334 (2018).

77. Huang, M. *et al.* Design of S-Substituted Fluorinated Aryl Sulfonamide-Tagged (S-FAST) Anions to Enable New Solvate Ionic Liquids for Battery Applications. *Chemistry of Materials* **31**, 7558–7564 (2019).

78. Neese, F. Software update: the ORCA program system, version 4.0. *Wiley Interdiscip Rev Comput Mol Sci* **8**, e1327 (2018).

79. RDKit. https://www.rdkit.org/.

80. Bannwarth, C., Ehlert, S. & Grimme, S. GFN2-xTB - An Accurate and Broadly Parametrized Self-Consistent Tight-Binding Quantum Chemical Method with Multipole Electrostatics and Density-Dependent Dispersion Contributions. *J Chem Theory Comput* **15**, 1652–1671 (2019).

81. Vosko, S. H., Wilk, L. & Nusair, M. Accurate spin-dependent electron liquid correlation energies for local spin density calculations: a critical analysis. *Can J Phys* **58**, 1200–1211 (1980).

82. Stephens, P. J., Devlin, F. J., Chabalowski, C. F. & Frisch, M. J. Ab Initio calculation of vibrational absorption and circular dichroism spectra using density functional force fields. *Journal of Physical Chemistry®* **98**, 11623–11627 (1994).

83. Lee, C., Yang, W. & Parr, R. G. Development of the Colle-Salvetti correlation-energy formula into a functional of the electron density. *Phys Rev B Condens Matter* **37**, 785–789 (1988).

84. Weigend, F. & Ahlrichs, R. Balanced basis sets of split valence, triple zeta valence and quadruple zeta valence quality for H to Rn: Design and assessment of accuracy. *Physical Chemistry Chemical Physics* **7**, 3297–3305 (2005).

85. Rappoport, D. & Furche, F. Property-optimized Gaussian basis sets for molecular response calculations. *J Chem Phys* **133**, 134105 (2010).

86. Chai, J. Da & Head-Gordon, M. Long-range corrected hybrid density functionals with damped atom–atom dispersion corrections. *Physical Chemistry Chemical Physics* **10**, 6615–6620 (2008).

87. Marenich, A. V., Cramer, C. J. & Truhlar, D. G. Universal solvation model based on solute electron density and on a continuum model of the solvent defined by the bulk dielectric constant and atomic surface tensions. *Journal of Physical Chemistry B* **113**, 6378–6396 (2009).

88. Perdew, J. P., Burke, K. & Ernzerhof, M. Generalized Gradient Approximation Made Simple. (1996).

89. Kresse, G. & Furthmü, J. Efficient iterative schemes for ab initio total-energy calculations using a plane-wave basis set. (1996).

90. Kresse, G. & Hafner, J. Ab initio molecular dynamics for open-shell transition metals. *Phys Rev B* **48**, (1993).

91. Grimme, S., Ehrlich, S. & Goerigk, L. Effect of the damping function in dispersion corrected density functional theory. *J Comput Chem* **32**, 1456–1465 (2011).

92. Grimme, S., Antony, J., Ehrlich, S. & Krieg, H. A consistent and accurate ab initio parametrization of density functional dispersion correction (DFT-D) for the 94 elements H-Pu. *J Chem Phys* **132**, 154104 (2010).

93. Mandai, T., Yoshida, K., Ueno, K., Dokko, K. & Watanabe, M. Criteria for solvate ionic liquids. *Physical Chemistry Chemical Physics* **16**, 8761–8772 (2014).

94. Trigg, E. B. & Winey, K. I. Nanoscale layers in polymers to promote ion transport. *Mol Syst Des Eng* **4**, 252–262 (2019).

95. Trigg, E. B. *et al.* Self-assembled highly ordered acid layers in precisely sulfonated polyethylene produce efficient proton transport. *Nat Mater* **17**, 725–731 (2018).

96. Rosen, B. M. *et al.* Dendron-mediated self-assembly, disassembly, and self-organization of complex systems. *Chem Rev* **109**, 6275–6540 (2009).

97. Impéror-Clerc, M. Thermotropic cubic mesophases. *Current Opinion in Colloid and Interface Science* vol. 9 370–376 Preprint at https://doi.org/10.1016/j.cocis.2004.12.004 (2005).

98. Balagurusamy, V. S. K., Ungar, G., Percec, V. & Johansson, G. Rational design of the first spherical supramolecular dendrimers self-organized in a novel thermotropic cubic liquid-crystalline phase and the determination of their shape by X-ray analysis. *J Am Chem Soc* **119**, 1539–1555 (1997).

99. Dierking, I. Textures of Liquid Crystals. *Textures of Liquid Crystals* (2003) doi:10.1002/3527602054.

100. Goossens, K., Lava, K., Bielawski, C. W. & Binnemans, K. Ionic Liquid Crystals: Versatile Materials. (2016) doi:10.1021/cr400334b.

101. Schulz, M. D., Wagener, K. B., Schulz, M. D., Wagener The George, K. B. & Butler, J. Precision Polymers through ADMET Polymerization. *Macromol Chem Phys* **215**, 1936–1945 (2014).

102. Gaines, T. W., Bell, M. H., Trigg, E. B., Winey, K. I. & Wagener, K. B. Precision Sulfonic Acid Polyolefins via Heterogenous to Homogenous Deprotection. *Macromol Chem Phys* **219**, 1700634 (2018).

103. Lucero, J. M., Romero, Z., Moreno, A., Huber, D. L. & Simocko, C. ADMET polymerization in affordable, commercially available, high boiling solvents. *SN Appl Sci* **2**, 1–8 (2020).

104. Russell, K. E., Hunter, B. K. & Heyding, R. D. *Monoclinic polyethylene revisited*. vol. 38 (1997).

105. Alexander, K. C., Ganesh, P., Chi, M., Kent, P. & Sumpter, B. G. Grain boundary stability and influence on ionic conductivity in a disordered perovskite—a first-principles investigation of lithium lanthanum titanate. *MRS Commun* **6**, 455–463 (2016).

106. Peters, A., Korte, C., Hesse, D., Zakharov, N. & Janek, J. Ionic conductivity and activation energy for oxygen ion transport in superlattices — The multilayer system CSZ (ZrO2 + CaO) / Al2O3. *Solid State Ion* **178**, 67–76 (2007).

107. He, X., Sun, H., Ding, X. & Zhao, K. Grain Boundaries and Their Impact on Li Kinetics in Layered-Oxide Cathodes for Li-Ion Batteries. *Journal of Physical Chemistry C* **125**, 10284–10294 (2021).

108. Ue, M. & Mori, S. *Mobility and Ionic Association of Lithium Salts in a Propylene Carbonate-Ethyl Methyl Carbonate Mixed Solvent*. (1995).

109. Mandai, T., Dokko, K. & Watanabe, M. Solvate Ionic Liquids for Li, Na, K, and Mg Batteries. *The Chemical Record* **19**, 708–722 (2019).

110. Henderson, W. A., Brooks, N. R. & Young, V. G. Tetraglyme-Li+ Cation Solvate Structures: Models for Amorphous Concentrated Liquid and Polymer Electrolytes (II). *Chemistry of Materials* **15**, 4685–4690 (2003).

111. Ichihashi, K. *et al.* Optimizing Lithium Ion Conduction through Crown Ether-Based Cylindrical Channels in [Ni(dmit)2]- Salts. *Chemistry of Materials* **30**, 7130–7137 (2018).

112. CRC Handbook of Chemistry and Physics 103rd Edition. *CRC Press* https://hbcp.chemnetbase.com/faces/contents/InteractiveTable.xhtml (2022).

113. Zhang, Z. *et al.* New horizons for inorganic solid state ion conductors. *Energy Environ Sci* **11**, 1945–1976 (2018).

114. Peng, J. *et al.* Human- and machine-centred designs of molecules and materials for sustainability and decarbonization. *Nature Reviews Materials 2022 7:12* **7**, 991–1009 (2022).

115. Vamathevan, J. *et al.* Applications of machine learning in drug discovery and development. *Nature Reviews Drug Discovery 2019 18:6* **18**, 463–477 (2019).

116. Liu, Y. *et al.* Machine Learning Boosting the Development of Advanced Lithium Batteries. *Small Methods* **5**, 2100442 (2021).

117. Bradford, G. *et al.* Chemistry-Informed Machine Learning for Polymer Electrolyte Discovery. *ACS Cent Sci* (2023) doi:10.1021/ACSCENTSCI.2C01123/ASSET/IMAGES/LARGE/OC2C01123_0007.JPEG.

118. Ren, F. *et al.* Accelerated discovery of metallic glasses through iteration of machine learning and high-throughput experiments. *Sci Adv* **4**, (2018).

119. Pollice, R. *et al.* Data-Driven Strategies for Accelerated Materials Design. *Acc Chem Res* **54**, 849–860 (2021).

120. Gómez-Bombarelli, R. *et al.* Automatic Chemical Design Using a Data-Driven Continuous Representation of Molecules. *ACS Cent Sci* **4**, 268–276 (2018).

121. Burger, B. *et al.* A mobile robotic chemist. *Nature 2020 583:7815* **583**, 237–241 (2020).

122. MacLeod, B. P. *et al.* Self-driving laboratory for accelerated discovery of thin-film materials. *Sci Adv* **6**, (2020).

123. Seifrid, M. *et al.* Autonomous Chemical Experiments: Challenges and Perspectives on Establishing a Self-Driving Lab. *Acc Chem Res* **14**, 25 (2022).

124. Xie, T. *et al.* Accelerating amorphous polymer electrolyte screening by learning to reduce errors in molecular dynamics simulated properties. *Nature Communications 2022 13:1* **13**, 1–10 (2022).

125. Basics of EIS: Electrochemical Research-Impedance Gamry Instruments. https://www.gamry.com/application-notes/EIS/basics-of-electrochemical-impedance-spectroscopy/.

126. De Gans, B. J. & Schubert, U. S. Inkjet printing of well-defined polymer dots and arrays. *Langmuir* **20**, 7789–7793 (2004).

127. Lazanas, A. C. & Prodromidis, M. I. Electrochemical Impedance Spectroscopy–A Tutorial. *ACS Measurement Science Au* (2022) doi:10.1021/ACSMEASURESCIAU.2C00070/ASSET/IMAGES/LARGE/TG2C00070_0032.JPEG.

128. Why 4-point measurements? - BioLogic Learning Center. https://www.biologic.net/topics/why-4-points-measurements/.

129. Gorecki, W. *et al.* NMR, DSC, and conductivity study of a poly(ethylene oxide) complex electrolyte : PEO(LiClO4)x. *Solid State Ion* **18–19**, 295–299 (1986).

130. Zhou, D., Mei, X. & Ouyang, J. Ionic conductivity enhancement of polyethylene oxide-LiClO4 electrolyte by adding functionalized multi-walled carbon nanotubes. *Journal of Physical Chemistry C* **115**, 16688–16694 (2011).

131. Weston, J. E. & Steele, B. C. H. Effects of inert fillers on the mechanical and electrochemical properties of lithium salt-poly(ethylene oxide) polymer electrolytes. *Solid State Ion* **7**, 75–79 (1982).

132. Maccallum, J. R., Smith, M. J. & Vincent, C. A. THE EFFECTS OF RADIATION-INDUCED CROSSLINKING ON THE CONDUCTANCE OF LiOO 4.PEO ELECTROLYTES. *Solid State Ion* **11**, 307–312 (1984).

133. Aziz, S. B., Woo, T. J., Kadir, M. F. Z. & Ahmed, H. M. A conceptual review on polymer electrolytes and ion transport models. *Journal of Science: Advanced Materials and Devices* vol. 3 1–17 Preprint at https://doi.org/10.1016/j.jsamd.2018.01.002 (2018).

134. Iragorri, J. I., Cesteros, L. C. & Katime, I. Morphological and kinetics study of PEO/PVC blends. *Polym Int* **25**, 225–228 (1991).

135. Pielichowski, K. & Flejtuch, K. Differential scanning calorimetry studies on poly(ethylene glycol) with different molecular weights for thermal energy storage materials. *Polym Adv Technol* **13**, 690–696 (2002).

136. Colligative properties - Wikipedia. https://en.wikipedia.org/wiki/Colligative_properties.

137. Lan, T. & Torkelson, J. M. Substantial spatial heterogeneity and tunability of glass transition temperature observed with dense polymer brushes prepared by ARGET ATRP. *Polymer (Guildf)* **64**, 183–192 (2015).

138. Mano, J. F., Gómez Ribelles, J. L., Alves, N. M. & Salmerón Sanchez, M. Glass transition dynamics and structural relaxation of PLLA studied by DSC: Influence of crystallinity. *Polymer (Guildf)* **46**, 8258–8265 (2005).

139. Rajan, K. Materials informatics. *Materials Today* **8**, 38–45 (2005).

140. Peng, J. *et al.* Human- and machine-centred designs of molecules and materials for sustainability and decarbonization. *Nature Reviews Materials 2022 7:12* **7**, 991–1009 (2022).

141. Shields, B. J. *et al.* Bayesian reaction optimization as a tool for chemical synthesis. *Nature 2021 590:7844* **590**, 89–96 (2021).

142. Snoek, J., Larochelle, H. & Adams, R. P. Practical Bayesian Optimization of Machine Learning Algorithms.

143. Yang, K. *et al.* Analyzing Learned Molecular Representations for Property Prediction. *J Chem Inf Model* **59**, 3370–3388 (2019).

144. Schauser, N. S., Kliegle, G. A., Cooke, P., Segalman, R. A. & Seshadri, R. Database creation, visualization, and statistical learning for polymer Li+-electrolyte design. *Chemistry of Materials* **33**, 4863–4876 (2021).

145. Hatakeyama-Sato, K., Tezuka, T., Umeki, M. & Oyaizu, K. AI-Assisted Exploration of Superionic Glass-Type Li+ Conductors with Aromatic Structures. *J Am Chem Soc* **142**, 3301–3305 (2020).

146. Labet, M. & Thielemans, W. Synthesis of polycaprolactone: a review. *Chem Soc Rev* **38**, 3484–3504 (2009).

147. Fonseca, C. P., Rosa, D. S., Gaboardi, F. & Neves, S. Development of a biodegradable polymer electrolyte for rechargeable batteries. *J Power Sources* **155**, 381–384 (2006).

148. Eriksson, T. *et al.* Carbonyl-Containing Solid Polymer Electrolyte Host Materials: Conduction and Coordination in Polyketone, Polyester, and Polycarbonate Systems. *Macromolecules* (2022) doi:10.1021/ACS.MACROMOL.2C01683.

149. Watanabe, M., Rikukawa, M., Sanui, K. & Ogata, N. Effects of Polymer Structure and Incorporated Salt Species on Ionic Conductivity of Polymer Complexes Formed by Aliphatic Polyester and Alkali Metal Thiocyanate. *Macromolecules* **19**, 188–192 (1986).

150. Aziz, S. B. Li+ ion conduction mechanism in poly (ε-caprolactone)-based polymer electrolyte. *Iranian Polymer Journal (English Edition)* **22**, 877–883 (2013).

151. Mindemark, J., Sun, B., Törmä, E. & Brandell, D. High-performance solid polymer electrolytes for lithium batteries operational at ambient temperature. *J Power Sources* **298**, 166–170 (2015).

152. Lin, C. K. & Wu, I. Der. Investigating the effect of interaction behavior on the ionic conductivity of Polyester/LiClO4 blend systems. *Polymer (Guildf)* **52**, 4106–4113 (2011).

153. Kato, Y. *et al.* High-power all-solid-state batteries using sulfide superionic conductors. *Nature Energy 2016 1:4* **1**, 1–7 (2016).

154. Gopakumar, G., Abe, M., Hada, M. & Kajita, M. Dipole polarizability of alkali-metal (Na, K, Rb)–alkaline-earth-metal (Ca, Sr) polar molecules: Prospects for alignment. *J Chem Phys* **140**, 224303 (2014).

155. Gonzalez Puente, P. M. *et al.* Garnet-type solid electrolyte: Advances of ionic transport performance and its application in all-solid-state batteries. *Journal of Advanced Ceramics 2021 10:5* **10**, 933–972 (2021).

156. Lascaud, S. *et al.* Phase Diagrams and Conductivity Behavior of Poly(ethylene oxide)-Molten Salt Rubbery Electrolytes. *Macromolecules* **27**, 7469–7477 (1994).

157. Zheng, Q. *et al.* Optimizing Ion Transport in Polyether-Based Electrolytes for Lithium Batteries. *Macromolecules* **51**, 2847–2858 (2018).

158. Pesko, D. M. *et al.* Universal Relationship between Conductivity and Solvation-Site Connectivity in Ether-Based Polymer Electrolytes. *Macromolecules* **49**, 5244–5255 (2016).